DESIGN OF AQUEOUS-LIQUID CRYSTAL INTERFACES FOR BIOSENSING APPLICATIONS

INDU VERMA

A thesis submitted for the partial fulfillment of

the degree of Doctor of Philosophy

Department of Chemical Sciences

Indian Institute of Science Education and Research (IISER) Mohali

Knowledge city, Sector 81, SAS Nagar, Manauli PO, Mohali 140306, Punjab, India.

September 2019

DEDICATED TO

My Dear Papa

Declaration

The work presented in this thesis has been carried out by me under the guidance of **Dr. Santanu Kumar Pal** in the Department of Chemical Sciences, Indian Institute of Science Education and Research (IISER) Mohali, Mohali. This work has not been submitted in part or full for a degree, diploma, or a fellowship to any other university or institute. Whenever contributions of others are involved, every effort is made to indicate this clearly, with due acknowledgments of collaborative work and discussions. This thesis is a bonafide record of original work done by me and all sources listed within have been detailed in the bibliography.

Indu Verma

In my capacity as the supervisor of the candidate's thesis work, I certify that the above statements by the candidate are true to the best of my knowledge.

Dr. Santanu Kumar Pal

Acknowledgment

At the end of my graduate studies, it is a wonderful opportunity to thank all those who contributed in many ways to make this thesis possible and made the journey admirable for me. I want to express my sincere gratitude to the people who helped and supported me throughout the process.

First and foremost, I would like to thank my supervisor, **Dr. Santanu Kumar Pal**, for allowing me to carry out this thesis work in his laboratory and introducing the exciting field of liquid crystal based biosensors. I am highly thankful to my supervisor for his commitment and excellent teaching of the various facets of the field in a comprehensible manner, his encouragement, guidance, and suggestions from the initial to the final level of the thesis work. Without his assistance, this work would never have been materialized. I am profoundly grateful for his cordial understanding and amicable attitude towards work and life balance, which made my graduate study much easier.

I thank **Dr. Angshuman Roy Choudhury** and **Dr. Sugumar Venkataramani**, members of my doctoral committee, for timely and fruitful discussions during the annual assessment of my work. I am grateful to all the faculties of IISER for their teaching and constant encouragement.

I want to acknowledge the Department of Chemical Sciences and Biological Sciences for various departmental facilities like circular dichroism, spectrofluorometer, AFM, etc.

I thank our present director, **Dr. J. Gowrishankar**, our former directors, Prof. N. Sathyamurthy & Prof. Debi Prasad Sarkar, and former officiating directors, Prof. Siva Umapathy & Prof. Arvind, for providing the space and all the research and infrastructural facilities.

I am also thankful to current HOD, **Prof. Arulananda Babu**, and previous HOD, **Prof. K**. **S**. **Viswanathan** of the Department of Chemical Sciences for various departmental facilities.

I also appreciate the help and cooperation of the staff members of teaching laboratories, stores, purchase office, administrative offices, account section, library, and computing facility of IISER Mohali.

I want to thank Dr. Sumyra Sidiq, Dr. Dibyendu Das, Dr. Golam Mohiuddin, Dr. Manisha Devi, Dr. Rajib Nandi, Ipsita Pani, Neelima Rajeev, V. Swathylekshmi, Diksha Sharma and Shiny Maity for helping in various aspects of my thesis work. I also thank lab members of Dr. Samrat Mukhopadhyay's group for providing cuvettes for carrying out circular dichroism measurements and helping during some of the initial AFM experiments.

I am also thankful to my current and former lab-mates Shilpa, Sumyra, Monika, Dibyendu, Harpreet, Manisha, Ipsita, Musthafa, Supreet, Vidhika, Golam, Nazma, Rajib, Santosh, Subhrata, Shruti, Yogi, Joydip, Indu Bala, Varsha, Tarang, Diksha, Swathy, Neelima, Aayush. I am blessed to have the beautiful labmates who contributed to making the pleasant working atmosphere in the laboratory.

I wish to thank my dear friends Ipsita, Manisha, Vidhika, Supreet, and Musthafa for their positive camaraderie. They have showered love, care, affection during the tough times. Especially, I would like to thank Golam Bhaiya and Nazma Bhabhi. They have been great mentors and excellent moral support throughout the thesis work. Thank you for the delicious dinner times.

I express my sincere gratitude to my parents, **Smt. Hemlata** and **Shri Narendra Verma**, my siblings, **Chiku**, **Arshi**, and **Soni**, for their love and support. They always put things in perspective and provided motivation when the rigors of research and thesis writing seemed distressing. I thank my fiancée, **Monu**, for being my constant pillar of strength and comforter throughout this journey. I am also thankful to my grandparents, Smt. Krishna, Shri Revti Sharan, Late Smt. Chandro, and Shri Raghubeer for their countless blessings. Especially, I would like to state about my Nani (Krishna), who regularly inquired about my research work and showed a keen interest in knowing about the social impact of my research. I would also like to thank my cousins Rocky and Shrey, Mama (Shri Pramod Kumar), Mami (Smt. Kalpana) and my whole family. It is the immense love and belief of them that carried me this far. I sincerely acknowledge my friends Punni, Gursharan, Nav, Navneet, Mek, Akki, and Yashu for their encouragement and care throughout my ups and downs. I am also grateful to my school teachers (Anju Mam, Indu Mam, Naveen Sir, Sanjay Sir, Bhasin Sir) for their valuable teachings and blessings. Finally, I thank the almighty for making me able to stand where I stand today.

Lastly, I acknowledge **IISER Mohali** for granting partial international travel support to participate in the International Liquid Crystal Conference held in Kyoto, Japan, in 2018. I am thankful to **IISER Mohali** for providing research fellowship for five years, financial support to carry out the experimental work, and also for all the research facilities that facilitated me to complete my Ph.D.

Indu Verma

Contents

Chapter 1

Introduction: Liquid Crystal Biosensors

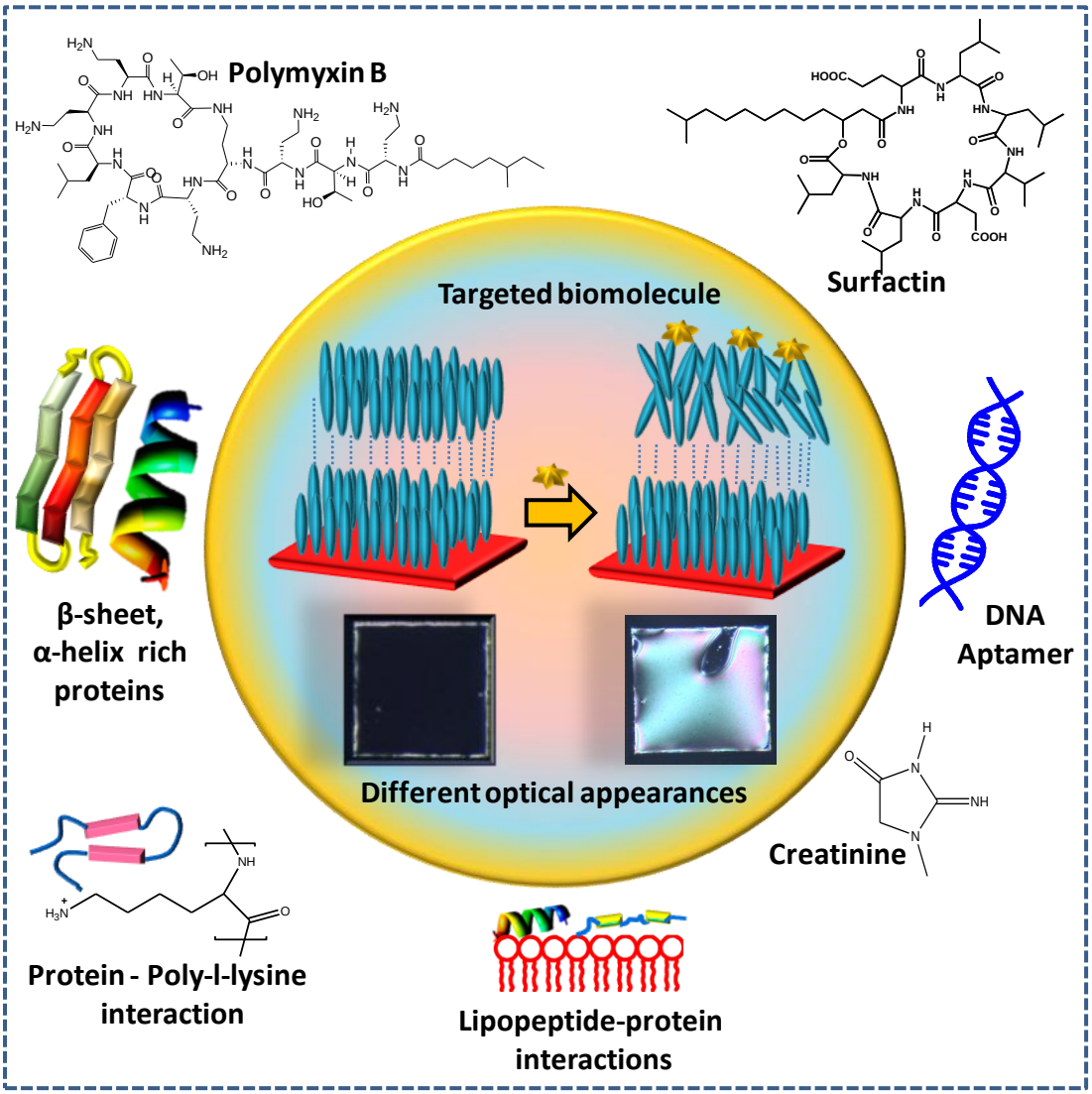

After serving in the display market for decades, liquid crystal (LC) materials are spreading their reach to the shining field of optical and biosensing technology. LC-based biosensors can allow label-free imaging of biochemical processes. Thus, LCs present a favorable opportunity to devise stimuli-responsive interfaces that can mimic the biological systems and direct the behaviors of the biological systems.

1.1 Outline

The basis of life and all biological processes is administrated by intermolecular interactions between biomolecules in a living being. Molecular recognition plays a critical role in biological interactions between biological elements, such as proteins, DNA, cells, and lipids. Any disorder or failure in the normal manner of action of interaction may generate medical ailments. Thus, the development of an understanding of such molecular-level interactions is crucial for numerous basic and applied areas of sciences such as bioinspired materials, therapeutics, diagnostics, and biosensors. In that context, bio-interfaces (interface formed between the biological element and any organic/inorganic material) play a crucial role in aiding the understanding of interactions between biomolecules and surfaces. In this thesis, we are primarily interested in constructing simple methodologies using stimuli-responsive interfaces formed by liquid crystals to detect important biomolecular interactions and biochemical events occurring at those interfaces. Implications of such interfaces in label-free biosensing will be discussed.

"Before cure, comes the diagnosis." Therefore, throughout history, efforts have been made to develop more effective technologies for rapid and accurate diagnosis of medical conditions. The development of medical diagnostic technology is one of the most important fields of applied research since it directly influences the overall health of the universal population. There has always been an imperative demand for highly sensitive and selective analytical methodologies capable of detecting such biological molecules or contaminants even at trace levels. Such a device, assay, or method which can detect a bio-chemical substance is known as a biosensor.[1,2] It involves two main components: (1) a biological component or bio-receptor which is essentially a recognition site to interact with the analyte, and (2) a transducer or detector element that identifies the interaction between bio-receptor and analyte and generates a measurable output signal which can be correlated with the presence of the target analyte in the sample. Bio-receptors are generally any sensitive biologically derived material such as an antibody, enzymes, proteins, nucleic acids, cells, or micro-organisms. A transducer could be optical, electrochemical, electronic, piezoelectric, and so.[3] The vital characteristics of a biosensor are (a) the selectivity of the bio-receptor for the specific target analyte even in the presence of other interfering species and (b) sensitivity of the transducer to detect the analyte at low concentration levels. A broad range of different materials has been investigated over the past decades for the design of interfaces that enable required

interactions with biological entities.[4-11] However, in most of the cell-based and biochemical assays, labeling is required, which complicates the sample preparation, limits the effective throughput, and increases the overall cost. Thus, the development of label-free sensors is a novel approach to achieve cost-effective and simple multiplexed detection systems.

Liquid crystals (LCs) are materials that combine properties of both liquids (fluidity) and crystalline solids (alignment of molecules). After scientific and technological revolution brought about by LCs in multibillion-dollar display technology, they are demonstrating excellent biomedical implications in optical imaging and diagnostics.[12-38] The alignment of LCs is highly susceptible to interfaces/surfaces that they are in contact with which can be communicated to the LC bulk phase up to a hundred micrometers away from the stimulus. LC materials are optically anisotropic; therefore, their orientational changes (for example, from planar to homeotropic alignment wrt interface) can be readily visualized (with the naked eye) under cross polarizers. The elasticity of LCs and their fluidity enable the surface-induced LC responses (such as stimuli induced deviation in the director) within tens of milliseconds, which allow the fast and real-time detection of bio-chemical analytes and events.[12-38] Thus, LCs can perfectly transduce the molecular-level information about subtle changes in the environment, thereby permitting a facile detection without the need for complex and expensive instrumentation.

This thesis mainly concentrates on the development of novel interfacial architectures formed between LC and aqueous environment for potential applications. The thermotropic nematic LCs used herein are immiscible with water, and thus presents an ideal interface which can be placed into contact with the analyte carrying fluid. The aim is to pre-requisitely stipulate such interfaces to detect targeted molecules and chemical events for the advancement of LCs in biosensing applications.

1.2 Liquid crystals

LCs are organic compounds which possess intermediary features of two major states of matter that is a crystalline solid and a liquid.[39-42] Typically, LCs have anisotropic physical properties like a solid and fluidity like a liquid. This remarkable feature gave them a combination of unique assets such as optical anisotropy, orientational ordering, electrical and magnetic properties along with the free-flowing nature. The LC can be categorized into many phases depending on the temperature or the concentration of the molecules in a

solution, as well as on the shape of the LC molecules. Thermotropic LC phases are obtained between the crystalline and the isotropic phase by changing the temperature (Figure 1.1). Lyotropic LC phases can be generated by changing the concentration of the organic molecules in a solution. Based on the shapes of the LC molecules, they can be divided into subphases such as calamitic and discotic. While the calamitic LC consists of rod-shaped molecules, the discotic LC contains disc-shaped molecules. Based on the molecular organization in a mesophase, or its symmetry, LCs are subdivided into nematics, smectics, cholesterics, and columnar mesophases. The work in this thesis has included nematic LCs, which consist of rod-shaped molecules.

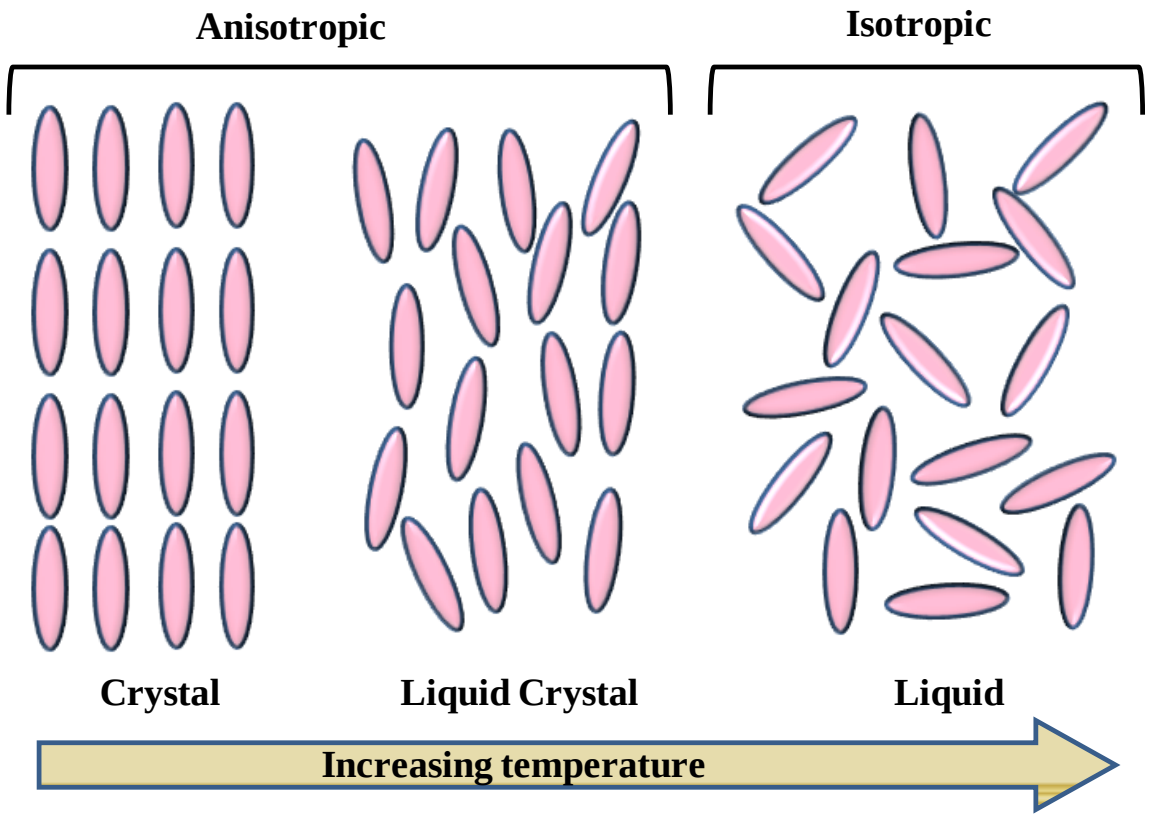

Figure 1.1. Cartoon illustration showing the emergence of the LC phase between solid and liquid state upon heating the solid material.

Extensive research on the development of LC materials over two decades has enabled its entry into the billion-dollar technology of LC displays that are now a household name. Apart from this common application of LCs, they have been studied over a decade for the development of non-display applications such as biological sensors, chemical sensors, actuators, color-changing fabrics, thermography and so on.[12-38,43-47]

1.2.1 Discovery of liquid crystal science

The discovery of the LC phase and materials does not imply that this phase was unknown to nature. LC phases are ubiquitously present in natural surroundings. For instance, DNA in living matter, cell wall cellulose in plants and fruits, collagen in bones, cornea or fish scales and chitin in the exoskeletons of insects exhibit LC ordering.[48-52] However, scientists were only aware of three physical states of matters, i.e., solid, liquid and gas.[42] It was only in late 19th century when Friedrich Reinitzer, an Austrian botanist, studied a derivative of cholesterol (cholesterol benzoate) and observed a turbid liquid state at 145 ºC that changed to clear liquid upon further heating to 179 ºC.[53] He consulted this unusual melting behavior with a German physicist Otto Lehmann. Lehmann carried out the optical characterization of the turbid phase under a polarizing microscope.[54] He concluded that the turbid phase observed by Reinitzer displayed properties of both solid and liquid and thus coined the term "crystalline liquid". Soon in 1922, the French crystallographer Georges Friedel credibly suggested that LCs represented a new state of matter and then classified the LC phases as nematic, schematic, and cholestric.[55] The term "mesogens" was also coined to describe the molecules forming LC phase (mesophase). Between the 1960s and 1970s, there were several advances made in LC science to develop new and useful LC phases.[56] In the starting, the applications of LCs were limited to small-sized displays such as pocket calculators and digital watches.[57,58] The future of LC science changed when in 1988, Washizuka et al. of Sharp Corporation demonstrated a TV-type color display of 14 inches which suggested that LC displays could replace the standard-at-the-time cathode ray tubes.[59] From the prototype in 1964 to the essential device in the electronic industries in 2007, the LC display technology has come a long way. It was in the early 2000s when Abbott with his co-workers first demonstrated that LCs could potentially be useful as ideal optical biosensors due to their stimuli-responsive features.[12] Since then, the scientific community is putting tremendous efforts to understand the basic principles behind designing such LC-based devices for sensing applications.[12-38] Now, Platypus technologies, a Madison-based company, along with researchers of University of Wisconsin-Madison have also commercialized an LC-based sensor for detection of toxic gases.[60] Crystal Diagnostics, a Kent-based company, is already developing innovative LC technology for rapid detection of several pathogens which is co-invented by researchers of the Liquid Crystal Institute and Northeastern Ohio University College of Medicine.[61]

1.2.2 Thermotropic nematic phase

The nematic phase is the most widely investigated LC phase and belongs to the class of thermotropic LCs. As discussed above, the thermotropic LCs display mesophase as a function of temperature. These are characterized either as calamitic nematic or discotic nematic depending upon the geometry/shape of constituent molecules. Figure 1.2a shows the molecules arranged in a nematic LC. The molecules possess a long-range orientational order and no long-range positional order. This implies that the LCs have a statistical preference to align along a particular direction, which is known as the director and defined by a vector of unit length ~n. In a nematic, the molecules tend to rotate freely around their long molecular axes, and there is no change in the director on turning the molecules upside-down even if chemical compositions on the two ends are different. Hence, the sign of the director is not significant and directions $\vec{n}$ and $-\vec{n}$ are always equivalent.

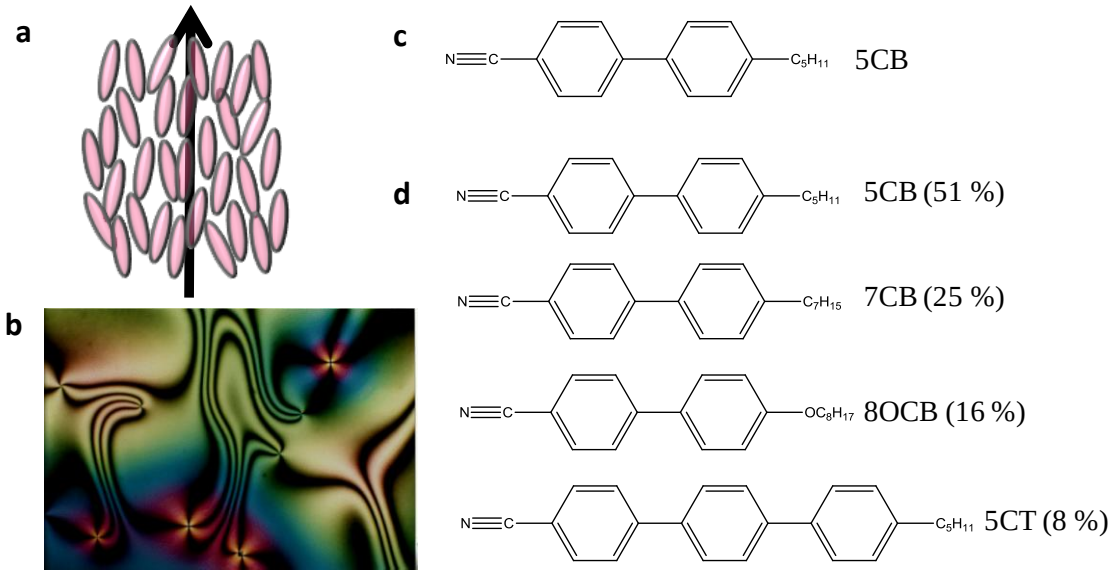

Figure 1.2. (a) Schematic of a nematic mesophase depicting long-range orientational ordering. The nematic phase has uniaxial symmetry, as indicated by the arrow. (b) Schlieren texture of a nematic mesophase [Courtesy: National Science Foundation, https://www.nsf.gov/news/mmg/mmg_disp.jsp?med_id=59511]. Chemical components of (c) 5CB and (d) E7.

In the bulk medium, the direction of the director is random, or it is defined by an external field. Whereas in confined systems, the director is characterized by the boundary

conditions presented at the interface LC is in contact with. Another characteristic of nematics is the thread-like texture (Figure 1.2b).[41]

The study herein utilizes the two most commonly known LC materials that exhibit nematic mesophase at room temperature, which are 5CB and E7 (Figure 1.2c,d). The 5CB (4-cyano-4'-n-pentylbiphenyl) displays the nematic mesophase from 18 ºC up to 34 ºC, above which it becomes isotropic fluid. It was the first LC compound synthesized that exhibited a nematic phase near room temperature. E7 LC is an amalgam of four different alkoxycyanobiphenyls: 51 wt.% 5CB, 25 wt.% 4-cyano-4'-*n*-heptyl-biphenyl (7CB), 16 wt.% 4-cyano-4'-*n*-oxyoctyl-biphenyl (8OCB), and 8 wt.% 4-cyano-4'-*n*-pentyl-p-terphenyl (5CT). The E7 exhibits a nematic phase within a long range of temperature, i.e., between -10 ºC to 60 ºC. In this study, we are primarily interested in these thermotropic nematic LCs for studying interfacial interactions for applications in biosensing.

1.2.3 Properties and Characteristics

1.2.3.1 Order parameter

The characteristic difference between a nematic phase and an isotropic liquid is generated by the degree of orientational ordering of the molecules which is quantified by an order parameter, *S*. S is defined in Equation 1.1 as shown below.[41]

$$\boldsymbol{S} = < \frac{\mathbf{3}\boldsymbol{cos^2\theta}\mathbf{-1}}{\mathbf{2}} > \qquad 1.1$$

θ stands for the angle formed between the director and the long molecular axis. In the clear isotropic phase, *S* is equal to zero, whereas *S* is equal to one for a crystal phase (in case of perfectly orientational ordering). Its value for a nematic phase usually ranges between 0.3 and 0.7.

1.2.3.2 Optical anisotropy (Birefringence)

Much like every anisotropic material, LCs are also birefringent. This implies that they exhibit different properties for light traveling with the electric field components parallel and perpendicular to the director or optic axis. Thus, the refractive indices of an LC are different in distinct directions, for instance: parallel to the director (known as extraordinary axis, $n_{\parallel}$), and normal to the director (known as ordinary axis, $n_{\perp}$).

Accordingly, the numerical difference $\Delta n = n_{\parallel} - n_{\perp}$ between these refractive indices (called ''birefringence'') is non zero. The nematic phases are generally optically positive, i.e., $n_{\parallel} > n_{\perp}$. For an optically negative phase, $n_{\parallel} < n_{\perp}$, as shown in Figure 1.3.

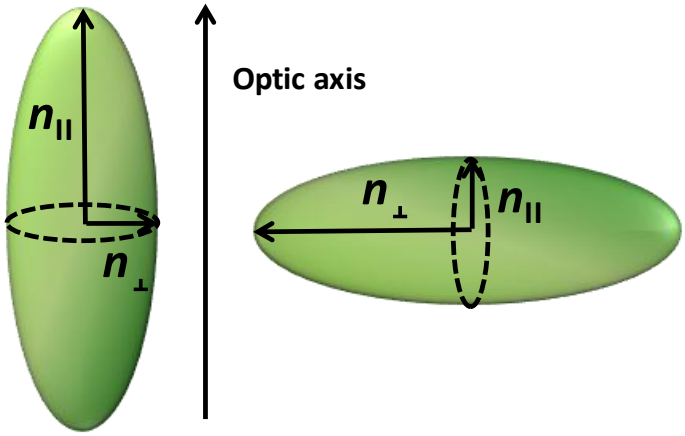

Figure 1.3. Schematic illustration of samples showing optically positive (left) and optically negative (right) behavior.

1.2.3.3 Surface-induced anchoring of LC

In the absence of any external force or contacting surfaces, the director field in the equilibrium state is uniform, which is governed by the internal ordering of the mesophase. However, interaction with any surface can influence the inherent ordering, leading to a distinct equilibrium state. Thus, the orientational ordering of LCs is extremely susceptible to the interfacial interactions between the mesogens and the confining medium. This phenomenon is known as surface-induced anchoring of LCs. The LC director (with respect to the surface) with the lowest free-energy orientation is generally termed as the easy axis of the LC.[62,63] Application of an external field or presence of a surface can induce a deviation in the director from the easy axis (Figure 1.4a). The amount of energy, which is required to move the director from the easy axis, is known as anchoring energy (W_a). It characterizes the anchoring strength quantitatively. Thus, the interfacial free energy, which is orientation-dependent, is often expressed as[42,64]

$$S = S_0 + \frac{1}{2} W_a \sin^2(\theta_s - \theta_e) \qquad 1.2$$

Where S is the total interfacial free energy, S_0 represents the orientation-independent component of interfacial free energy, θ_s is the orientation of surface director, and θ_e is the orientation of the easy axis.

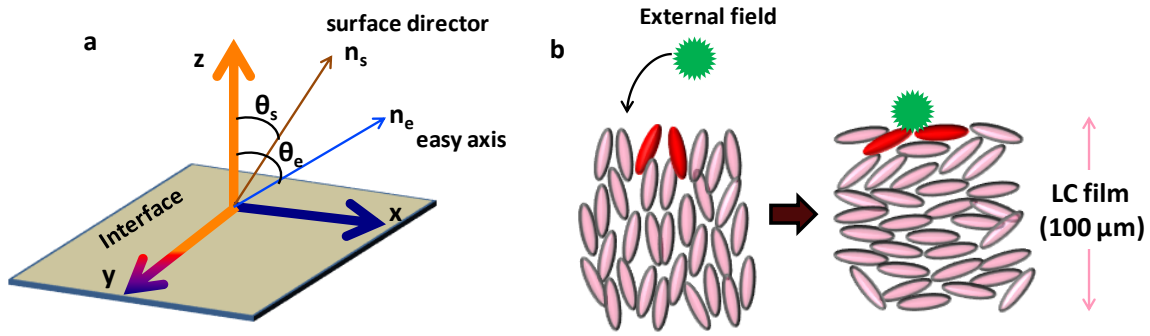

Figure 1.4. (a) Schematic illustration of the director and the easy axis of a nematic LC. (b) Orientational transitions of nematic LCs as a response to interfacial interactions. Redrawn from Ref. [42].

It is well established that the typical values of W_a are 10^{-3}-10^{-2} mJ/m^2.[42,64,65] Therefore, perturbation of the interfacial energetics on this scale, which can occur due to delicate change in the topography and chemical functionality of an LC interface, can potentially lead to orientational transitions in LCs. Unlike isotropic liquids, this surface-induced orientational preference is communicated over a distance of 100 μm (much greater than the size of nematic mesogen) from an interface due to the long-range ordering of LCs as shown in Figure 1.4b. The distinct ordering of LCs generates an anisotropic optical property that is easily characterized by using optical methods.[41,42,66]

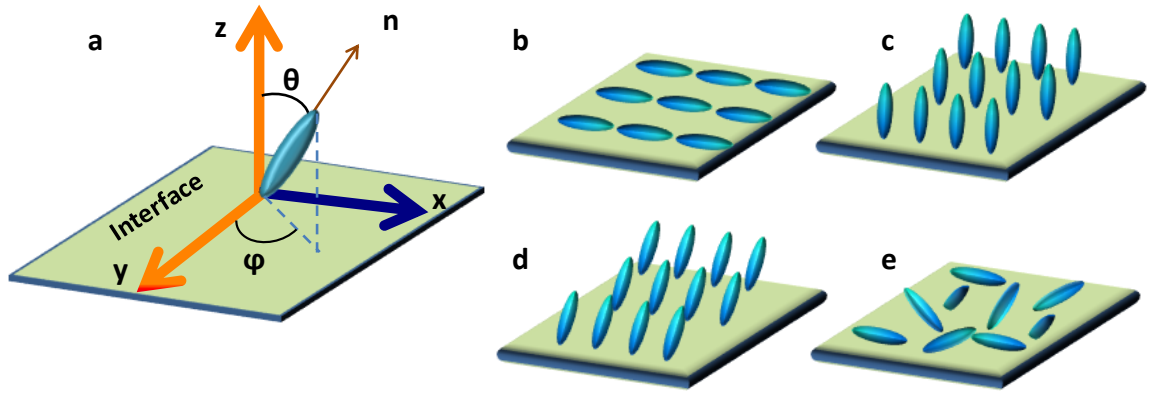

Figure 1.5. (a) Schematic demonstration of the two distinctive anchoring angles: polar angle (θ) and the azimuthal angle (ϕ). Anchoring of nematic LC on a surface: (b) uniform planar anchoring, (c) homeotropic anchoring, (d) tilted anchoring, and (e) degenerate planar anchoring. Redrawn from Ref. [42].

The orientation of the LC molecules on a surface is expressed by two angular components, azimuthal anchoring ϕ and polar anchoring θ, as shown in Figure 1.5a. The

polar angle is the angle formed between *n* and the substrate normal, y. The azimuthal angle ϕ represents an in-plane orientation of LC director with respect to reference azimuthal axis, x. Thus, the anchoring can be orientation of the director represented in Figure 1.5b-e: 1) $\theta = \pi/2$, ϕ = constant for uniform planar, 2) $\theta = 0$ for homeotropic and 3) $0 < \theta < \pi/2$, ϕ = constant for tilted anchoring and 4) $\theta = \pi/2$, ϕ = arbitrary for degenerate planar anchoring.[42]

1.2.3.4 Elastic energy

Long-range orientation within molecules in the LC phase generates elastic properties of LCs. For a nematic phase, the mesogens are uniformly aligned along with the director in the lowest free energy state. External forces (such as an electric field or confined boundary conditions) typically lead to deformation of the medium from its lowest energy configuration. Nematics deformations are usually of three basic modes: splay, twist, and bend as shown, schematically, in Figure 1.6. According to Frank and Oseen equation, in a confined LC system, an arbitrary curvature of a director can be expressed in terms of the above-mentioned deformations along with their associated elastic constants K_{11}, K_{22}, and K_{33}.[41]

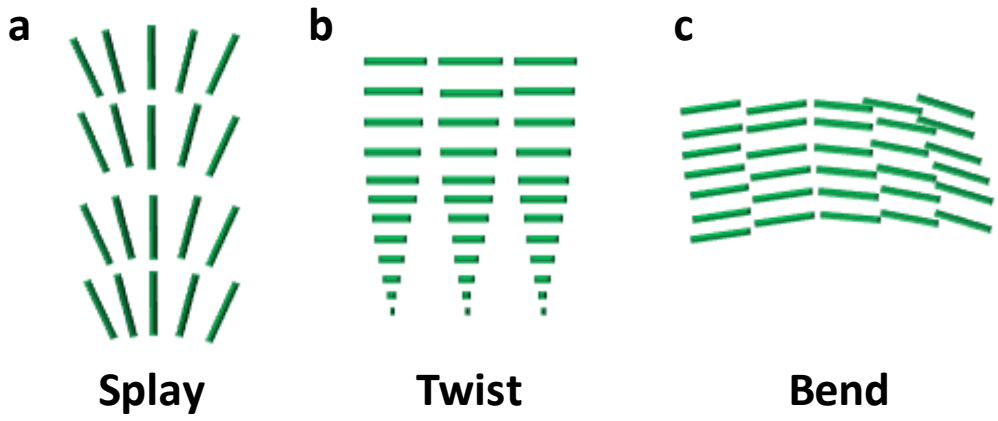

Figure 1.6. Schematic illustrations of three modes of deformation in LCs: (a) splay, (b) twist, and (c) bend. Redrawn after de Gennes and Prost.[41]

The LC elastic free energy density (F_d) coupled with the strain of a nematic LC is described in Equation 1.3 below [42,64,65]:

$$\boldsymbol{F_d = \frac{1}{2} K_{11}(\nabla.\hat{n})^2 + \frac{1}{2} K_{22}(\hat{n}.\nabla \times \hat{n})^2 + \frac{1}{2} K_{33}(\hat{n} \times (\nabla \times \hat{n}))^2} \quad 1.3$$

where n represents the director of the nematic LC.

The three elastic constants usually are of the order of 10^{-11} N.[41,65] Understanding the elasticity behavior of LC is essential in the study of the order parameter fluctuations and defect stability present in them. The relative importance of elastic energy stored within the LC film and orientation-dependent surface energetics contribution to the total free energy of LC depends on the geometry of the LC system and motivates many of the interesting interfacial phenomena.

1.3 Liquid crystals-aqueous interfaces: A biosensing tool

The combination of surface anchoring, elastic energy, and birefringence of LCs makes its potential utility as an optical sensing tool. The orientation of LCs, being highly susceptible to interfacial interactions, can be amplified into the LC bulk phase up to a hundred micrometers away from the interface. This cooperative behavior allows label-free visualization to detect and transduce the molecular-level information on surfaces as the LC presents distinct optical appearance (example bright and dark images) under polarized light. The elasticity of LC and their fluidity enable the surface-induced LC responses (such as stimuli induced deviation in the director) within tens of milliseconds, which allow the fast and real-time detection of bio-chemical analytes and events. Thus, identification of the orientations of LCs near interfaces facilitates the development of LC-based sensors that respond to the chemical and biological signals. In this thesis, we focused on interfaces formed between aqueous phases and thermotropic LCs, because of two main reasons: (a) interface formed is deformable due to immiscibility of thermotropic LC with water; (b) incorporation of aqueous phase at one side retains the natural activity of biological analytes and enables the investigations on the influence of biomolecular interaction on LCs.

Inspired by potential applications of LCs in chemical and biological sensing, a variety of approaches have been applied by the scientific community to generate LC-aqueous interfaces for investigating interfacial events, which include stabilization of LC films in micro-fabricated structures.[12,13,16,20] The widely known geometries of LC-aqueous interface are planar and curved interfaces of LCs. I will sequentially discuss the two geometries. The prototype for planar interfaces between LC and aqueous phase was demonstrated by Brake and Abbott in 2002.[12] The cartoon schematic for the same is shown in Figure 1.7a.

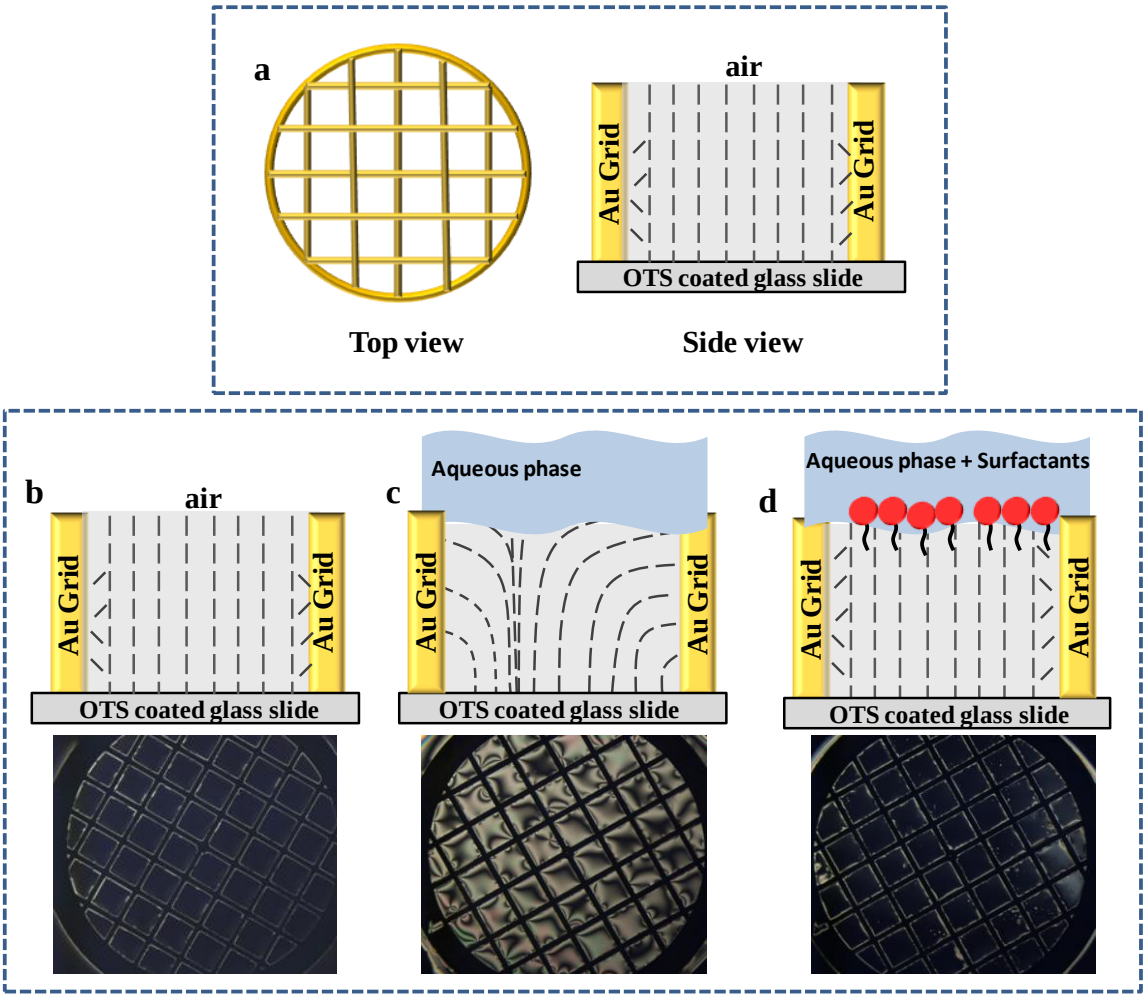

Figure 1.7. (a) Experimental design and explanation of the principle of LC biosensors designed by Abbott's group[12]. Redrawn with permission.[64] Representative POM images (only meant to show the typical optical appearance of LC film under POM) and corresponding cartoon illustration of the LC orientation in contact with (b) air, (c) water, and (d) amphiphile in the aqueous phase.

This approach used the placement of a metallic TEM grid onto a glass substrate. Prior to use, the glass substrate is chemically modified to define the ordering of LC at the bottom face. Two silanes, octadecyltrichlorosilane (OTS) or dimethyloctadecyl[3-(trimethoxysilyl)propyl]ammonium chloride (DMOAP), are mostly used to treat glass as they generate strong homeotropic (perpendicular) anchoring of most nematic LCs.[13] The LC material is then filled into the pores of the grid, which provides the mechanical support to LC against aqueous phase through capillary forces between the LC and the metal. The thickness of the LC film (when there is no excess LC on the film) is approximately the same as that of the grid. Figure 1.7a shows the director of the LC

inside one square of the grid. The bottom substrate of the LC film is in contact with OTS that aligns LC molecules perpendicular to the surface plane. The top surface of the LC is in contact with air, which also promotes homeotropic anchoring, thus inducing a uniformly perpendicular alignment of the director throughout the bulk. Such an arrangement of LC director yields a black image under crossed polarizers as shown in Figure 1.7b. Subsequently, the supported LC film is submerged in an aqueous solution to generate an approximately uniform LC-aqueous interface (Figure 1.7c). Water (or an aqueous buffer) usually align the LC director parallel to the substrate (''planar'' alignment), which generates hybrid configuration in bulk.[12,13] The effective birefringence in hybrid conditions is non-zero, and thus, the optical texture appears bright and inhomogeneous between crossed linear polarizers (Figure 1.7c). When surfactants are added into the aqueous phase, a dark optical appearance is produced, which is consistent with the homeotropic (perpendicular) orientation of LC (Figure 1.7d).[12]

Progressive research established that the adsorption of amphiphiles induces the homeotropic orientation of LCs at LC-aqueous interfaces.[16,64,67] The influence of the molecular structure (e.g., branching, chain length, etc.) and interfacial organization of adsorbed amphiphiles has been investigated in detail to derive the correlation between on the ordering of the LCs and intermolecular interactions between adsorbates/mesogens.[64] The study also provides strong evidence that the lateral hydrophobic interactions between hydrocarbon chains of mesogens and amphiphile mainly drives the homeotropic ordering of LC at aqueous interfaces. Logically, the hydrophilic part of the amphiphile would face the aqueous phase, while the hydrocarbon tails would intercalate into the LC medium. The nematic elasticity of the LC has been found to play a significant role in directing the interfacial arrangement of molecular assemblies.[68] An LC-aqueous interface is very susceptible to the presence of amphiphiles, such as naturally occurring phospholipids that form the main component of a biological membrane, thus several biomolecular interactions have been investigated using such interfaces. A wide range of designs has been developed using the biomimetic nature of this interface for sensing biomolecular phenomena. The reorganization of the phospholipids in the presence of specific biomolecular interactions with proteins has been found to trigger ordering transitions in the LCs.[13] It is also known that the highly specific event of DNA hybridization occurring at LC-aqueous interface induces an orientational transition of LC.[33] LCs offer potential implications in sensing as they trigger an ordering transition based on the molecular

structure of analytes present at the interface. For instance, lipids induce a homeotropic ordering of LC; however, proteins promote a planar anchoring of LC at the aqueous interface.[12] Not only this, LCs exhibited distinct ordering based on the aggregated states of proteins.[13,69] In recent years, the LC-based interfaces have been applied as an optical tool to detect several biomolecules, biomarkers and toxic analytes such as acetylcholinesterase[70], bile acids[71], cellulase and cysteine,[72] pesticides[73], glucose[74], heavy metal ions such as Cu^{2+}, Hg^{2+},[75-77] human breast cancer cells[78], and so on. With this exceptional ability to detect subtle interfacial variations, interfaces formed between LCs and aqueous phases characterize an exciting and promising class of stimuli-responsive materials for technological advancement. Development in experimental and theoretical studies of the alignment process in LC, which is the physical basis of LC biosensors, will continue to give insight into the interfacial interactions to grow more sensitive and efficient use of the alignment mechanisms.

Another interesting platform for LC-based biosensors is LC-in-water emulsion. The simplest process for the preparation of LC emulsion in water is by sonication and vortex mixing of LC and aqueous media (e.g., 5 μL of LC in 0.5 mL of water).[79] This methodology generates LC droplets with the polydispersed population of diameters ranging in several micrometers (Figure 1.8a). Monodispersed LC droplets can be prepared using polyelectrolyte multilayer capsules as templates[80] or by using microfluidics[81]. In some confined LC systems as in droplet geometry, the surface-anchoring conditions are unlikely to be satisfied through the continuous strain of the LC. Thus, as a result of the high local elastic free energy density of the LC, the topological defects are generated in the LC to satisfy the boundary conditions.[82-84] These defects are defined as the localized regions of LC in which the orientational order of the LC is significantly reduced as compared to that of the bulk LC.[85,86] Textures observed in nematic droplets depend upon the droplet sizes and the anchoring conditions. The respective equilibrium director configuration is determined by the delicate balance of energetic involving bulk elastic energy contributions and surface energy contributions. The bulk elastic energy of LC droplet is linearly proportional to the radius of the droplet (KR; K and R, respectively, represent the elastic constant of LC and the droplet radius), whereas surface energy varies with the square of the R (WR^2; W is the anchoring strength coefficient).[65,87,88] The thermodynamic considerations led to the proposition that for large droplet radii ($R > K/W$), the energetic surface contribution dominates. Whereas in small

droplets (R < K/W), the influence of topological constraints enforced by the interface disappears and the director configuration is then concluded exclusively by the bulk elasticity of the LC.[89]

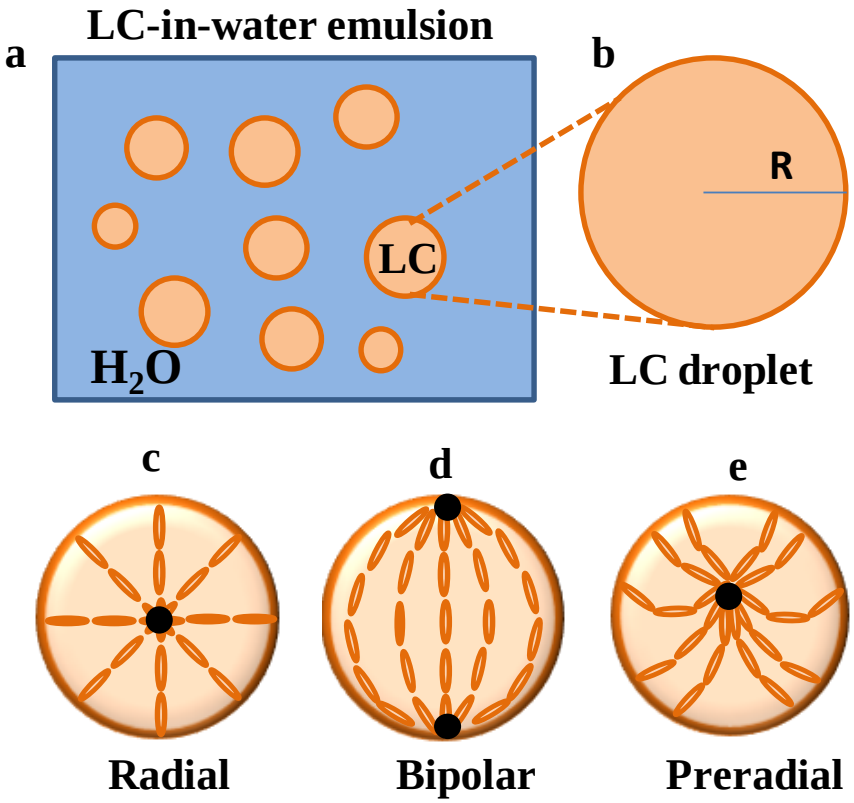

Figure 1.8. Schematic illustrations of (a) polydispersed LC droplets in water. (b) An enlarged version of a LC droplet with radius R; (c-e) the director configurations for (c) homeotropic (radial), (d) tangential (bipolar), and (e) tilted (pre-radial) anchoring of the LC at the droplet interface. Black solid circles in (c-e) represent topological defects in LC droplets. Adapted from Ref. [66,88].

The defects in LC droplets can provide a simple probe to identify the orientation of LC at the interface. Besides visualizing these point defects by polarized light microscopy, they are more readily viewed using bright-field microscopy (the removal of the analyzer in a polarized light microscope) because they strongly scatter light due to different refractive index as compared to defect-free regions.[85,86] When the ordering of LC is homeotropic with respect to the interface, the director adopts a so-called radial configuration within the droplet.[88] The radial configuration is identified by a single point defect positioned at the central core of the droplet (Figure 1.8c). When the orientation of LC is planar at the interface, then the director adopts a bipolar configuration within the droplet in which two

point defects (called boojums) are formed at the opposite poles of the droplet (Figure 1.8d).[88] The third possible director configuration is pre-radial configuration in which the orientation of the LC is tilted at a droplet's interface. It also exhibits a single point defect similar to the radial one; however, this defect is located away from the center and near the surface of the droplet (Figure 1.8e). The contribution of defects to the total free energy of a droplet is often neglected as it is typically two orders of magnitude lesser than the elastic and surface anchoring energies. In spite of this, defects play an important role in directing the interactions of LC droplets with some biological amphiphiles (for example, endotoxin).[79] The rich phases, large surface areas, and exclusive tunable optical properties of LC droplets offer a promising design of functional LC materials that responds to remarkably low concentrations of biologically relevant species. In those studies, the role of topological defects has been importantly discussed. Thus, this aspect of LC-based biosensors represents an exciting domain of materials chemistry that warrants extensive research.

1.4 Significance of biomolecules/analytes addressed in the study

1.4.1 Polymyxin B

Polymyxin B (PmB) is a naturally occurring lipopeptide produced by *Bacillus polymyxa.* It consists of a heptapeptide ring attached to a peptidic tail and a short acyl chain. It is the oldest and strongest antibiotic drug that is used to treat multidrug-resistant bacteria.[90] Its molecular structure allows the organization of self-assembly with the presentation of highly dense peptide functionalities at the exterior of various surfaces and nanostructures. Its antibacterial mechanism is considered to be driven by a range of molecular interactions with bacterial membrane followed by its organization at phospholipids interface and penetration into the membrane leading to the disruption of bacterial cells integrity.[91,92] PmB, which is otherwise structurally disordered in aqueous solution, exhibits the higher-order structure with a combination of fixed and flexible regions (associated with the head group and backbone, respectively) at phospholipid interfaces. Such association allows this small peptide to carry out a set of varied tasks with a high degree of structural specificity.[91] Interestingly, polymyxin nonapeptide, a derivate of PmB, which lacks the acyl chain displays no or little bactericidal effect on microorganisms consistent with the loss of conformational flexibility in the molecule.[93,94] The free amino groups of PmB is known to interact with negatively charged

phospholipids and serum constituents in tissues which causes its deactivation *in vitro.*[95-97] This intervention not only decreases its efficacy but leads to tissue toxicity as well due to its accretion in different body organs.[98-100] Thus, the threat of the post-antibiotic era and inadequate therapeutic options[101,102] is compelling scientific community to progress towards the development of simple approaches to recognize the possible interactions of serum proteins with subsisting antibiotics to modify the drug design consequently. In part A of the 2nd chapter of this thesis, we discuss the influence of self-assembly of PmB on the orientational ordering of LCs at aqueous-LC interfaces. PmB laden LC-aqueous interfaces have been further employed to monitor the adsorption behavior of several serum proteins.

1.4.2 Surfactin

Surfactin (SFN) is a powerful bio-surfactant produced by the Gram-positive bacteria *Bacillus subtilis*. It is constructed of a cyclic heptapeptide head group connected with a 12–16 carbon atoms long hydrophobic fatty acid tail.[103] Due to its amphiphilic structure, it is capable of reducing the surface tension of water from 72 mN/m to 27 mN/m even at 20 μM of concentration.[104,105] As a consequent strong surface activity, it has shown potential in bioremediation of heavy metals and enhanced oil recovery.[104,106] These amphipathic features enable the SFN molecule to interact with biomembranes and disrupt the membrane integrity.[107,108] Therefore, it is known to exhibit effective biological characteristics such as antibacterial, antiviral, antitumor, and hemolytic activities.[109,110] Compared with the chemical surfactants, SFN is gaining an enormous interest because of its versatile applications, natural production, high biodegradability, and retained activity at extreme temperatures and pH.[111] In solution, the heptapeptide loop of surfactin adopts a 'horse saddle' shape with β-sheet conformation.[112,113] Previously, efforts have been made in order to evaluate their ability to penetrate and interact with lipid membranes by using certain studies such as fluorescence microscopy, Brewster angle microscopy, and atomic force microscopy at lipid monolayer model systems.[114-122] Similarly, the adsorption behavior of SFN on solid-liquid and air-liquid interfaces has been studied using various techniques.[123,124] These techniques are time-consuming, laborious, expensive, and demand skilled expertise. In this thesis, Part B of 2nd chapter uncovers the interaction of SFN with LC at the LC-aqueous interface and corresponding ordering transitions of the LC. These lipopeptidic laden LC-aqueous interfaces are highly regarded as stimuli-responsive systems with a potential application in the detection of toxic amyloids.

1.4.3 Proteins

Proteins are biopolymers of amino acids (polypeptides), connected by peptide bonds. The amino acid sequence is encoded by its gene, establishes a protein's structure and function. Inside living organisms, they are most abundantly content and are involved in nearly every process within the cells. They perform a large set of functions such as catalysis of metabolic reactions, transportation of molecules, providing structures and mechanical stability to cells and tissues, DNA replication, and so on. Proteins often are involved in interactions with other proteins, DNA, lipids, carbohydrates, and other molecules for function. The structure of a protein is known to play a crucial role in performing its function. In chapters 2 and 5 of this thesis, we demonstrate application of decorated LC-aqueous interfaces (PLL-LC, PmB-LC, SFN-LC) to report the label-free imaging of adsorption events of several proteins (bovine serum albumin, concanavalin A and fibronectin as mentioned below). Thus, it would be useful to provide a brief introduction to these proteins discussed in different parts of this thesis.

1.4.3.1 Bovine serum albumin

Albumin is the most abundant protein that exists in serum (about 60% of the total protein content). It is one of the oldest discovered and most intensely studied proteins.[125] Serum albumins attract a lot of scientific attention in understanding the drug pharmacodynamics and pharmacokinetics as the nature and strength of interactions between albumins and small molecules are associated with the extent of drug absorption, distribution, metabolism, and excretion.[126] In such studies, bovine serum albumin (BSA) is usually considered as a relevant model, due to its structural resemblance with human serum albumin (approximately 76%), its low cost and wide accessibility.[127,128] The BSA molecule is a globular protein which consists of 583 amino acids and has a molecular mass of 66.4 kDa.[125] The secondary structure of BSA is mainly composed of α-helices (60%), with the remaining polypeptide chain arranging in turns, in extended or flexible regions between subdomains.[125] Serum albumins are mainly the transporter proteins which carry and dispose many endogenous and exogenous compounds (such as drugs, hormones, and fatty acids) by forming a molecular complex.[129] This group of proteins also helps in maintaining the blood osmotic pressure and blood pH.[130,131]

1.4.3.2 Concanavalin A

In living beings, interactions between carbohydrates and proteins form the basis for many important physiological processes, and alteration in such interactions can cause pathological states such as bacterial and viral infections, inflammation, cancer metastasis, and so on.[132] Thus, understanding of such interactions has attracted a great deal of attention to aid in the realization of biological processes and the development of biosensors for diagnostics. Concanavalin A (Con A) is one such lectin protein that can bind to certain saccharides with high specificity.[133] It is an all-β protein composed of 237 amino acid residues. Under neutral conditions, it exists as a tetramer in which each subunit has two divalent cation binding sites, each for Mg^{2+} and Ca^{2+}.[133] It is known to bind various sugars, glycoproteins, and glycolipids, specifically to the α-D-mannosyl and α-D-glucosyl residues.[134] Interactions of ConA with the cellular membrane glycoprotein are known to trigger several biochemical processes such as agglutination, cell mitogenesis, and apoptosis.[135-137] Therefore, it is widely used as a model protein in biology and biochemistry. Several approaches have been reported to detect ConA.[138-140] Also, ConA shares structural homology with human serum amyloid protein, which is abundantly found in toxic amyloid deposits in several neurological disorders.[141] Moreover, ConA displays structural flexibility due to lack of disulfide bonds which favors the conformational changes in the protein.[142] Overall, understanding of its aggregation mechanism is of a great scientific deal for a range of biomedical applications.

1.4.3.3 Fibronectin

Fibronectin (FibN) is a dimeric glycoprotein in which monomers of approximately 220–250 kDa are connected by disulfide bonds.[143] The protein exists in two forms: 1) a soluble form which is present in bodily fluids and 2) insoluble fibrillar state which is present in the extracellular matrix (ECM), connective tissues, and basement membranes.[144] This insoluble form of FibN performs most of its known biological functions ranging from embryogenesis, tissue repair, blood clotting, inflammation, tumorigenesis, and cellular migration.[145,146] The reorganization of FibN dimers into fibrillar matrices cell is a complex multistep process that is initiated and mediated by adherence of cells to surfaces. The initial step involves a reversible interaction of FibN with the $\alpha_5\beta_1$ integrin (via the Arg-Gly-Asp sequence) present at the cell surface.[147] The subsequent intermolecular association triggers the formation of large detergent-insoluble fibrillar matrices of

FibN.[148-150] For a detailed understanding of the fibril formation pathway, cell-based assays present several complications, including lack of control over other dynamic events during cell attachment. In 1999, Vogel et al. identified cell-free conditions under which FibN is extended into fibrillar networks near a monolayer of dipalmitoyl phosphatidylcholine (DPPC) (biomimetic surface).[151] The fibrillar aggregates of FibN have been found in some pathological states such as kidney glomerulopathy.[152] In several other diseased states, the concentration of FibN in bodily fluids has been found largely deviated from the normal range.[153] Techniques such as enzyme-linked immunosorbent assay[154] and SDS-PAGE[155] are widely used for detecting FibN but present limitations in terms of laborious procedures and complicated operation.

1.4.4 DNA and Aptamers

Deoxyribonucleic acid (DNA) is the basis of all living forms. It is the main component of chromosomes and located inside the nucleus of cells. It stores the genetic information which is used in the proper functioning of biological processes inside living organisms. Natural DNA is a duplex made of up of two DNA strands (also known as a polynucleotide). Each DNA strand is composed of nucleobases (guanine, adenine, cytosine, and thymine), deoxyribose sugar and the phosphate backbone. The two strands are connected by Watson Crick hydrogen bonding i.e. three H-bonds are linked between G-C and two between the A-T bases (Figure 1.9).[156] Over the past two decades, development in oligonucleotide technology has brought substantial advancement in nanotechnological applications such as therapeutics and diagnostics.[157-159] Especially, nucleic acid-based metal sensors have been developed due to several desirable structural properties of polynucleotides.[160] Firstly, nucleotides are highly stable, cost-effective, easy to modify as compared to the existing diagnostic motifs such as antibodies. Secondly and importantly, anionic phosphate backbone of nucleic acids allows electrostatic attraction with metal ions whereas various nucleobases coordinate with metal ions with different affinities.[161-163] The strategy behind the application of nucleic acids for sensing is to generate functional nucleic acid sequences, commonly called aptamers, that can accommodate specific metal coordination sites through tertiary or secondary folding.[160] The aptamers are isolated from a huge library of nucleic acids containing 10^{13} to 10^{16} random sequences by the method of SELEX (systematic evolution of ligands by exponential enrichment).[164,165] In chapter 3 of this thesis, we discuss a novel LC sensor for detection of toxic lead (II) ions by exploiting the aptamer-metal ion binding. Such

systems form the basis of new soft materials that permit LC ordering to propagate from the macroscale to the optical scale with remarkable sensitivity. In chapter 6, we report the fabrication and application of polymer-coated LC droplet emulsion towards the development of DNA based drug nanocarriers.

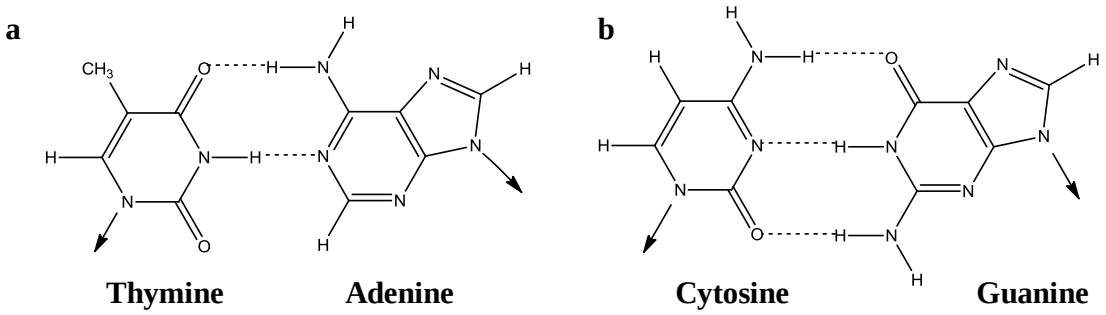

Figure 1.9. Hydrogen bonding between nucleobases: (a) two H-bonds between A-T and (b) three H-bonds between G-C.

1.4.5 Creatinine

In tissues and organs, creatinine is spontaneously produced during the biological conversion of creatine (an energy source for many biological processes) into phosphocreatine catalyzed by creatine kinase.[166] Creatinine is ubiquitously found in serum, erythrocytes and all bodily secretions, such as sweat, bile, and gastrointestinal fluids. After its generation in muscles and other body parts, it is excreted unchanged by kidneys primarily by glomerular filtration. When there is a deficiency in the filtration by kidneys, the blood creatinine concentrations rise. Therefore, creatinine concentrations in blood and urine may be useful to estimate the creatinine clearance, which acts as an important indicator for renal health and muscular functioning.[167,168] Creatinine emerged as the second most examined biomolecule for clinical analysis after glucose. The typical range of creatinine levels in the serum of healthy adults is 50-100 μM. Creatinine levels outside this range indicate renal disease (100-500 μM), kidney failure (≥800 μM) or muscular malfunctioning (≤ 40 μM).[166] The most common clinical test performed for creatinine levels in both blood and urine is based on the Jaffe method.[169] The Jaffe method involves the colorimetric readout of the specimen generated in the presence of picric acid. The reaction between creatinine and picric acid forms a chromogen that adsorbs within the wavelength range of 470-550 nm, and thus the color of the specimen turns red. The reaction is highly sensitive to temperature and pH but is non-specific for

creatinine due to interference from other serum components such as proteins. However, it is still widely used due to its cost-effectiveness and rapid analysis (~15 min). The chapter 4 of the thesis discusses the fabrication of a LC-based sensor for specific and label-free detection of creatinine up to its healthy levels.

1.5 Polarizing optical microscopy

Polarizing optical microscopy (POM) is a simple method that makes use of polarized light for imaging birefringent materials, including LCs. The optical appearance of LC when viewed under POM determines the orientational ordering of LCs. Typically, the illuminated light passes through a linear polarizer and is transmitted through the sample. The transmitted light is passed from another polarizer at the top (called "analyzer") (Figure 1.10).

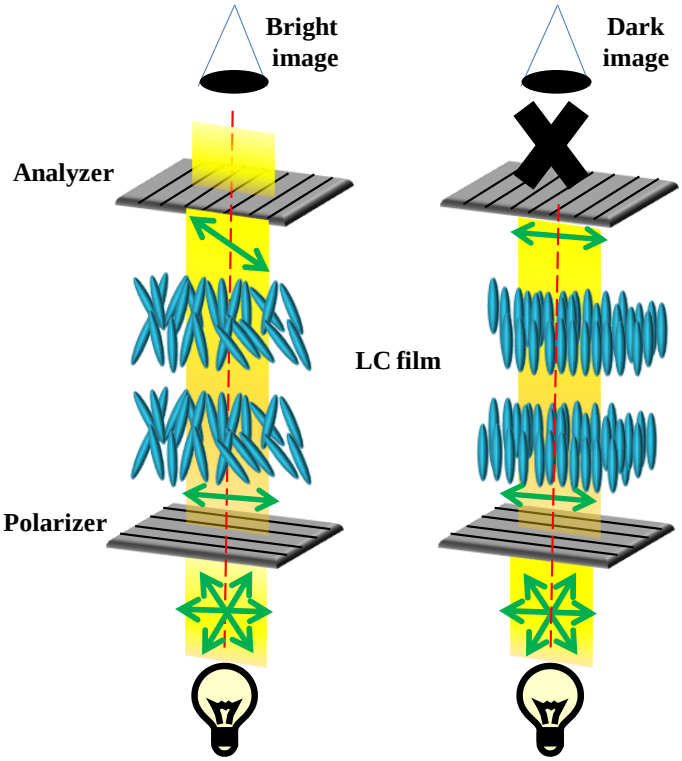

Figure 1.10. The working principle of a polarized optical microscope equipped with crossed-polarizers. Different orientations of LCs, when observed between crossed polarizers, generate distinct optical appearance.

The two polarizers are arranged perpendicularly to each other. Since LCs are birefringent, two distinct refractive indices are generated depending on the polarization of the light and the director of the LC. This may rotate the plane of polarization of the transmitted light.[40,41] As discussed above, several anchoring conditions of LCs are often explained as

homeotropic (perpendicular to the interface), planar (parallel to the interface), or tilted (at some acute angle to the interface). When the LC molecules are arranged in tilted fashion [i.e., the orientation of the LC molecules is perpendicular to the bottom surface (homeotropic alignment on DMOAP/OTS) and is parallel on the top surface], some component of the light passes through the thin film of the LC. This phenomenon results in the colored texture when viewed under crossed polarizers (Figure 1.10a). However, when the LC molecules are oriented perpendicular to the surface, the polarized light will be completely blocked by the analyzer, and the corresponding LC optical texture appears uniformly dark (Figure 1.10b).

1.6 Organization of the thesis

This thesis will describe the work done using thermotropic LCs for recognizing and imaging the molecular level interactions occurring at the aqueous interface along with an implication in the detection of certain interfacial events and analytes of biological importance.

1.6.1 Ordering transitions in LCs in presence of cyclic amphiphiles

Previously known sensors that utilize LC-aqueous interfaces are mostly based on orientations of LCs influenced by the organization of linear amphiphiles at those interfaces. In that context, the effect of cyclic amphiphiles on the ordering of LCs at aqueous interfaces remains relatively unexplored. Thus, the development and understanding of such systems present ample opportunities to design new LC-based multifunctional assays. Divided into two parts, the second chapter[170,171] elucidates the design of two novel stimuli-responsive LC-aqueous interfaces based on two different cyclic lipopeptides. In the first part, we have explored the interactions of a naturally occurring cyclic lipopeptide, PmB, with LCs at aqueous interfaces. The self-assembly of PmB at those interfaces induces a homeotropic anchoring of LC molecules driven by a combination of hydrophobic and ionic interactions between PmB and LC molecules. The orientation of LCs at PmB laden LC-aqueous interface further changes to planar/tilted in the vicinity of anionic proteins (BSA and hemoglobin). The dynamic response and the ordering of LCs are mainly influenced by electrostatic interactions possible between PmB and the protein molecules. We further observed that PmB decorated LC-aqueous interface is highly sensitive to the secondary structure of proteins even at nanomolar concentrations. Briefly, β-sheet rich proteins (ConA and FibN) lead to the formation of

elongated and fibrillar shaped optical domains of LC which are visibly different than that formed by globular and α-helical proteins (bovine serum albumin and hemoglobin). In the second part, a detailed investigation is carried out to understand the self-assembly of another cyclic lipopeptide, SFN, at aqueous-LC interfaces. Contrary to PmB laden interfaces, which restrict the imaging of only cationic proteins, SFN laden interfaces trigger an orientational ordering transition of LC molecules in contact with both anionic and cationic proteins. Overall, the cyclic lipopeptide based LC systems could be useful for sensitive and label-free optical detection of amyloidogenic proteins, which are abundantly found in several neurological disorders.

1.6.2 Aptamer based LC platform for detecting toxic metal ions

Detection of macromolecules by LCs has been easily achieved wherein ordering of LCs can sense the macromolecular binding events at nanomolar (nM) concentrations. However, the application of LCs to detect metal ions at aqueous interfaces remains a challenge in terms of selectivity and sensitivity. This is due to the following reasons. First, the system requires a high concentration of ions to induce an ordering transition of the LC molecules. Second, several metal ions have identical properties that pose challenges in terms of selectivity. Third, high mobility of ions imposes difficulty to form stable interfaces. In the third chapter[172], we have described a simple strategy for label-free detection of lead (II) ions (Pb^{2+}) utilizing an aptamer-ion binding event at LC-aqueous interfaces at nM concentration. Needless to say, Pb^{2+} is the second most abundant toxic metal ion and a major pollutant of soil and groundwater. In this work, we have exploited competitive binding events among a cationic surfactant, cetyltrimethylammonium bromide (CTAB), Spinach RNA (SRNA), and Pb^{2+} ions that lead to changes in the ordering of LCs (& thus optical appearances) at aqueous-LC interfaces. It is well known that LCs exhibit a homeotropic orientation in the presence of CTAB due to lateral hydrophobic interactions between hydrocarbon tails of CTAB molecules and the LCs. Interestingly, we have observed a change in the optical appearance (dark to bright) in the presence of the complex between SRNA and CTAB (SRNA-CTAB complex). Upon the introduction of Pb^{2+} ions, SRNA, and CTAB, the optical appearance of the LC at the aqueous-LC interface is changed from bright to dark. This change in the optical signal is mainly dependent on the competitive binding event between CTAB-SRNA and SRNA-Pb^{2+} at the LC interface and mainly induced by the reorganization of free CTAB molecules at those interfaces. Thorough investigation using fluorescence imaging,

competitive binding assay, and circular dichroism reveals that Pb^{2+} ions cause stabilization of G-quadruplex structures of SRNA. This may weaken the interactions between SRNA and CTAB molecules, which promote the self-assembly of CTAB molecules at the interface. Besides, the sensor exhibits good selectivity and a lower detection limit of 3 nM which is well below the approved levels of Pb^{2+} ions in drinking water. We have also demonstrated the applicability of the LC-based sensor in tap water for Pb^{2+} ion detection. Unlike laboratory-based heavy metal ion assays and existing LC-based techniques, this design is simpler in the context of instrumentation, easy optical readout, and can be envisaged to detect other toxic heavy metal ions.

1.6.3 Ordering transitions of LC enabled detection of creatinine

Examining creatinine levels in the blood is of immense significance during the diagnosis of renal health. The existing conventional methods for the laboratory analysis of creatinine suffer from limitations such as interference from other metabolites, complex and expensive instrumentation, to name a few. In the fourth chapter[173], we have designed a label-free biosensor using LCs for the detection of creatinine. The strategy involves (a) the construction of a pH-responsive LC-aqueous interface by doping LC with a pH-sensitive moiety, hexylbiphenyl carboxylic acid (HBA) and (b) utility of enzymatic catalysis of creatinine by creatinine deiminase that produces ammonium ions. The presence of creatinine and creatinine deiminase in the system increases the local pH of aqueous phase that deprotonates the HBA molecules in the LC film. The deprotonated form of HBA is more surface active than the protonated one. This, in turn, reorients the LC molecules from planar to homeotropic due to the self-assembly of amphiphilic HBA molecules at the interface leading to a distinct optical signal. The optical dynamic response (response time) of the LC to this enzymatic event directly correlates with the concentration of creatinine. Therefore, this system can be used to differentiate creatinine levels that of healthy adults and patients with renal disease. This approach is specific and can detect the concentration of creatinine up to 50 μM, i.e., that of the healthy adult.

1.6.4 Real-time imaging of proteins by poly-L-lysine coated LC droplets

Micrometer sized LC droplets suspended in aqueous phase have emerged as a simple optical method with immense potential in biosensing and bio-imaging. The different director configurations of LC droplets impart distinct optical appearances of the droplets under cross polarizers and bright-field microscopy. However, the characterization of

droplets remains comparatively difficult (with respect to LC-aqueous interfaces in planar geometry) due to the high mobility of the droplets. Earlier attempts to image LC droplets include immobilization of the droplets and introduction of glycerol in the emulsion. Both these methods tend to affect the ordering of LCs within the droplets which may interfere with the actual goal of sensing targeted analytes. In the fifth chapter[174,175], we have demonstrated a simple strategy for studying protein adsorption at poly-L-lysine (PLL) coated LC droplets. PLL-LC droplets show radial director configuration which remains stable even after coming in contact with the glass slide's surface. Divided into two parts, this chapter discusses the fabrication and application of LC droplets in real-time imaging of several interfacial events. In the first part, we have studied the ordering transition of PLL-LC droplets in contact with anionic proteins (bovine serum albumin, concanavalin A and cathepsin D). The introduction of proteins induces a rapid director configuration transition in droplets (mainly due to ionic interactions between PLL and proteins) to pre-radial/bipolar leading to a distinct change in the optical appearance of LC droplets. An important correlation is found between isoelectric points of proteins and sensitivity of LC droplets which suggests the role of different binding affinities of protein and PLL. In the second part of this chapter, we have discussed a detailed investigation about the adsorption and subsequent structural changes in a protein, FibN, in contact with PLL-LC droplets. FibN is a multifunctional glycoprotein whose altered conformational states are involved in several pathological conditions. Therefore, understanding of its adsorption properties at polymeric interfaces is of great research interest. In that direction, PLL-LC droplets present a simple cell-free route to probe the label-free imaging of FibN. A director configurational change of LC from radial to bipolar/pre-radial is observed in the presence of FibN. We have observed that the ordering transitions can be specifically and effectively tuned using divalent cations (such as Ca^{2+} ions). The interfacial interactions of FibN with PLL trigger a structural transformation of globular FibN molecules into an elongated form at the aqueous-LC interface as confirmed by fluorescence, circular dichroism, and atomic force microscopy measurements. This chapter provides the first study based on LC droplets to understand the polymer induced conformational changes of proteins at LC-aqueous interfaces.

1.6.5 Advancement of LC droplets towards design of DNA based drug carriers

As the DNA-based drug delivery materials begin to progress towards clinical use, the development of relevant designs to learn drug release behavior as well as the release

mechanism is gaining significant research attention. The sixth chapter[176] explores the utility of PLL-LC droplets for the detection of DNA and demonstrates an important and novel application of LC droplets in controlled drug delivery. The addition of DNA (ssDNA or dsDNA) triggers a director configuration transition from radial to pre-radial/bipolar within those droplets. Surprisingly, the subsequent introduction of complementary ssDNA to ssDNA adsorbed PLL-LC droplets does not result in any change in the director configuration of the LC droplets. Atomic force microscopy and fluorescence imaging suggest that this is likely due to the formation of nano-polyplexes of DNA and PLL at those interfaces. In addition, we have observed that dsDNA adsorbed PLL droplets can initiate a controlled release of an encapsulated model drug (propidium iodide) within dsDNA. The study shows the potential application of DNA sensing using PLL-LC droplets toward the development of DNA-based drug carriers.

References

1. Fan, X.; White, I. M.; Shopova, S. I.; Zhu, H.; Suter, J. D.; Sun Y. *Anal. Chim. Acta* **2008**, *620*, 8–26.
2. Bănică, Florinel-Gabriel (2012). Chemical Sensors and Biosensors: Fundamentals and Applications. Chichester, UK: John Wiley & Sons. p. 576.
3. Mehrotra, P. *J Oral Biol Craniofac Res.* 2016, 6, 153–159.
4. Bozzini, S.; Petrini, P.; Tanzi, M. C.; Zürcher, S.; Tosatti, S. *Langmuir* **2009**, *26*, 6529–6534.
5. Prime, K. L.; Whitesides, G. M. *Science* **1991**, *252*, 1164−1167.
6. Li, L. Y.; Chen, S. F.; Zheng, J.; Ratner, B. D.; Jiang, S. Y. *J. Phys. Chem. B* **2005**, *109*, 2934−2941.
7. Kühnau, U.; Petrov, A. G.; Klose, G.; Schmiedel, H. *Phys. Rev. E* **1999**, *59*, 578−585.
8. Stuart, M. A. C.; Huck, W. T. S.; Genzer, J.; Muller, M.; Ober, C.; Stamm, M.; Sukhorukov, G. B.; Szleifer, I.; Tsukruk, V. V.; Urban, M.; Winnik, F.; Zauscher, S.; Luzinov, I.; Minko, S. *Nat. Mater.* **2010**, *9*, 101−113.
9. Bhat, R. R.; Chaney, B. N.; Rowley, J.; Liebmann-Vinson, A.; Genzer, J. *Adv. Mater*. **2005**, *17*, 2802−2807.
10. Halstenberg, S.; Panitch, A.; Rizzi, S.; Hall, H.; Hubbell, J. A. *Biomacromolecules* **2002**, *3*, 710−723.
11. Curtis, A.; Wilkinson, C. *Biomaterials* **1997**, *18*, 1573−1583.
12. Brake, J. M.; Abbott, N. L. *Langmuir* **2002**, *18*, 6101−6109.
13. Brake, J. M.; Daschner, M. K.; Luk, Y. Y.; Abbott, N. L. *Science* **2003**, *302*, 2094−2097.
14. Brake, J. M.; Daschner, M. K.; Abbott, N. L. *Langmuir* **2005**, *21*, 2218−2228.
15. Kim, E. B.; Lockwook, N.; Chopra, M.; Guzman, O.; Abbott, N. L.; de Pablo, J. J. *Biophys. J.* **2005**, *89*, 3141-3158.
16. Lockwood, N. A.; de Pablo, J. J.; Abbott, N. L. *Langmuir* **2005**, *21*, 6805-6814.
17. Lockwood, N. A.; Mohr, J. C.; Ji, L.; Murphy, C. J.; Palecek, S. P.; de Pablo, J. J.; Abbott, N. L. *Adv. Funct. Mater.* **2006**, *16*, 618-824.
18. Park, J. S.; Teren, S.; Tepp, W. H.; Beebe, D. J.; Johnson, E. A.; Abbott, N. L. *Chem. Mater.* **2006**, *18*, 6147−6151.
19. Brake, J. M.; Abbott, N. L. *Langmuir* **2007**, *23*, 8497−8507.

20. Sivakumar, S.; Wark, K. L.; Gupta, J. K.; Abbott, N. L.; Caruso, F. *Adv. Funct. Mater.* **2009**, *19*, 2260−2265.
21. Lin, I. H.; Meli, M. V.; Abbott, N. L. *J. Colloid Interfaces Sci.* **2009**, *336*, 90-99.
22. Gupta, J. K.; Zimmerman, J. S.; de Pablo, J. J.; Caruso, F.; Abbott, N. L. *Langmuir* **2009**, *25*, 9016-9024.
23. Bi, X.; Hartono, D.; Yang, K. L. *Adv. Funct. Mater.* **2009**, *19*, 3760-3765.
24. Hartono, D.; Qin, W. J.; Yang, K. L.; Yung, L. Y. L. *Biomaterials* **2009**, *30*, 843−849.
25. Hartono, D.; Lai, S. L.; Yang, K. L.; Yung, L. Y. L. *Biosens. Bioelectron.* **2009**, *24*, 2289-2293.
26. Hartono, D.; Xue, C. Y.; Yang, K. L.; Yung, L. Y. L. *Adv. Funct. Mater.* **2009**, *19*, 3574-3579.
27. Kinsinger, M. I.; Buck, M. E.; Abbott, N. L.; Lynn, D. M. *Langmuir* **2010**, *26*, 10234-10242.
28. Bi, X.; Yang, K. L. *Biosens. Bioelectron.* **2010**, *26*, 107-111.
29. Tan, L. N.; Bertics, P. J.; Abbott, N. L. *Langmuir* **2010**, *27*, 1419-1429.
30. Tan, H.; Yang, S.; Shen, G.; Yu, R.; Wu, Z. *Angew. Chem. Int. Ed.* **2010**, *49*, 8608-8611.
31. Kinsinger, M. I.; Sun, B.; Abbott, N. L.; Lynn, D. M. *Adv. Mater.* **2007**, *19*, 4208-4212.
32. Park, J. S.; Abbott, N. L. *Adv. Mater.* **2008**, *20*, 1185−1190.
33. Price, A. D.; Schwartz, D. K. *J. Am. Chem. Soc.* **2008**, *130*, 8188−8194.
34. Birchall, L. S.; Ulijn, R. V.; Webb, S. J. *Chem. Commun.* **2008**, 2861−2863.
35. Sadati, M.; Apik, A. I.; Armas-Perez, J. C.; Martinez-Gonzalez, J.; Hernandez-Ortiz, J. P.; Abbott, N. L.; de Pablo, J. J. *Adv. Funct. Mater.* **2015**, *25*, 6050–6060.
36. Eimura, H.; Miller, D. S.; Wang, X.; Abbott, N. L.; Kato, T. *Chem. Mater.* **2016**, *28*, 1170-1178.
37. Adamiak, L.; Pendery, J.; Sun, J.; Iwabata, K.; Gianneschi, N. C.; Abbott, N. L. *Macromolecules* **2018**, *51*, 1978−1985.
38. Kim, Y.-K.; Huang, Y.; Tsuei, M.; Wang, X.; Nathan C. Gianneschi, N. C.; Abbott, N. L. *Chemphyschem* **2018**, *19*, 2037-2045.
39. Chandrasekhar, S. *Liquid Crystals*, Cambridge University Press, **1992**.
40. Collings, P. J. *Liquid crystals: nature's delicate phase of matter*, Princeton University Press, **2002**.

41. de Gennes, P. G.; Prost, J. *The physics of liquid crystals*, Oxford University Press, **1994**.
42. Collings, P. J.; Hird, M. *Introduction to Liquid Crystals Chemistry and Physics*, Taylor & Francis: London, **1997**.
43. Gupta, V. K.; Skaife, J. J.; Dubrovsky, T. B.; Abbott, N. L. *Science* **1998,** *279*, 2077-2080.
44. Shah, R. R.; Abbott, N. L., *Science* **2001**, *293*, 1296-1299.
45. Yang, K. L.; Cadwell, K.; Abbott, N. L. *Sens. Actuator B-Chem.* **2005**, *104*, 50-56.
46. Xu, H.; Bi, X. Y.; Ngo, X. M.; Yang, K. L. *Analyst* **2009**, *134*, 911-915.
47. Lagerwall, J. P. F.; Scalia, G. *Curr. Appl. Phys* **2012**, *12*, 1387e1412.
48. Rey, A. D. *Soft Matter* **2010**, *6*, 3402–3429
49. (a) Bouligand, Y. *Tissue Cell* **1972**, 4, 189-217, 192-217.; (b) Livolant, F.; Bouligand, Y. *J. Phys. (Paris)* **1986**, 47, 1813-1827.
50. Neville, A. C. *Biology of Fibrous Composites, Cambridge University Press, New York,* **1993**.
51. Besseau, L.; Bouligand, Y. *Tissue Cell* **1998**, *30*, 251-260.
52. Giraud-Guille, M. M. *Int. Rev. Cytol.* **1996**, *166*, 59-101.
53. Reinitzer, F. *Monatsh. Chem.* **1888**, *9*, 421–441.
54. Lehmann, O.; *Flussige Kristalle* , Engelmann, Leipzig, **1904**.
55. Friedel, G. *Ann. Phys.* **1922**, *18*, 273-474.
56. Kawamoto, H. *Proc. IEEE* **2002**, *90*, 460-500.
57. "Ultra thin 7 mm pocket calculator EL-8125 and EL-8025 (light gray background and high contrast black numerals)," Sharp Corp. News Release, Nov. 11, 1976.
58. Seiko digital watch catalog, Nov. 1976.
59. Nagayasu, T.; Oketani, T.; Hirobe, T.; Kato, H.; Mizushima, S.; Take, H.; Yano, K.; Hijikigawa, M.; Washizuka, I. "A 14-in-diagonal fullcolor a-Si TFT LCD," in Proc. Int. Display Research Conf., San Diego, CA, Oct. **1988**, 56–58.
60. http://www.platypustech.com/sensors.
61. http://www.crystaldiagnostics.com/our-company
62. Jerome, B. *Rep. Prog. Phys.* **1991**, *54*, 391–451.
63. Gupta, V. K.; Abbott, N. L. *Phys. Rev. E* **1996**, *54*, 4540–4543.
64. Lockwood, N. A.; Gupta, J. K.; Abbott, N. L. *Surf. Sci. Rep.* **2008**, *63*, 255–293.
65. Lavrentovich, O. D. *Liq. Cryst.* **1998**, *24*, 117-125.

66. Miller, D. S.; Carlton, R. J.; Mushenheim, P. C.; Abbott, N. L. *Langmuir* **2013**, *29*, 3154−3169.
67. Brake, J. M.; Mezera, A. D.; Abbott, N. L. *Langmuir* **2003**, *19*, 6436–6442.
68. Brake, J. M.; Daschner, M. K.; Abbott, N. L. *Langmuir* **2005**, *21*, 2218−2228.
69. De Tercero, M. D.; Abbott, N. L. *Chem. Eng. Commun.* **2009**, *196*, 234–251.
70. Wang, Y.; Hu, Q.; Guo, Y.; Yu. L. *Biosensors and Bioelectronics* **2015**, *72*, 25–30.
71. He, S.; Liang, W.; Cheng, K.-L.; Fang, J.; Wu, S.-T. *Soft Matter* **2014**, *10*, 4609-4614.
72. Wang, Y.; Hu, Q.; Tiana, T.; Gao, Y.; Yua, L. *Colloids Surf. B* **2016**, *147*, 100–105.
73. Wang, Y.; Hu, Q.; Tiana, T.; Yua, L. *Sensors and Actuators B Chemical* **2017**, 238, 676–682.
74. Khan, M.; Park, S.-Y. *Anal. Chem.* **2014**, *86*, 1493−1501.
75. Li, G.; Gao, B.; Yang, M.; Chen, L.-C.; Xiong, X.-L. *Colloids Surf. B* **2015**, *130*, 287–291.
76. Chen, C.-H.; Lin, Y.-C.; Chang, Y.-C.; Lee, A. S. H. *Anal. Chem.* **2015**, *87*, 4546−4551.
77. Singh, S. K.; Nandi, R.; Mishra, K.; Singh, H. K.; Singh, R. K.; Singh, B. *Sensors and Actuators B* **2016**, *226*, 381–387.
78. Ding, W.; Gupta, K. C.; Park, S.-Y.; Kim, Y.-K.; Kang, I. K. Biomater Sci. **2016**, 4, 1473-1484.
79. Lin, I. H.; Miller, D. S.; Bertics, P. J.; Murphy, C. J.; de Pablo, J. J.; Abbott, N. L. *Science* **2011**, *332*, 1297−1300.
80. Sivakumar, S.; Gupta, J. K.; Abbott, N. L.; Caruso, F. *Chem. Mater.* **2008**, *20*, 2063−2065.
81. Khan, W.; Choi, J. H.; Kim, G. M.; Park, S. Y. *Lab Chip* **2011**, *11*, 3493−3498.
82. Koenig, G. M. J.; de Pablo, J. J.; Abbott, N. L. *Langmuir* **2009**, *25*, 13318–13321.
83. Koenig, G. M. J.; Lin, I. H.; Abbott, N. L. *Proc. Natl. Acad. Sci. U.S.A.* **2010**, *107*, 3998–4003.
84. Koenig, G. M. J.; Ong, R.; Cortes, A. D.; Moreno-Razo, J. A.; de Pablo, J. J.; Abbott, N. L. *Nano Lett.* **2009**, *9*, 2794–2801.
85. Ruhwandl, R. W.; Terentjev, E. M. *Phys. Rev. E* **1997**, *56*, 5561−5565.
86. Zhang, Z. X.; van Duijneveldt, J. S. *Soft Matter* **2007**, *3*, 596−604.

87. Huang, W.; Tuthill, G. F. *Phys. Rev. E* **1994**, *49*, 570−574.
88. Drzaic, P. S. *Liquid Crystal Dispersions*; World Scientific Publishing Company: Singapore, **1995**.
89. Tomar, V.; Hernandez, S. I.; Abbott, N. L.; Hernandez-Ortiz, J. P.; de Pablo, J. J. *Soft Matter* **2012**, *8*, 8679–8689.
90. Storm, D. R.; Rosenthal, K. S.; Swanson, P. E. *Annu. Re*V. *Biochem.* **1977**, *46*, 723-763.
91. Bruch, M. D.; Cajal, Y.; Koh, J. T.; Jain. M. K. *J. Am. Chem. Soc.* **1999**, *121*, 11993-12004.
92. Domingues, M. M. et al. *Biopolymers* **2012**, *98***,** 338–344.
93. Cajal, Y.; Rogers, J.; Berg, O. G.; Jain, M. K. *Biochemistry* **1996**, *35*, 299-308.
94. Cajal, Y.; Ghanta, J.; Easwaran, K.; Surolia, A.; Jain, M. K. *Biochemistry* **1996**, *35*, 5684-5695.
95. Ziv, G.; Sulman, F. G. *Antimicrob. Agents Chemother.* **1972**, *1972*, 206-221.
96. Kunin, C. M.; Bugg, A. *J. Infect. Dis*. **1971**, *124*, 394-400.
97. Craig, W. A.; Kunin, C. M. Annu. Rev. Med. 1976, 27, 287-300.
98. Wise, R. *Clin. Pharmacokinet.* **1986**, *11*, 470−482.
99. Merrikin, D. J.; Briant, J.; Rolinson, G. N. *J. Antimicrob. Chemother.* **1983**, *11*, 233−238.
100. Schmidt, S.; Rock, K.; Sahre, M.; Burkhardt, O.; Brunner, M.; Lobmeyer, M. T.; Derendorf, H. *Antimicrob. Agents Chemother.* **2008**, *52*, 3994−4000.
101. *Nature* **495,** 141; 2013.
102. http://www.who.int/drugresistance/documents/surveillancereport/en/
103. Liu, J.F.; Mbadinga, S.M.; Yang, S.Z.; Gu, J.D.; Mu, B.Z. *Int. J. Mol. Sci.* **2015**, *16*, 4814-4837.
104. Rosenberg, E.; Ron, E.Z. *Appl. Microbiol. Biotechnol.* **1999**, *52*, 154–162.
105. Ishigami, Y.; Osman, M.; Nakahara, H.; Sano, Y.; Ishiguro, R.; Matsumoto, M. *Colloids Surf. B* **1995**, *4*, 341–348.
106. Cavalcante Barros, F.F.; de Quadrosi, C.P.; Pastore, G.M. *Cienc. Tecnol Aliment.* **2008**, *28*, 979–985.
107. Brötz, H.; Sahl, H.-G. *J. Antimicrob. Chemother.* **2000**, *46*, 1–6.
108. Heerklotz, H.; Seelig, J. *Eur. Biophys. J.* **2007**, *36*, 305–314.
109. Peypoux, F.; Bonmatin, J. M.; Wallach, J. *Appl. Microbiol. Biotechnol.* **1999**, *51*, 553–563.

110. Wu, Y.S.; Ngai, S. C.; Goh, B. H.; Chan, K. G.; Lee, L. H.; Chuah, L. H. *Front Pharmacol.* **2017**, *8*, 1-22.

111. Banat, I. M.; Franzetti, A.; Gandolfi, I.; Bestetti, G.; Martinotti, M. G.; Fracchia, L.; Smyth, T. J.; Marchant, R. *Appl. Microbiol. Biotechnol.* **2010**, *87*, 427–444.

112. Bonmatin, J.-M.; Laprevote, O.; Peypoux, F. *Comb. Chem. High Throughput Screen* **2003**, *6*, 541–556

113. Bonmatin, J.-M.; Genest, M.; Labbé, H.; Ptak, M. *Biopolymers* **1994**, *34*, 975–986.

114. Bougis, P.; Rochat, H.; Pieroni, G.; Verger, R. *Biochemistry* **1981**, *20*, 4915.

115. Bos, M. A.; Nylander, T. *Langmuir* **1996**, *12*, 2791-2797.

116. Gonzales-Christen, J.; Vergne, I.; Sumuth, R.; Sidobre, S.; Prats, M.; Tocanne, J. F.; Lane´elle, G. *Biochim. Biophys. Acta* **1998**, *1368*, 97-107.

117. Fainerman, V. B.; Zhao, J.; Vollhardt, D.; Makievski, A. V.; Li., J. B. *J. Phys. Chem. B* **1999**, *103*, 8998-9007.

118. Sun, Y.-T.; Wang, S.-X.; Sui, S.-F. *Colloids Surf. A* **2000**, *175*, 105.

119. Zhao, J.; Vollhardt, D.; Brezesinski, G.; Siegel, S.; Wu, J.; Li, J. B.; Miller, R. *Colloids Surf., A* **2000**, *171*, 175.

120. Xicohtencatl-Cortes, J.; Mas-Oliva, J.; Castillo, R. *J. Phys. Chem. B* **2004**, *108*, 7307-7315.

121. McConlongue, C. W.; Vanderlick, T. K. *Langmuir* **1997**, *13*, 7158-7164.

122. Eeman, M.; Deleu, M.; Paquot, M.; Thonart, P.; Dufrene, Y. F. *Langmuir* **2005**, *21*, 2505-2511.

123. Song, C.-S.; Ye, R. Q.; Mu, B. Z. *Colloids and Surfaces A: Physicochem. Eng. Aspects* **2007**, *302*, 82–87.

124. Onaizi, S. A.; Nasser, M. S.; Al-Lagtah, N. M. A. *Eur Biophys J* **2016**, *45*, 331–339.

125. Peters, T. J. All about Albumin: Biochemistry, Genetics, and Medical Applications. San Diego: Academic Press; **1995**.

126. Sathyadevi, P.; Krishnamoorthy, P.; Jayanthi, E.; Butorac, R. R.; Cowley, A. H.; Dharmaraj, N. *Inorganica Chimica Acta*. **2012**, *384*, 83–96.

127. Urquiza, N. M.; Naso, L. G.; Manca, S. G.; Lezama, L.; Rojo, T.; Williams P. A. M.; Ferrer, E. G. *Polyhedron* **2012**, *31*, 530–538.

128. Xiang, Y.; Wu, F. *Spectrochim Acta A Mol Biomol Spectrosc.* **2010**, 77, 430-436.

129. Bal, W.; Christodoulou, J.; Sadler, P.J.; Tucker, A. J. *Inorg. Biochem.* **1998** *70, 33-39.*

130. Gharagozlou, M.; Boghaei, D. M. *Spectrochim Acta A Mol Biomol Spectrosc.* **2008**, *71, 1617-22.*

131. Krishnamoorthy, P.; Sathyadevi, P.; Cowley, A. H.; Butorac, R. R.; Dharmaraj, N. *Eur J Med Chem.* **2011**, *46*, 3376-3387.

132. Lis, H.; Sharon, N. *Chemical Reviews* **1998**, *98*, 637–674.

133. Hardman, K.D.; Ainsworth, C.F. *Biochemistry* **1972**, *11*, 4910–4919.

134. Loris, R.; Hamelryck, T.; Bouckaert, J.; Wyns, L. *Biochimica et Biophysica Acta*. **1998**, *1383,* 9–36.

135. Akhand, A. A.; Pu, M. Y.; Du, J.; Kato, M.; Suzuki, H.; Hamaguchi, M.; Nakashima, I. *Eur. J. Immunol.* **1997**, *27*, 1254–1259.

136. Amin, A. R. M. R.; Paul, R. K.; Thakur, V. S.; Agarwal, M. L. *Cancer Res.* **2007**, *67*, 5617–5621.

137. Fayad, R.; Sennello, J. A.; Kim, S. H.; Pini, M.; Dinarello, C. A.; Fantuzzi, G. *Eur. J. Immunol*. **2005**, *35*, 2304–2312.

138. Chen, Q.; Wei, W.; Lin, J. M. *Biosens. Bioelectron*. **2011**, *26*, 4497– 4502.

139. Fukui, S.; Feizi, T.; Galustian, C.; Lawson, A. M.; Chai, W. G. *Nat. Biotechnol.* **2002**, *20*, 1011–1017.

140. Disney, M. D.; Zheng, J.; Swager, T. M.; Seeberger, P. H. *J. Am. Chem. Soc*. **2004**, *126*, 13343–13346.

141. Emsely, J.; White, H. E.; OHara, B. P.; Oliva, G.; Srinivasan, N. et al. *Nature* **1994**, *367*, 338–345.

142. Vetri, V.; Librizzi, F.; Militello, V.; Leone, M. *Eur. Biophys. J.* **2007**, *36*, 733–741.

143. Potts, J.; Campbell, I. D. *Curr. Opin. Cell Biol*. **1994**, *6*, 648-655.

144. Hynes, R. O. (1990) *Fibronectins* (Springer, New York).

145. Chifflet, S.; Bolatto, C.; Tolosa, S. *J. Biochem. Biophys. Meth.* **2004**, *59*, 139–143.

146. Asem, E. K.; Conkright, M. D. *Comp. Biochem. Physiol*. **1995**, *112*, 247–255.

147. Quade, B. J.; McDonald, J. A. *J. Biol. Chem.* **1988**, *263***,** 19602–19609.

148. Hocking, D. C.; Smith, R. K.; McKeown-Longo, P. L. *J. Cell Biol.* **1996**, *133*, 431–444.

149. Aguirre, K. M.; McCormick, R. J.; Schwarzbauer, J. E. *J. Biol. Chem.* **1994**, *269*, 27863–27868.

150. Morla, A.; Ruoslahti, E. *J. Cell Biol.* **1992,** *118***,** 421–429.

151. Baneyx, G.; Vogel, V. *PNAS* **1999**, *96*, 12518-12523

152. Gemperle, O.; Neuweiler, J.; Reutter F. W.; Hildebrandt F.; Krapf, R. *Am J Kidney Dis.* **1996**, *28, 668-675.*

153. Stathakis, N. E.; Fountas, A.; Tsianos, E. *J. Clin. Pathol.* **1981**, *34*, 504–508.

154. White, D. G.; Hall, J. W.; Bramdli, D. W.; Gehris, A. L.; Bennett, V.D. *Exp. Cell Res.* **1996**, *224*, 391-402.

155. Gmeiner, B.; Leibl, H.; Zerlauth, G.; Seelos, C. *Arch. Biochem. Biophys*. **1995**, *321*, 40-42.

156. Watson, J. D.; Crick, F.H. *Nature* **1953**, *171*,737–738.

157. Siddhesh, D.; Patil, David G. Rhodes; Burgess, D. J. *AAPS J.* **2005**, *7*, E61–E77.

158. Wang, J. *Nucleic Acids Res.* **2000**, *28*, 3011-3016.

159. Palecek, E.; Fojta, M. *Anal. Chem*. 2001, 73, 75A-83A.

160. Zhou, W.; Saran, R.; Liu, J. *Chem. Rev*. **2017**, *117*, 8272−8325.

161. Sigel, H. *Chem. Soc. Rev*. **1993**, *22*, 255− 267.

162. Sigel, R. K.; Sigel, H. *Acc. Chem. Res.* **2010**, *43*, 974−984.

163. Izatt, R. M.; Christensen, J. J.; Rytting, J. H. *Chem. Rev*. **1971**, *71*, 439−482.

164. Tuerk, C.; Gold, L. *Science* **1990**, *249*, 505−510.

165. Ellington, A. D.; Szostak, J. W. *Nature* **1990**, *346*, 818−822.

166. Narayanan, S.; Appleton, H. D. *Clin. Chem*. **1980**, *26*, 1119-1126.

167. Peake, M.; Whiting, M. *Clin Biochem Rev*. **2006**, *27*, 173–184.

168. Dalton, N. R. *Clinical Chemistry* **2010**, *56*, 687–689.

169. Toora, B. D.; Rajagopal, G. *Indian J. Exp. Biol*. **2002**, *40*, 352-354.

170. Verma, I.; Rajeev, N.; Mohiuddin, G.; Pal, S. K. *J. Phys. Chem. C* **2019**, *123*, 6526-6536.

171. Verma, I.; Valsala Selvakumar, S. L.; Pal, S. K. *J. Phys. Chem. C* **2019**. DOI: 10.1021/acs.jpcc.9b10275.

172. Verma, I.; Devi, M.; Sharma, D.; Nandi, R.; Pal, S. K. *Langmuir* **2019**, *35*, 7816-7823.

173. Verma, I.; Sidiq, S.; Pal, S. K. *Liq. Cryst*. **2016**, *43*, 1126-1134.

174. Verma, I.; Sidiq, S.; Pal, S. K. *Liq. Cryst*. **2019**, *46*, 1318-1326.

175. Verma, I.; Pani, I.; Sharma, D.; Maity, S.; Pal, S. K. *J. Phys. Chem. C* **2019**, *123*, 13642-13650.

176. Verma, I.; Sidiq, S.; Pal, S. K. *ACS Omega* **2017**, *2*, 7936-7945.

Chapter 2

Ordering of Liquid Crystals in the Presence of Cyclic Lipopeptides at Aqueous Interfaces: Potential Application in Label-Free Detection of Amyloidogenic Proteins

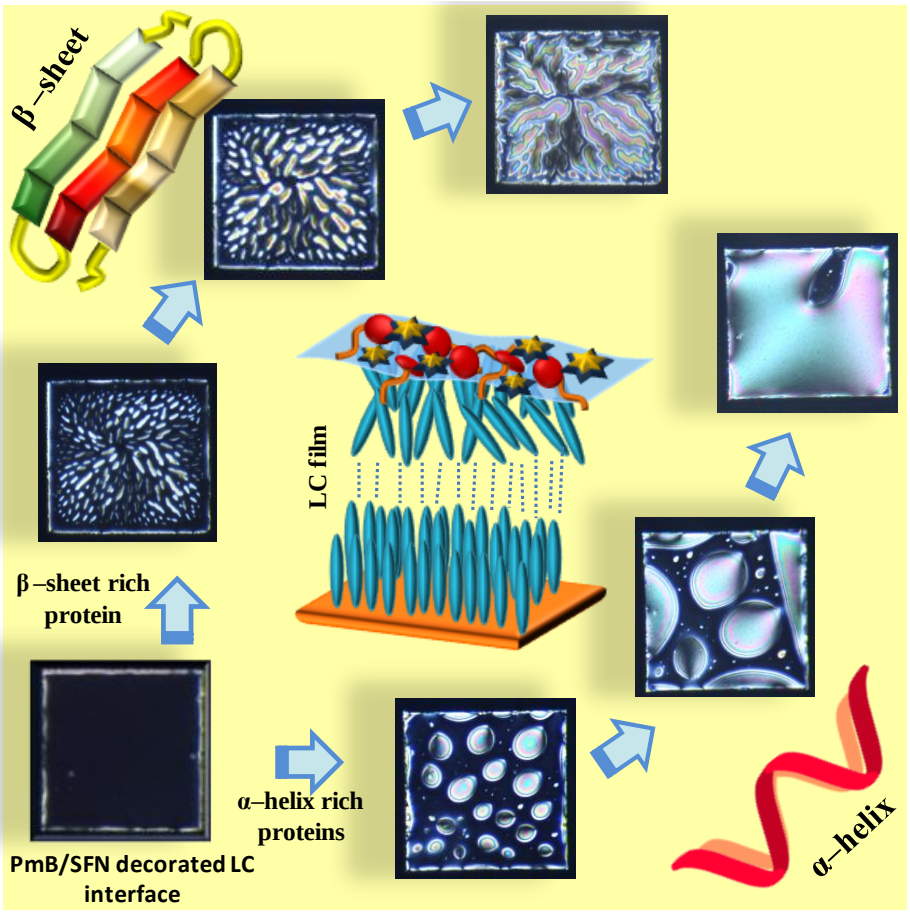

Here, we report the orientational behavior of liquid crystals (LCs) influenced by two cyclic lipopeptides, polymyxin B (PmB) (Part A) and surfactin (SFN) (Part B) at aqueous-LC interfaces. Such lipopeptidic-based LC interfaces distinctly amplify the adsorption of β-sheet-rich proteins through appearances of fibril-like spatial patterns, which are, however, not observed in the presence of α-helix-rich proteins. Such changes in the optical patterns of the LC in contact with proteins occur at nanomolar concentrations at those interfaces, and thus the method could be useful to label-free detect toxic amyloids.

2.1 Part A: Ordering Transitions in Liquid Crystals Triggered by Polymyxin B: Potential Application in Label-Free Detection of Amyloidogenic Proteins

2.1.1 Introduction

Interfaces formed between nematic liquid crystals (LC) and aqueous phases have been recently realized as responsive systems that can allow the visualization of the dynamics of biomolecular adsorption through naked eye.[1-15] The engineering of such surfaces along with immobilization of biomolecules on solid interfaces has brought substantial evolution in the field of LC-based label-free chemo/biosensors.[1-26] LCs, an interesting class of soft matter, exhibits both fluidity as well long-range orientational order where mesogens align themselves along a particular direction commonly known as the director of the LC.[27,28] It is known that adsorbates at LC-aqueous interfaces can change the orientations of interfacial LC molecules and this change in the orientations can be communicated up to 100 μm into the bulk LC phase through cooperative interactions. In such micrometer thick LC films, the orientation-dependent surface energy of the LC is comparable to the elastic energy stored within the film and thus leads to change in the orientations of the LCs in contact with small disturbance due to adsorbates at those interfaces.[1-6] As LCs are optically anisotropic, these subtle changes resulting in different orientational transitions can be easily visualized through naked eye under crossed polars. Pioneered by Abbott, LC-aqueous interfaces have been extensively explored to envisage the self-assembly of surfactants, phospholipids, and proteins.[1-10] Linear surfactants and phospholipids promote homeotropic orientation of the LC (dark optical appearance) at the interface through a change in the easy axis associated with the coupling between the aliphatic tails of the adsorbed amphiphiles and the mesogens at those interfaces. However, adsorption of peptide-based biomolecules at the interface does not cause any significant changes in the ordering of LC, and the LC molecules adopt a planar/tilted orientation consistent with bright appearances under cross polars.[12] Past studies suggest that these changes in orientational order of LC are largely manipulated by the molecular structure of the amphiphiles[11,12] (e.g., tail length or head group), variation in aqueous phase[6,11-14] (e.g., pH or ionic strength) or by physio-chemical events in the aqueous phase that can disrupt these molecular assemblies at interfaces (such as the specific protein binding[10] or DNA hybridization[15]). Such LC sensing systems based on linear amphiphiles (e.g., chemically synthesized surfactants and expensive phospholipids) laden interfaces are well understood and developed over a past decade for numerous sensing applications. However, until

today, there are no reports on the effects of cyclic lipopeptides on the ordering transition of the LCs at aqueous interfaces. In this work, we aimed to explore interactions of a naturally occurring cyclic bio-surfactant, Polymyxin B (PmB), with LCs at aqueous interfaces towards the realization of the novel bio-sensing systems.

Cyclic lipopeptides have attracted immense attention in pharmaceutical, biomedical sciences as an alternative to chemically synthesized surfactants with the additional advantages of their antimicrobial and antifungal properties.[29,30] They are molecules composed of peptidic cyclic head group and fatty tails which are naturally expressed in microorganisms due to the enhanced *in vivo* stability of the cyclized head group compared to the linear counterparts.[31] This unique molecular structure facilitates the self-assembly into a range of nanostructures such as micelles, vesicles, nanosheets, etc. depending on the hydrophile/lipophile balance of the molecules as well as interactions between the peptide units.[32] Its bioactivity is also associated with the strong amphipathic behavior demonstrated at cell membranes and various surfaces/interfaces. As a proof of concept, we chose Polymyxin B (PmB), a surface-active lipopeptide produced by *Bacillus polymyxa.* It is composed of a cyclic heptapeptide ring with an exocyclic peptidic tail capped with a short fatty acid chain (Figure 2.1). PmB is the strongest and oldest antibiotic that had to be recently re-introduced clinically to treat multidrug-resistant superbugs.[33]

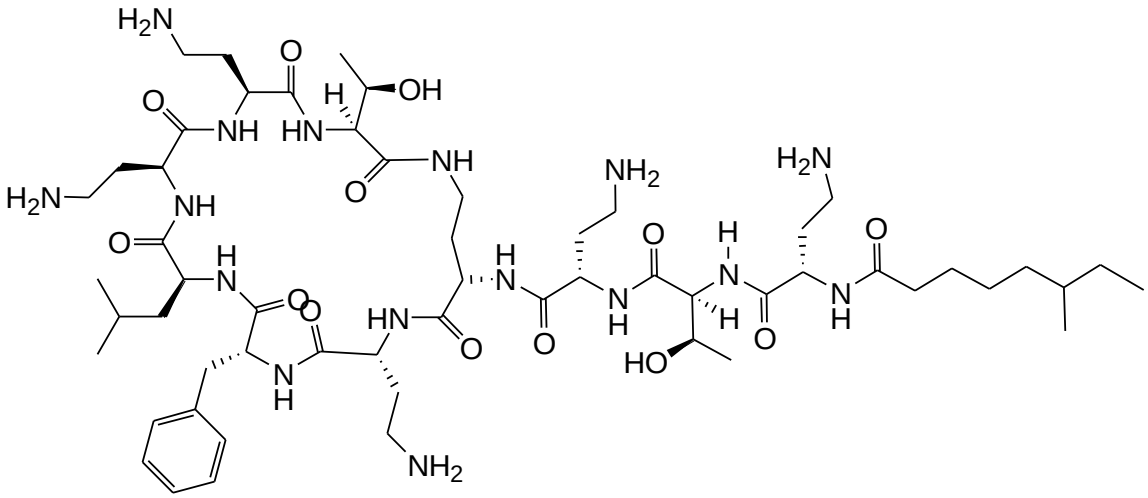

Figure 2.1. Chemical structure of PmB, a decapeptide antibiotic formed by a hydrophilic 7-member ring and linear N-terminal region of 3 amino acids and a hydrophobic fatty acid tail.

Several reports suggest that PmB usually gets inactivated *in vitro* by tissues due to binding of its five free amino groups with negatively charged membrane phospholipids and serum components.[34-36] This interference not only causes loss in its efficacy but results in tissue toxicity as well due to its accumulation in liver, kidney and lungs.[37] Therefore, with the threat of approaching post-antibiotic era[38] and limited therapeutic options,[39] it is of utmost importance to devise strategies to understand the possible interactions of existing antibiotics with serum proteins so as to develop the drug design accordingly.

2.1.2 Objective

The study reported here was motivated by two broad goals. First, we sought to develop principles to tailor the interfacial properties of an aqueous−LC interface using PmB lipopeptide. As PmB offers additional peptidic functionalities (Figure 2.1a) over previously studied conventional and linear amphiphiles at LC-aqueous interface, it would be of great interest to study the orientational behavior of the LC influenced by the organization of such complex structures. We hypothesized that unique composition of PmB (e.g., amino functionalities and acyl tail) would strongly couple to the ordering of LC due to a range of non-covalent interactions that can be easily visualized by polarised optical microscopy (POM). In addition, the presence of several H-bonding sites in PmB may alter the ordering of the LC at the interface. We would also employ Density Functional Theory (DFT) calculation in the gas phase to understand the nature and strength of intermolecular interaction between LC and PmB molecules. Our second objective was to explore whether the PmB decorated aqueous-LC system would allow the adsorption of proteins at the interface that could trigger an orientational response of the LC. It should be noted that such an interfacial event may induce an ordering transition of the LCs depending on nature of proteins (e.g., the varying electronegative charge density and secondary structural features of a protein). We discuss a significant application of the PmB-decorated LC interface that detects amyloids (β-sheet rich protein aggregates) at a nanomolar concentration which are immensely associated with cytotoxicity and diseases such as Alzheimer, parkinson's disease, huntington's, amyloidosis and neurodegenerative disorders.[40-42] The technique can surpass the contemporary techniques (eg. fluorescence, spectroscopic and NMR which usually require μM to mM concentration of peptides) used to characterize amyloids[43] as it yields a direct optical signature specifically to amyloids at low concentrations without need of complex and expensive instrumentation.

2.1.3. Results and Discussion

2.1.3.1 Ordering transition of LC in presence of PmB

The first series of experiments were carried out to investigate the ordering of 5CB LC in the presence of PmB at aqueous-LC interfaces (Figure 2.2). 5CB was first confined in the pores of gold electron microscopy grids supported on N,N-dimethyl-n-octadecyl-3-aminopropyltrimethoxysilyl chloride (DMOAP)-treated glass slides. As reported earlier, DMOAP at the bottom interface and air at top interface anchor 5CB in a perpendicular (homeotropic) orientation imparting dark optical appearance under crossed polars.[4] Subsequently, the optical appearance of the LC becomes bright when the glass side is immersed in aqueous buffer (20 mM Tris-buffered saline (TBS)) at pH 7.4, consistent with a tilted/planar ordering transition of LC induced by water (Figure 2.2a). Interestingly, when 0.1 mg/mL PmB (well below its critical micellar concentration[44]) was introduced into the aqueous phase, LC molecules (which were initially planar at LC-aqueous interface) adopt homeotropic orientation rapidly within 1 min (Figure 2.2b). The bright to dark transition exhibited by LC can be attributed to the adsorption of PmB molecules at the interface as shown schematically in Figure 2.2d. It is known that homeotropic ordering of LC generated by adsorption of an amphiphile usually arises due to lateral hydrophobic interaction between aliphatic chains of LC and amphiphile.[4] However, classical surfactants like alkyltrimethylammonium halides with short alkyl chain (C_nTAB, n=8) fails to anchor LC molecules homeotropically at interface suggesting the role of tail length in dictating the orientation of 5CB.[11-12] Therefore, given the short alkyl chain length linked to the N-terminus of PmB, it is quite not straightforward to assume if the exhibition of homeotropic orientation by LC is only due to lateral interactions of PmB alkyl tails with the hydrophobic alkyl chains of 5CB. We believe that a combination of interactions involving head group-head group (amino group of PmB and CN of 5CB)[25] or/and tail-tail interactions influences the orientation of LC which will be facilitated if PmB acyl tail intercalates into LC medium while the hydrophilic head group faces aqueous phase. This type of arrangement is also consistent with the previous reports on binding mode of PmB with other phospholipids.[45] Thus, to elucidate the individual role of PmB's head group and fatty chain to anchor the LC, another experiment was carried out where optical LC film was contacted with an aqueous solution of 0.1 mg/mL polymyxin B nonapeptide (PmBN). PmBN is a derivative of PmB which lacks the terminal acyl chain and subsequently demonstrates an inactive form of PmB.[45]

Interestingly, it was found that in the presence of PmBN, LC turned dark in most of the grid squares while in some, it remained tilted with respect to interface normal (Figure 2.2c).

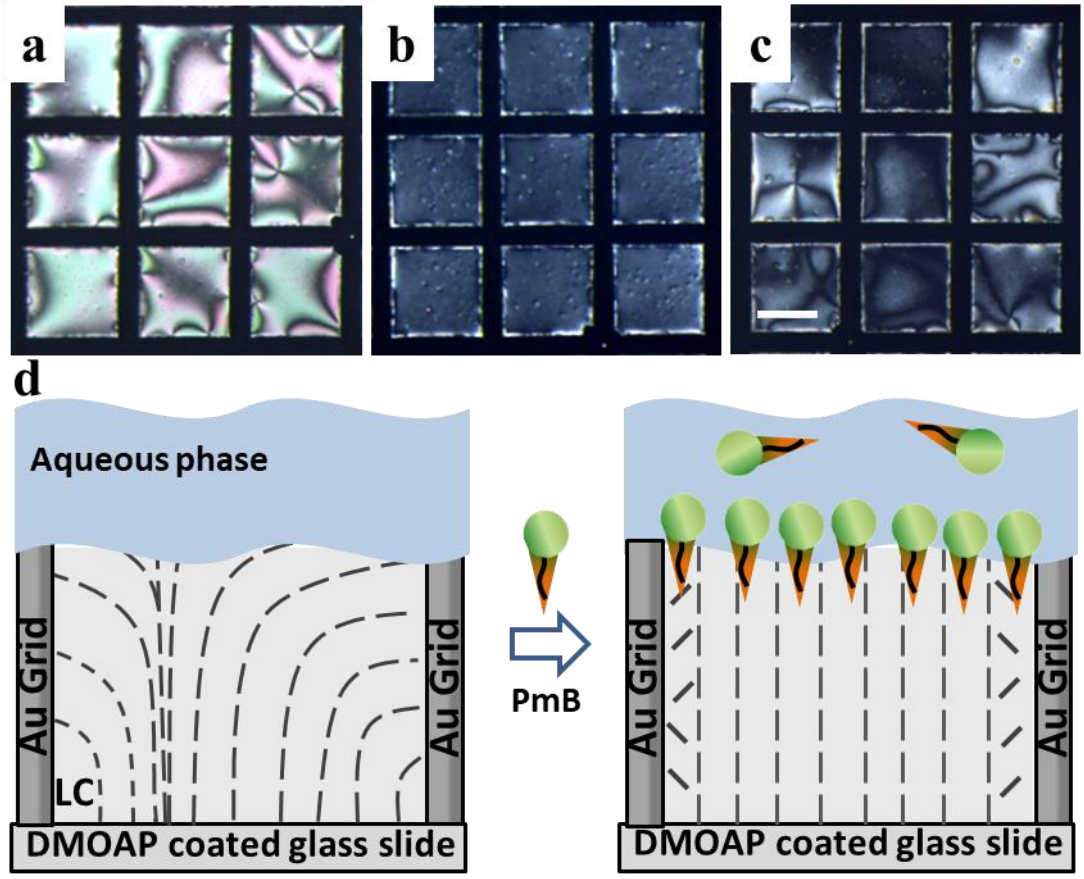

Figure 2.2. Polarized optical micrographs (crossed polars) of 5CB LC hosted within a gold TEM grid supported on DMOAP functionalized glass slides in contact with (a) 20 mM TBS; (b) 0.1 mg/mL PmB at 1 min; (c) 0.1 mg/mL PmBN at 5 min. The bright texture of LC changes to dark introduction of PmB at LC-aqueous interface while LC exhibit both tilted and homeotropic ordering in the presence of PmBN. Schematic in (d) (Not to scale) illustrates the director configuration of LC at distinct ordering adopted at aqueous-interface before and after adsorption of PmB. Scale bar = 200 μm.

The initial homeotropic/tilted ordering of LC can only be attributed to the intermolecular interactions between amino groups of PmBN and CN of 5CB (e.g., electrostatic interactions or H-bonding or/and both) at LC-aqueous interface.[25] However, LC molecules subsequently reoriented themselves back to planar after 15-20 min which implies the unstable assembly of PmBN at interface associated with a loss in structural amphiphilicity of peptide and the subsequent desorption of hydrophilic PmBN molecules

from the interface into the bulk aqueous phase (Figure 2.3). This observation is in contrary to that with the assembly of PmB, where LC remains homeotropic for 3 hours or so in the presence of bulk 0.1 mg/mL PmB (Figure 2.3). These results confirm that although headgroup-headgroup interactions between 5CB and peptidic moieties (*via* ionic interactions or/and hydrogen bonding) can induce the homeotropic ordering in LC (even for a shorter time), the acyl tail (hydrophobic interactions) of PmB is essential to maintain the stable homeotropic anchoring of LCs at the aqueous interface. This type of binding mode would facilitate the penetration of the PmB into LC medium while the hydrophilic head group of PmB can preferentially localize at the interface in contact with the aqueous phase. These results are in line with the previous report which suggests that unique structural features of PmB molecule such as well defined rigid and flexible regions impart the conformational space to its structure and enables a complex set of interactions (both electrostatic as well as hydrophobic) with cell membranes or lipid vesicles.[45]

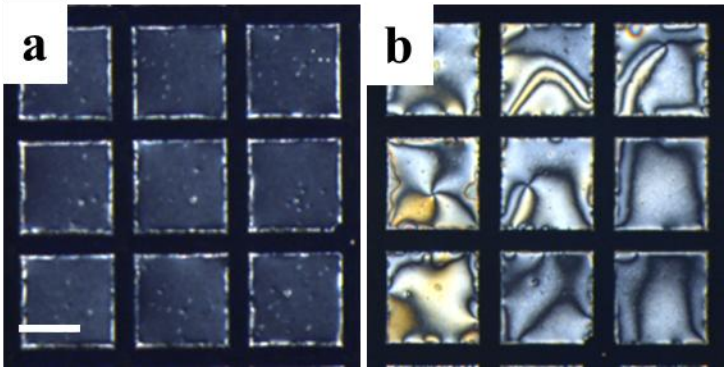

Figure 2.3. Polarized optical micrographs (crossed polars) of 5CB hosted within a gold TEM grid supported on DMOAP functionalized glass slides in contact with A) 0.1 mg/mL PmB after 2 hours and B) 0.1 mg/mL PmBN in 20 mM TBS (pH 7.4) after 10 min. Scale bar = 200 μm.

The comparatively robust association of 5CB with PmB than that with nonapeptide strongly resembles their respective antimicrobial and surface activity at phospholipids interfaces.[45] Therefore, to understand the molecular aspects associated with the superior stability amongst the PmB-5CB and PmBN-5CB complexes, we performed computational calculations in the gas phase based Density Functional Theory. After optimization of both the complexes (Figure 2.4a,b), it has been found that the energy of stabilization of PmB-5CB complex is much lower than that of PmBN-5CB ($E_{Pmb\text{-}5CB}$ <<<< $E_{PmbN\text{-}5CB}$) complex (Table 2.1).

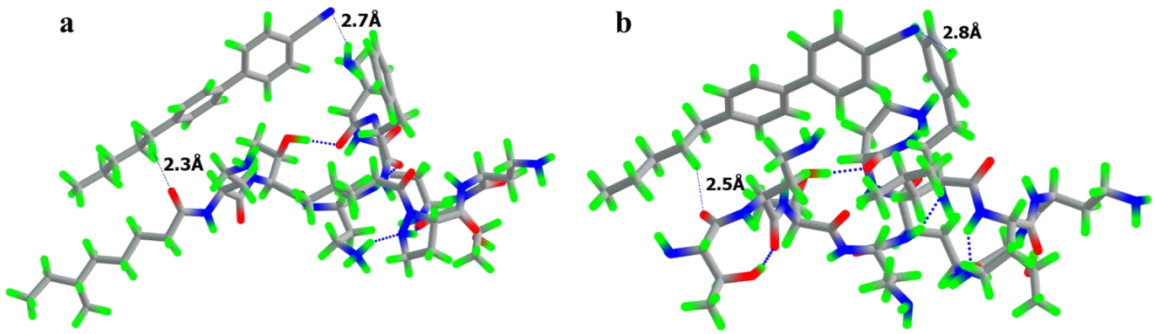

Figure 2.4. DFT optimized geometry of (a) PmB-5CB and (b) PmBN-5CB complexes.

Table 2.1: DFT optimized energy and binding energy of the studied complexes

Complex	Optimized energy (kJ/mol)	Binding energy (kJ/mol)
PmBN-5CB	-12427675.3	30.5
PmB-5CB	-12597485.6	51.2

Likewise, the binding energy of PmB-5CB complex is found to be greater than PmBN-5CB complex ($BE_{Pmb\text{-}5CB} > BE_{PmbN\text{-}5CB}$; Table 2.1). To get a better physical understanding of the interactions within the constituent molecules of the complexes, electrostatic potential (ESP) map was generated (Figure 2.5). In PmB-5CB complex, the interaction between PmB and 5CB is found to be better than PmBN and 5CB in PmBN-5CB complex mainly due to the presence of the alkyl chain in PmB molecule. It should be noted that in the ESP map of PmB-5CB complex, the electronic charges are almost homogeneously distributed throughout the complex without having any electronegative red centers. However, in the case of PmBN-5CB complex, the electronic charges are not homogeneously distributed, having five electronegative red centers (Figure 2.5). This homogeneity in electronic charge distribution around the surface of the complex PmB-5CB also indicates the stronger and more stable attractive interaction (as also reported in some earlier systems[46]) between PmB and 5CB molecules than that in the PmBN-5CB complex. After minute observation of both the complexes, we have found that there is similar sort of H-bonding forming between the cyclic head group (of PmBN and PmB) and -C≡N of 5CB which is accountable for the stability of the homeotropic anchoring of LC. Although in the case of PmBN, the stability is found to be transient due to the absence of the aliphatic chains (Figure 2.3b). These results along with our experimental

findings strongly suggest that PmB molecules can organize more efficiently and systematically at LC-aqueous interface as compared to PmBN consistent with the topological flexibility of PmB molecules associated with a range of non-covalent interactions with LC.

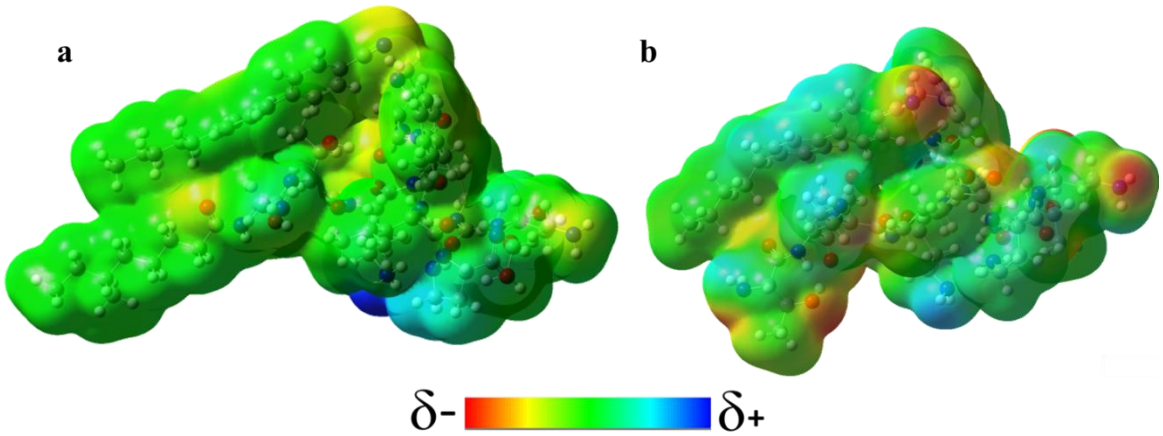

Figure 2.5. Molecular electrostatic potential distribution of (a) PmB-5CB and (b) PmBN-5CB complexes.

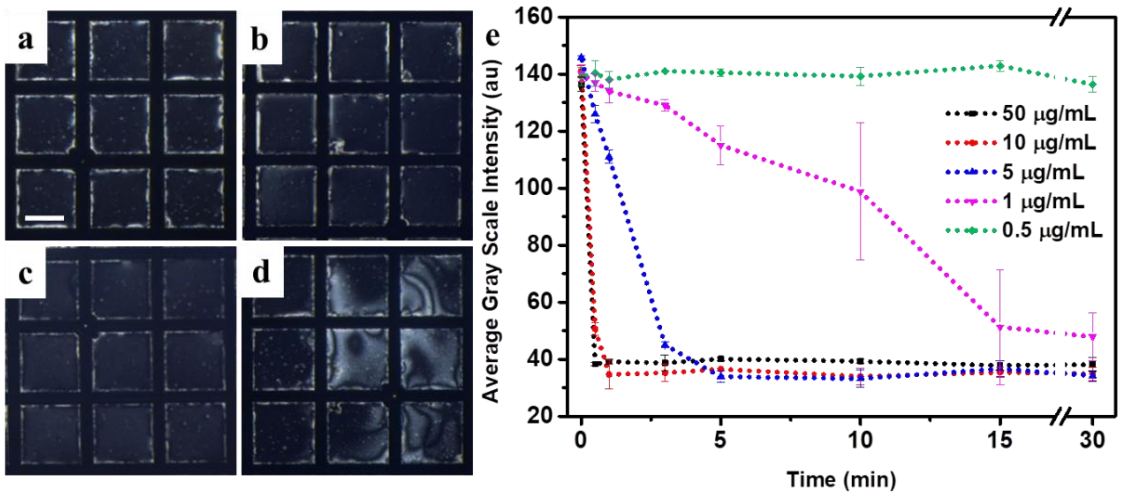

Figure 2.6. Polarized optical micrographs of 5CB-aqueous interface in contact with 20 mM TBS in presence of different concentration of PmB: (a) 0.05, (b) 0.01, (c) 0.005 and (d) 0.001 mg/mL at 15 min. (e) Plot of average grayscale intensity of POM images of 5CB laden with different concentration of PmB as a function of time. Scale bar = 200 μm.

Next, we sought to determine the lowest concentration of PmB in bulk phase at which LC can demonstrate an ordering transition. For this, LC film was contacted with an aqueous solution containing different concentrations of PmB and optical appearance of the LC was observed under crossed polars. As evident from Figure 2.6a-d, the ordering of LC turned homeotropic within 15 min as the concentration varied from 0.05 to 0.005 mg/mL of bulk

PmB. In contrast, 0.001 mg/mL of PmB induces tilted alignment of LC within 15 min and complete dark appearance within 30 min. Below 0.001 mg/mL, no ordering transition was observed. Image analysis allows the investigation of dynamic adsorption of PmB at LC-aqueous interface through the optical response of LC. The average grayscale intensity of the corresponding POM images, when plotted as a function of time (Figure 2.6e), shows that as the bulk concentration of PmB was reduced, the time required by LC to establish a homeotropic ordering increased. For example, for concentration more than 50 μg/mL, the intensity dropped rapidly to a minimum (dark appearance) within 5 min while for 1 μg/mL of PmB, the intensity decreased gradually over 15 min and arrived at lowest within 30 min. It was found that 1 μg/mL PmB (0.76 μM) was the minimum concentration which was able to trigger homeotropic ordering of LC. This amount required to induce a homeotropic ordering in LC at the aqueous interface is comparatively lower than that required by previously studied linear amphiphiles (ranging few μM to mM).[12]

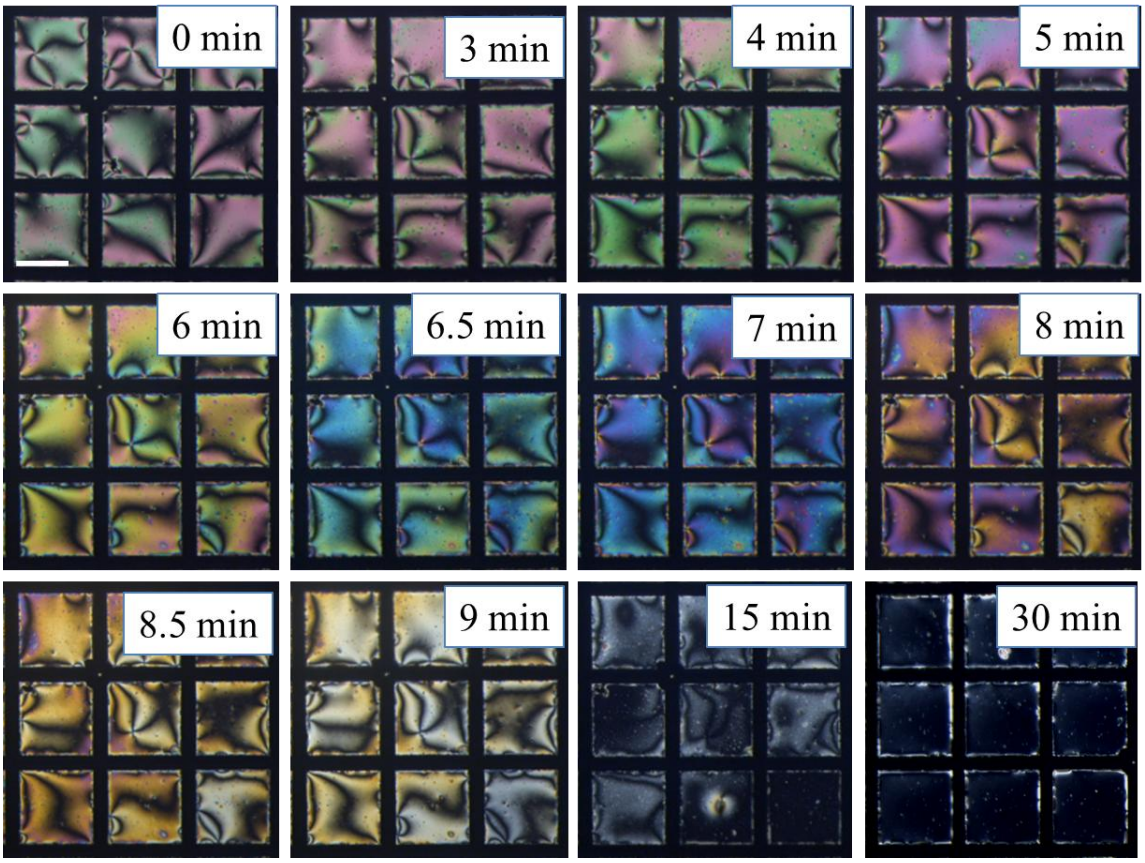

Figure 2.7. Time-lapse POM images of 5CB-aqueous interface showing dynamic response of LC to 0.001 mg/mL PmB placed in 20 mM TBS. Interference colors produced shows the different tilt of 5CB orientation at the interface. Scale bar = 200 μm.

Since the sensitivity of PmB detection at LC-aqueous interfaces lies in μM range which is well below the toxic levels of PmB in human serum and tissues, the LC-based design can be the facile, label-free and rapid method for PmB determination in clinical and analytical settings.[47] It was also observed that at a lower concentration of PmB such as 1 μg/mL, a bright to dark transition takes place via continuous tilt of LC director (different birefringence) with respect to interface normal (Figure 2.7). This transition is a way similar to the ordering induced in LC by water-soluble surfactants such as sodium dodecyl sulfate (SDS).[4]

2.1.3.2 Adsorption of proteins on PmB laden LC-aqueous interface

The current design of LC-aqueous interface decorated with PmB molecules exposes the cationic peptidic functionalities at the interface which can strongly interact with anionic biomolecules and can perturb the assembly of PmB at the interface. Thus, we hypothesized that the optical state of LC could be triggered from dark to bright, facilitated by adsorption of anionic proteins at the interface as schematically shown in Figure 2.8a. As proof of concept, we chose two proteins: bovine serum albumin (BSA) and human hemoglobin (Hb). Both proteins are main constituents of blood serum; however, BSA is highly negatively charged protein as compared to Hb at experimental pH of 7.4 (See Appendix A for details). A series of experiments were carried out to monitor the optical response of PmB decorated aqueous-LC interface followed by the introduction of BSA and Hb at physiological conditions (pH 7.4) (Figure 2.8b-e). The first experiment was performed with Tris buffer as a control to confirm that additional buffer (without any protein) did not alter the optical appearance of LC and LC remained homeotropic at least for 2 hours (Figure 2.8b). Next, we observed that optical appearance turned completely bright in the presence of 300 nM of BSA and Hb within less than 3 and 15 min, respectively (Figure 2.8c,d). We hypothesis that the reorientation of LCs from perpendicular to planar state is facilitated by the adsorption of anionic peptide molecules at the interface (evident late) which might weaken the coupling of PmB with LC. To confirm the same, in another control experiment, an aqueous solution of a cationic protein, cytochrome c was introduced onto PmB laden LC-aqueous interface. Under these conditions, the optical appearances of LC remained dark within the observation period (2 hr) (Figure 2.8e) confirming that LC adopted homeotropic alignment at the interface. This observation suggests that reorientation of LC is mainly influenced by electrostatic

interactions (apart from the other non-covalent interactions) between anionic proteins and cationic amino groups of PmB at LC-aqueous interface.

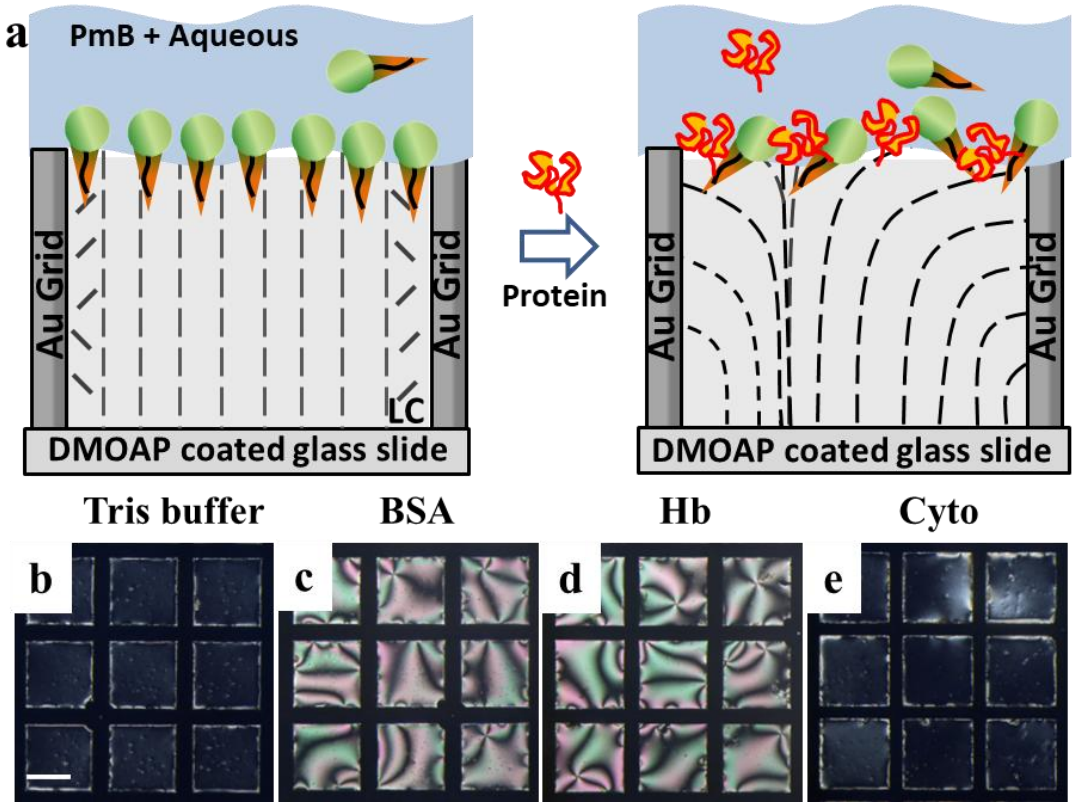

Figure 2.8. Schematic illustration in (a) depicts the plausible adsorption of protein molecules and subsequent ordering transition of LC at the PmB laden LC-aqueous interface. Optical micrographs (crossed polarizers) of 5CB in contact with an aqueous solution of 0.1 mg/mL PmB after the introduction of (b) Tris buffer, (c) BSA at 3 min, (d) Hb at 15 min and (e) Cyto at 2 hr. The final concentration of proteins was 300 nM. Scale bar = 200 μm.

Besides detecting the presence of proteins, it is essential to find out the sensitivity of proteins at PmB laden aqueous-LC interfaces. Therefore, in the next series of experiments, the PmB laden LC films were placed in contact with different concentrations of two proteins. Figure 2.9 reflects the final equilibrium optical state of LC upon incubation with varying concentrations of BSA and Hb for 2 hours at PmB decorated aqueous-LC interface. The optical appearance of the LC changed to bright in contact with at least 5 nM and 7 nM of BSA and Hb, respectively, at those interfaces. Further lowering the concentration of the proteins resulted in coexistence of bright and dark regions/domains in the LC film. For example, we observed the appearance of small

bright domains at 3 nM concentration of BSA (Figure 2.10a). In case of Hb, at 6 nM concentration, a co-existence of bright and dark regions was observed in the LC film consistent with insufficient interactions of the protein with PmB at that concentration (Figure 2.11a). The normalized mean grayscale intensity of the polarized light images of the LC film grid as a function of the concentrations of BSA and Hb is shown in Figure 2.10 and 2.11b, respectively.

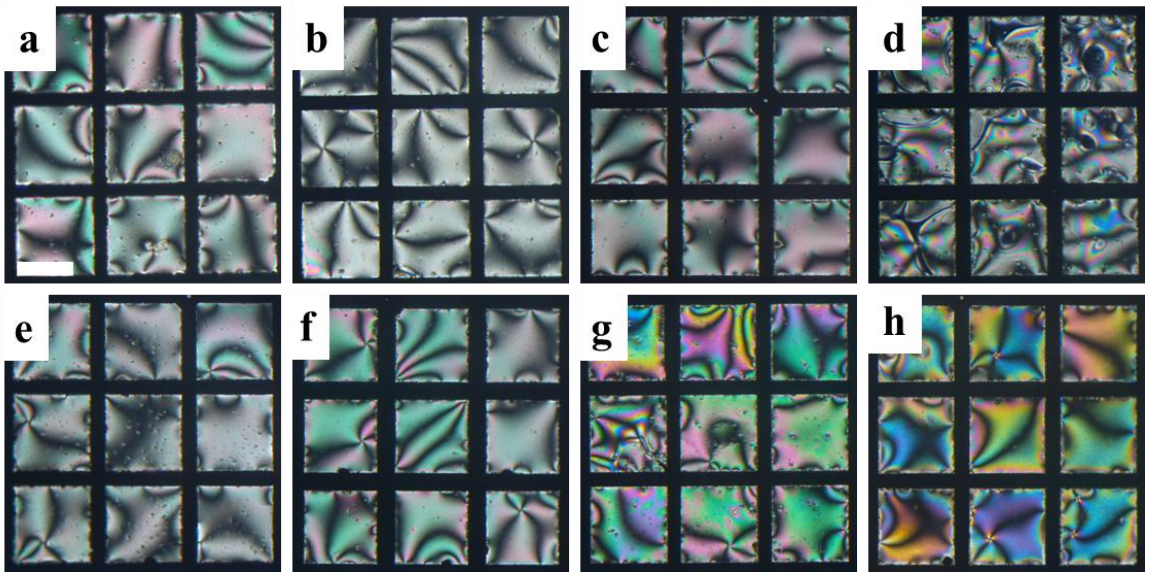

Figure 2.9. Optical micrographs (crossed polarizers) of 5CB in contact with aqueous solution of 0.1 mg/mL PmB after incubation with (a,e) 50 nM, (b,f) 20 nM, (c,g) 10 nM, (d) 5 nM and (h) 7 nM of (a-d) BSA and (e-h) Hb for 2 hours. Scale bar = 200 μm.

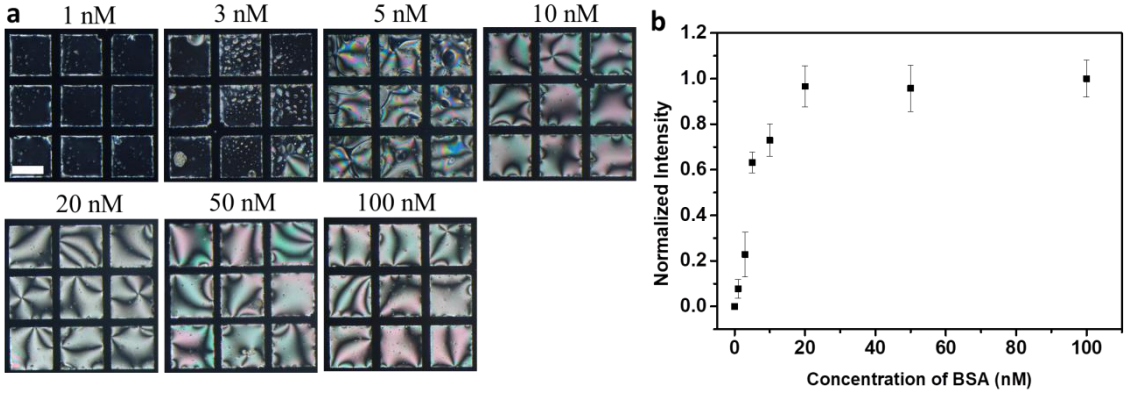

Figure 2.10. Optical micrographs (crossed polarizers) of 5CB in contact with an aqueous solution of 0.1 mg/mL PmB after incubation with different concentration of BSA for 2 hours. Numbers indicated above the particular image indicates the concentration of BSA corresponding to that image. Scale bar = 200 μm. Graph (b) represents the normalized intensity of micrographs (shown in a) as a function of the concentration of BSA.

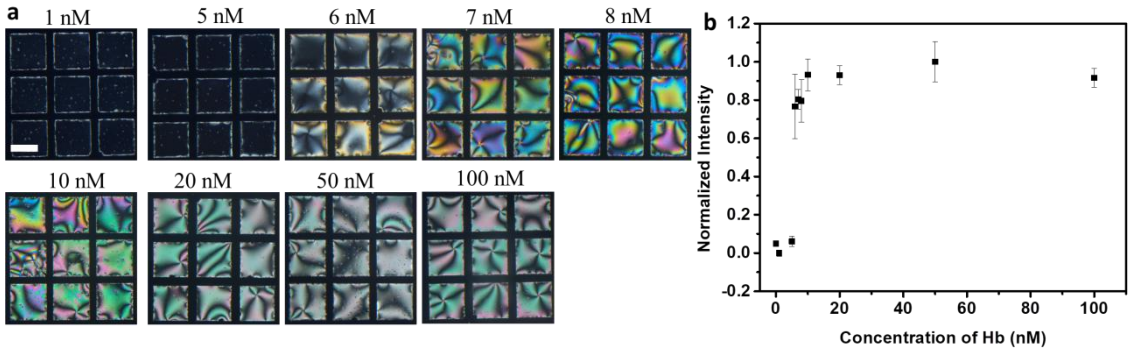

Figure 2.11. Optical micrographs (crossed polarizers) of 5CB in contact with an aqueous solution of 0.1 mg/mL PmB after incubation with different concentration of Hb for 2 hours. Numbers indicated above the particular image indicates the concentration of Hb corresponding to that image. Scale bar = 200 μm. Graph (b) represents the normalized intensity of micrographs (shown in a) as a function of the concentration of Hb.

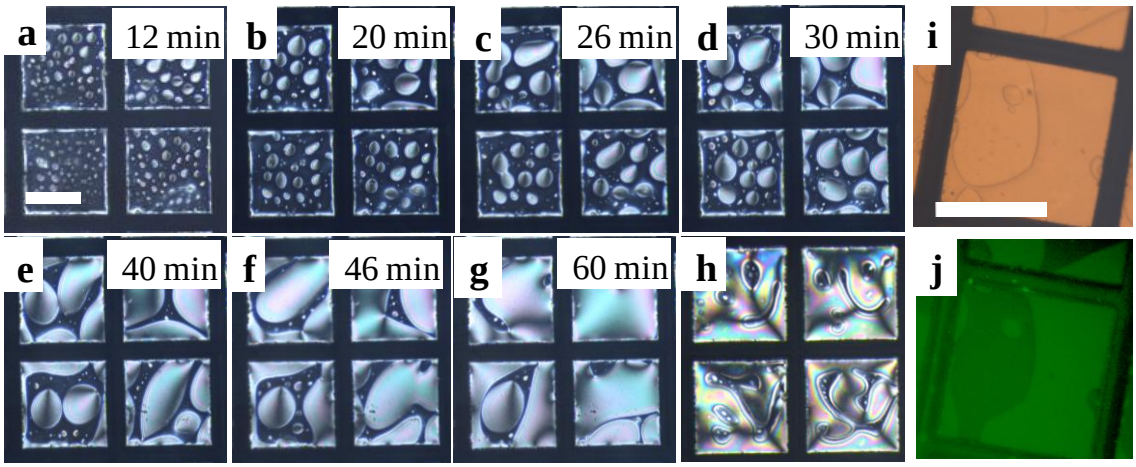

Figure 2.12. (a-g) Time-lapse polarized optical images that show the dynamic response of the LC to the adsorption of 10 nM BSA to a PmB decorated aqueous-5CB interface. Inset indicates the time at which the image was captured. Bright globular domains start growing and coalesce over time leading to complete planar ordering of LC. POM image in (h) shows the BSA (20 nM) adsorbed PMB-LC interface at 20 min in an independent experiment. The adsorption of BSA at the interface led to the formation of beautiful spatial patters that sometimes can resemble *emojis* also. (i) Bright-field and corresponding epifluorescence images (j) of the optical appearance of PmB laden aqueous-LC interface after incubation with FITC labeled BSA. Scale bar = 200 μm.

It is important here to note that in case of lower concentrations of BSA, the dark to bright transition of LC occurred along with the formation and evolution of pear-shaped beautiful

spatial patterns of LC which grow over time to coalesce together as illustrated in Figure 2.12a-h. The appearance and coalescence of such bright domains induced by BSA signify the dynamic lateral distribution of BSA at the PmB laden LC-aqueous interfaces and subsequent lateral mobility of the BSA-PmB complex.[48-50] Thus, to confirm the adsorption of BSA at the interface, we employed epifluorescence microscopy after incubating the LC-aqueous interface with FITC-labelled BSA. Epifluorescence and corresponding bright image demonstrate that BSA was highly localized in bright domains of LC which confirms that the BSA molecules are indeed present on the interface and caused the formation of bright domains consistent with the planar ordering of LC beneath those regions at the interface (Figure 2.12i, j). It was observed that interfacial domains that are initiated by BSA are not formed at the isotropic phase of LC suggesting the role of LC's nematic elasticity on the formation of the optical domains (Figure 2.13). This is consistent with the prior reports that the formation of assemblies/domains (due to long-range interactions) are driven by the nematic elasticity of LC and are not present when adsorbates are in the vicinity of isotropic interface.[48-50]

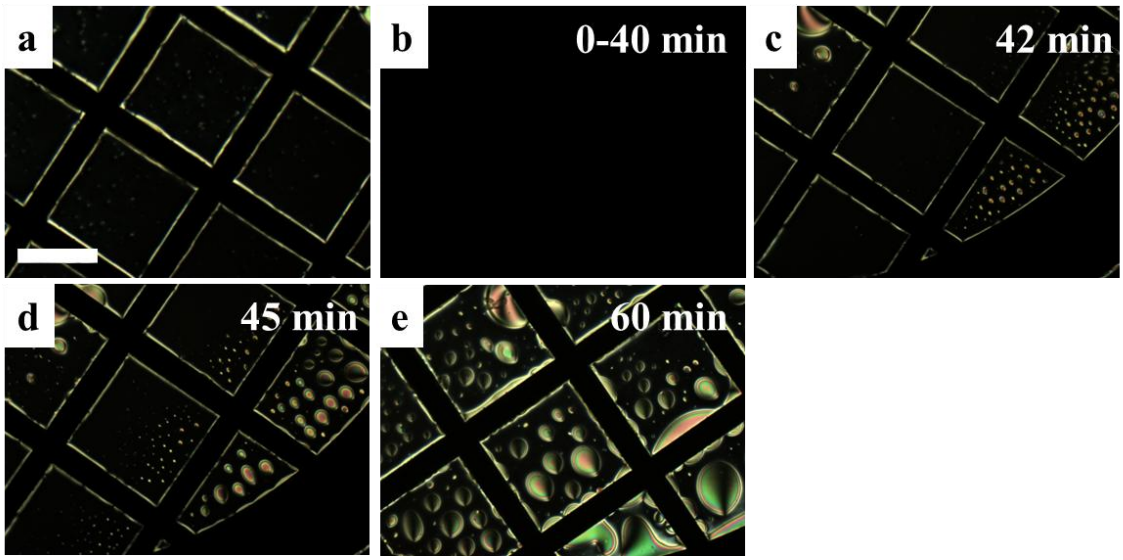

Figure 2.13. POM images of the optical response of the LC to the adsorption of BSA at a PmB laden 5CB-aqueous interface. The times are indicated after the introduction of 5 nM BSA into the aqueous phase. The PmB laden 5CB was first at room temperature (a) exhibiting homeotropic ordering. The LC film was subsequently heated and incubated at an isotropic phase of 5CB (38 ^{o}C) for the 40 min (b) and cooled down to nematic phase (c-e). Images were captured under Nikon Eclipse LV100POL polarizing microscope

equipped with a Q-imaging camera and a Linkam heating stage (LTS 420). Scale bar = 200 μm.

A few observations were noted regarding dynamic LC behavior in the presence of proteins. As the concentration of proteins is lowered, the time required by the LC to attain a planar/tilted orientation increased significantly. E.g., 50 nM and 20 nM BSA took approximately 8 min and 25 min, respectively, to establish the bright optical appearance of the LC at PmB-laden aqueous-LC interfaces. Similarly, 50 nM and 20 nM Hb demonstrate planar ordering of LC in approximately 13 and 30-40 min, respectively, at those interfaces. We plotted the average grayscale intensity of optical micrographs as a function of time that relates the optical response of the LC as the basis to investigate the dynamics of adsorption of proteins at the interface. It can be inferred in Figure 2.14a that as the concentration of BSA increased, the initiation time (can be defined as the time when the transition of LC from dark to bright begins) decreased. The higher protein concentration (e.g., 50 nM BSA) reaches an upper plateau (can be defined as the point where intensity reaches to its maximum value) at a faster rate as compared to the lower concentration (e.g., 10 nM BSA). However, the initialization of upper plateau does not necessarily mean the saturation point as the protein molecules are likely still adsorbing at the interface beyond this point of time. These results suggest the time-dependent transitional behavior of LC as a function of the quantity of protein introduced in the system. Thus, the dynamic response of this LC-based design can be correlated to quantify the bulk concentration of a protein. Second, we compared the optical responses of LC towards the same concentration of BSA and Hb. It was found that at an equal concentration of each protein, the dynamic response of LC was found faster towards BSA as compared to that towards Hb (Figure 2.14b). Comparing the behavior of BSA and Hb at 10 nM clearly indicates the significant difference in both the initiation time as well duration to reach the upper plateau (Figure 2.14b). BSA shows an initiation time of~10-20 min and reaches the maximum intensity at~60-70 min, whereas Hb takes initiation time of approximately 40-50 min and reaches to maxima in between 90-120 min. The different behaviors in the optical response of the LC in the presence of Hb and BSA (almost similar molecular weight) at PmB-laden interfaces suggest that the ordering transition of LC triggered by proteins is mainly driven by the electrostatic forces between the anionic protein molecules (BSA/Hb) and the positively charged PmB. It can further be best explained in accordance with their isoelectric points and zeta potential values (See

Appendix A for details). Both BSA and Hb possess hydrophobic cavities; however, at physiological pH, BSA is more electronegative than Hb or Cyto (a cationic protein). Thus, besides hydrophobic interactions contributing to protein–lipopeptide interactions here, electrostatics between the charged protein and PmB's peptidic groups are of longer range and seem to play a dominating role. Thus, more the electronegative protein, more facile adsorption of protein at PmB-laden interfaces which could disrupt the PmB molecules efficiently at those interfaces. These results suggest the potential application of PmB laden LC interface for label-free imaging of protein adsorption based on their mutual affinity towards the lipopeptide.

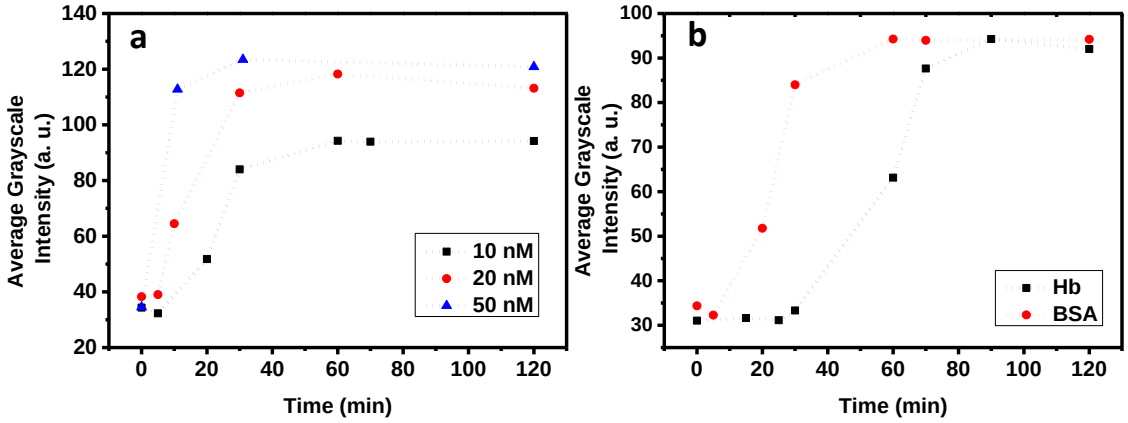

Figure 2.14. (a) Average grayscale intensity of micrographs plotted as a function of time to compare the dynamic optical response of PmB laden LC-aqueous interface to different concentration of BSA. The plot in (b) demonstrates the comparison of average grayscale intensity of 10 nM BSA and 10 nM Hb evolving as a function of time.

2.1.3.3 Optical response of PmB laden LC-aqueous interface to β-sheet rich proteins

Till now, we studied the orientational response of LC triggered by proteins whose native secondary structures in the bulk phase are rich in α-helix motifs.[51,52] Therefore, our next goal was to investigate if proteins rich in β-sheet structure could trigger distinct spatial patterns at the lipopeptide laden aqueous-LC interface that may enable the label-free identification of such proteins. The goal is highly motivated by the fact that determination of secondary structures of peptides is of scientific relevance to find the efficient treatment for amyloid (protein deposition) related diseases such as Alzheimer's, Parkinson's, and prion diseases.[53] As proof of concept, we chose two proteins: fibronectin (FibN) and concanavalin A (ConA) as they adopt a secondary structure rich in β-sheet and β-turns in bulk aqueous solutions (Refer Appendix A) and known to form amyloids under certain

conditions.[54-57] ConA, despite being a plant lectin, is of particular importance here because it displays significant structural analogy with the human amyloid-β peptide (known for its role in Alzheimer's diseases).[58] On the other hand, FibN is a glycoprotein which is abundantly present in human blood plasma as well as an extracellular matrix where it performs diverse biological functions ranging from tissue repairing to cell migration depending on its oligomerization state.[59] However, excessive deposition of insoluble FibN aggregates contributes to multiple malignancies such as scarring, fibrosis, and glomerulopathy.[60,61] It is noted that both ConA and FibN are negatively charged proteins at physiological pH (See Appendix A). Therefore, the adsorption of these proteins can also be promoted at cationic-PmB decorated LC-aqueous interface leading to an ordering transition of LC.

Given the biological relevance of these proteins, we aimed to detect FibN and ConA by monitoring the optical response of PmB loaded LC-aqueous interface. To our surprise, both ConA and FibN (300 nM) triggered the formation of small thin bright domains across the grid squares in less than 1-2 min (Figure 2.15a-h). We further postulate that these elongated/branched like structures which correspond to planar/tilted alignment of LC could be due to adsorption of the peptide aggregates at the interface. Therefore, we incubated the PmB laden LC-aqueous interface with FITC labeled ConA (~ 60 nM) and analyzed the LC film under an epifluorescence microscope. It was found that the bright elongated domains of LC observed under bright field corresponded to the highly fluorescent ConA rich regions under an epifluorescence microscope (Figure 2.15 i,j). These results confirm that these bright LC regions are highly accumulated with ConA where ConA molecules can interact with PmB layer, via electrostatic forces mainly. Such an event can disrupt the coupling of LC and PmB to result in a planar and bright state of LC.

To further confirm the morphology of peptides aggregates formed at PmB laden LC interfaces, atomic force microscopy (AFM) of the pre-incubated LC interface with ConA and FibN was carried out. AFM images provide the substantial evidence of the morphology of the peptide aggregates as a fibrillar network of these peptides were observed with an average diameter ranging from 4 to 8 nm (Figure 2.16) which may correspond to amyloid fibrils as per the prior reports.[55,57] It is important to note here that these fibrillar structures were not observed under AFM, bright field and cross polars when either of the proteins was incubated with PmB free LC-aqueous interface and the optical

appearance of LC remained bright with no signatures of the fibrillar network at the interface (Figure 2.17). These observations strongly suggest that aggregation of the peptides is mediated at the interface only in the presence of PmB layer which is further optically amplified by LC medium. Although aggregation nature of FibN and ConA in the presence of PmB has not been explored previously, recent reports provide a line of evidence that aggregation of ConA and FibN can be promoted by ionic interaction with surfactants/lipids along with stabilization of amyloid fibrils.[55,57,62] However, it is remarkable that the designed LC-based system can act as label-free technique to specifically detect Amyloidogenic peptides.

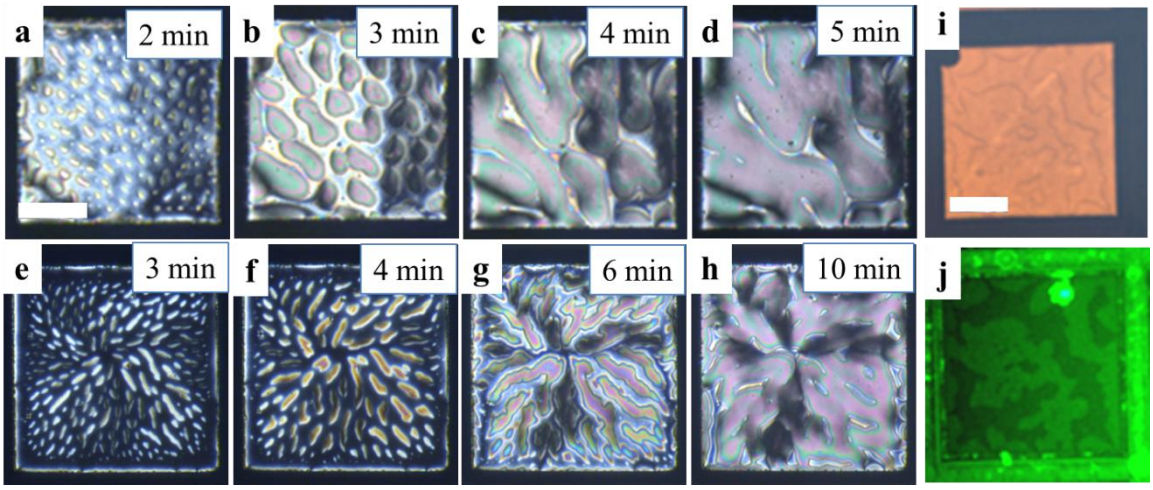

Figure 2.15. Dynamic response of LC to Amyloidogenic proteins: Optical micrographs (crossed polarizers) of 5CB in contact with aqueous solution of 0.1 mg/mL PmB followed by introduction of (a-d) ConA and (e-h) FibN. Inset indicates the times at which images were obtained following injection of oligopeptides into aqueous solution. The final concentration of proteins was 300 nM. (i) Bright-field and corresponding epifluorescence image (j) of PmB laden aqueous-LC interface after incubation with FITC labeled ConA (50 nM). Scale bar = 100 μm.

Next, the sensitivity of FibN and ConA was investigated using PmB laden LC-aqueous interface. For the same, PmB laden LC-interface was incubated with the two proteins for 2 hours and optical behavior of LC was recorded under crossed polars (Figure 2.18). It was observed that as the concentration of ConA and FibN was lowered to 50 nM, the bright domains corresponding to the planar alignment of LC were observed along with comparatively less dark regions.

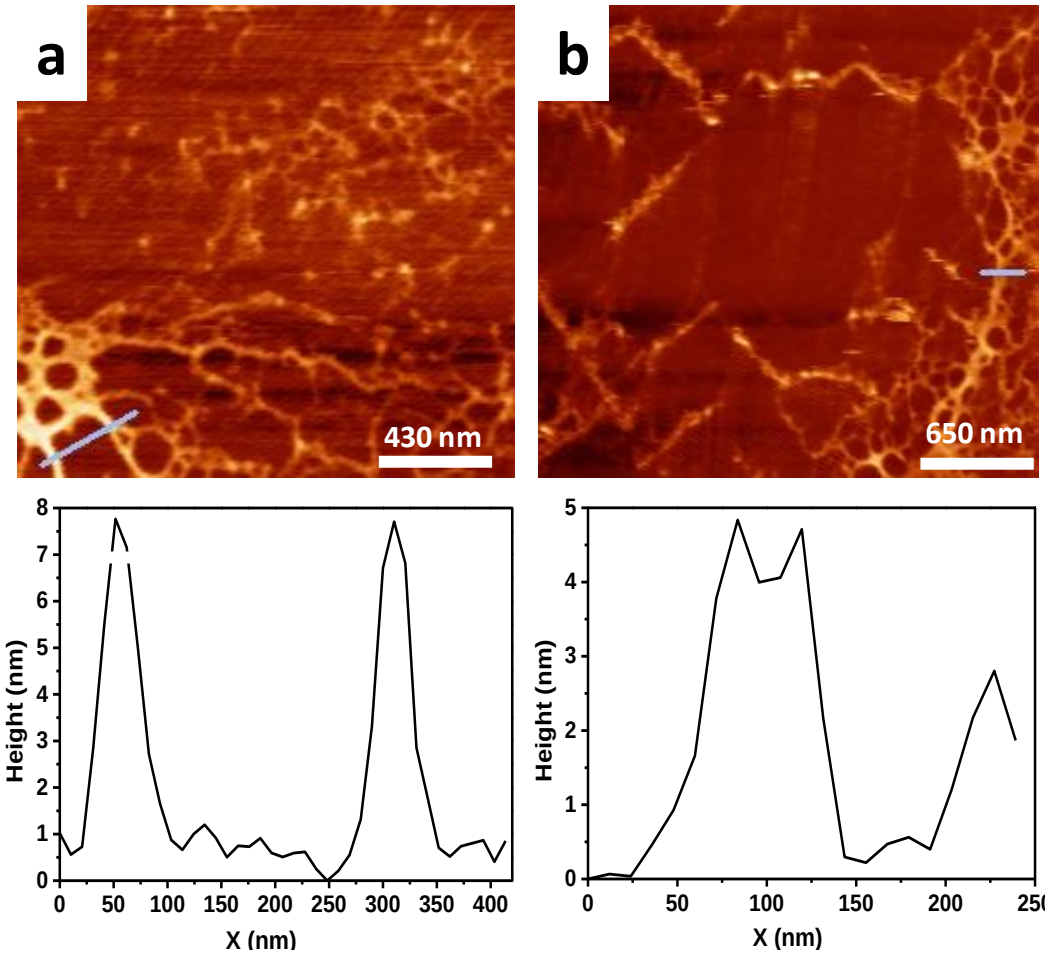

Figure 2.16. Atomic force microscopy images showing the topography of fibrillar aggregates of ConA (a) and FibN (b) respectively, formed at PmB laden LC-aqueous interface.

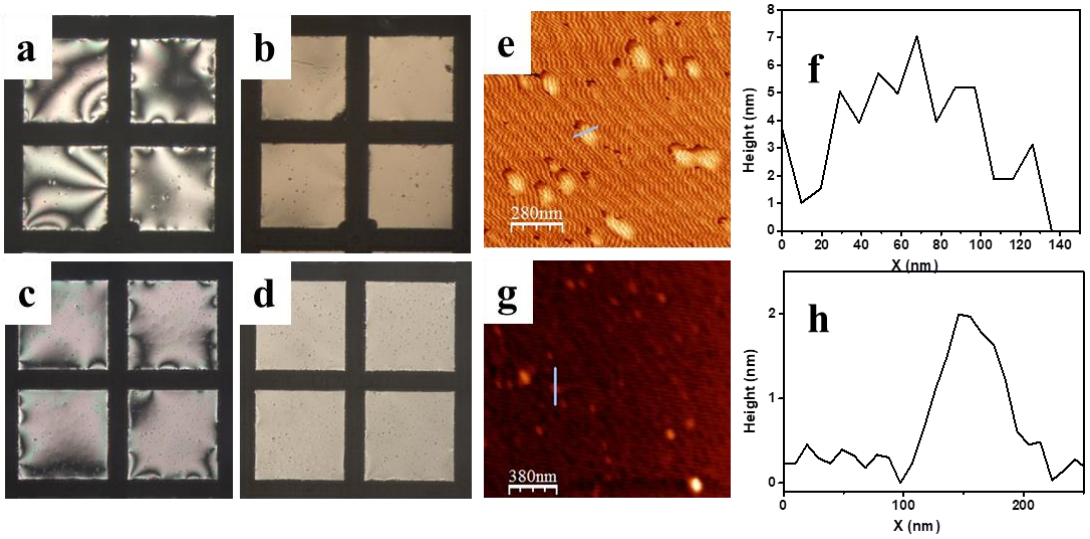

Figure 2.17. (a,c) POM and corresponding (b,d) bright-field images of PmB free LC-aqueous interface after incubation with 300 nM (a,b) ConA and (c,d) FibN for 2 hours.

(e,g) AFM images and (f,h) their corresponding height profiles showing surface morphology of (e) ConA and (g) FibN at PmB free aqueous-LC interface.

The bright domains had grown and coalesced together to envelop the maximum area around the grid square. However, the shapes of domains clearly look elongated and different than that formed by BSA (pear-shaped). As the concentration of proteins was further decreased to 10 nM and 5 nM, extended bright domains were observed at certain areas across the grid squares but the thickness of bright domains decreased and corresponding fraction of dark regions increased with decrease in the concentration of proteins. These results signify the lower quantity of adsorbed proteins upon lowering the concentration of proteins and thus, fewer bright domains were observed. Careful investigation showed that ConA could trigger the formation of bright LC domains at a concentration as low as 3 nM (Figure 2.18a). Below 3 nM, no changes in the optical appearance were observed over the periods for which we used the LC filled grids in the experiment reported in this work (hours).

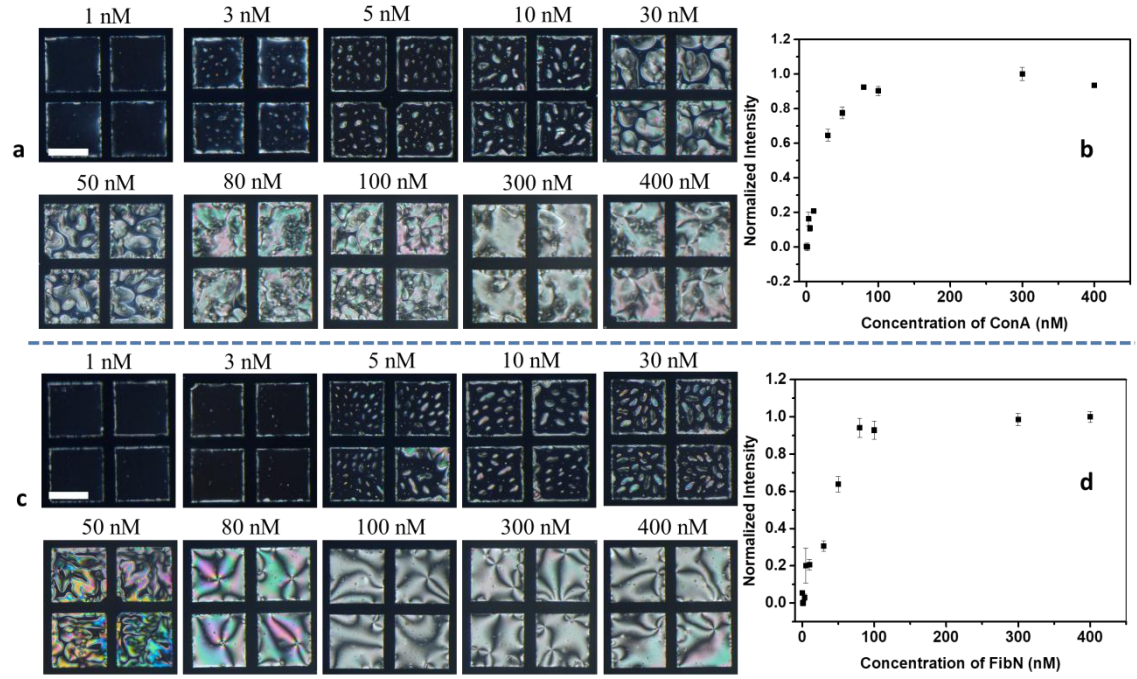

Figure 2.18. Response of LC to different concentration of β-sheet rich proteins: Optical micrographs (crossed polarizers) of 5CB in contact with an aqueous solution of 0.1 mg/mL PmB followed by incubation with different concentration of (a) ConA and (c) FibN for 2 hr. Concentration of the protein is depicted at the top of the particular image. Graphs in (b) and (d) represent average grayscale intensities of micrographs in (a,c)

plotted against different concentrations of ConA and FibN, respectively. Scale bar = 200 μm.

The change in the optical intensity of polarized light images of the LC filled grids as a function of the concentration of ConA is plotted in the graph (Figure 2.18b). The behavior of FibN was found to be similar (formation of elongated domains) as it was observed for ConA at PmB laden aqueous-LC interface. An ordering transition of the LC was observed at 5 nM of FibN at those interfaces (Figure 2.18c). Below 5 nM of FibN, no ordering transition was noticed over the time periods used in the experiment. The measured intensity of light transmitted through the film of LC filled grids as a function of different concentrations of FibN is shown in Figure 2.18d. In addition, the optical response of LC was found relatively faster towards ConA than FibN (Figure 2.19) which could be attributed to more facile interaction between PmB molecules and ConA due to the more electronegative nature of ConA in comparison to FibN. Such discrete and fast optical behavior of LC to the ultra-low concentration of β-sheet rich proteins not only allows the facile characterization of amyloid-forming proteins by the naked eye but demonstrates a potential application of PmB laden aqueous-LC interface to monitor the dynamics of aggregation of proteins qualitatively as well as qualitatively.

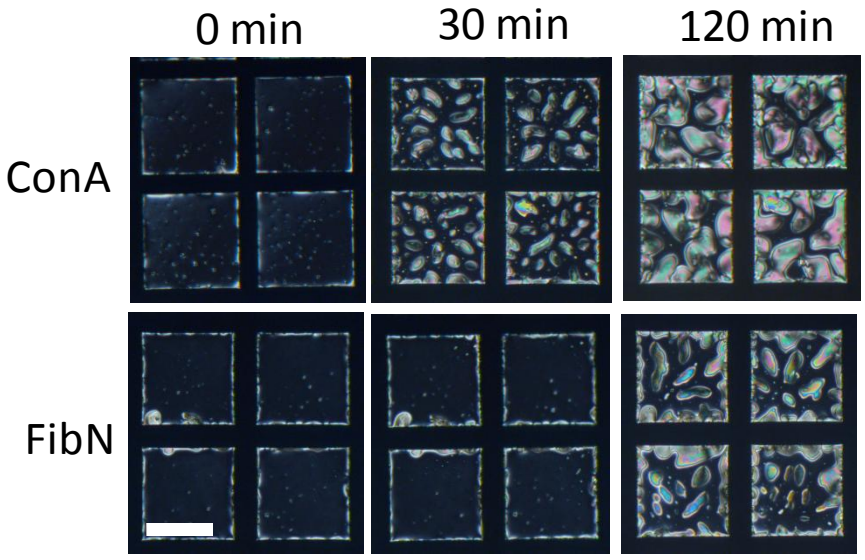

Figure 2.19. Time-lapse optical micrographs (crossed polarizers) of 5CB in contact with an aqueous solution of 0.1 mg/mL PmB followed by exposure to 30 nM of ConA and FibN. Scale bar = 200 μm.

Here, we have studied the detection of FibN using LC at PmB laden aqueous interfaces for the first time. In addition, the system was explored for detection of various other proteins such as BSA, Hb, and ConA. There are only a few reports regarding the detection of BSA and Hb at LC-aqueous planar interfaces which are driven by intermolecular interactions between proteins and amphiphilic molecules.[7,63-67] For example, Park et al. have shown that LC-aqueous interface decorated with two different block copolymers, (poly(acrylic acid)-b-(poly(4-cyanobiphenyl-4-oxyundecylacrylate) and poly((4-cyanobiphenyl-4'-oxyundecylacrylate)-b-((2-dimethyl amino) ethyl methacrylate))), can detect the BSA upto 950 nM and 30 nM, respectively.[63,64] In another report by the same group, another polymer (quaternized poly(4-vinylpyridine)-b-poly(4-cyanobiphenyl-4'-oxyundecylacrylate) laden LC-aqueous interface was able to detect BSA and Hb up to 45 nM and 139 nM concentrations, respectively.[65] Yang et al. reported that by exploiting a cationic surfactant laden LC-aqueous interface, the detection limit of BSA was found to be 60 nM.[66] The ordering transition of the LC in all these studies are triggered primarily by the ionic interactions between proteins and amphiphiles. In the present case, we found that the detection limits for BSA and Hb are 3 nM and 7 nM, respectively, which is much lower in comparison to the prior reports[63-66]. Recently, we found that lipopolysaccharide (LPS) decorated LC-aqueous interface demonstrated comparable sensitivity towards BSA (10 nM) and Hb (5 nM) in which ordering transitions were mainly found to be driven by the hydrophobic interactions between LPS and proteins.[7] In another instance, Yu et al. reported that LC-aqueous interface decorated with a non-ionic surfactant can detect both ConA and BSA with a better detection limit.[67] However, both ConA and BSA led to a similar texture of LC without exhibiting any distinctly shaped domain based on the secondary structure of proteins. On the other hand, the PmB-LC platform demonstrated a unique optical texture (elongated domains) to ConA as compared to BSA (globular domains) indicating the exceptional significance of PmB laden LC-aqueous interface towards differentiating BSA and ConA exclusively based on their structural motifs. In terms of this finding, it is worthwhile to mention that Abbott group demonstrated that at lipid decorated LC-aqueous interfaces, penetration of proteins into lipid monolayer causes the generation of LC domains (with planar/tilted alignment) whose shapes are strongly dependent on the secondary structure of proteins.[48-50] When compared to these studies,[48-50] the current study provides a detailed quantitative investigation regarding adsorption phenomenon of proteins with an improved sensitivity towards proteins (e.g., BSA). In context of detection of β-sheet rich proteins, the modus

operandi of PmB-LC design is also simpler as compared to the lipid counterparts as it eradicates the laborious step of prefabricating LC sensor (i.e., tedious preparation of lipid monolayer with controlled surface density using Langmuir Blodgett technique or a long process of preparation and characterization of liposomes) and simply operates by immersing the LC film into aqueous solution of PmB followed by protein introduction. On the top, this LC-based optical method is label-free and advantageous over the subsisting techniques such as circular dichroism, biomarkers, fluorescence and NMR which usually requires the micromolar concentration of proteins and complex instrumentation.[43]

2.1.4 Conclusions

We report a new design of stimuli-responsive LC interface based on a cyclic lipopeptide, PmB. Utilizing anisotropic optical properties of thermotropic LC, it was possible to visualize the adsorption dynamics of PmB at fluidic interface formed between water and LC. As per prior reports, surfactants with shorter chain length (8 carbon) and peptides independently impart planar ordering to LC. However, PmB, which has a short hydrocarbon chain promotes a fast (< 1 min) homeotropic orientation of LC consistent with the organization of PmB molecules at the fluidic interfaces giving dark appearances under crossed polarizers. By performing experiments with PmB nonapeptide, it was found that the homeotropic ordering of LC is greatly influenced by a range of supramolecular interactions arising by the collective contribution from peptidic moieties and the acyl chain of PmB where acyl tail can deepen inside hydrophobic LC phase and hydrophilic peptidic groups interact with the aqueous phase. Computational analysis substantiates that the acyl chain of PmB strongly influences the ordering of LC as evidenced by stronger interaction of mesogen with PmB as compared to that with PmBN. We further demonstrate the application of this positively charged LC-aqueous interface to detect and monitor the dynamic adsorption of various serum proteins. A subsequent reorientation of LC from homeotropic to planar state occurred when a negatively charged protein (BSA and Hb) effectively adsorbs at the interface as confirmed by fluorescence microscopy also. A direct relationship is observed between the ionic nature of the adsorbed proteins and the LC anchoring: More the electro-negativity of protein, faster and sensitive response of LC. Moreover, it was demonstrated that the PmB laden aqueous-LC interface could promote aggregation of β-sheet rich proteins (ConA and FibN) at the interface, primarily driven by ionic interactions with PmB molecules, which was

amplified by LC through the formation of elongated bright domains. The appearance of fibril shaped bright domains on the interface was confirmed by AFM to be the fibrillar networks of ConA and FibN. The anchoring of LC can transduce the aggregation phenomenon at protein concentration as low as 5 nM. These differences in the optical response of LC to peptide fibrils could serve as the basis for a possible detection and quantification of toxic amyloids at very early stages and very low concentrations. This lipopeptide based scheme is label-free and has successfully utilized LCs as a transduction element that responds optically to the dynamic binding of serum proteins at interfaces. Using this type of rational design, we will extend the scope of this approach towards detection of other biomolecular interactions and provide insights into the detailed molecular understanding of the LC reorientation influenced by such interfacial events. Overall, the results of this study motivate to move towards more sustainable lipopeptides based LC materials for the development of novel and multifunctional assays.

2.1.5 Experimental Section

2.1.5.1 Materials

Bovine serum albumin (BSA), concanavalin A from Canavalia ensiformis (Jack bean) (ConA), fibronectin (FibN), human haemoglobin (Hb), cytochrome c from equine heart, fluorescein conjugated BSA (FITC-BSA), fluorescein conjugated ConA (FITC-ConA), polymyxin B sulphate (PMB), polymyxin nonapeptide hydrochloride (PmBN), 4-Cyano-4-pentylbiphenyl (5CB), N,N-dimethyl-N-octadecyl-3-aminopropyltrimethoxysilyl chloride (DMOAP), hydrochloric acid, sodium hydroxide and 20 mM tris buffered saline (TBS) (pH 7.4) were purchased from Sigma-Aldrich (St. Louis, MO). Other chemicals like sulfuric acid, chloroform and hydrogen peroxide (30% w/v) were purchased from Merck (Mumbai, India). Ethanol was bought from Changshu Hongsheng Fine Chemical Co., Ltd. A Milli-Q-system (Millipore, bedford, MA) was used to perform the deionization of DI water source. Glass microscopic slides of Fisher's Finest Premium grade were obtained from Fischer Scientific (Pittsburgh, PA). Gold specimen TEM grids (specifications: 20 μm thick, 50 μm wide bars, 283 μm grid spacing) were purchased from Electron Microscopy Sciences (Fort Washington, PA).

2.1.5.2 Surface modification of glass slides with DMOAP

First, organic impurities were removed from the surface of glass slides using piranha solution [70:30 (% v/v) H_2SO_4:H_2O_2].[5,13] Briefly, the glass slides were immersed in

piranha solution for 30 min at 100 °C. The slides were then rinsed with plenty of DI water and ethanol followed by drying under a stream of gaseous N_2. Then, the slides were kept in an oven to 120 °C for 2 to 3 hr. The "piranha-cleaned" glass slides were then modified with DMOAP as per prior procedures.[5,13] Briefly, the slides were immersed into aqueous solution of DMOAP (0.1% (v/v)) for 30 min at room temperature. The slides were then rinsed with DI water to remove the excess DMOAP from the surface and dried under a stream of N_2 before finally heating at 100 °C for 3-4 hr.

2.1.5.3 Preparation of aqueous solutions of PmB and proteins

Stock solution of PmB (2 mg/mL) and proteins (BSA, Hb, Cyto and ConA) were prepared by dissolving solid material in 20 mM TBS. The aqueous solution of fibronectin was prepared by incubating solid fibronectin in 20 mM TBS at 37 °C for 20-30 min. Further dilution of the desired solution was done in 20 mM TBS.

2.1.5.4 Preparation of optical cells

DMOAP functionalized surfaces were assembled into optical glass wells as follows: Cleaned gold TEM specimen grids were placed on a DMOAP-coated glass slide. Then, approximately 0.2 μL of 5CB LC was poured on grids and the excess LC was removed with the help of a Hamilton syringe which produces a uniform interface. Subsequently, the glass slide was immersed in a glass optical well containing 20 mM TBS followed by addition of a constant volume of stock PmB solution (100 μL) to achieve a certain final concentration. In order to study the adsorption of proteins, LC film was first incubated with an aqueous solution of 0.1 mg/mL PmB for 5 min followed by addition of a certain volume (100-3 μL) from the stock aqueous solution of proteins to obtain a desired final concentration. For fluorescence microscopy, PmB laden LC film was prepared by the above method followed by incubation with approximately 10-15 nM FITC-BSA or 60 nM FITC-ConA for 1 to 1.5 hour. The total volume of aqueous solution in the well was kept 2 mL.

2.1.5.5 Characterization of LC-aqueous interface under crossed polars

The ordering of the LC was observed under a Zeiss polarizing microscope (Scope. A1) equipped with crossed polars using objectives of magnification 50X, 100X and 200X. All the images were captured with an exposure time of 120 ms using an AxioCam Camera. The average grayscale intensity of the images was measured by processing at least 3

squares of TEM grid using Image J free access software (developed by U. S. National Institutes of Health, Bethesda, MD). For time-dependent adsorption of proteins, the average grayscale intensity of micrographs was measured from the whole four squares of the TEM grid. For quantification of protein, the average grayscale intensity was measured from individual nine (for BSA and Hb) and four (for ConA and FibN) squares of TEM grid and data normalization was performed to account for variations in deviations in instrumental (microscope) settings such as the intensity of light and focal depth.

2.1.5.6 Epifluorescence imaging of LC-aqueous interface

A Zeiss (Scope. A1) fluorescence microscope was used to image the protein-laden aqueous-LC interface under a fluorescence filter cube of a 460 nm excitation filter and a 534 nm emission filter. An AxioCam camera equipped with the microscope was used to capture the images.

2.1.5.7 DFT calculations

Full geometry optimizations were carried out by Gaussian 09 program package without imposing any constraints.[68] The DFT calculations were carried out in the framework of the generalized gradient approximation (GGA) using Becke3–Lee–Yang–Parr hybrid functional (B3LYP) exchange-correlation functional and the 6-31G (d, p) basis set. B3LYP functional with the standard basis set 6-31G were applied due to its successful application for larger organic molecules, as well as hydrogen-bonded systems in the past.[69-71]

2.1.5.8 Atomic force microscopy

An Innova atomic force microscope (Bruker) was employed in the tapping mode to obtain AFM images. For imaging, the silicon nitride cantilever probe with a radius ~8 nm was used. For the preparation of the sample, PmB laden or PmB free (as per requirement) LC film was pre-incubated with 300 nM of desired protein for 2 hours. Then, the LC film was taken out in the air and LC material (containing proteins at the interface) was pipetted out by a micropipette before drop-casting on a freshly cleaved, water-washed muscovite mica (Grade V-4 mica from SPI, PA). Before scanning, the mica was allowed to air dry for 15–20 min. The images were collected in NanoDrive (v8.03) software at a resolution of 512 × 512 pixels. The collected AFM images were further processed and analyzed using WSxM version 4 beta 8.1 software.[72]

2.2. Part B: Surfactin Laden Aqueous-Liquid Crystal Interface Enabled Identification of Secondary Structure of Proteins

2.2.1 Introduction

Proteins form the main constituent of biological processes; their structures and interactions with cellular environment/membranes are closely associated with specific functions executed in health and disease.[73] In particular, abnormal and extracellular deposition of proteins (amyloids) is considered the primary cause of major incurable diseases such as type II diabetes and neurodegenerative disorders including Huntington's, Alzheimer's and Parkinson's diseases.[74] Unambiguously, all the amyloid fibrils share a common secondary structure of polypeptide backbones which is dominated by β-sheet conformation therefore this structural property forms the major basis for identification of amyloids.[75] Existing techniques for protein studies, including NMR, X-ray crystallography, atomic force microscopy and circular dichroism (CD) to name a few, potentially enable the access to different levels of conformational information.[75,76] However, many of these methods have restrictions concerning required sample preparation, output analysis and real-time monitoring under physiological conditions. Some of these techniques, such as CD and NMR, require expensive and sophisticated instrumentation or large quantities of samples (micro to millimolar), which restrict investigations on costly proteins. Similarly, many techniques are restricted to bulk measurements or thick layers of peptides, which are not appropriate for replicating nanometer-thin biological/organic interfaces.[77] Hence, there is an immense need for the development of label-free, sensitive and simple tools for in vitro detection of secondary structures of proteins in their native states for early biodiagnostics of neurological disorders which can be circuitously beneficial for the advancement of therapeutics.

In recent years, liquid crystals (LCs) have been significantly recognized as stimuli-responsive materials that hold technological applications in biosensing and diagnostics.[1,3,5,6,13,23-25,78] In particular, orientations of LCs, owing to their weak anchoring energy of the order 1–10 μJm^{-2}, are highly sensitive to the molecular events occurring at the fluidic interface formed between LC and aqueous media. This orientational order of LC, which can be amplified over 100 μm from the interface, gives rise to the anisotropic optical properties which in turn enable its label-free characterization under polarized light.[79,80] Previously, LC-aqueous interfaces have been utilized for amplification and

transduction of highly specific molecular interactions such as antibody-antigen binding assay[10] and DNA hybridization[15]. Concerning protein-based studies, careful investigation using LC has been carried out by several groups to understand the interfacial phenomenon regarding protein binding events and consequent lateral organization of the biomolecules at LC-aqueous interfaces.[7,48-50,63-67,81-84] It is well known that proteins trigger a negligible change in orientations of LC, therefore to achieve an optical signal for protein, it is important, prior to protein adsorption, to decorate the LC-aqueous interface with amphiphiles that promote homeotropic orientations of LC. Thus, previous protein-related studies at LC-aqueous interfaces vastly comprise of linear amphiphiles such phospholipids and conventional water-soluble surfactants and polymers. [7,48-50,63-67,82-84] Recently, Yang et al. reported the investigation on self-assembly behavior of an amphiphilic lipopeptide at LC-aqueous interfaces.[85] Thus, we went beyond and asked if it is possible to design a new LC system that allows the direct visualization of peptidic residues by the homeotropic alignment of LC. In that direction, we recently made an advancement using cyclic lipopeptide, polymyxin B (PmB), which could trigger a homeotropic ordering of LC supported by topological flexibility of its cyclic peptidic headgroup and the linear acyl tail.[81]

2.2.2 Objective

Inspired by the same, our approach herein is based on another naturally occurring cyclic lipopeptide, surfactin (SFN). Structurally, SFN consists of a peptidic headgroup with seven amino acids and a hydrocarbon chain attached to it (as shown in Figure 2.20a). Due to its amphipathic construction, it is known to exhibit notable surface and bioactive properties such as antibacterial, antiviral, hemolytic activities.[86] We speculated that hydrophobic lipid tails of SFN might facilitate the homeotropic alignment of LC at the aqueous interface while the anionic peptide functionalities (in the headgroup) may direct the adsorption of proteins at the interface in a controlled manner leading to a change in the ordering of LCs at the interface as proposed in Figure 2.20b. The study is highly motivated by the fact that interfacial behavior of cyclic lipopeptides remains relatively unexplored at LC-aqueous interface and such systems could be useful as highly sensitive and multifunctional detection assays.[81] Herein, we used five biologically relevant proteins as model proteins to account the detailed study of LC's orientations driven by intermolecular interactions between proteins and SFN molecules at the aqueous-LC interface. In particular, we aimed to investigate how orientations of LC will be influenced

by physico-chemical properties and secondary structure of a range of proteins which can serve as label free basis for detection of toxic amyloids.

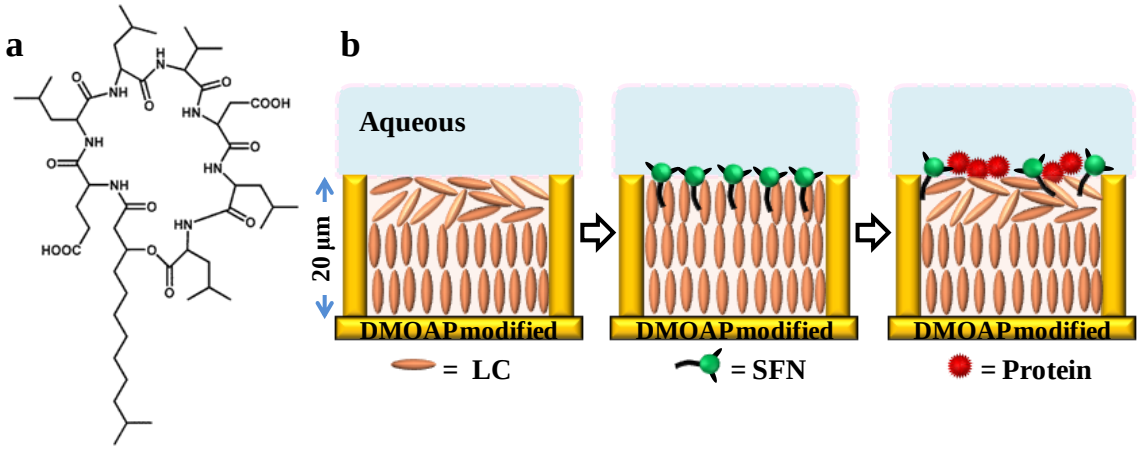

Figure 2.20. (a) Chemical structure of SFN: A hydrophobic tail connected to a heptapeptide ring. (b) Proposed schematic illustration of the orientation of LCs coupled with self-assembly of SFN and subsequent adsorption of proteins at aqueous–LC interfaces. The nematic LC is confined within a TEM grid supported on the glass slides coated with DMOAP.

2.2.3 Results and Discussion

2.2.3.1 Ordering transitions in LC in presence of SFN

The first experiment was carried out to examine the orientational response of LC film in contact with an aqueous solution of SFN in DI water. Briefly, E7 nematic LC was confined within 20 µm thick TEM grid supported on a DMOAP modified glass slide to make a stable and uniformly planar LC film. E7 film when viewed in air demonstrated dark optical appearance under crossed polarizers. As the DMOAP-coated glass slides construct strong homeotropic (perpendicular) anchoring of the LC at the bottom surface, the dark appearance of the liquid crystal reflects a perpendicular anchoring of the LC at the LC-air interface. When immersed in DI water, the LC film exhibited bright optical appearances under crossed polars (Figure 2.21a), consistent with the hybrid/planar alignment of LC at the aqueous-LC interface as per prior reports.[3] Interestingly, when the aqueous solution of SFN (final concentration was 75 µM in bulk phase) was introduced onto LC film, the orientations of LC turned homeotropic within 1 min and LC appeared dark (Figure 2.21b-d). The rapid ordering transition of LC from planar to homeotropic indicates the adsorption of SFN molecules at aqueous-LC interfaces, mainly caused by

lateral hydrophobic interactions between long hydrocarbon tails of SFN and LC molecules. The deposition of a preformed monolayer of SFN on LC film induced a homeotropic ordering of LCs at the LC-aqueous interfaces (See Appendix B for details), thus confirming the adsorption/self-assembly of SFN at those interfaces. The above result suggests a potential implication of LC for label-free detection and identification of certain bacterial strains (on the basis of secretion of SFN) and subsequent detection of bacterial fouling.[87,88]

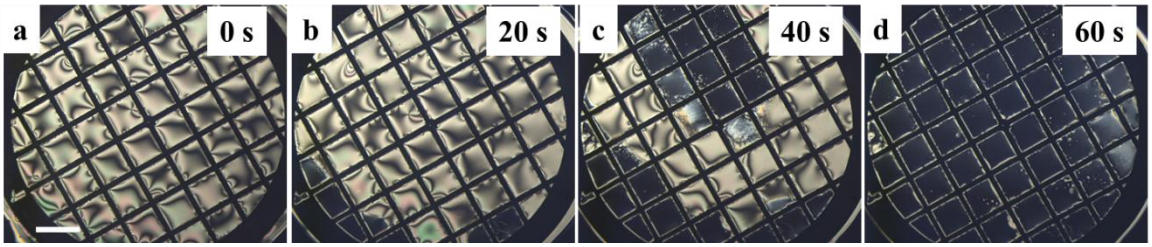

Figure 2.21. Optical micrographs (cross polars) of E7 film on a DMOAP-glass slide after the introduction of SFN (75 μM) in the aqueous phase. Scale bar = 400 μm.

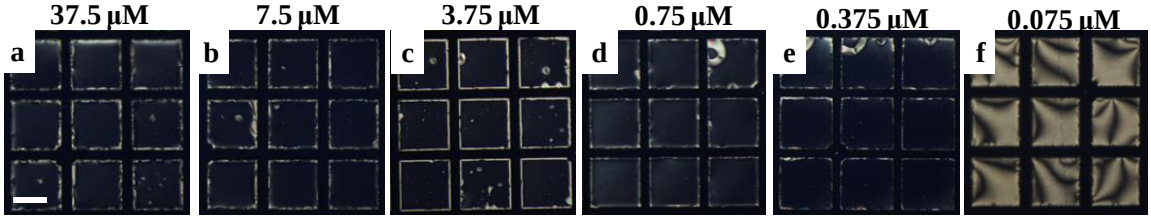

Figure 2.22. Polarized optical micrographs of E7 films in contact with DI containing different concentration of SFN (indicated at the top). Scale bar = 200 μm.

Our next goal was to determine the optical response of LC towards lower concentrations of SFN. Figure 2.22 demonstrates the POM images of LC depicting ordering of LC at various concentrations of SFN. Interestingly, it was observed that as the concentration of SFN was sequentially decreased, the response time of LC to exhibit homeotropic ordering increases significantly suggesting the concentration-dependent ordering transition of LC towards SFN. For e.g., 37.5 and 7.5 μM of SFN led to dark optical appearance of LC within 2 min (Figure 2.22a,b), while 3.75, 0.75 and 0.375 μM of SFN took approximately 5-7 min, 1 hr, and 2.5 hr, respectively to align the LC molecules homeotropically (Figure 2.22c-e). Moreover, LC did not show a change at 0.075 μM of SFN and optical appearance of LC remained bright till the time observed (8 hr) (Figure 2.22f). This high

sensitivity of LC towards SFN could be useful as the label-free detection and estimation assay for SFN at micromolar concentration range in samples.

2.2.3.2 Orientational response of SFN laden LC-aqueous interface to proteins

As observed above, SFN promotes a homeotropic orientation of LC at the aqueous interface, and thus, we next examined if the ordering of LC underneath SFN decorated interface can be perturbed by a variety of proteins in the vicinity of the interface at physiological pH (pH 7.2). First, we selected four proteins for the study- bovine serum albumin (BSA), human hemoglobin (Hb), cytochrome c (Cyto) and concanavalin A (ConA). Structurally, each one of them consists of at least a hydrophobic pocket and adopts mainly α-helical secondary structure in bulk phase[89-91] (except ConA which is an all β-sheet protein[81]). However, they differ in their physicochemical properties such as overall ionic charge as recently confirmed by us through zeta potential measurements at physiological pH[81]: BSA (most anionic) > ConA (anionic) > Hb (slightly anionic) > Cyto (highly cationic),. Prior to exposure to proteins, the SFN (7.5 μM)-laden aqueous/E7 interface was exchanged with tris buffered saline (TBS) (1mM, pH 7.2) to remove free SFN from the bulk solution. The homeotropic ordering of LC remained stable for several hours (8 hr or so) in TBS (Figure 2.23a). Next, an aqueous solution of 400 nM Hb was introduced onto the SFN laden LC film followed by monitoring the optical response of LC under cross polars. Interestingly, Hb triggered a reorientation of LC from homeotropic to planar within 3 min of addition and the optical appearance of LC turned bright (Figure 2.23b).

Combined with our previous report[7,81], the planar/tilted orientation of the LCs is associated with of an interfacial phenomenon, whereby Hb molecules adsorb at the aqueous–LC interface. This, in turn, can perturb the organization of interfacial SFN molecules, thereby triggering a reorientation of LC from homeotropic to planar/tilted. We believe that besides possible electrostatic and other noncovalent interactions (such as H-bonding), strong hydrophobic interactions between Hb and negatively charged SFN molecules (i.e., between aliphatic tails of SFN and hydrophobic motif of Hb) play an important role in the ordering transition of SFN decorated LCs (See Appendix B for fluorescence study). Consequently, SFN laden LC-aqueous interfaces were exposed to 400 nM of BSA, Cyto, and ConA to examine if LC would undergo an ordering transition similar to that of SFN-Hb as described above. We observed that the optical appearance of

LC switched from dark to bright in all the cases within 15 min (Figure 2.23c-e). We note two important observations regarding LC's optical response here, which will be experimentally explored and discussed sequentially. First, in all the cases, an ordering transition of LC arose towards a planar alignment irrespective of the charge on a particular protein suggesting a complex interplay of ionic and hydrophobic interactions between anionic SFN and protein molecules in driving the ordering transition of LC. Second, the bright optical patterns of LC triggered by the proteins, especially ConA, (Figure 2.23e) differed in terms of the shape of LC domains. This suggests the important correlation between this observation of distinct shaped optical domains and the secondary structure of proteins. It is important to note here that SFN did not influence the native secondary structure of proteins in aqueous solution as confirmed by circular dichroism (See Appendix B).

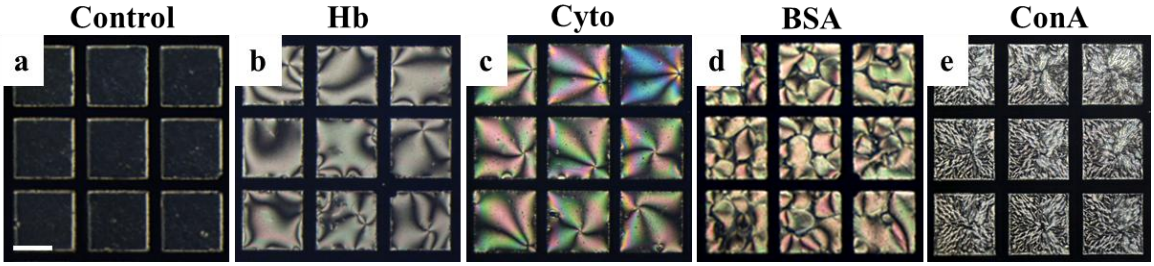

Figure 2.23. Polarized optical micrographs of SFN laden LC film in contact with (a) TBS, (b) Hb, (c) Cyto, (d) BSA and (e) ConA. The final concentration of Hb, Cyto, and ConA was 400 nM. Scale bar = 200 μm.

First, we aimed to elucidate the nature of molecular interactions dominating the ordering transition of LC. For the same, we carried out a series of experiments at a constant concentration of protein and compared the optical dynamic response of SFN laden LC-aqueous interface towards proteins. Here, we chose BSA, Hb, and Cyto as each of them represents highly anionic, moderately anionic, and cationic protein, respectively. Figure 2.24-2.26 represents the polarized optical images of SFN-laden LC-aqueous interface taken at certain time intervals after the introduction of 50 nM of Hb, Cyto and BSA, respectively. As before, it was observed that all three proteins were capable of triggering a planar orientation of LC. However, Hb induced the fastest planar ordering of LC (within 5 min) while Cyto and BSA were relatively slower to do so. The ordering of LC became completely planar within approximately 30 and 60-70 min for Hb and Cyto, respectively. Whereas, in the case of BSA, we observed co-existence of bright and dark regions even

after 7 hours of incubation time (Figure 2.26). BSA and Hb, which are of comparable molecular weights (64-66 kDa) and thus considerable effect of interfacial density on ordering transition could be neglected, differ in overall ionic charge (BSA is more negatively charged than Hb) at physiological pH. Thus, despite being subjected to possible electrostatic repulsions between BSA/Hb and anionic SFN molecules at the interface, these anionic proteins could trigger an ordering transition in LC and thus indicated the prominent role of other non-covalent interactions such as hydrophobic interactions (Refer Appendix B) and hydrogen bonding. Whereas, a cationic protein Cyto, despite being a low molecular weight protein (~ 12 kDa) triggered a faster reorientation of LC to planar as compared to that of a bigger protein like BSA indicating facile attractive ionic interaction between anionic SFN and Cyto. In a nutshell, these findings strongly suggest that the reorientation of LC underneath SFN decorated LC-aqueous interface is strongly coupled with several supramolecular interactions between protein and SFN molecules; however, the rate of ordering transition is mainly determined by nature of intermolecular electrostatic forces between them.

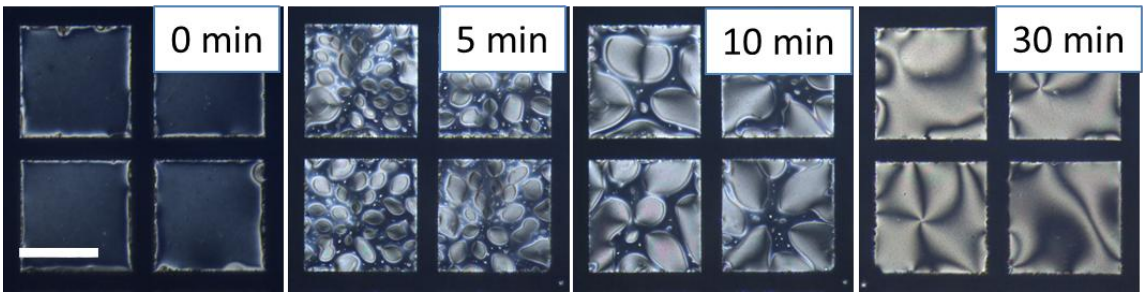

Figure 2.24. Time-lapse polarized optical micrographs of SFN laden aqueous-LC interface after the introduction of 50 nM Hb. Inset indicates the time at which the image was captured. Scale bar = 200 μm.

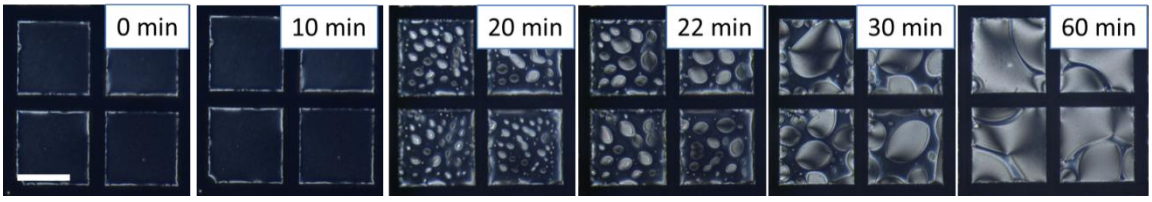

Figure 2.25. Time-lapse polarized optical micrographs of SFN laden aqueous-LC interface after the introduction of 50 nM Cyto. Inset indicates the time at which the image was captured. Scale bar = 200 μm

To investigate the sensitivity of SFN-laden LC-aqueous interface towards Hb, BSA, and

Cyto, SFN laden LC aqueous interface was incubated against various concentrations of proteins for 2 hrs. It was observed that as the concentration of each protein was decreased, the bright regions corresponding to the tilted/planar orientation of LCs decreased (Figure 2.27-2.29). We further realized that besides qualitative visualization of these subtle events, orientational transitions of LC can sensitively report the presence of these proteins at bulk concentration as low as 3, 5 and 10 nM for Hb, BSA and Cyto, respectively and thus presents applicability of LC-based assay as a biosensor to detect various complex biological interactions at nanomolar concentration regime.

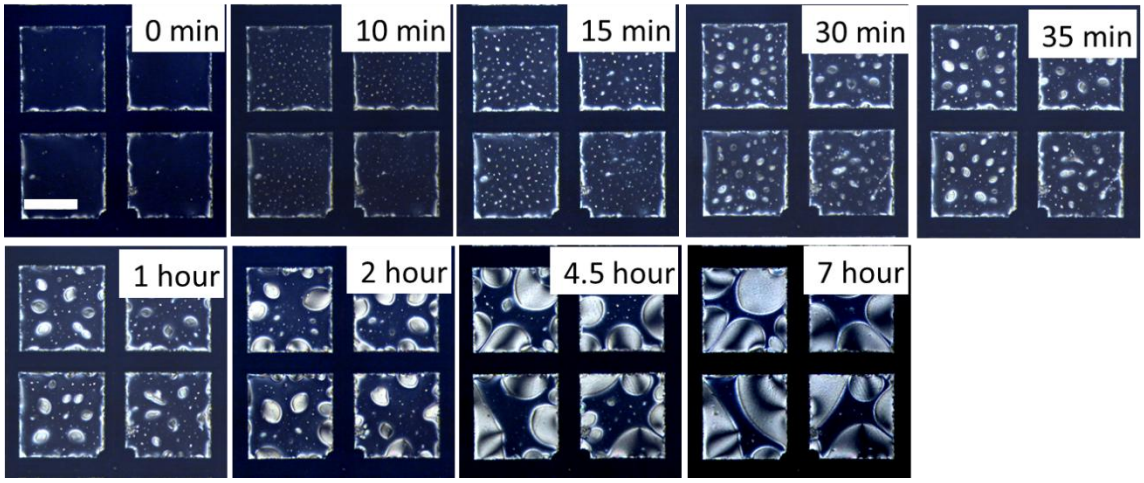

Figure 2.26. Time-lapse polarized optical micrographs of SFN laden aqueous-LC interface after the introduction of 50 nM BSA. Inset indicates the time at which the image was captured. Scale bar = 200 μm.

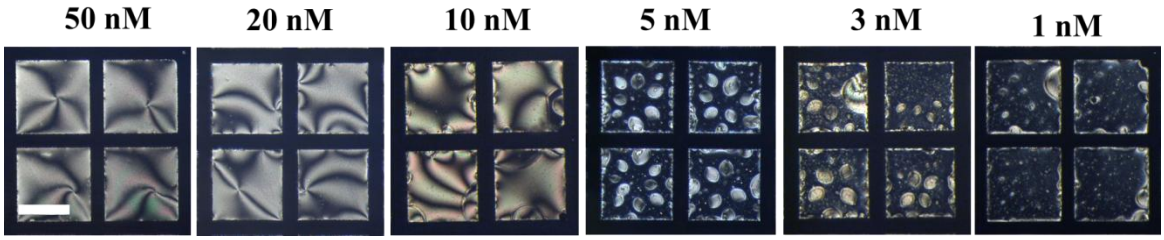

Figure 2.27. Optical micrographs (crossed polarizers) of SFN laden E7 films incubated against the different concentration of Hb. Scale bar = 200 μm.

The second and common phenomenon observed during the above experiments is that the homeotropic to planar transition of LC occurred through the development of small rounded/pear-shaped domains on the interface. These domains were laterally mobile at the interface and evolved with time to ultimately coalesce into each other over the

interface. Thus, to investigate the correlation between the emergence of the spatial patterns and location of protein at the interface, we used epifluorescence microscopy and fluorescently labeled protein.

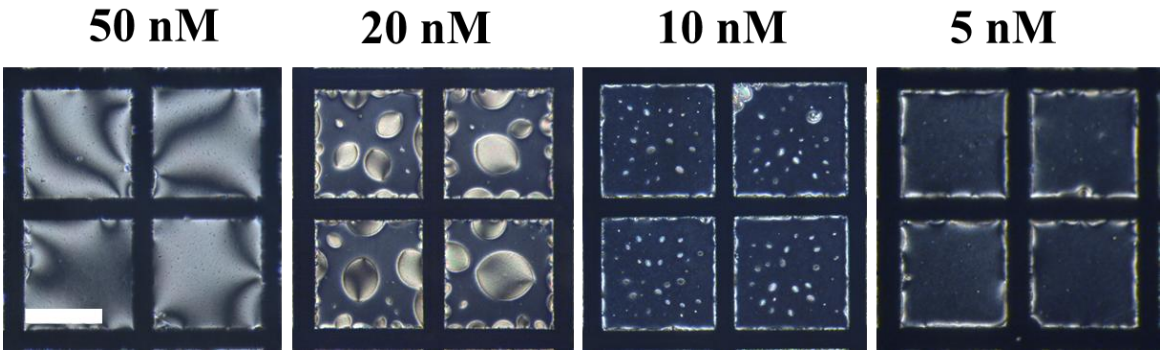

Figure 2.28. Optical micrographs (crossed polarizers) of SFN laden E7 films incubated against the different concentration of Cyto. Scale bar = 200 μm.

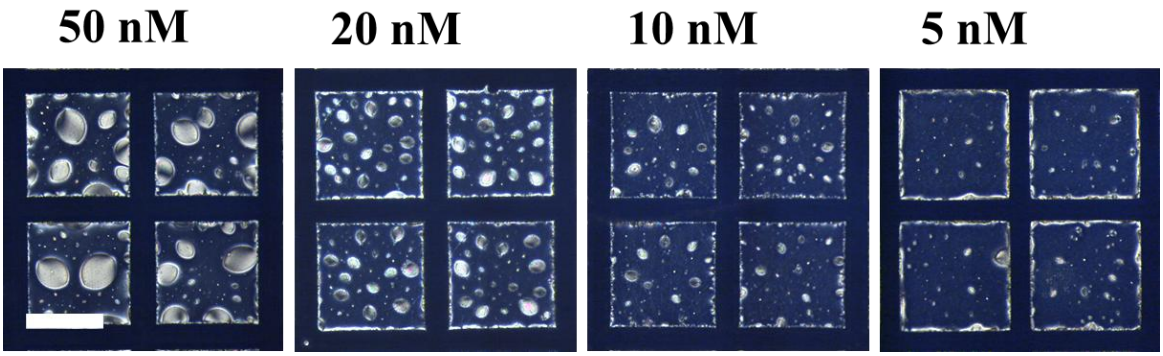

Figure 2.29. Optical micrographs (crossed polarizers) of SFN laden E7 films incubated against the different concentration of BSA. Scale bar = 200 μm.

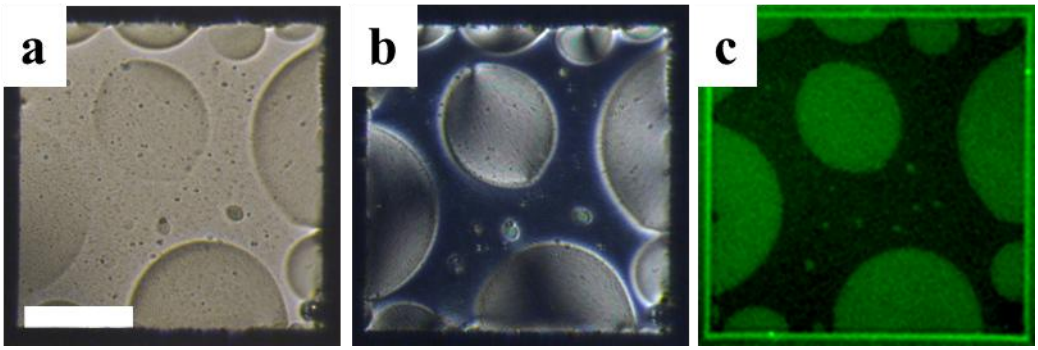

Figure 2.30. Bright-field (a), polarized light micrograph (b) and epifluorescence (c) images of SFN laden aqueous-LC interface after incubation with FITC labeled BSA. Scale bar = 100 μm.

Figure 2.30a-c includes the bright field, POM, and corresponding epifluorescence microscopy images of a SFN-laden LC-aqueous interface after incubation with FITC labeled BSA. As evident, the pear-shaped domains (visible in the bright field image, Figure 2.30a) which correspond to the planar/tilted optical domains of LC (under polarized light Figure 2.30b) are highly accumulated with FITC-BSA molecules (epifluorescence image, Figure 2.30c). This result confirmed that the spatial patterns of LC observed in the above study define the adsorption of protein in the confined domains on the interface of LC. Previous studies have also revealed similarly shaped spatial patterns formed by α-helical rich proteins such as BSA and Cyto at phospholipids/cyclic-lipopeptide decorated LC-aqueous interfaces.[48,81]

2.2.3.3 Distinct optical response to β-sheet rich proteins

As observed earlier in Figure 2.23, ConA (a β-sheet rich protein) triggered a planar ordering of LC at SFN laden-LC-aqueous interface along with emergence of fibril like structures at the interface as contrary to BSA, Hb and Cyto (α-helix rich proteins) which resulted in formation of globular spatial patterns at the SFN laden LC-aqueous interface. Thus, the different behavior of optical patterns of LC generated by ConA compelled us to gain an insight about the organization of these elongated domains of LC at the interface and the role of secondary structure of protein. In addition, ConA exhibits considerable structural resemblance to the human amyloid-β peptide (known for its role in Alzheimer's disease) therefore it can be of importance to detect ConA.[58] Therefore, we monitored the temporal evolution of spatial patterns at SFN laden LC-aqueous interface after injection of 50 nM ConA into the aqueous phase. Interestingly, we observed that small thin and bright domains, consistent with the distorted ordering of LC, nucleated within 20 min which grew anisotropically in one direction (30-70 min) with dendritic texture before finally merging (70 min - 5 hour) (Figure 2.31a). We further investigated the basis of the emergence of these bright domains of LC in presence of these proteins and thus conducted fluorescence microscopy using FITC labelled ConA. It was found that these elongated structures which correspond to planar/tilted orientation of LC are highly protein-rich regions (Figure 2.31b,c) and thus, confirms the compartmentalization of proteins in the form of domains at the interface.

The distinct appearance of elongated/fibril shaped domains caused by ConA led us to speculate SFN laden LC-aqueous interface could specifically assist in distinguishing

between proteins composed of different structural motifs (α-helical and β-sheet). Thus to confirm the same, in our next experiment, we chose another protein, fibronectin (FibN), as (a) its native secondary structure in solution is mainly composed of β-sheet secondary structure[19]; (b) its aggregates (amyloids) are found in certain physiological disorders.[60,61] Interestingly, we found that FibN also triggered the formation of elongated and bright optical patterns at SFN laden aqueous-LC interface which grew faster along the longer dimensions and coalesced with time (Figure 2.32).

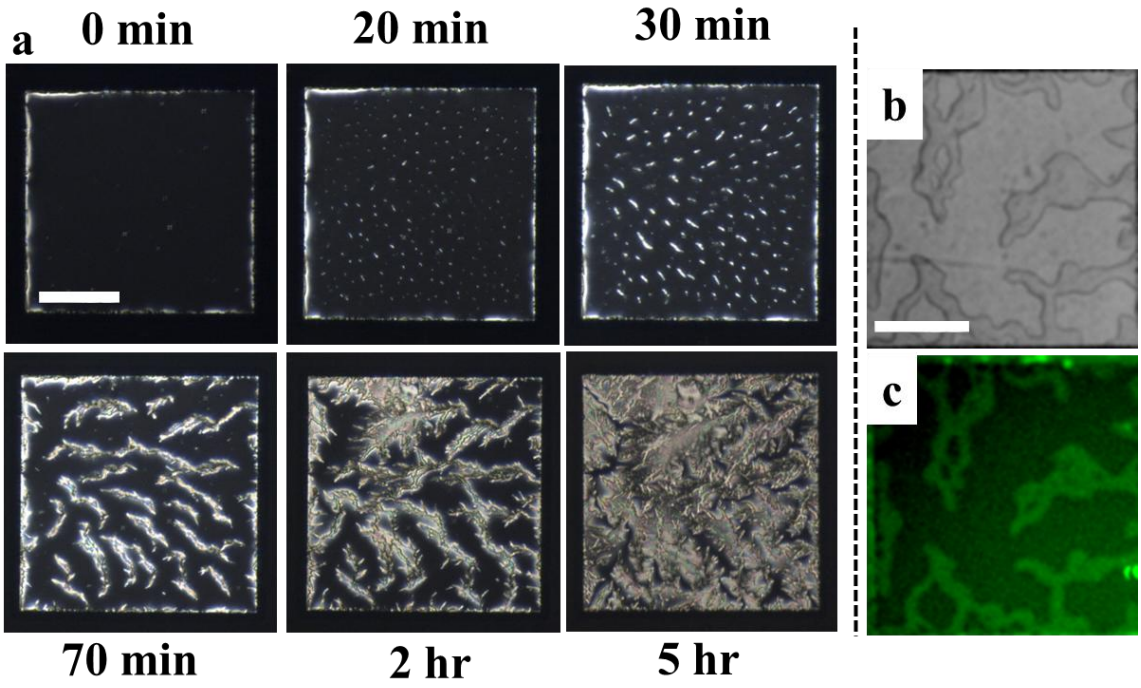

Figure 2.31. (a) Time-lapse POM images showing the dynamic response of LC to the adsorption of 50 nM ConA at SFN laden LC-aqueous interface. (b) Bright-field and (c) corresponding epifluorescence images of SFN laden aqueous-LC interface after incubation with FITC labeled ConA. Scale bar = 100 μm.

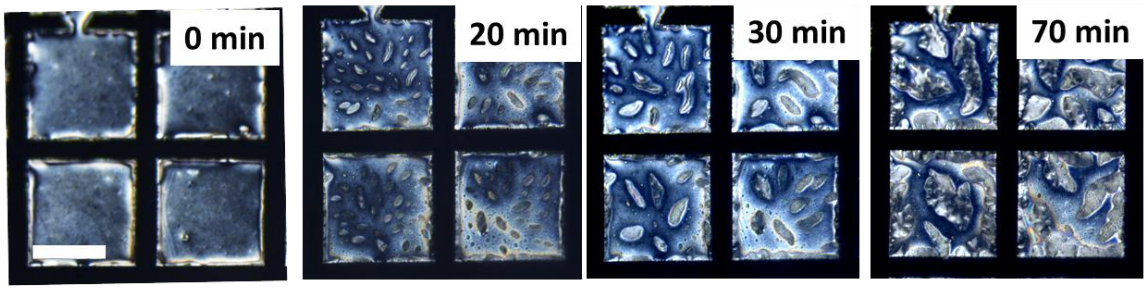

Figure 2.32. Time-lapse POM images showing the dynamic response of LC to the adsorption of 50 nM FibN at SFN laden LC-aqueous interface. Scale bar = 200 μm.

Moreover, the optical response of the SFN laden LC-aqueous interface was slightly faster towards FibN as compared to ConA. This observation could be due to the less overall anionic charge of FibN which allows the facile interactions between FibN and anionic SFN molecules. It is in good agreement with our above discussion of the role of ionic interactions in stating the response time of LC. It is important to state here that although the structures of domains formed by ConA and FibN differ in terms of thickness of domains; their anisotropic growth in one dimension and shape is reproducibly different (elongated, sharp at edges) from that formed by the above studied α-helical proteins (globular and smooth towards edges). Notably, in the absence of SFN, the optical appearance of LC remained unperturbed in the presence of ConA and FibN (Figure 2.33) and thus suggests the major role of interactions between SFN-proteins at the interface to trigger the above-described response of LC. The distinct patterned orientations of the LC to different structural motifs can be attributed to the stronger anchoring energy imparted by β-sheet rich proteins at LC interface as compared to α-helical proteins as shown by Abbott et al.[50] Overall, these findings indicated that the shapes of the LC domains at SFN-laden interface are strongly coupled with the secondary structures of proteins adsorbed at the interface and could serve as a simple optical probe to identify β-sheet rich motifs which are structurally known to dominate toxic amyloids.

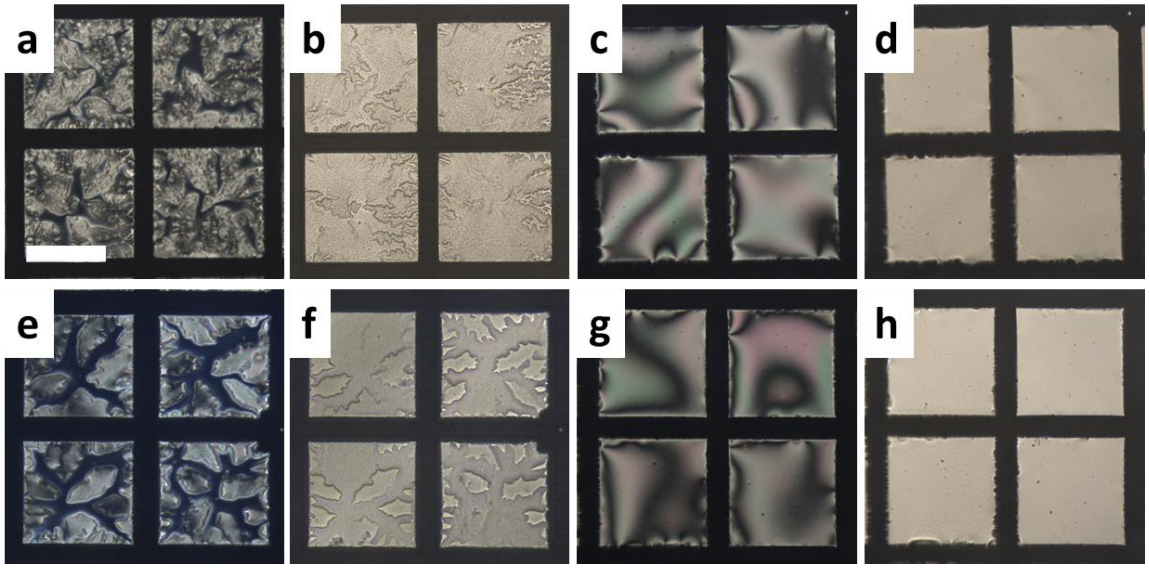

Figure 2.33. (a,c,e,g) Polarized light micrographs and corresponding bright-field images (b,d,f,h) of LCs following incubation of SFN laden aqueous-E7 Interface (a,b,e,f) and SFN free aqueous-E7 Interface (c,d,g,h) with 50 nM ConA (a-d) and 50 nM FibN (e-h) for 4 hr. Scale bar = 200 μm.

It is essential to explore the sensitivity of designed LC system towards such proteins beyond merely reporting the specific presence of β-sheet rich proteins. Thus, in the next series of experiments, SFN decorated LC film was incubated with different concentrations of ConA and FibN for 2 hours, followed by monitoring the orientation of LC under crossed polars. The bright optical domains of LC, consistent with the tilted/planar ordering of LC, with elongated shapes were present at the concentration of both proteins as low as 5 nM (Figure 2.34). In addition, as the concentration of ConA and FibN was sequentially decreased from 50 nM to 5 nM, the ratio of bright to dark regions and the size/thickness of optical domains decreased. Thus, the new lipopeptide based LC system not only caters the label-free imaging of protein adsorption at biomembrane-mimetic interfaces but can also distinguish between different structural motifs of proteins at nanomolar concentrations.

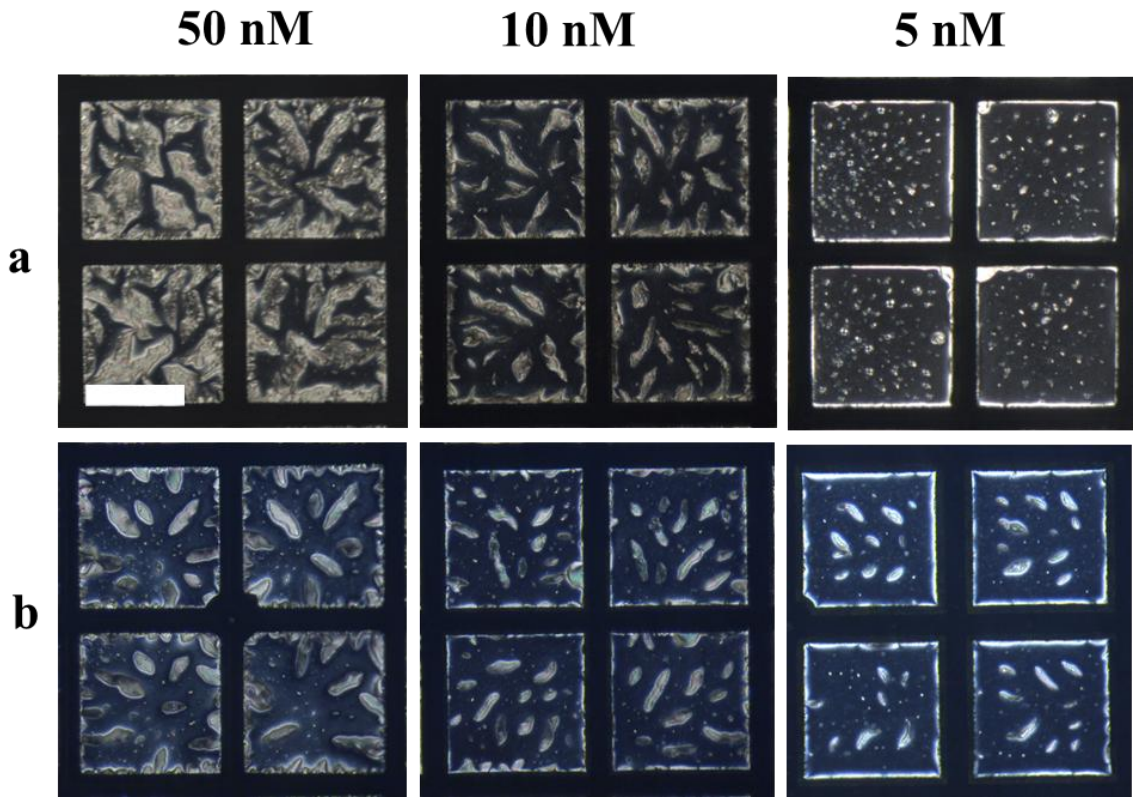

Figure 2.34. Optical micrographs (crossed polarizers) of SFN laden E7 films incubated against the different concentration of (a) ConA and (b) FibN for 2 hr. Scale bar = 200 μm.

Before concluding, we compare the sensitivity of current strategy with previous amphiphiles decorated LC-based systems concerning the detection of the above-studied proteins. Prior reports showed that LC-aqueous interface laden with different block co-

polymers could detect BSA up to 950, 30 nM and 45 nM, respectively.[63-65] Similar group reported the detection limit for Hb to be 139 nM using the polymer laden LC-aqueous interface.[65] A study by Alino et al. showed a cationic linear surfactant laden LC-aqueous interface could report BSA up to 60 nM of concentration.[66] Earlier, we had demonstrated that lipopolysaccharide-decorated LC-aqueous interface could detect Hb and BSA up to 5 nM and 10 nM, respectively.[7] In the current work, the orientational tranisitions of LCs enabled the detection of Hb and BSA upto 3 nM and 5 nM, respectively, which is significantly lesser than those reported earlier.[7,63-66] In another instance, Wang et al. utilized a nonionic surfactant decorated LC-aqueous interface to report presence of BSA and ConA with a superior detection limit.[67] However, the similar texture of LC was observed in presence of both ConA and BSA without demonstrating any distinctly shaped domain formation. [67] On the other hand, the SFN decorated LC-aqueous interfaces led to a distinct optical texture to ConA (elongated domains) and BSA (globular domains), pointing out the extraordinary significance of those interfaces toward differentiating the two proteins based on their structural motifs. In this context, it is important to cite that Abbott's group first reported that at lipid/phospholipid (linear amphiphiles) adsorbed LC-aqueous interfaces, addition of protein generated LC domains of planar/tilted alignment of LC and the shape of the domains highly depends on the secondary structure of proteins.[48-50] As compared to those studies, [48-50] the present work showed an enhanced sensitivity of LC-aqueous interfaces towards proteins (e.g., BSA, Cyto). The current methodology may be preferable over the existing phospholipids decorated LC-aqueous interfaces[48-50] (requires either prefabrication of lipid monolayer by Langmuir Blodgett technique or laborious methods for lipid vesicle/mixed vesicles preparation & their characterizations) due to simplicity of the design. The SFN laden LC-aqueous interfaces are also beneficial over recently reported PmB decorated LC-aqueous interfac[81] as it is able to report the secondary structure of proteins regardless their ionic nature.

2.2.4 Conclusions

In summary, we report a new method based on LCs to visually monitor the interfacial protein adsorption using LC films decorated with a bioactive cyclic amphiphile, SFN, in the aqueous phase. It is demonstrated that amphipathic SFN molecules induced a homeotropic orientation of LCs, owing to the self-assembly of SFN molecules at LC-aqueous interface, thus giving a dark optical appearance of LC under crossed polars. We further showed that at physiological pH, a range of proteins (Hb, Cyto, BSA, ConA, and

FibN) at nanomolar concentrations could trigger a reorientation of LC to planar leading to bright optical appearances of LC. Our study strongly suggests that the intermolecular interactions (hydrophobic and electrostatics) between protein molecules and SFN play an important role in dictating the dynamic response of LC. Specifically, the nature of electrostatic interactions between the anionic headgroup of SFN and proteins largely determines the response time of SFN decorated LCs. For instance, LCs demonstrated a faster reorientation when a cationic protein is in the vicinity of SFN laden LC-aqueous interface and vice versa. In addition, we found that adsorption of proteins causes a patterned orientation of LC at the interface which strongly depends on the native secondary structure of proteins. Proteins rich in α-helix (BSA, Cyto and Hb) generate globular spatial domains which are reproducibly different than the elongated domains triggered by β-sheet rich proteins (ConA and FibN). Thus, the developed LC design, which may have application in detection of toxic amyloids, offers exceptional advantages over conventional assays (such as NMR and CD) like simple and optical readout, label-free detection and minimal sample requirement. We believe that besides the planar geometry of LC−aqueous interfaces, assembly behavior of SFN at LC microdroplets (with a rounded geometry) and subsequent protein adsorption may facilitate another simple platform for label-free sensing through ordering transition of the LCs. Design and further exploration of such lipopeptide-decorated LC-based surfaces may enable the molecular-level understanding of various biomolecular interactions in controlled ways which would serve wide applications in interfacial and biosensing fields.

2.2.5 Experimental Section

2.2.5.1 Materials

Chemicals such as surfactin (from *Bacillus subtilis*) (SFN), bovine serum albumin (BSA), human hemoglobin (Hb), cytochrome c from equine heart (Cyto), concanavalin A from Canavalia ensiformis (ConA), fibronectin from bovine plasma (FibN), fluorescein-conjugated BSA (FITC-BSA), fluorescein-conjugated ConA (FITC-ConA), N,N-dimethyl-N-octadecyl-3-aminopropyltrimethoxysilyl chloride (DMOAP), hydrochloric acid, sodium hydroxide and 1 mM tris buffered saline (TBS) (pH 7.2) were purchased from Sigma-Aldrich (St. Louis,MO). E7 liquid crystal (LC), Sulfuric acid, chloroform and hydrogen peroxide (30% w/v) were purchased from Merck (Mumbai, India). Ethanol was obtained from Changshu Hongsheng Fine Chemical Co., Ltd. Deionization of

distilled water (DI water) source was performed by a Milli-Q-system (Millipore, Bedford, MA). Glass microscopic slides (Fisher's Finest Premium grade) were purchased from Fischer Scientific. Gold TEM grids (20 μm thickness, 50 μm wide bars, 283 μm grid spacing) were obtained from Electron Microscopy Sciences (Fort Washington, PA).

2.2.5.2 Preparation of aqueous solutions of SFN and proteins

Stock solution of SFN (~600 μM) was freshly prepared in 5 mM Tris-HCl buffer (pH 8.5). Stock solutions of proteins (BSA, Hb, Cyto and ConA) were prepared by dissolving solid chemical in 1 mM TBS (pH 7.2). An aqueous solution of FibN was prepared by incubating solid FibN in 1 mM TBS at 37 °C for 30 min. Dilution of SFN and proteins was done in 1 mM TBS (pH 7.2) for all the protein adsorption experiments.

2.2.5.3 Pretreatment of glass slides with DMOAP

Prior to DMOAP coating, glass microscope slides were cleaned with freshly prepared piranha solution [70% H_2SO_4, 30% H_2O_2] for 45 min at 100 °C. *Caution: Piranha solution reacts violently with organic materials. It should be handled with acute caution and neutralized carefully before disposing off. Do not store the solution in closed containers!* The slides were then rinsed with an excess amount of DI water and ethanol followed by drying under a stream of gaseous N_2. Then, the slides were stored in an oven to 120 °C for 3 hr. The "piranha-cleaned" glass slides were then modified with DMOAP using the previous report.[9,10] Briefly, the slides were immersed into 0.1% (v/v) DMOAP solution in DI water for 30 min at room temperature. The slides were then rinsed with DI water to remove the excess DMOAP from the surface and dried under a stream of N_2 before heating at 100 °C for 3-4 hr.

2.2.5.4 Preparation of LC films and optical cells

The DMOAP coated glass slides were cut into small squares and gold TEM specimen grids were placed on top of it. E7 was added into the grids using a Hamilton microsyringe and the excess LC was removed to form a planar interface. The E7 containing grid supported on DMOAP coated glass slide was then immersed in a glass well containing the aqueous buffer. Subsequently, a small volume from a stock solution of SFN was added into well to achieve a certain final concentration. For experiments of protein adsorption at LC-aqueous interface, SFN laden LC film was prepared as follows: first LC film was incubated with an aqueous solution of 7.5 μM SFN for 2 hours followed by an

exchange with 1 mM TBS (pH 7.2) to remove the excess SFN from bulk. Subsequently, a certain volume (100-5 μL) from the stock aqueous solution of proteins was added onto SFN laden LC film to obtain a desired final concentration. The total volume of glass well was kept 2 mL. Every experiment was repeated at least thrice.

2.2.5.5 Characterization of LC films under crossed polars

The orientation of LCs was analyzed under a Zeiss polarizing microscope (Scope. A1) which is equipped with crossed polars with objectives of magnification 50X, 100X and 200X. All the images were captured using an AxioCam Camera.

2.2.5.6 Imaging of LC-aqueous interface by epifluorescence microscopy

For fluorescence microscopy, SFN laden LC films were incubated with 50 nM FITC-BSA or 62 nM FITC-ConA for 3-5 hours, followed by exchanging the aqueous solution with 1 mM TBS to remove the background fluorescence. The samples were then viewed under a Zeiss (Scope. A1) fluorescence microscope using a fluorescence filter cube with a 460 nm excitation filter and a 534 nm emission filter. Images were obtained with an AxioCam camera.

References

1. Popov, P.; Mann, E. K.; Jakli, A. *J. Mater. Chem. B* **2017**, *5*, 5061−5078.
2. Carlton, R. J.; Hunter, J. T.; Miller, D. S.; Abbasi, R.; Mushenheim, P. C.; Tan, L. N.; Abbott, N. L. *Liq. Cryst. Rev*. **2013**, *1*, 29−51.
3. Sidiq, S.; Pal, S. K. *Proc. Indian Natl. Sci. Acad.* **2016**, *82*, 75–98.
4. Brake, J. M.; Abbott, N. L. *Langmuir* **2002**, *18*, 6101−6109.
5. Brake, J. M.; Daschner, M. K.; Luk, Y.-Y.; Abbott, N. L. *Science* **2003**, *302*, 2094−2097.
6. Sidiq, S.; Verma, I.; Pal, S. K.*Langmuir* **2015**, *31*, 4741−4751.
7. Das, D.; Sidiq, S.; Pal, S. K. *ChemPhysChem* **2015**, *16*, 753–760.
8. Seo, J. M.; Khan, W.; Park, S-.Y. *Soft Matter* **2012**, *8*, 198–203.
9. Pani, I.; Sharma, D.; Pal, S. K. *General Chemistry* **2018**, *4*, 180012-180012.
10. Popov, P.; Honaker, L. W.; Kooijman, E. E.; Mann, E. K.; Jákli, A. I. *Sens. Biosensing Res.* **2016**, *8*, 31–35.
11. Brake, J. M.; Mezera, A. D.; Abbott, N. L. *Langmuir* **2003**, *19*, 6436-6442.
12. Lockwood, N. A.; Gupta, J. K.; Abbott, N. L. *Surf Sci Rep.* **2008**, *63*, 255-293.
13. Verma, I.; Sidiq, S.; Pal, S. K. *Liq. Cryst.* **2016**, *43*, 1126– 1134.
14. Bi, X.; Hartono, D.; Yang, K-L. *Adv. Funct. Mater*. **2009**, *19*, 3760–3765.
15. Price, A. D.; Schwartz, D. K. *J. Am. Chem. Soc*. **2008**, *130*, 8188−8194.
16. Su, H.-W.; Lee, Y.-H.; Lee, M.-J.; Hsu, Y.-C.; Lee, W. *J. of Biomedical Optics* **2014**, *19*, 077006.
17. Lin, C.-H.; Lee, M.-J.; Lee, W. *Appl. Phys. Lett*. **2016**, *109*, 093703-1–4.
18. Lee, M. J.; Chang, C.-H.; Lee, W. *Biomed. Opt. Express*. **2017**, *8*, 1712–1720.
19. Chiang, Y.-L.; Lee, M. J.; Lee, W. *Dyes Pigm*. **2018**, *157*, 117-122.
20. Lee, M.-J.; Chiang, Y.-L.; Karn, A.; Wu, P.-C.; Lee, W. *SPIE Organic Photonics + Electronics* **2018**, *10735*, Liquid Crystals XXII; 1073509.
21. Lee, M.-J.; Lin, C. H.; Lee, W. *SPIE Organic Photonics + Electronics* **2015**, *9565*, Liquid Crystals XIX; 956510.
22. Chen, C.-H.; Lin, Y.-C.; Chang, H. H.; Lee, A. S. Y. *Anal. Chem*. **2015**, *87*, 4546-4551.
23. Verma, I.; Sidiq, S.; Pal, S. K. *Liq. Cryst*. **2019**, *46*, 1318-1326.
24. Verma, I.; Sidiq, S.; Pal, S. K. *ACS Omega* **2017**, *2*, 7936–7945.

25. Sidiq, S.; Prasad, G. V. R. K.; Mukhopadhaya, A.; Pal, S. K. *J. Phys. Chem. B* **2017**, *121*, 4247– 4256.
26. Wei, Y.; Jang, C.-H. *J. Mater. Sci.* **2015**, *50*, 4741–4748.
27. Kleman, M.; Lavrentovich, O. D. *Soft Matter Physics: An Introduction*; Springer: New York, **2003**.
28. de Gennes, P. G.; Prost, J. *The Physics of Liquid Crystals*; Clarendon Press: Oxford, **1993**.
29. Banat, I. M.; Franzetti, A.; Gandol, I.; Bestetti, G.; Martinotti, M. G.; Fracchia, L.; Smyth, T. J.; Marchant, R. *Appl. Microbiol. Biotechnol*. **2010**, *87*, 427-444.
30. Bonmatin, J. M.; Laprevote, O.; Peypoux, F. *Comb. Chem. High Throughput Screen.* **2003**, *6*, 541-556.
31. Raaijmakers, J. M.; de Bruijn, I.; Nybroe, O.; Ongena, M. *FEMS Microbiol. Rev.* **2010**, *34*, 1037−1062.
32. Hamley, I. W. *Chem. Commun*. **2015**, *51*, 8574-8583.
33. Storm, D. R.; Rosenthal, K. S.; Swanson, P. E. *Annu. Rev. Biochem.* **1977**, *46*, 723-763.
34. Ziv, G.; Sulman, F. G. *Antimicrob. Agents Chemother*. **1972**, *2*, 206-213.
35. Kunin, C. M.; Bugg, A. *J. Infect. Dis*. **1971**, *124*, 394-400.
36. Craig, W. A.; Kunin, C. M. *Annu. Rev. Med*. **1976**, *27*, 287-300.
37. Schmidt, S.; Rock, K; Sahre, M.; Burkhardt, O.; Brunner, M.; Lobmeyer, M. T.; Derendorf, H. *Antimicrob. Agents Chemother*. **2008**, *52*, 3994−4000.
38. The antibiotic alarm. *Nature* **495**, *141*, 2013, DOI: 10.1038/495141a.
39. http://www.who.int/drugresistance/documents/surveillancereport/en/. (accessed Nov 12, 2018).
40. Benilova, I.; Karran, E.; Strooper. B. D. *Nat. Neurosci.* **2012**, *15*, 349-357.
41. Cao, P.; Abedini, A.; Wang, H.; Tu, L.-H.; Zhang, X.; Schmidt, A. M.; Raleigh, D. P. *Proc. Natl. Acad. Sci. USA* **2013**, *110*, 19279-19284
42. Ross, C. A.; Poirier. M. A. *Nat. Med.* **2004**, *10*, S10.
43. Vidal, R.; Ghetti, B. *Methods Mol. Biol*. **2011**, *793*, 241-258.
44. Katsu, T.; Yoshimura, S.; Tsuchiya, T.; Fujita, Y. *J. Biochem*. **1984**, *95*, 1645-1653.
45. Bruch, M. D.; Cajal, Y.; Koh, J. T.; Jain, M. K. *J. Am. Chem. Soc.* **1999**, *121*, 11993-12004.

46. Mecozzi, S.; West Jr., A. P.; Dougherty, D. A. *Proc. Natl. Acad. Sci. USA* **1996**, *93*, 10566-10571.
47. Shen, Y.; Liu, S.; Kong, L.; Li, D.; He, Y. *Sens. Actuators B* **2013**, *188*, 555-563.
48. Tercero, M. D. D.; Abbott, N. L. *Chem. Eng. Commun*. **2008**, *196*, 234-251.
49. Wang, X.; Yang, P.; Mondiot, F.; Li, Y.; Miller, D. S.; Chen, Z.; Abbott, N. L. *Chem. Commun*. **2015**, *51*, 16844-16847.
50. Sadati, M.; Apik, A. I.; Armas-Perez, J. C.; Martinez-Gonzalez, J.; Hernandez-Ortiz, J. P.; Abbott, N. L.; de Pablo, J. J. *Adv. Funct. Mater.* **2015**, *25*, 6050–6060.
51. Takeda, K.; Shigeta, M.; Aoki, K. *J. Colloid Interface Sci*. **1987**, *117*, 120–126.
52. Li, R.; Nagai, Y.; Nagai, M. *J. Inorg. Biochem*. **2000**, *82*, 93–101.
53. Ye, S.; Li, H.; Yang, W.; Luo, Y. *J. Am. Chem. Soc*. **2014**, *136*, 1206–1209.
54. Bhattacharyya, L.; Koenig, S. H.; Brown, R. D.; Brewer, C. F. *J. Biol. Chem*. **1991**, *266*, 9835–9840.
55. Khan, J. M.; Khan, M. S.; Ali, M. S.; Al-Shabib, N. A.; Khan, R. H. *RSC Adv*. **2016**, *6*, 38100-38111.
56. Fruh, S. M.; Schoen, I.; Ries, J.; Vogel, V. *Nat. Commun.* **2015**, *6*, 7275-7285.
57. Pellenc, D.; Berry, H.; Gallet, O. *J. Colloid Interface Sci.* **2006**, *298*, 132–144.
58. Emsley, J.; White, H. E.; O'Hara, B. P.; Oliva, G.; Srinivasan, N.; Tickle, I. J.; Blundell, T. L.; Pepys, M. B.; Wood, S. P. *Nature* **1994**, *367*, 338–345.
59. To, W. S.; Midwood, K. S. *Fibrogenesis Tissue Repair* **2011**, *4*, 21.
60. Stoffels, J. M. J.; de Jonge, J. C.; Stancic, M.; Nomden, A.; van Strien, M. E.; Sisková, Z.; Maier, O.; Ffrench-Constant, C.; Franklin, R. J.; Hoekstra, D.; Zhao, C.; Baron. W. *Brain* **2013**, *136*, 116–131.
61. Castelletti, F.; Donadelli, R.; Banterla, F.; Hildebrandt, F.; Zipfel, P. F.; Bresin, E.; Otto, E.; Skerka, C.; Renieri, A.; Todeschini, M.; Caprioli, J.; Caruso, R. M.; Artuso, R.; Remuzzi, G.; Noris, M. *Proc. Natl. Acad. Sci.* **2008**, *105*, 2538–2543.
62. Baneyx, G.; Vogel, V. *Proc. Natl. Acad. Sci. U S A.* **1999**, *96*, 12518–12523.
63. Seo, J. M.; Khan, W.; Park. S.-Y. *Soft Matter* **2012**, *8*, 198–203
64. Omer, M.; Khan, M.; Kim, Y. K.; Lee, J. H.; Kanga, I.-K.; Park, S.-Y. *Colloids Surf. B* **2014**, *121*, 400–408.
65. Omer, M.; Park, S.-Y *Anal. Bioanal. Chem.* **2014**, *406*, 5369–5378.
66. Alino, V. J.; Sim, P. H.; Choy, W. T. Fraser, A.; Yang, K.-L. *Langmuir* **2012**, *28*, 17571−17577.

67. Wang, Y.; Hu, Q.; Tian, T.; Gao, Y.; Yu, L. *Analytica Chimica Acta* **2016**, *937*, 119-126.
68. Frischet, M. J. et al. GAUSSIAN 09 (Revision B.01), Gaussian, Inc., Wallingford, CT, **2010**.
69. Leach, A. R. Molecular Modelling – Principles and Applications, Pearson education limited, England, 2nd edn, **2001**.
70. March, N. H. *J. Phys. Chem*. **1982**, *86*, 2262-2267.
71. Kryachko, E. S.; Ludena, E. V. Energy Density Functional Theory of Many-Electron System. Kluwer, Dordrecht; **1990**.
72. Horcas, I.; Fernandez, R.; Gomez-Rodríguez, J. M.; Colchero, J.; Gomez-Herrero, J.; Baro, A. M. *Rev. Sci. Instrum*. **2007**, *78*, 013705.
73. Zhao, X.; Pan, F.; Xu, H.; Yaseen, M.; Shan, H.; Hauser, C. A. E.; Zhang, S.; Lu, J. *Chem. Soc. Rev*. **2010**, *39*, 3480-3498.
74. Iadanza, M. G.; Jackson, M. P.; Hewitt, E. W.; Ranson, N. A.; Radford, S. E. *Nat. Rev. Mol. Cell Biol.* **2018**, *19*, 755–773.
75. Sunde, M.; Serpell, L.C.; Bartlam, M.; Fraser, P.E.; Pepys, M.B.; Blake, C.C. *J. Mol. Biol*. **1997**, *273*,729-739.
76. Nilsson, M.R. *Methods* **2004**, *34*, 151-160.
77. Etezadi, D.; Warner IV, J. B.; Ruggeri, F. S.; Dietler, G.; Lashuel, H. A.; Altug, H. *Light Sci. Appl.* **2017**, *6*, 17029.
78. Woltman, S. J.; Jay, G. D.; Crawford, G. P. *Nat. Mater*. **2007,** *6*, 929–938.
79. Bai, Y.; Abbott, N. L. *Langmuir* **2011**, *27*, 5719–5738.
80. Collings, P. J.; Hird, M. Introduction to Liquid Crystals Chemistry and Physics. London: Taylor & Francis, **1997**.
81. Verma, I.; Rajeev, N.; Mohiuddin, G.; Pal, S. K. *J. Phys. Chem. C* **2019**, *123*, 6526-6536.
82. Pani, I.; Swasthi, H. M.; Mukhopadhyay, S.; Pal, S. K. *J. Phys. Chem. C* **2019**, *123*, 1305-1312.
83. Badami, J. V.; Bernstein, C.; Maldarelli, C.; Tu, R. S. *Soft Matter* **2015**, *11*, 6604-6612.
84. Hu, Q. Z.; Jang, C. H. *Analyst* **2012**, *137*, 567-570.
85. Yang, X.; Tian, Y.; Li, F.; Yu, Q.; Tan, S. F.; Chen, Y.; Yang, Z. *Langmuir* **2019**, *35*, 2490-2497.

86. Liu, J. F.; Mbadinga, S. M.; Yang, S. Z.; Gu, J. D.; Mu, B. Z. *Int. J. Mol. Sci.* **2015**, *16*, 4814–4837.
87. Park, J.; Ku, S. K.; Seo, D.; Hur, K.; Jeon, H.; Shvartsman, D.; Seok, H. K. ; Mooney, D. J.; Lee, K. *Chem. Commun.* **2016**, *52*, 10346–10349.
88. Ravindran, S. J.; Kumar, R.; Srimany, A.; Philip, L.; Pradeep, T. *Anal. Chem.* **2018**, *90*, 988−997.
89. Peters, T. J. All about albumin: biochemistry, genetics, and medical applications. San Diego, Calif.: Academic Press, **1995**.
90. Perutz, M. F. *Ann. Rev. Biochem.* **1979**, *48*, 327-386.
91. Dobbs, A. J; Anderson, B. F.; Faber, H. R; Baker, E. N. *Acta Crystallogr. D Biol. Crystallogr.* **1996**, *52*, 356-368.

CHAPTER 3

Liquid Crystal Based Detection of Pb (II) Ions using Spinach RNA as Recognition Probe

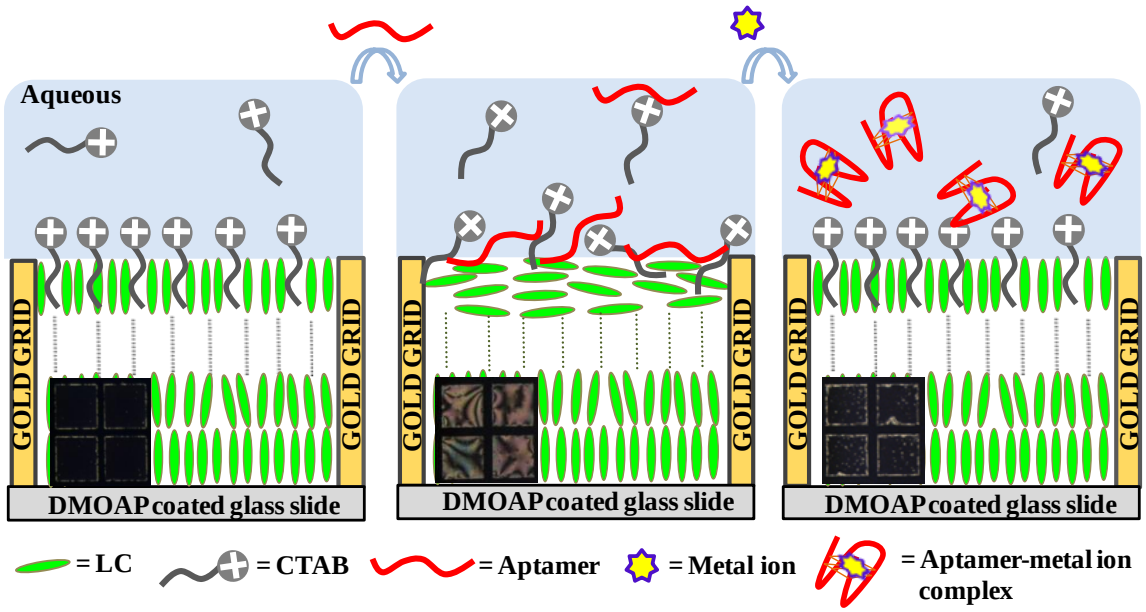

We discuss a novel and simple strategy for specific detection of lead (Pb^{2+}) ions using liquid crystals (LC) at aqueous-LC interfaces. The system involves switching of ordering transitions of LC molecules tuned by the competitive binding among a cationic surfactant, an aptamer (consists of a Pb^{2+} binding site) and the Pb^{2+} ions. LCs adopt a homeotropic orientation in contact with a cationic surfactant, cetyltrimethylammonium bromide (CTAB) at the aqueous-LC interface. The ordering of LC subsequently changed to planar in the presence of aptamer at those interfaces. When target Pb^{2+} ions were introduced into the CTAB-aptamer system, the ordering of LC changed to homeotropic primarily due to the formation of compact quadruplex structures of the aptamer with Pb^{2+} ions. The sensor exhibited a detection limit of 3 nM which is well below than the permissible limit of Pb^{2+} in drinking water. Application of LC-based sensor for the detection of Pb^{2+} in tap water is also demonstrated.

3.1 Introduction

Thermotropic liquid crystals (LCs) associated with the long-range orientational order in the mesophase can easily amplify and transduce the molecular level information from the interface that they are in contact with.[1-20] Such interfacial interactions of LC with various external stimuli can trigger an orientational transition in micrometers thick LC film (up to 100 μm).[1-5] Since LCs are birefringent materials, polarized microscopy allows the characterization of distinct director profiles through different optical appearances. This ability of LC to sensitively report the small changes in the environment via distinct optical signals have successfully led to the development of label-free LC-based sensors over a decade.[1-3] Previously, interfaces formed between LC and aqueous phases have been successfully exploited for detection of various biochemical events like DNA hybridization[8] and adsorption[9], aptamer-small molecule binding[10], cell adhesion[12,13], protein adsorption[2,14-17], antigen-antibody binding[18,19], enzymatic reactions,[20,21] and so on. These LC-based systems are heavily based on the orientational transitions of the LC triggered by macromolecular binding events occurring at these interfaces which can be reported even at nanomolar concentrations of the target analyte. However, in the aqueous phase, utilization of LC-based strategies to detect toxic metal ions poses challenges in terms of selectivity and sensitivity due to the following reasons. (i) The system requires a high concentration of ions (above μM) to exert an ordering transition of the LC,[22-24] (ii) identical properties of several metal ions in terms of ionic radii, charge, and so on, and (iii) high mobility of the ions in bulk phases due to their small size. For example, Singh et al. reported the LC sensor for Hg (II) ions with the detection limit of 0.5 μM using specific affinity of mercuric ions towards dithiocarbamate amphiphile.[23] Hu et al. exploited the enzyme-metal interactions to observe ordering transitions of LC to report Copper (II) ions with 10 μM of concentration.[24] Interestingly, oligonucleotides based recognition event of Hg (II) ions has been demonstrated to effectively disturb the orientations of LC up to 0.1 nM of target concentrations.[25] However, the design is complex and counter-productive due to the involvement of three different oligonucleotides probes required to generate an optical signal for detection of Hg (II).

Previously, it has been shown that interfacial adsorption of oligonucleotides can trigger a change in the orientation of LC at decorated LC-aqueous interfaces driven by non-covalent intermolecular interactions.[8-11] For example, our recent study found that at poly-L-lysine (a cationic polypeptide) coated LC-aqueous interface, the ordering of LC is

mainly influenced by irreversible formation of polyplexes driven by electrostatic interaction between phosphate backbone of DNA and cationic peptide moieties and thus both *single stranded*-DNA and *double stranded*-DNA produce a same orientational state of LC droplets.[9] However, at surfactant laden LC-aqueous interfaces, ordering of LC is determined by electrostatic as well as hydrophobic interactions between nucleobases and the LC molecules.[9-11] Thus, *single stranded*-DNA (exposed nucleobases) and *double stranded*-DNA or small biomolecules bound DNA (unexposed nucleobases) trigger distinct LC orientation at cationic surfactant decorated interface, i.e., planar for former and homeotropic for latter. Motivated by these reports, we sought to decorate LC interface with a cationic surfactant and examine the possibility to design an aptamer-based LC sensor for detection of heavy metal ions.

Over a decade, aptamers, which are functional nucleic acid sequences, have emerged as a molecular recognition element due to their astounding feature to detect a variety of targets ranging from biomolecules to metal ions. They offer exceptional advantages such as strong affinity towards a particular target and numerous advantages over immunosensors such as robust stability in aqueous solution, simple design and cost-effective synthesis.[26] The detection principle of aptamer-based sensors is usually associated with a conformational change such as the formation of a duplex or a G-quadruplex upon binding with the target.[27] Particularly, G-quadruplex structures are non-canonical four-stranded secondary structures formed by hydrogen-bonded guanine residues in tetrad fashion which can be significantly stabilized or promoted by coordination interactions between carbonyl oxygen atoms of guanine and metal ions. They perform numerous regulatory roles in controlling biological processes.[27]

3.2 Objective

Considerable progress has been made recently to develop aptamer-based biosensors for detection of heavy metal ions based on electrochemical, fluorescence and colorimetric methods as summarized in Table 3.1. However, such techniques impose certain limitations in their practical application such as aptamer immobilization process, requirement of fluorophores, expensive or complex instrumentation and chemiluminescent products for signal readout.[28-34] In this work, we sought to design and develop a simple LC-based biosensor for ultrasensitive detection of heavy metal ions

where aptamer would act as target recognition probe and the binding event would be easily amplified by LC in the form of an optical output.

Table 3.1: Comparison of oligonucleotide-based methods for the detection of Pb^{2+} ions

S. No.	Detection Method	Strategy	Detection limit	Response Time	Reference
1.	Fluorescence	Folding of Spinach RNA into G-quadruplex	6 nM	15 min	28
2.	Colorimetric	Formation of G-quadruplex DNAzyme	32 nM	4 min	29
3.	Colorimetric	Multi-functionalized gold nanoparticles by DNAzyme and barcode DNA	20 nM	6 min	30
4.	Photoelectro -chemical	Hemin intercalated K^+-stabilized G-quadruplex	4nM	NA	31
5.	Electro-chemical	G-quadruplex based biosensor	4.2 nM	30 min	32
6.	Fluorescence	Pb^{2+}-induced allosteric G-quadruplex	1 nM	30 min	33
7.	Fluorescence	A Lead(II)-Driven DNA duplex−quadruplex exchange	20 nM	NA	34
8.	Liquid Crystal	G-quadruplex formation in SRNA	3 nM	1 min-20 min	Our work

In our system, we utilized the self-assembly of cationic surfactant, cetyltrimethylammonium bromide (CTAB) at LC-aqueous interface that imparts homeotropic anchoring (via lateral hydrophobic interaction between hydrocarbon tails of CTAB and LC). Addition of negatively charged aptamer can disturb the self-assembly of CTAB at the interface due to interactions between CTAB and aptamer thus leading to a planar alignment of LC.[1,8] However, in the presence of heavy metal ions, we hypothesized that conformational changes in aptamer could be induced due to specific strong interactions between metal ions and aptamers. This, in turn, would weaken the interaction between CTAB and aptamer at the interface, thereby promoting the coupling of CTAB molecules with LCs to produce a homeotropic ordering as illustrated in Scheme

3.1. We would test the hypothesis to report the detection of lead (II) ions (Pb^{2+}) as it is the second most abundant toxic metal ion and a major pollutant of soil and groundwater.[35-37] Here, we chose a Spinach RNA aptamer (SRNA) (Sequence is elaborated in Experimental Section) which is recently shown to exhibit specific binding affinity to Pb^{2+} followed by G-quadruplex formation.[28] Lastly, we will also confer the probable mechanism about the coupling of the orientational ordering of LC with an interfacial event associated with structural changes in aptamer upon binding to the metal ion target.

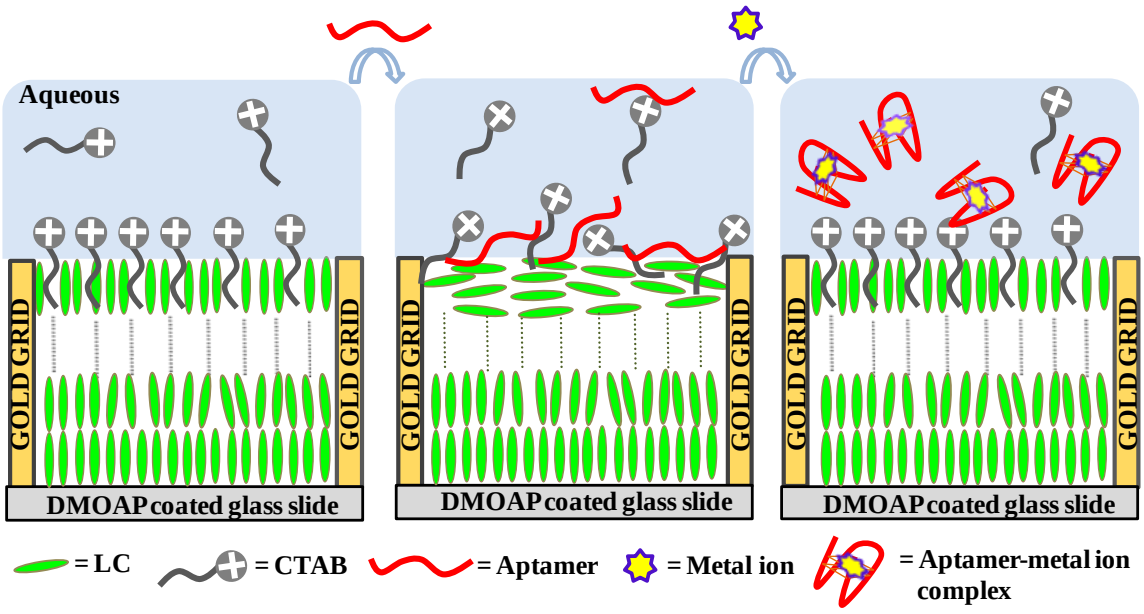

Schematic 3.1. Schematic demonstration of the proposed design for label-free LC sensor for detection of Pb^{2+} ions based on self-assembly of CTAB at interface influenced by conformational changes in aptamer upon binding with the target ion. (Cartoon depiction not to scale)

3.3 Results and Discussion

3.3.1 Fabrication of aptamer-based LC sensor

Our first set of experiments was performed to determine the optical behavior of the LC in the presence of different concentrations of CTAB at physiological pH (pH 7.4). For the same, 5CB (4-Cyano-4-pentylbiphenyl) LC was first confined in the gold transmission electron microscopy (TEM) grids supported on N,N-dimethyl-n-octadecyl-3-aminopropyltrimethoxysilyl chloride (DMOAP)-modified glass slides.[2,4] It is known that DMOAP at the bottom interface and air at top anchors 5CB in a perpendicular

(homeotropic) orientation imparting dark optical appearance under crossed polarizers. When the same LC film supported by a TEM grid was contacted with the aqueous buffer solution, LC exhibited bright optical appearance consistent with the planar/tilted alignment of LC induced by water molecules at those interfaces. However, in contact with an aqueous solution of CTAB, LC was found to be aligned homeotropically, leading to dark optical appearances of the LC. As reported, the dark optical response of LC is mainly due to self assembly of CTAB molecules at the interface driven by lateral hydrophobic interactions between alkyl chains of CTAB and the 5CB LC.[1] In our experiments, the minimum concentration of the CTAB was found to be 7 μM that exhibit stable ordering at the interface for at least 30 min. Thus, further studies were carried out with 7 μM CTAB. Next, we aimed to study the optical behavior of LC film in the presence of CTAB and SRNA complex. Figure 3.2 shows the POM images illustrating the dynamic response of LC-aqueous interface after the introduction of CTAB and various concentrations of the aptamer. It was found that for 200 nM or higher concentrations of SRNA, the LC remained in planar orientation during the observation time of 20 minutes (min). However, LC turned dark within 20 min at 150 nM or lower concentrations of SRNA. This suggests that a sufficiently high concentration of SRNA can effectively adsorb at LC-aqueous interface facilitated by electrostatic interactions with CTAB where hydrophobic nucleobases of aptamer can interact with the LC phase. Such interaction of the aptamer would disturb the organization of CTAB molecules at the interface and lead to a planar orientation of the LC.[8] Since 200 nM is the minimum concentration of SRNA required to achieve bright orientation of LCs, this concentration was used for further experiments to detect Pb^{2+} ions.

Our next experiment was carried out to investigate the effect of the introduction of Pb^{2+} on the CTAB and SRNA designed LC-aqueous interface. Interestingly, upon introduction of a pre-incubated mixture of CTAB, SRNA, and 300 nM Pb^{2+}, the optical appearance of LC film changed to dark within 1 min which remained stable for at least 20 min or so (Figure 3.3a-c). This observation led us to speculate that the presence of Pb^{2+} may induce structural changes in SRNA that leads to the organization of interfacial CTAB molecules onto the aqueous-LC interface to result in the dark optical appearance of LC. In order to investigate the structural changes of SRNA in the presence of Pb^{2+}, we carried out solution-phase measurements of circular dichroism (CD) and a competitive binding assay. CD spectra of free SRNA aptamer displayed a typical signature of quadruplex structure

with parallel conformation, as evident from the presence of a positive peak around 270 nm and a negative peak around 240 nm (Figure 3.3d).[38,39] In the presence of Pb^{2+}, an increase in ellipticity at 270 nm peak suggests that stabilization of the parallel quadruplex structure of SRNA by Pb^{2+} as reported earlier[28].

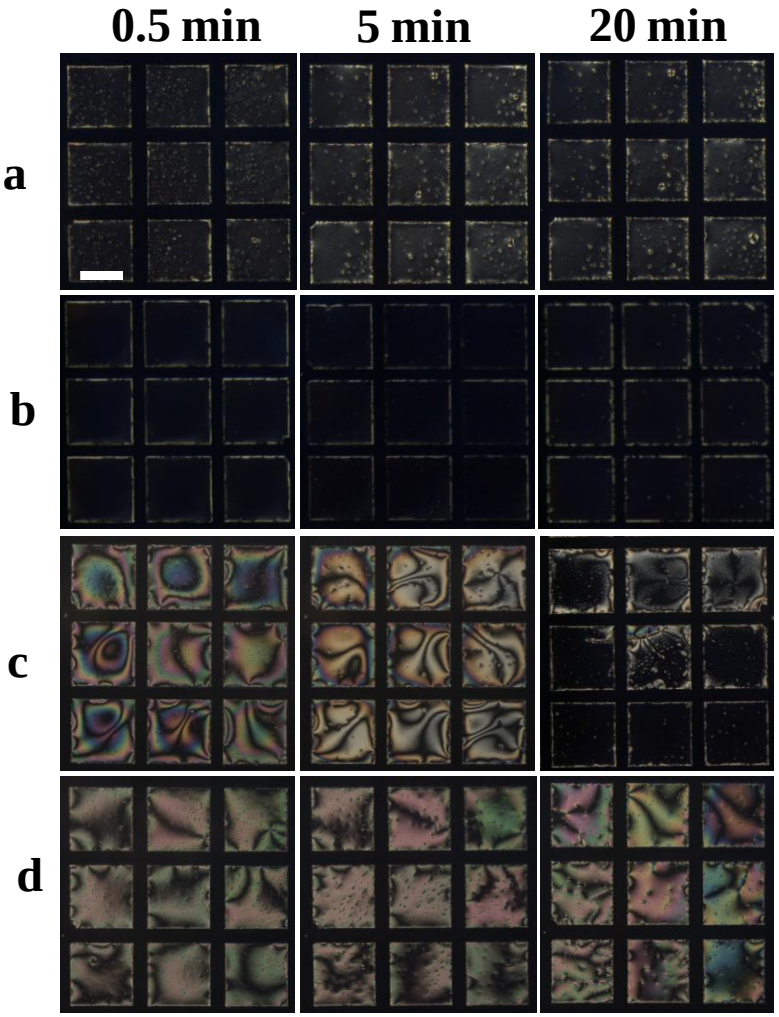

Figure 3.1. Polarized optical images of 5CB film hosted within a gold TEM grid on a DMOAP functionalized glass substrate after the introduction of an aqueous solution of CTAB at concentrations of (a) 10 μM; (b) 7 μM; (c) 5 μM and (d) 3 μM. Images were taken at 0.5, 5 and 20 min after the addition of the CTAB. (Scale bar = 200 μm).

Next, Thioflavin T (ThT) based competitive fluorescent assay was performed to confirm the strength of quadruplex formed and gain insights into the mode of binding between Pb^{2+} and SRNA. In our experiments, we found that ThT, which exhibits negligible fluorescence intensity in the buffer, showed a huge enhancement in fluorescence intensity at 485 nm in presence SRNA (Figure 3.3e, 3.4a). Based on the recent report[40], this

significant enhancement in fluorescence intensity of ThT indicates that ThT dye can bind and recognize the G-quadruplex motif in SRNA via non-covalent interactions. However, the addition of Pb^{2+} leads to a rapid decrease in fluorescence which confirms the competitive binding of Pb^{2+} into quadruplex of SRNA and displacement of ThT from the SRNA.

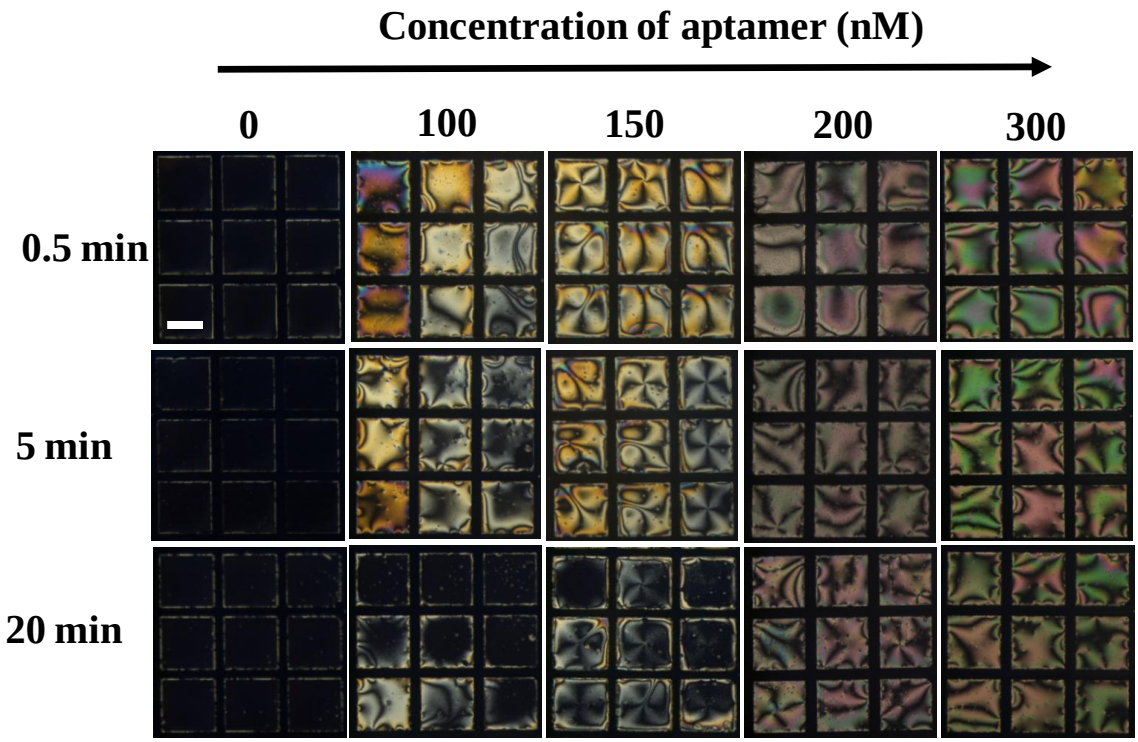

Figure 3.2. Polarized optical images of 5CB film hosted within a gold TEM grid on a DMOAP functionalized glass substrate after the introduction of 7 μM CTAB pre-incubated with different concentration of SRNA. Time indicates the instant at which images were captured after the introduction of aqueous solution on LC film. Scale bar = 200 μm.

Further, we confirmed that the fluorescence of ThT is enhanced only upon complexation with SRNA and not due to other intermolecular interactions such as complex of ThT-Pb^{2+}, SRNA, or SRNA-Pb^{2+} (Figure 3.4b). In another experiment, we sequentially added the small volumes of nanomolar Pb^{2+} solution to the complex of ThT and SRNA. We observed that the quenching of fluorescence was triggered by Pb^{2+} in a concentration-dependent manner. The dissociation constant was calculated as 1.57 ± 0.03 μM (Figure 3.4c,d), which is in good agreement with the literature[28], indicating a good binding affinity of SRNA towards Pb^{2+}. These results indeed confirmed that Pb^{2+} could strongly

bind and stabilize the G-quadruplex motif in SRNA aptamer, and its competitively robust affinity for aptamer enabled the facile displacement of ThT dye from SRNA-ThT complex as depicted by cartoon illustration in Figure 3.3f.

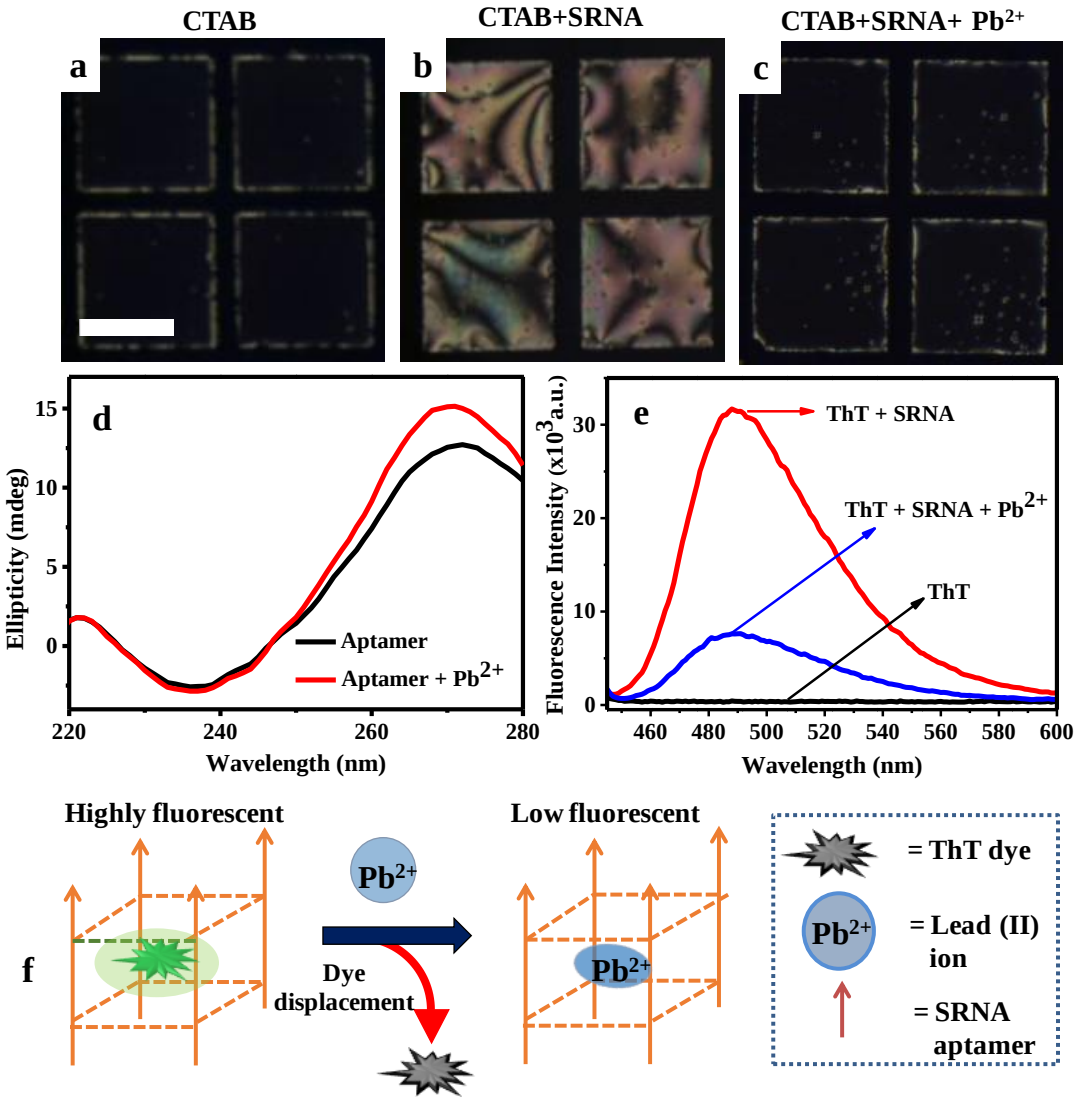

Figure 3.3. (a-c) Polarized optical images of LC film in contact with (a) 7 μM CTAB, (b) mixture of 7 μM CTAB and 200 nM SRNA, (c) pre-incubated mixture of 7 μM CTAB, 200 nM SRNA and 300 nM Pb^{2+} at 1 min. (Scale bar = 200 μm). (d) CD spectra of 15 μM aptamer in absence and presence of 15 μM Pb^{2+}. (e) Fluorescence spectra of ThT when incubated with SRNA (500 nM) in absence and presence of Pb^{2+} ions (65 nM). (f) Cartoon schematic illustrates the Pb^{2+} triggered displacement of ThT from the SRNA G-quadruplex which results in the decline of ThT fluorescence.

To determine the extent to which aptamer adsorbs at aqueous-LC interfaces in the presence of CTAB, we performed epifluorescence microscopy measurements using 5'6-

FAM (Fluorescein)-labelled SRNA (FAM-SRNA). Inspection of Figure 3.5a, b reveals that the aqueous-LC interfaces which were incubated in the presence of (FAM) SRNA-CTAB complex, exhibited strong fluorescence (Figure 3.5b and 3.5d) in comparison to the control (only SRNA, Figure 3.5a). This confirms preferential adsorption of SRNA at the interface in the presence of CTAB. Next, to provide additional insight into the adsorption behavior of the aptamer in the presence of Pb^{2+} ions at the aqueous-LC interface, we again performed fluorescence microscopy measurements at those interfaces in contact with (FAM) SRNA-Pb^{2+}-CTAB complex. As can be seen from Figure 3.5c and 3.5d, the fluorescence intensity of the aqueous solution of the complex at the LC interface decreases within an observation time (20-30 minutes) reported in this work.

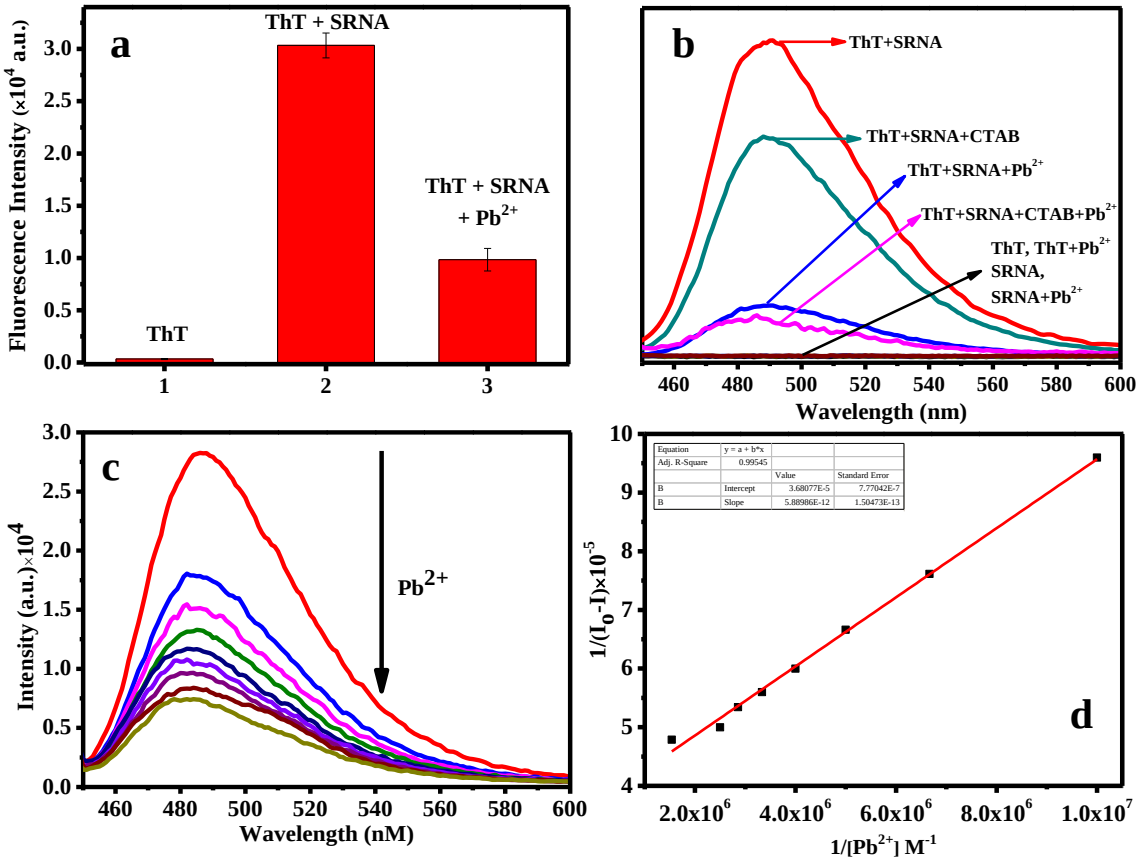

Figure 3.4. Pb^{2+} induced ThT displacement: (a) Plot of fluorescence intensity of ThT in different state: pure ThT, in presence of SRNA and in a mixture of SRNA and Pb^{2+}. (b) Fluorescence spectra of free ThT and when incubated with Pb^{2+} ions (650 nM); of SRNA with and without Pb^{2+}; of ThT in a mixture of SRNA (500 nM) and Pb^{2+} ions; ThT in mixture of SRNA and CTAB; ThT in a mixture of SRNA+CTAB+Pb^{2+}. (c) Fluorescence

spectra of a mixture of ThT and SRNA following sequential addition of Pb^{2+} (0-650 nM). (d) Benesi-Hildebrand Plot for calculation of binding constant of SRNA with Pb^{2+} ions.

While in the presence of Pb^{2+}, there is residual fluorescence of the (FAM) SRNA at the aqueous-LC interfaces (Figure 3.5c), the quantification of fluorescence intensity indicates a low density of SRNA at those interfaces. This is likely due to desorption of some SRNA-Pb^{2+} complex from the interface to the bulk solution. The lower density of SRNA at the interface did not hinder the CTAB molecules to self-assemble at the LC-aqueous interfaces and thus resulted in homeotropic orientation (dark appearance under crossed polars).

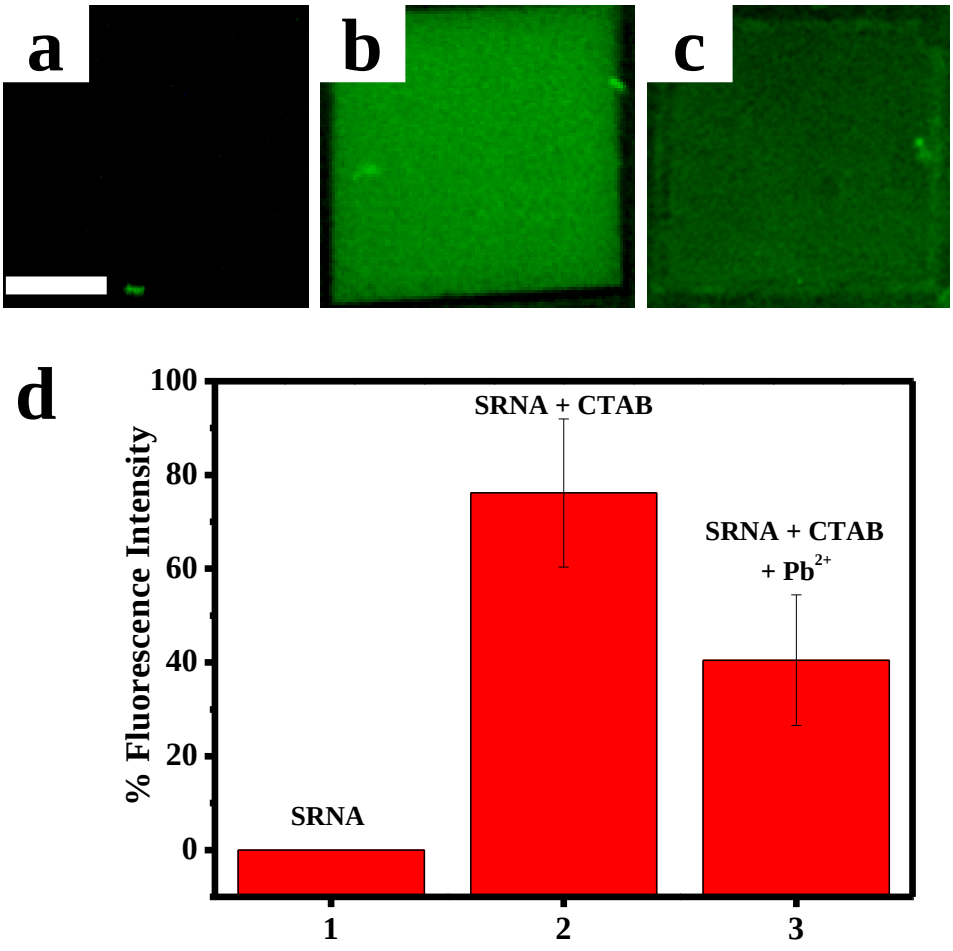

Figure 3.5. Epifluorescence imaging of LC-aqueous interface incubated with (a) FAM-SRNA, (b) pre-incubated mixture of FAM-SRNA and CTAB, (c) pre-incubated mixture of FAM-SRNA, CTAB, and Pb^{2+}. (d) The intensity of micrographs of LC-aqueous interface incubated with SRNA, SRNA+CTAB and SRNA+CTAB+Pb^{2+} complexes. Scale bar =100 μm

Based on the results described above, it is clear that the homeotropic anchoring of the LC in the presence of CTAB (Figure 3.3) is due to lateral hydrophobic interactions between hydrocarbon tails of CTAB molecules and the LCs, leading to a dark optical appearance at the aqueous-LC interface. On addition of negatively charged aptamer, a planar/tilted orientation of the LC is observed which is likely due to electrostatic interactions between CTAB and aptamer (SRNA-CTAB complex), that impede the CTAB molecules from self-assembly at those interfaces (Figure 3.3b). However, in the presence of Pb^{2+} ions, the optical appearance of the LC at the aqueous-LC interface is changed from bright to dark (Figure 3.3c). This change in the optical signal is mainly dependent on the competitive binding event between CTAB-SRNA and SRNA-Pb^{2+} at the LC interface. It should be noted that the interactions for Pb^{2+} with the SRNA aptamer are likely to be much stronger than that of CTAB with aptamer (being a non-specific electrostatic interaction) which are supported by ThT-fluorescence and FAM-SRNA experiments (Figure 3.4,3.5). Therefore, the strong binding affinity of Pb^{2+} ions towards SRNA (which forms a stable G-quadruplex complex and induces a conformational change in SRNA as confirmed by CD and ThT assay, Figure 3.3d-e) are likely to weaken the interactions between CTAB-SRNA complex. This event results in free CTAB molecules which can now reorganize and self-assemble at aqueous-LC interfaces leading to dark optical appearances.

3.3.2 Detection limit of LC sensor

Our next goal was to determine the sensitivity and response time of the LC-based sensor, for which we compared the dynamic response of the LCs at different concentrations of Pb^{2+} ions at the interface. Figure 3.6 shows that for concentrations of Pb^{2+} ions ranging from 3 nM to 300 nM, LCs exhibit dark optical appearances within 20 min. We made two additional observations from Figure 3.6. First, we noted that response time (time taken to achieve homeotropic anchoring) increases as a function of a decrease in the concentration of Pb^{2+} ions (from 300 nM to 3 nM) at the LC interface (Figure 3.7). For example, the sensor took 5 min and 15 min in the presence of 75 nM and 20 nM Pb^{2+}, respectively. A further decrease to 3 nM of the Pb^{2+} concentration, the response time increases to 20 min. Second, below 3 nM, we did not observe any noticeable change in the optical appearance of the LC within 30 min or so. As discussed above, the response of the sensor is primarily governed by the competitive binding interactions (between CTAB-SRNA and Pb^{2+}-SRNA) which are responsible for self-assembly of CTAB molecules at LC-aqueous interface. It is likely that with a decrease in concentrations of Pb^{2+} ions, CTAB molecules

take longer time to self-assemble at the interface causing a delay in ordering transition and thus, the response time of the LC. This also suggests that the response time to detect Pb^{2+} ions primarily depends on the kinetic behavior of the CTAB molecules at the LC-aqueous interface This type of competitive binding interactions based LC-sensors have been reported earlier.[41-44] Quantification of the light intensity transmitted through the film of LCs, as shown in Figure 3.8a, reveals that response time differs as a function of the concentration of Pb^{2+} ions. We observed that with the decrease in Pb^{2+} concentration, the macroscopic appearance of the LC changes continuously. Analysis of the average grayscale intensity (*GI*) also corroborates with the optical appearance of the LC and varies drastically at all concentrations. For example, at 300 and 150 nM of Pb^{2+} ions at the interface, the *GI* value drops to a minimum within 1 min, while 75 nM and 30 nM of Pb^{2+} exhibit least *GI* values in approximately 7 min and 15 min, respectively (Figure 3.8a). Similarly, *GI* values in case of 5 nM and 3 nM of Pb^{2+} ions reached minima within 20 min. Further decrease in the concentration of Pb^{2+} to 1.5 nM, *GI* values retains its maxima within the observation period reported in this work, consistent with a planar/tilted ordering of the LCs.

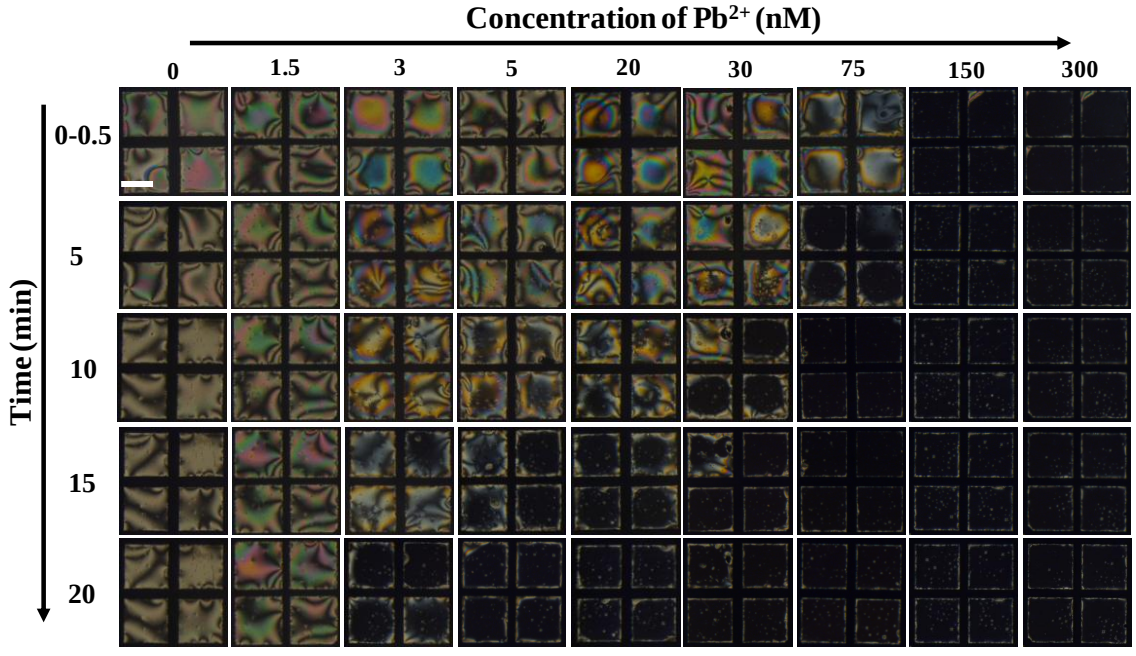

Figure 3.6. Time-lapse polarized optical images of 5CB-aqueous interface laden with 200 nM SRNA and 7 μM CTAB showing the dynamic response of LC to the presence of different concentration of Pb^{2+} from (0-300 nM) at different time intervals. Scale bar = 200 μm.

Therefore, measurement of *GI* as a function of time may provide a direct estimation of a range of Pb^{2+} concentration in the bulk aqueous solution. Figure 3.8b compares the *GI* values for the various concentrations of Pb^{2+} ions which indicated that *GI* values remained almost constant at a concentration of 3 nM or more after 20 min. The detection limit of Pb^{2+} of the LC-based sensor is found to be 3 nM, which is well below the maximum permissible level for Pb^{2+} concentration in drinking water (72 nM).[45]

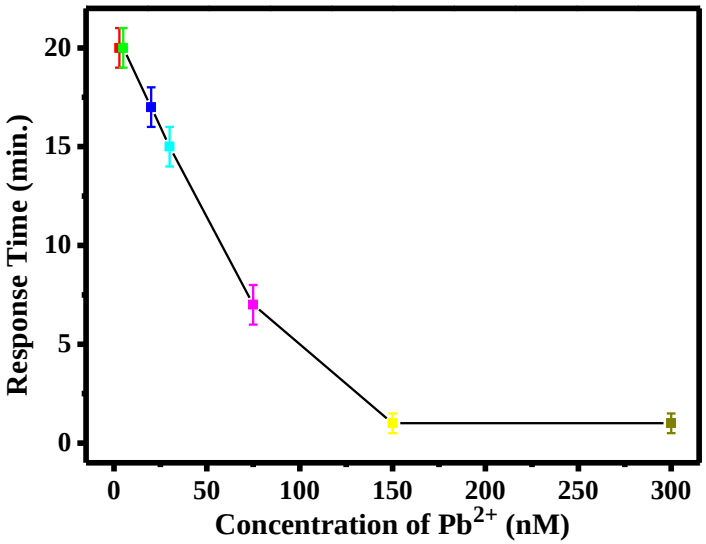

Figure 3.7. Plot of the response time of the LC-based sensor in contact with different concentrations of Pb^{2+} ions.

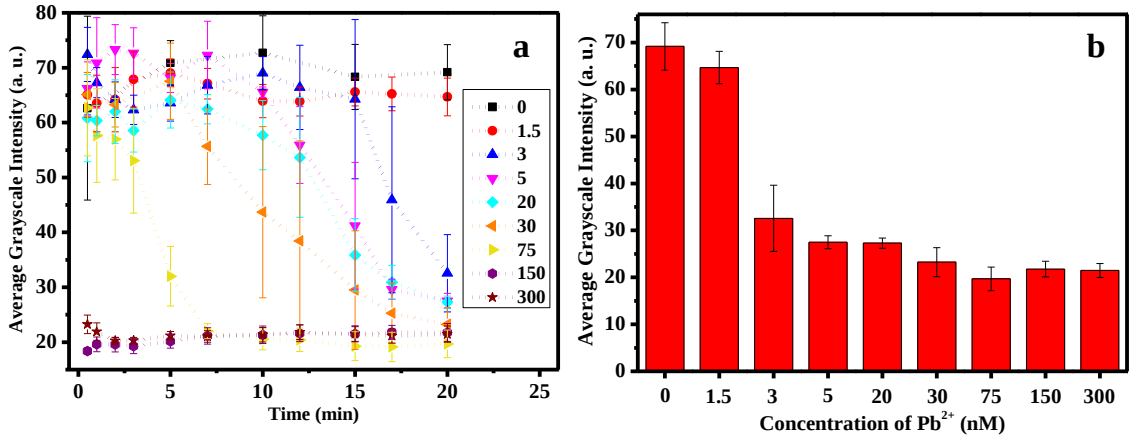

Figure 3.8. Quantification of Pb^{2+} ions: (a) Graph representing the average grayscale intensity of the LC micrographs as a function of time at different concentrations of Pb^{2+} by considering 4 square in a grid (depicted in inset nM). The initial time point indicates 0-

0.5 min. (b) Plot showing the correlation between the concentration of Pb^{2+} and average grayscale intensity of the LC sensor at 20 min.

3.3.3 Effect of pH and ionic strength of aqueous media

The sensitivity of the LC-based sensor was found dependent on pH and ionic strength of the aqueous media (Figure 3.9-3.11). We observed that the optical appearance of the LC was dark in the presence of CTAB (7 µM) at pH 3.6 to 8. In the presence of CTAB (7 µM)-SRNA (200 nM) complexes, LC exhibited bright appearance between pH 5 and pH 7.4 (Figure 3.9). Thus, we investigated the optical response of the LC system for the detection of Pb^{2+} at pH 5. We found that at pH 5, the LC system could detect Pb^{2+}; however, the response of LC slowed down as compared to that at pH 7.4 (Figure 3.10).

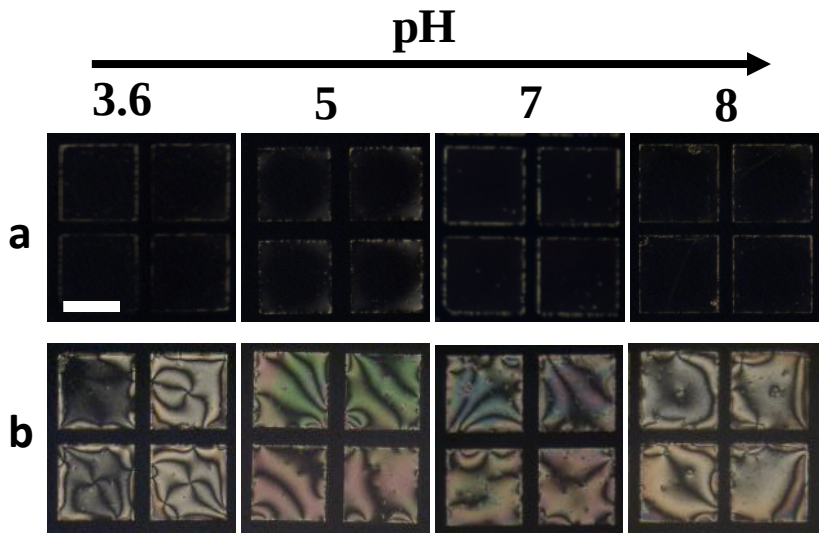

Figure 3.9. Polarized optical images of 5CB film hosted within a gold TEM grid on a DMOAP functionalized glass substrate in presence of (a) 7 µM CTAB and (b) pre-incubated mixture of 7 µM CTAB and 200 nM SRNA at different pH. (Scale bar = 200 µm).

Similarly, we carried out the experiments at different ionic strengths of Hepes buffer ranging from 1 mM to 100 mM. It was found that the optical appearance of the LC remained dark in the presence of CTAB at that range of ionic strength of the buffer (Figure 3.11, upper panel). Similarly, complexes of CTAB and SRNA demonstrated bright appearances of LC at 1, 10 and 30 mM Hepes buffer, however at increasing strength of buffer to 50, 80 and 100 mM, LC demonstrated the coexistence of bright and dark regions (Figure 3.11, lower panel). These results are consistent with the previous

report where authors showed that higher ionic strength (100 mM) in bulk aqueous phase screened the electrostatic interactions among cationic surfactant molecules and lead to tightly packed surfactant monolayer at the aqueous-LC interface.[10] Since the LC remained bright in presence of CTAB-SRNA at 1 mM, 10 mM, and 30 mM Hepes buffer, we performed detection of Pb^{2+} in those buffer concentrations. The response time for the detection of Pb^{2+} is found to be slower as a function of increasing the ionic strength of the buffer from 1 mM to 30 mM (Figure 3.12).

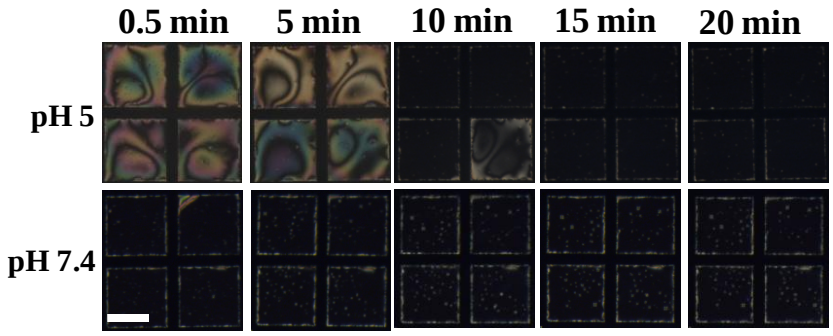

Figure 3.10. Time-dependent optical response of LC to 150 nM Pb^{2+} in the presence of 200 nM SRNA and 7 μM CTAB at pH 5 and 7.4 (depicted at left). (Scale bar = 200 μm)

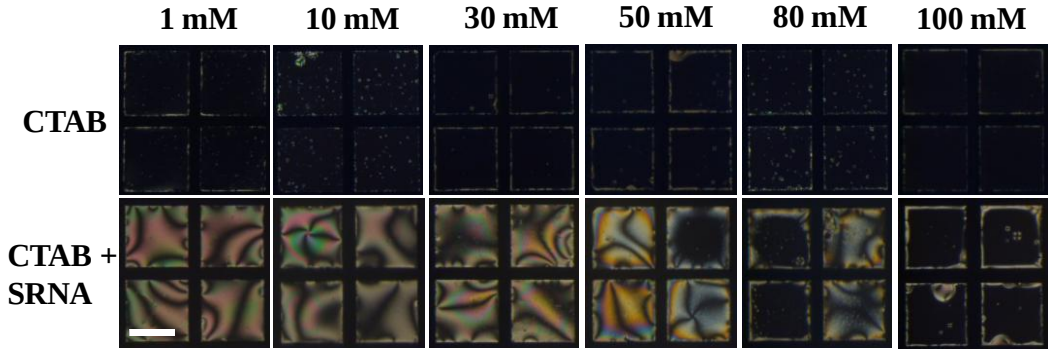

Figure 3.11. Polarized optical images of 5CB film hosted within a gold TEM grid on a DMOAP functionalized glass substrate in presence of 7 μM CTAB (top row) and a pre-incubated mixture of 7 μM CTAB and 200 nM SRNA (bottom row) at different ionic strength of Hepes buffer (depicted at the top of the image). (Scale bar = 200 μm).

3.3.4. Selectivity of LC sensor

Characteristically, biosensors must be highly specific towards a particular analyte for practical applicability. Therefore, we tested the LC-based sensor with different environmentally relevant heavy divalent metal ions and found it highly selective towards

Pb^{2+}. As can be seen in Figure 3.13a-e, the LC sensor remains bright in the presence of 75 nM of Co^{2+}, Hg^{2+}, Ni^{2+} and Zn^{2+} within the observation time of 20 min, while it changed to dark within 5-10 min in the presence of a similar concentration of Pb^{2+}. Similarly, the plot of *GI* of images after a constant 20 min of incubation of metal ions shows that intensity dropped to least only when Pb^{2+} is contacted with LC film (Figure 3.13f). ThT assay also confirms the excellent selectivity of SRNA towards Pb^{2+} ions over other metal ions (Figure 3.14). These observations demonstrate its potential application for selective analysis of Pb^{2+} over other competitive metal ions.

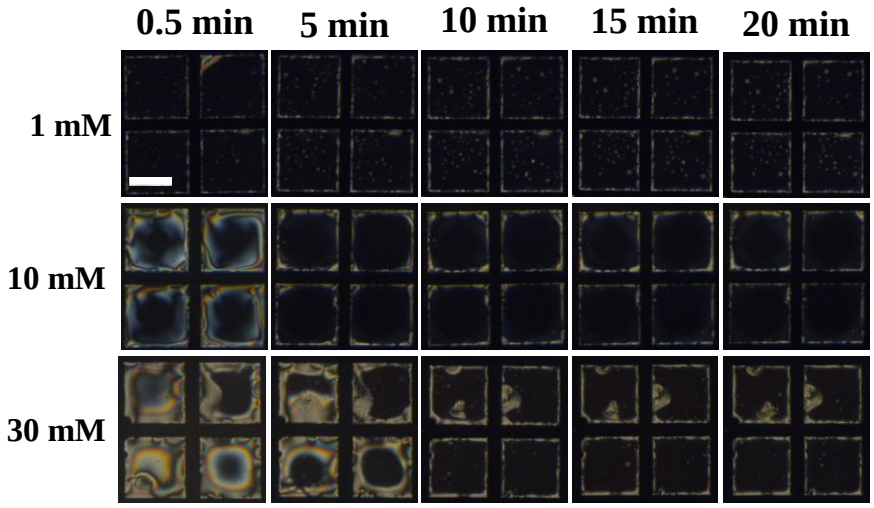

Figure 3.12. Time-dependent optical response of LC to 150 nM Pb^{2+} in the presence of 200 nM SRNA and 7 μM CTAB at different ionic strengths of buffer (depicted at left panel). (Scale bar = 200 μm)

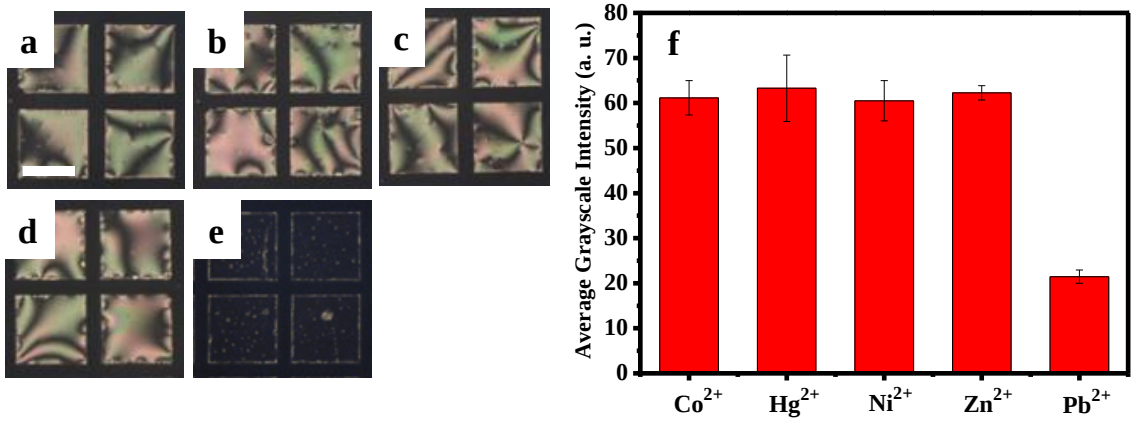

Figure 3.13. Selectivity of LC Sensor: Polarized optical images of 5CB-aqueous interface laden with 200 nM aptamer and 7 μM CTAB in presence of 75 nM of (a) Co^{2+}, (b) Hg^{2+}, (c) Ni^{2+}, (d) Zn^{2+} and (e) Pb^{2+}. The plot in (f) compares the average grayscale intensity of POM images captured against different metal ions at 20 min. Scale bar = 200 μm.

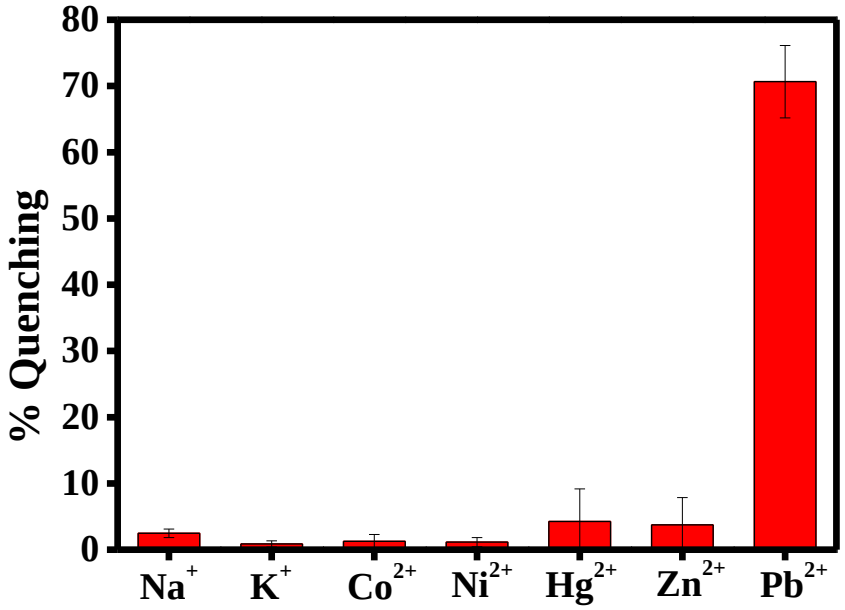

Figure 3.14. Selectivity by ThT assay: Fluorescence quenching of ThT in the aqueous solution of ThT-SRNA by different metal ions.

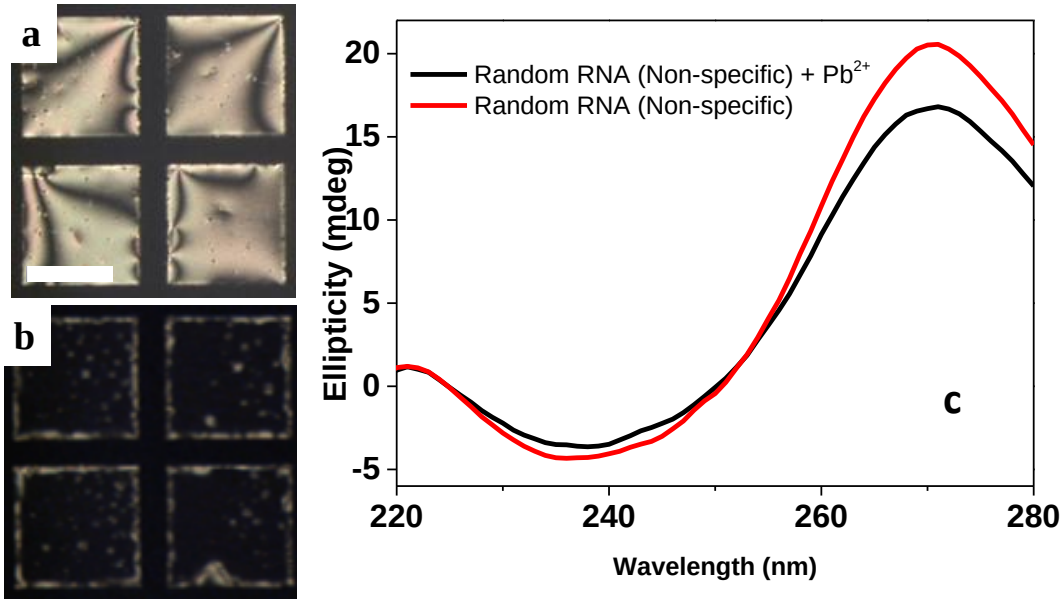

Figure 3.15. Specificity of SRNA aptamer: Polarized optical images of 5CB-aqueous interface laden with 7 μM CTAB and 150 nM Pb^{2+} with (a) 200 nM random aptamer sequence (non-specific) (b) 200 nM SRNA aptamer (specific). Images were taken after 20 min of addition of aqueous solution. Scale bar = 200 μm. (c) CD of Random RNA aptamer (non-specific) in the absence and presence of Pb^{2+}.

In another experiment, we confirmed the specificity of aptamer sequence for Pb^{2+} by employing a random RNA aptamer sequence of a similar number of nucleotide bases and

monitored the optical response of LC in the presence of 150 nM Pb^{2+}. Figure 3.15a,b demonstrates that the ordering of LC remained bright in the presence of a random RNA aptamer while LC exhibits dark appearance when SRNA aptamer is employed. This observation emphasizes that Pb^{2+} specifically binds to the particular SRNA aptamer and optical response of LC is strongly coupled with the specific binding event of Pb^{2+} and SRNA. CD study also confirms the destabilization of quadruplex structures of random aptamer in the presence of Pb^{2+} (Figure 3.15c). Non-specific RNA aptamer adopts parallel G-quadruplex conformation as evident with positive and negative bands at 270 and 240 nm, respectively. A significant decrease in the ellipticity of both bands in presence Pb^{2+} signifies the destabilization of quadruplex structures in RNA aptamer by caused by non-specific binding of metal ions with aptamers which is consistent with the prior reports.[46,47] These results are consistent with the recent study which demonstrated excellent selectivity and specificity of SRNA towards Pb^{2+}.[31]

3.3.5 Detection of Pb^{2+} in tap water

Motivated by the above results, we then validated the performance of our sensor for Pb^{2+} detection in tap water. In the presence of a pre-incubated mixture of CTAB, SRNA and tap water sample (without lead ions), LC exhibited bright optical appearances up to observation period of 20 min consistent with our above findings (Figure 3.16a). Interestingly, when a pre-incubated mixture of CTAB, SRNA and tap water (spiked with Pb^{2+} ions) was introduced onto LC system, the optical appearance of LC turned completely dark within 20 min (Figure 3.16b). These results demonstrate a possible real-life application of the designed apta-LC sensor for detecting Pb^{2+} in tap water.

Before we conclude, we compare the detection limit of the designed LC sensor with that obtained in the recently reported oligonucleotide-based approaches for selective detection of Pb^{2+} associated with a range of techniques such as fluorescence, colorimetric, electrochemical and photo-electrochemical (Table 3.1).[28-34] These techniques require expensive/complex instrumentation, incorporation of fluorophores and chemiluminescent products for signal readout, whereas the designed LC-based method is simple, easy to handle and offers label-free detection by naked eye with a comparable or low detection limit (3 nM). Further, there are several conventional techniques such as atomic absorption and emission spectroscopy and inductively coupled plasma optical emission spectrometry and so on which offer high sensitivity and selectivity to detect lead ions.[48] But these

techniques are time-consuming, costly, require a skilled technician to handle the bulky instruments and are difficult for on-site detection. The significant advantages of LCs in applications involving the detection of heavy metal ions are the following. For example, the LC-based sensor system does not require labeling of the analyte, does not require the use of electroanalytical apparatus and the detection can be performed in ambient light, without the need for electrical power (passive sensors). It also provides a spatial resolution of micrometers and LC reorder on time scales of minutes or less, allowing dynamic phenomena to occur at the aqueous interfaces. In addition, the sensing system is sufficiently simple, and it offers a platform which is very cheap, lightweight, easy to handle and the primary observation of detection can be performed in locations remote from the laboratories by using a smartphone which may find a point of care applications.[49]

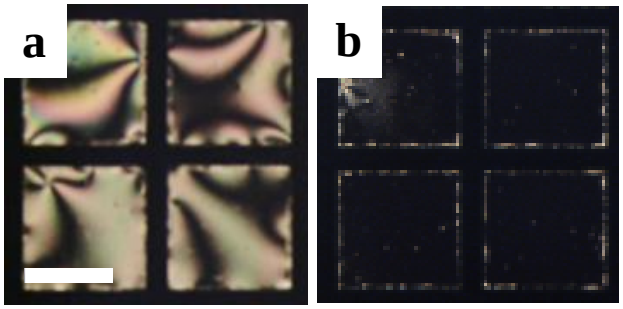

Figure 3.16. Detection of Pb^{2+} in tap-water: Polarized optical images of 5CB-aqueous interface laden with 200 nM SRNA and 7 μM CTAB in presence of tap water adulterated with (a) 0 and (b) 150 nM Pb^{2+}. Scale bar = 200 μm.

3.4 Conclusions

In this work, we reported a new type of LC-based biosensor for detection of heavy metal ions in the aqueous phase. This strategy relies on the stabilization of SRNA G-quadruplex by Pb^{2+}, which generates a distinct orientation of LC. Further, we provided ample evidence in support of the proposed mechanism associated with the competitive and strong binding of SRNA and Pb^{2+} using CD and ThT displacement assay. Our experiments establish that addition of Pb^{2+} leads to (i) the formation of Pb^{2+}-SRNA complexes and (ii) a decrease in density of SRNA on the liquid crystal interface, but additional studies are required to determine which of these processes underlie the response of the LCs to the Pb^{2+}. The LC sensor demonstrates high selectivity towards Pb^{2+} over other divalent heavy metal ions and can report up to 3 nM of the target

concentration. While the aptamer-based sensors for detection of heavy metals are being explored in other fields, this is the first report at LC-aqueous interface, to the best of our knowledge, using aptamer which can effectively tune the orientational transitions of LC in presence of nanomolar concentrations of metal ion target. It is further noted that although RNA quadruplexes are thermodynamically more stable structures as compared to its DNA counterpart, the cost of the sensor could be made potentially cheaper if a DNA version of the aptamer is selected from a pool of DNA that have Pb^{2+} binding G-rich sequence.[28,44,50] This aptamer-based LC approach can be potentially extended as a detection tool for other toxic metal ions and the development of such sensors is currently ongoing in our laboratory.

3.5 Experimental Section

3.5.1 Materials

The Spinach RNA (SRNA) (sequence 5'-GGGGAGAAGGACGGGUCCAGUGCGAAACACGCACUGUUGAGUAGAGUGUGAGCUCCC-3'), 5'6-FAM labeled SRNA and a random RNA sequence (GGGAGGACGAUGCGGAUCAGCCAUGUUUACGUCACUCCUUGUCAAUCCUCAUCGGC) were customized and purchased from Integrated DNA Technologies and used without further purification. Metal salts like lead (II) acetate trihydrate (Pb^{2+}), mercury (II) chloride, sulfuric acid and hydrogen peroxide (30% w/v) were obtained from Merck (Mumbai, India). Nickel (II) chloride hexahydrate, cobalt (II) acetate tetrahydrate, zinc (II) acetate dihydrate were obtained from Alfa Aesar. 4-Cyano-4-pentylbiphenyl (5CB LC), N,N-dimethyl-Noctadecyl-3-aminopropyltrimethoxysilyl chloride (DMOAP), cetyltrimethylammonium bromide (CTAB), hydrochloric acid (HCl), sodium hydroxide (NaOH) and HEPES [4-(2-hydroxyethyl)-1-piperazineethanesulfonic acid] were obtained from Sigma-Aldrich (St. Louis, MO). Ethanol was purchased from Changshu Hongsheng Fine Chemical Co., Ltd. Distilled water (DI water) was deionized by a Milli-Q-system (Millipore, Bedford, MA). Glass microscopic slides of finest Premium grade were purchased from Fischer Scientific (Pittsburgh, PA). Transmission electron microscopy gold grids (20 μm thickness, 50 μm wide bars, 283 μm grid spacing) were obtained from Electron Microscopy Sciences (Fort Washington, PA).

3.5.2 Coating of glass microscope slides with DMOAP

Coating of DMOAP at glass surfaces was performed as per the reported procedures.[1,21] Briefly, glass slides were cleaned with piranha solution (70:30 (% v/v) H_2SO_4:H_2O_2) for 30 min at 100 °C.[1] [*Caution: Handle and dispose piranha solution with intensive care*.] The slides were then subsequently washed with the plentiful amount of DI water followed by a final rinsing with ethanol. The slides were then finally dried under a stream of gaseous N_2, followed by heating at 100 °C for 2 to 3 hr. The "piranha-cleaned" glass slides were then modified with DMOAP.[2] Briefly; the slides were kept into 0.1% (v/v) DMOAP solution in DI water for 30 min. The slides were then rinsed with plenty of DI water to remove the excess DMOAP from the surface and the slides were subsequently dried under a stream of N_2 before keeping in an oven at 100°C for 3-4 hr.

3.5.3 Preparation of LC thin films

DMOAP functionalized glass slides were cut into small square-shaped slides of an approximate dimension of 1.5 X 1.5 cm^2. Then, the cleaned gold TEM grids were placed on DMOAP-coated glass slide. The grids were then filled with approximately 0.2 μL of 5CB, and the excess LC was removed with the help of a Hamilton syringe to produce a uniform interface. DMOAP provides strong homeotropic anchoring to LC at LC-glass interface giving dark appearance under crossed polarizers.[1] A drop of aqueous solution (100 μL) of interest was carefully poured onto the TEM grid using a micropipette, without disturbing the LC followed by observation under a microscope. The hydrophobic surface (DMOAP) of glass supports the non-wetting of water drop on the glass.

3.5.4 Preparation of aqueous solutions of CTAB, Aptamer, and heavy metal ions

All the aqueous solutions were freshly prepared in 1 mM Hepes buffer (pH 7.4). Stock solution of CTAB (1 mM) and metal ions (9 μM) were prepared by dissolving solid material in 1 mM Hepes (pH 7.4) at room temperature (RT). The aptamer was diluted from its stock solution (2.4 μM) prior to use. A complex of CTAB and aptamer was prepared by mixing certain volumes from their stock solution for 30 min to yield the desired final concentration. To detect lead ions, equal volumes of an aqueous solution of Pb^{2+} and aptamer solution were incubated for one hour followed by addition of the same volume of CTAB stock solution. The final concentration of aptamer and CTAB remains 200 nM and 7 μM CTAB with varying concentrations of Pb^{2+}. After 30 min of addition of

CTAB, the sample was introduced onto the LC grid followed by observing under microscope. A similar procedure was followed for the selectivity experiments with other heavy metal ions. For detection of lead in tap water, tap water (source: IISER Mohali) was spiked with a stock solution of Pb^{2+} and further diluted with Hepes buffer (1:4 v/v). The tap water sample was then incubated with 200 nM SRNA for 1 hour before contacting subsequently with an aqueous solution of 7 μM CTAB for another 30 min. The final concentration of Pb^{2+} was kept 150 nM in the (aptamer-CTAB-tap water) system. Every experiment was repeated at least thrice. It should be noted that the aqueous samples must be free of surfactants, lipids, proteins, and fats as they can affect the ordering of LCs at aqueous interface.

3.5.5 Optical characterization of LC films

The director profiles and ordering of LC were characterized by placing the LC film under Zeiss polarizing microscope which is equipped with cross polarizers. The LC film was observed under an objective power of 50X and all the images were captured using an AxioCam Camera. For the investigation of the grayscale intensity of the images (GI), images were processed using ImageJ free access software (developed by U. S. National Institutes of Health, Bethesda, Maryland, USA). Briefly, for each time point, GI values of four squares of a TEM grid were measured, averaged out and errors were calculated.

3.5.6 Fluorescence imaging of aqueous –LC interface

A silicone isolater (4.5 mm in diameter and 1.7 mm in depth) was pressed on a DMOAP coated glass slide to avoid the leakage of aqueous solution between glass slide and silicone isolator. A TEM grid was placed in the well formed between glass slide and silicone isolater. Aqueous samples of FAM-SRNA, FAM-SRNA-CTAB and FAM-SRNA-CTAB-Pb^{2+} were prepared as described above. The final concentrations of FAM-SRNA, CTAB and Pb^{2+} were 200 nM, 7 μM and 300 nM, respectively. The LC film containing 40 μL of the aqueous solution of interest was incubated for 30 min under dark, followed by washing with the buffer to remove background fluorescence. Then, the LC film was observed under a fluorescence microscope (Zeiss (Scope. A1) with a fluorescence filter cube with a 460 nm excitation filter and a 534 nm emission filter. Images were obtained with an AxioCam camera at constant exposure time (900 ms). Every experiment was repeated at least thrice.

3.5.7 Steady-state fluorescence of ThT

All the steady-state fluorescence measurements were performed on a FluoroMax-4 spectrofluorometer from Horiba Jobin Yvon at room temperature. Samples were prepared by incubation of stock solution of SRNA aptamer and ThT) for 1 hour followed by the addition of a very small volume of Pb^{2+} stock (2 μL). Final concentrations of SRNA, Pb^{2+} and ThT were 500 nM, 65 nM and 500 nM respectively. For selectivity, the concentration of all metal ions was kept 65 nM. For recording ThT fluorescence, the samples were excited at 440 nm and the emission spectra were recorded. The fluorescence intensity of ThT (three measurements) was collected at the following parameters: λ_{ex} = 440 nm, excitation slit width = 3 nm, emission slit width = 3 nm, integration time = 0.1 seconds. All the fluorescence data were obtained using the FluorEssence software (provided with the instrument) which were later re-plotted using Origin Pro version 9 software. For the titration experiments, a constant volume of stock solution of Pb^{2+} was added into an equimolar mixture of ThT and aptamer at a concentration of 500 nM and spectra were collected by the above method. Every experiment was repeated at least thrice.

3.5.8 Calculation of dissociation constant for SRNA and Pb^{2+}

The binding constant, K_a, was determined using the Benesi-Hildebrand equation:

$$\frac{1}{(I - I_o)} = \frac{1}{[K_a(I_{max} - I_o)[M^{x+}]n]} + \frac{1}{I_{\max} - I_o}$$

where I_o is the emission intensity of the host in the absence of guest, I is the emission intensity of the host recorded in the presence of an added guest, I_{max} is the emission intensity in the presence of added $[M^{x+}]_{max}$ and K_a represents the binding/association constant. On the addition of various amount of Pb^{2+} into the ThT+SRNA solution, fluorescence intensity decreased. Dissociation Constant was calculated by using Benesi-Hildebrand equation as 1.57 ± 0.03 μM (measured by 3 different sets of calculations).

3.5.9 Circular dichroism measurements

The far-UV CD spectra were recorded on a Chirascan spectrophotometer (Applied Photophysics, U.K.) in a 1 mm path length quartz cell with a scan range of 220−280 nm and step size of 1 nm. A CD spectrum of free aptamer was recorded at a concentration of 15 μM aptamer in 1mM HEPES buffer. Mixtures of SRNA aptamer/random aptamer and

Pb^{2+} were prepared 1 hour prior to the spectrum collection by adding their stock solution to provide the final concentration 15 μM aptamer and 15 μM Pb^{2+}. For each sample, the spectra were averaged over 5 scans and were corrected against the buffer signal using the ProData software provided with the CD instrument. The spectra were plotted using OriginPro 9.0 software.

References

1. Brake, J. M.; Abbott, N. L. *Langmuir* **2002**, *18*, 6101–6109.
2. Brake, J. M.; Daschner, M. K.; Luk, Y.-Y.; Abbott, N. L. *Science* **2003**, *302*, 2094–2097.
3. Carlton, R. J.; Hunter, J. T.; Miller, D. S.; Abbasi, R.; Mushenheim, P. C.; Tan, L. N.; Abbott, N. L. *Liq. Cryst. Rev.* **2013**, *1*, 29−51.
4. Sidiq, S.; Pal, S. K. Liquid Crystal Biosensors: New Approaches. *Proc. Indian Natl. Sci. Acad.* **2016**, *82*, 75–98.
5. Popov, P.; Mann, E. K.; Jakli, A. *J. Mater. Chem. B* **2017**, *5*, 5061−5078.
6. Kleman, M.; Lavrentovich, O. D. *Soft Matter Physics: An Introduction*; Springer: New York, **2003**.
7. de Gennes, P. G.; Prost, J. *The Physics of Liquid Crystals*; Clarendon Press: Oxford, **1993**.
8. Price, A. D.; Schwartz, D. K. *J. Am. Chem. Soc*. **2008**, *130*, 8188−8194.
9. Verma, I.; Sidiq, S.; Pal, S. K. *ACS Omega* **2017**, *2*, 7936–7945.
10. Noonan, P. S., Roberts, R. H., Schwartz, K. *J. Am. Chem. Soc.* **2013**, *135*, 5183–5189.
11. McUmber, C. A.; Noonam, P. S.; Schwartz, D. K. *Soft Matter* **2012**, *8*, 4335–4342.
12. Sidiq, S.; Prasad, G. V. R. K.; Mukhopadhaya, A.; Pal, S. K. *J. Phys. Chem. B* **2017**, *121*, 4247– 4256.
13. Manna, U.; Zayas-Gonzalez, Y. M.; Carlton, R. J.; Caruso, F.; Abbott, N. L.; Lynn, D. M. *Angew. Chem. Int. Ed.* **2013**, *52*, 14011–14015.
14. Verma, I.; Sidiq, S.; Pal, S. K. *Liq. Cryst*. **2019**, *46*, 1318-1326.
15. Das, D.; Sidiq, S.; Pal, S. K. *ChemPhysChem* **2015**, *16*, 753–760.
16. Seo, J. M.; Khan, W.; Park, S-.Y. *Soft Matter* **2012**, *8*, 198–203.
17. Pani, I.; Sharma, D.; Pal, S. K. *General Chemistry* **2018**, *4*, 180012–180012.
18. Popov, P.; Honaker, L. W.; Kooijman, E. E.; Mann, E. K.; Jákli, A. I. *Sens. Biosensing Res.* **2016**, *8*, 31–35.
19. Lee, K.; Gupta, K. C.; Park, S.-Y.; Kang, I.-K. *J. Mater. Chem. B* **2016**, *4*, 704–715.
20. Bi, X.; Hartono, D.; Yang, K-L. *Adv. Funct. Mater*. **2009**, *19*, 3760–3765.
21. Verma, I.; Sidiq, S.; Pal, S. K. *Liq. Cryst.* **2016**, *43*, 1126–1134.

22. Carlton, R. J.; Gupta, J. K.; Swift, C. L.; Abbott, N. L. *Langmuir* **2012,** *28*, 31–36.
23. Singh, S. K.; Nandi, R.; Mishra, K. Singh, H. K.; Singh, R. K.; Singh, B. *Sens. Actuators, B* **2016**, *226*, 381-387.
24. Hu, Q.-Z.; Jang, C. H. *Colloids Surf. B* **2011**, *88*, 622−626.
25. Yang, S.; Wu, C.; Tan, H.; Wu, Y.; Liao, S.; Wu, Z.; Shen, G.; Yu, R. *Anal. Chem*. **2013**, *85*, 14−18.
26. Thiviyanathan, V. Gorenstein, D. G. *Proteomics Clin. Appl.* **2012,** *6*, 563–573.
27. Liu, J. W.; Cao, Z. H., Lu, Y. *Chemical Reviews* **2009**, *109*, 1948–1998.
28. Gupta, S. D.; Shelke, S. A.; Li, N. S.; Piccirilli, J. A. *Chem. Commun.* **2015**, *51*, 9034–9037.
29. Li, T.; Wang, E.; Dong, S. *Anal. Chem*. **2010**, *82*, 1515–1520.
30. Wang, Z.; Chen, B.; Duan, J.; Hao, T.; Jiang, X.; Guo, Z.; Wang, S.*J. Anal. Chem*. **2015**, *70*, 339–345.
31. Wang, G.-L.; Gu, T.-T.; Dong, Y.-M.; Wu, X. M.; Li, Z. J. *Electrochem. Commun.* **2015**, *61*, 117–120.
32. Bala, A.; Pietrzak, M.; Górski, L.; Malinowska, E. *Electrochim. Acta* **2015**, *180*, 763–769.
33. Guo, L.; Nie, D.; Qiu, C.; Zheng, Q.; Wu, H.; Ye, P.; Hao, Y.; Fu, F.; Chen, G. *Biosens. Bioelectron.* **2012**, *35*, 123– 127.
34. Li, T.; Dong, S.; Wang, E. *J. Am. Chem. Soc.* **2010**, *132*, 13156–13157.
35. Chen, P.; Greenberg, B.; Taghavi, S.; Romano, C.; Lelie, D.; He, C. *Angew. Chem. Int. Ed.* **2005**, *44*, 2715–2719.
36. Kim, Y.; Johnson, R. C.; Hupp, J. T. *Nano Lett.* **2001**, *1*, 165–167.
37. Devi, M.; Dhir, A.; Pradeep, C. P. *RSC Adv*. **2016**, *6*, 112728–112736.
38. Kypr, J.; Kejnovska, I.; Renciuk, D.; Vorlickova, M. *Nucleic Res.* **2009**, *37*, 1713-1725.
39. Monchaud, D.; Allain, C.; Teulade-Fichou, M. P. *Bioorg. Med. Chem. Lett.* **2006**, *16*, 4842-4845.
40. Xu, S.; Li, Q.; Xiang, J.; Yang, Q.; Sun, H.; Guan, A.; Wang, L.; Liu, Y.; Yu, L.; Shi, Y.; Chen H.; Tang, Y. *Sci. Rep.* **2016**, 6, 24793.
41. Zuo, F.; Liao, Z.; Zhao, C.; Qin, Z.; Li, X.; Zhang, C.; Liu, D. *Chem. Commun.* **2014**, *50*, 1857-1860.
42. Deng, J.; Lu, X.; Constant, C.; Dogariu, A.; Fang, J. *Chem. Commun.* **2015**, *51*, 8912-8915.

43. Ma, H.; Kang, Q.; Wang, T.; Xiao, J.; Yu, L. *Colloids Surf. B* **2019**, *173*, 178-184.
44. Ma, H.; Kang, Q.; Wang, T.; Yu, L. *Colloids Surf. B* **2019**, *173*, 616-622.
45. http://www.who.int/water_sanitation_health/dwq/chemicals/lead.pdf Accessed: November, 2018
46. Manning, G. S. *Q. Rev. Biophys*. **1978**, *11*, 179-246.
47. Manning, G. S.; Ray, J. *J. Biomol. Struct. Dyn*. **1998**, *16*, 461-476.
48. Wang, W.; Jin, Y.; Zhao, Y.; Yue, X.; Zhang, C. *Biosens. Bioelectron.* **2013,** *41***,** 137-142.
49. Nandi, R.; Pal, S. K. *Analyst* **2018**, *143*, 1046-1052.
50. Tuerk, C.; Gold, L. *Science* **1990**, *249*, 505−510.

Chapter 4

Detection of Creatinine using Surface-Driven Ordering Transitions of Liquid Crystals

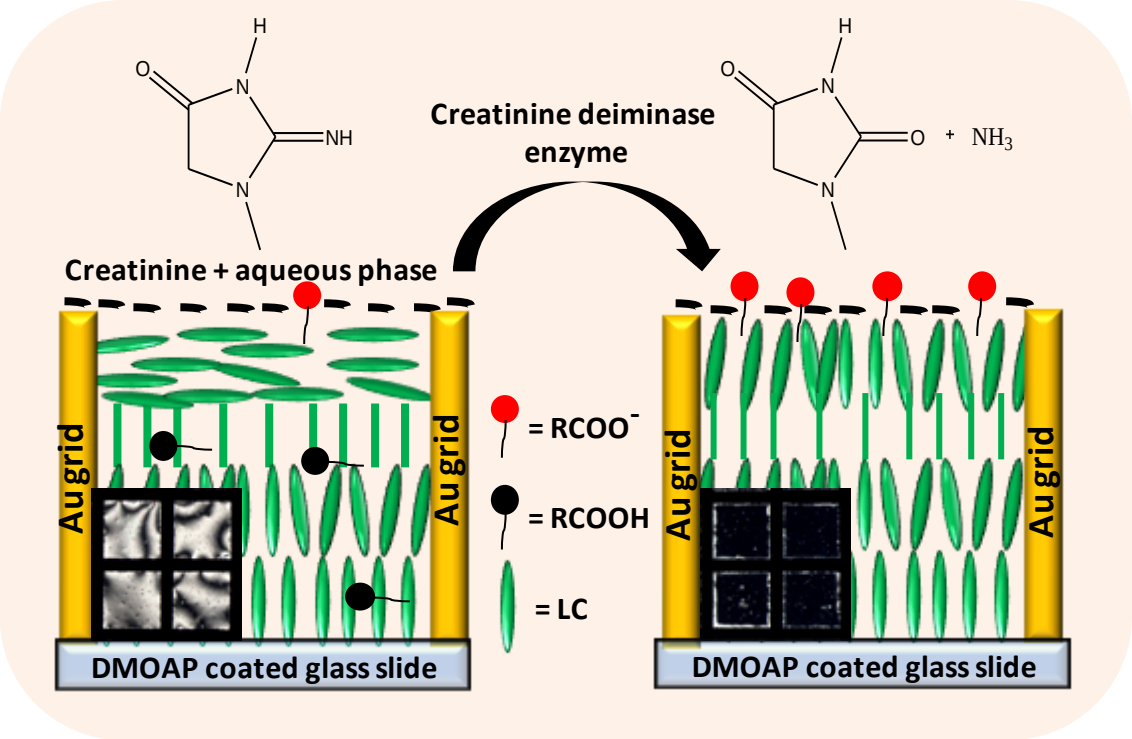

Determining creatinine levels in the blood is of great importance in the detection of high risk for renal failure. Here, we report a simple methodology for real-time monitoring of creatinine employing surface-driven ordering transitions in liquid crystals (LCs) by changing pH in the presence of creatinine deiminase enzyme. Interestingly, in the presence of creatinine deiminase, an ordering transition of LC was observed resulting from enzymatic reactions (giving rise to NH_4^+ ions) that can change the local pH values and lead to the dark optical appearance of the LC. Our approach could detect the creatinine levels as low as that of the healthy adult (~50 µM) and can be successfully applied to measure the higher concentration of creatinine in real-time using dynamic optical response of the LC.

Reproduced with permission from Taylor and Francis (Verma, I.; Sidiq, S.; Pal, S. K. *Liq. Cryst.* **2016**, *43*, 1126-1134.)

4.1 Introduction

Creatinine is an important indicator of renal health.[1-3] Being a waste product (with no further biological function), it is removed by the kidneys from the circulatory system via glomerular filtration. The creatinine level in body fluids ranges from 40-150 µM in healthy adults and 1000 µM or more in patients with renal dysfunction while level less than 40 µM may indicate decreased muscles mass.[4] The conventionally employed methods for the laboratory analysis of creatinine are based on colorimetry using the Jaffe's reaction[5] or the enzymatic colorimetric method[6] where creatinine is enzymatically catalyzed in multiple steps to release H_2O_2 that is further quantified. However, most of these methods have their own limitations. For example, colorimetric methods suffer interference from numerous metabolites and drugs found in biological samples.[7] On the other hand, the enzymatic assays are complex, costly, and time-consuming.[8] Therefore, point-of-care creatinine testing for the detection and monitoring of chronic kidney disease is necessary to have fast and reliable results.[9] These testing methods are generally based on potentiometric and amperometric detection systems. Potentiometric sensors are based on the hydrolysis of creatinine by creatinine iminohydrolase (CIH) or creatinine deiminase (CD), which generates ammonia that can be detected[10-12] while amperometric biosensors involve the conversion of creatinine to glycine (three-stage conversion) followed by the detection of hydrogen peroxide liberated *via* electrode[13]. Although these detection systems have excellent operational stability, short response time, and high sensitivity, the operating system is complex and limits their widespread use. The majority of the currently available techniques are not applicable to point-of-care treatment for chronic kidney disease. This is because the kits available in the market are too large to carry and therefore, cannot be used as a portable device.[14] However, capillary electrophoresis as a scale down version of laboratory technique has been developed but currently have the drawback of being unable to detect creatinine levels as low as that of a healthy adult (50 µM).[15] Therefore, it is important to develop a new label-free biosensor which is simple, easy to use, and specific to creatinine with short response time and can detect creatinine levels as low as 50 µM.

Liquid crystals (LC) have been known to transduce and amplify the chemical and biological molecular events (at aqueous interfaces) into visual outputs detectable by naked eye.[16-31] For instance, past studies have demonstrated that a range of amphiphiles such as surfactants[18,21] and phospholipids[16,22,23] at the aqueous-LC interface leads to the

changes in the optical appearance of the LC, consistent with an ordering transition of the LC. The changes in the alignment of the LC molecules result from the coupling between the aliphatic tails of the adsorbed amphiphiles and the mesogens of the LCs.[16] It is also reported that when polymers and surfactants containing pH-sensitive functional groups are adsorbed at the aqueous-LC interface, the ordering of LCs becomes responsive as a function of pH.[28-35] For example, Kinsinger et al. designed an amphiphilic polymer (by conjugation of poly(ethylene imine) with N-[3-(dimethylamino)-propyl]acrylamide) and demonstrated that assembly of this functionalized polymer at aqueous-LC interface responds reversibly to pH changes in the aqueous phase (although the response time is very long~ 10h).[28] They concluded that ordering of the polymer at the interface is responsible for the pH-dependent changes in the orientation of the LCs. Yet, it is still unclear whether the system can be employed to detect small pH changes as they only observed the different orientational response of the LCs at pH 9.0 and 5.0. Lee et al. reported the pH-responsive aqueous-LC interface functionalized with pH-responsive poly(acrylicacid-b-4-cynobiphenyl-4-oxyundecylacrylate) (PAA-b-LCP).[29] At low pH, the PAA block collapses showing the planar alignment of 5CB at an aqueous interface. As pH increases, the PAA chains become increasingly charged and swell, producing a change to homeotropic anchoring of the LCs.[29] Polyacrylic acid block liquid crystalline polymers were further exploited for detecting proteins through changes in pH at water-LC interface.[30] Using a similar strategy, glucose sensor has been developed by microsized coating droplets with PAA-b-LCP and covalently immobilizing glucose oxidase (GOx) to the PAA chains. The functionalized LC droplets change from radial to bipolar configuration upon coming in contact with glucose.[31] Bi et al. reported a LC-based sensor in which when LC is doped with 4'-pentyl-biphenyl-4-carboxylic acid (PBA), it shows change in its optical appearance from bright to dark when pH of the aqueous phase changes from 6.9 to 7.0.[32] They suggested that orientational transitions of 5CB can be the result of the protonation and deprotonation of PBA at the aqueous/LC interface.

4.2 Objective

In this work, our goal was to develop a label-free strategy using LCs for sensitive and selective detection of creatinine in aqueous media. For the same, we aimed to exploit a chemical reaction involving enzymatic hydrolysis of creatinine by creatinine deiminase to release ammonia and *N*-methylhydantoin (Figure 4.1a). It should be noted that we have selected enzymatic pathway to detect creatinine due to the high specificity of the enzyme-

based reaction, which also minimizes the possibility of interference from other biomolecules present in the specimen. The idea is to design a pH-responsive LC-aqueous interface that can be tuned during enzymatic catalysis of creatinine to result in the different optical signal of LC. To achieve same, we have used a well-known nematic 5CB LC and doped with another chemical, 4′-n-Hexylbiphenyl-4-carboxylic acid (HBA) as (a) its structures is nearly similar to 5CB LC and (b) it consists a pH-sensitive functional group. HBA has a carboxylic acid that may promote an alignment change when the local pH of the interface changes.

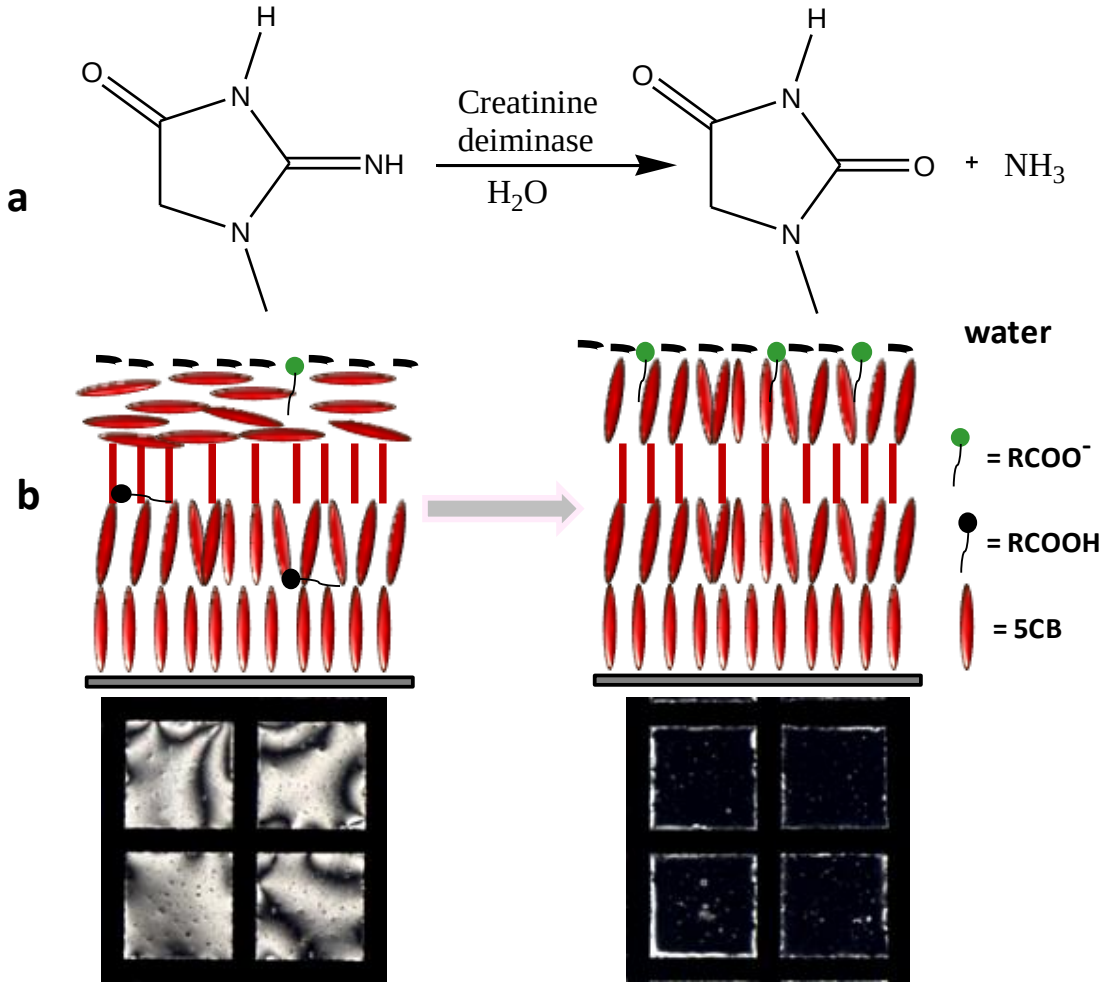

Figure 4.1. (a) The chemical reaction of hydrolysis of creatinine catalyzed by creatinine deiminase. (b) Schematic diagram showing the change in orientation of LCs upon enzymatic hydrolysis of creatinine.

The deprotonation of HBA molecules due to the release of ammonia (during hydrolysis of creatinine) can result in the homeotropic ordering of LC. An ordering transition was observed resulting from enzymatic reactions (giving rise to NH_4^+ ions) that can change

the local pH values (Figure 4.1b). This may promote the self-assembly of amphiphilic deprotonated HBA molecules at the interface leading to the dark optical appearance of the LC.

4.3 Results and Discussion

4.3.1 Optical response of LC to enzymatic hydrolysis of creatinine

Our first experiment employed polarizing optical microscopy (POM) to determine the ordering of nematic 5CB in the presence of 0.3 % HBA at the aqueous-LC interface. First, we confined doped 5CB into a TEM grid supported on DMOAP coated glass slides followed by immersion into water. We observed a bright optical appearance of the LC under crossed polarizers as expected. Second, we immersed the grid containing HBA-doped 5CB in Millipore water (pH 7.2) in the presence of 1000 µM creatinine (Figure 4.2a). Inspection of Figure 4.2a demonstrates that the optical appearance of the LC remains invariant (i.e., tilted/planar orientation) in the presence of creatinine. Interestingly, when we introduced creatinine deiminase of concentration 0.04 mg mL^{-1}, the LC image became dark immediately (Figure 4.2b). In contrast, when pure 5CB was used in the experiment, the optical appearance of LC was bright (see below).

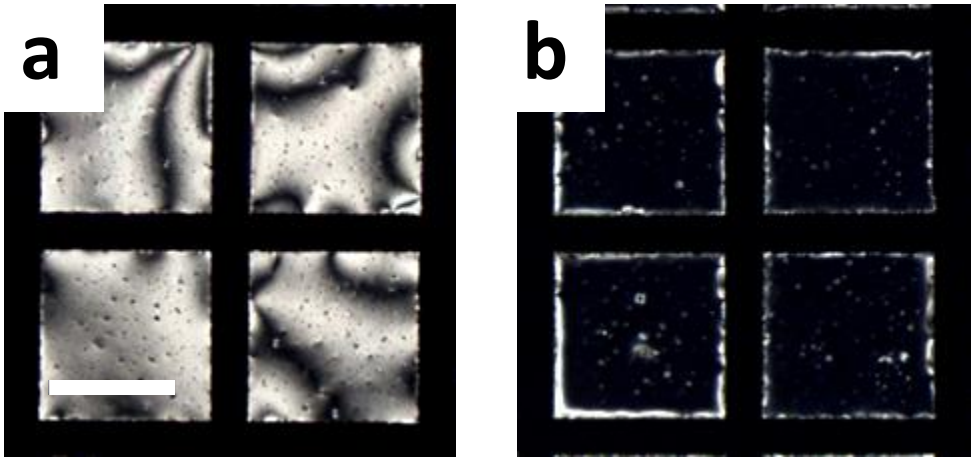

Figure 4.2. Polarized light microscopy images of the aqueous/doped-LC interface (a) in an aqueous solution of 1 mM creatinine and (b) after subsequent addition of an aqueous solution of 0.04 mg mL^{-1} creatinine deiminase. Scale bar = 200 µm.

From these results, it can be concluded that the released ammonium ions from enzymatic hydrolysis of creatinine have increased the pH of the system which deprotonates the pH-sensitive functional group of HBA resulting an ordering transition of the LC. It is also

evident that HBA played an important role in the observed ordering transition. Hydrolysis of 1000 µM creatinine produces enough amount of ammonia which deprotonates HBA acid molecules in 5CB, causing them to self-assemble at the LC-water interface, and thus we observed a change in the interfacial phenomena. In order to verify that the change of ordering of LCs is not caused by the creatinine deiminase alone, we performed a control experiment. The HBA doped 5CB grid was immersed in the aqueous solution of 0.04 mg mL^{-1} enzyme (without creatinine). Figure 4.3a shows that the optical micrographs of the LC at the aqueous-LC interface which shows bright optical appearance consistent with the planar orientation of the LCs at the aqueous interface. We observed that the optical image remains bright in the presence of the enzyme suggesting that the enzyme is unable to trigger an ordering transition (Figure 4.3b).

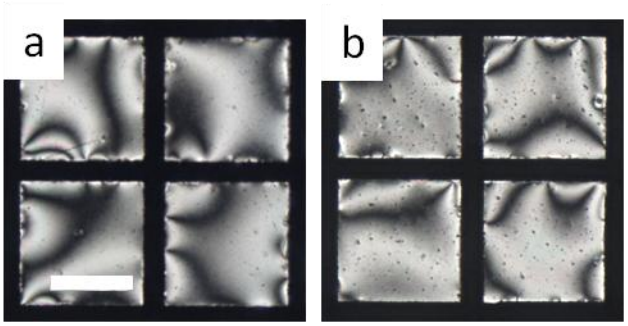

Figure 4.3. Effect of creatinine deiminase on the orientation of HBA doped 5CB: (a) polarized microscopy images of the aqueous–LC interface and (b) 0.04 mg mL^{-1} creatinine deiminase. Scale bar = 200 µm.

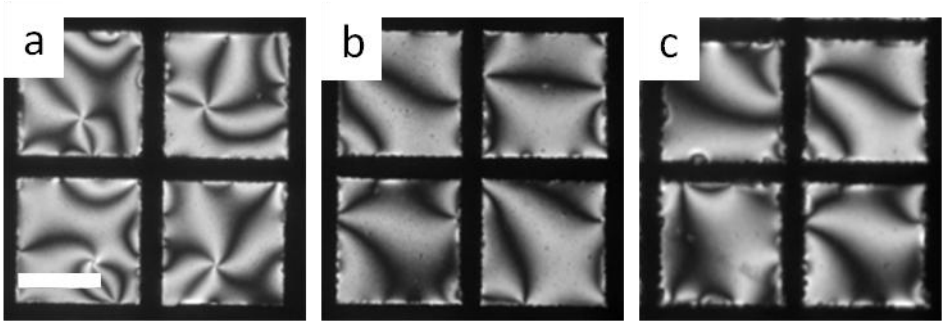

Figure 4.4. Effect of enzymatic hydrolysis of creatinine on the orientation of pure 5CB. Polarized microscopy images of (a) the aqueous–LC interface, (b) after addition of 1 mM creatinine and (c) after subsequent addition of creatinine deiminase. Scale bar = 200 µm.

Second, to further confirm that HBA molecules, when doped in 5CB, are responsible for the ordering transition (homeotropic), TEM grid was filled with pure 5CB followed by

immersion in an aqueous solution of creatinine (Figure 4.4a). Figure 4.4b shows that there was no change in the optical appearance of the LCs after addition of creatinine. When the enzyme was added subsequently in the system, the hydrolysis of the creatinine was also not observed to be able to change the orientation of LCs from planar to homeotropic at the LC-aqueous interface (Figure 4.4c).

4.3.2 Detection limit and selectivity

To probe the detection limit of the creatinine in the system, we investigated the effect of 0.04 mg mL^{-1} enzyme and different concentrations of creatinine on the optical dynamic response of the LC. Figure 4.5 shows that the optical appearance of the LC changes from bright to dark and its orientation from planar to homeotropic in 3 minutes when 1000 µM creatinine gets hydrolyzed in the presence of 0.04 mg mL^{-1} enzyme. The changes in the optical appearance of the LC from bright to dark occur over 5-25 minutes depending upon the concentration of the creatinine present in the system. We make two other additional observations regarding this result. First, we note that LC is able to respond up to a concentration of 50 µM. Second, below 50 µM no ordering transition was observed even after a period of 1 day. Even after increasing the concentration of the creatinine deiminase in the system from 0.04 to 0.08 mg mL^{-1}, hydrolysis of 40 µM creatinine did not affect the orientation of the HBA doped LCs and the system remains bright (Figure 4.6). One of the possible reasons is that the hydrolysis of 40 µM creatinine is not able to produce enough amount of ammonia which could deprotonate the HBA molecules and show the ordering. The ammonia being released from the enzymatic hydrolysis of 40 µM creatinine is neutralized by the bulk solution before it could deprotonate the HBA molecules. These results suggest that the system is capable of detecting the creatinine up to 50 µM which is close to the creatinine level in a healthy human. It also suggests that the concentration of creatinine can be estimated from the kinetic response of the LCs.

The concentration of creatinine present in the specimen can be estimated by measuring the average grayscale intensity of the optical images with respect to the time taken by LCs for the optical transition from bright to dark. Figure 4.7a shows the plot of the grayscale intensity of POM images taken at different interval times after addition of enzyme in the system containing a different concentration of creatinine. It is evident that hydrolysis of 1000 µM creatinine produces enough amount of ammonia causing very fast change (in 3 minutes) in the optical appearance of the LC from bright to dark. Decreasing

concentration to 500 µM does not have much effect on the response time of LCs anchoring transition as grayscale intensity dropped to its minimum in 5 minutes.

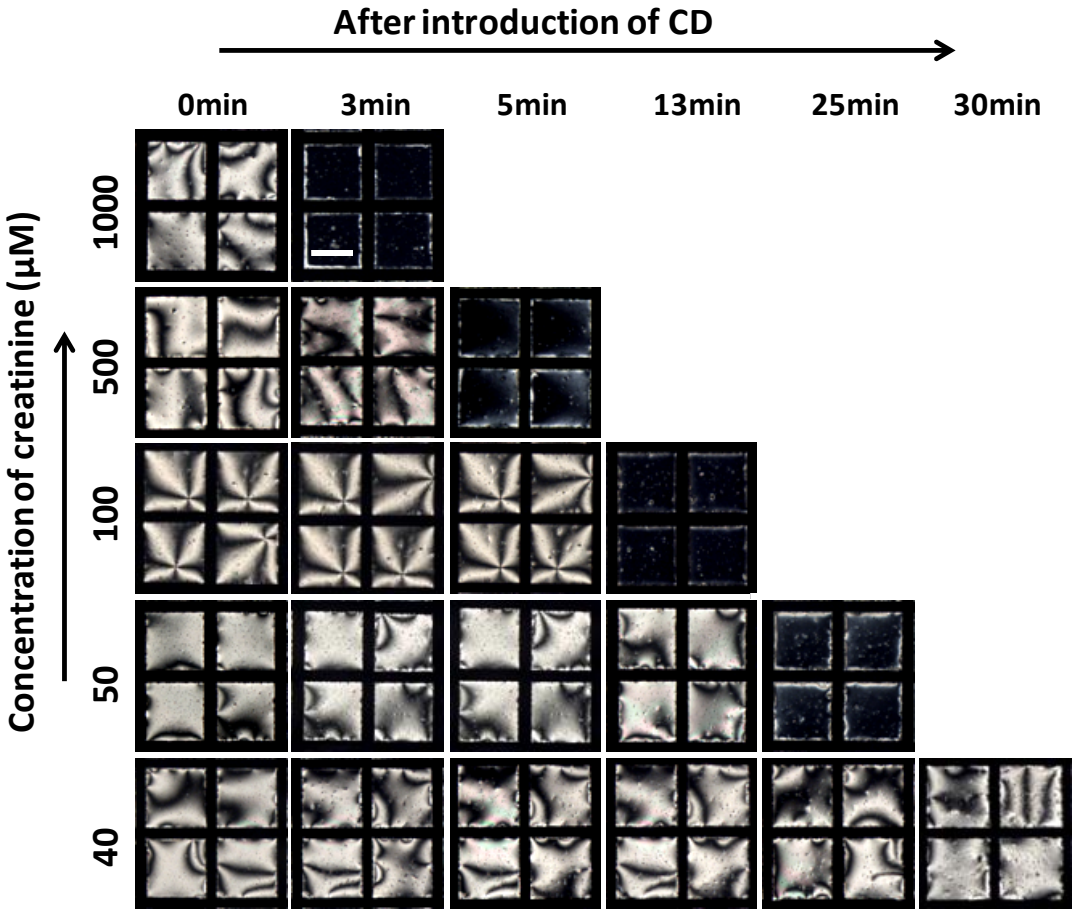

Figure 4.5. Dynamic response of LCs to the different concentrations of creatinine when hydrolyzed by the same amount of creatinine deiminase. Scale bar = 200 µm.

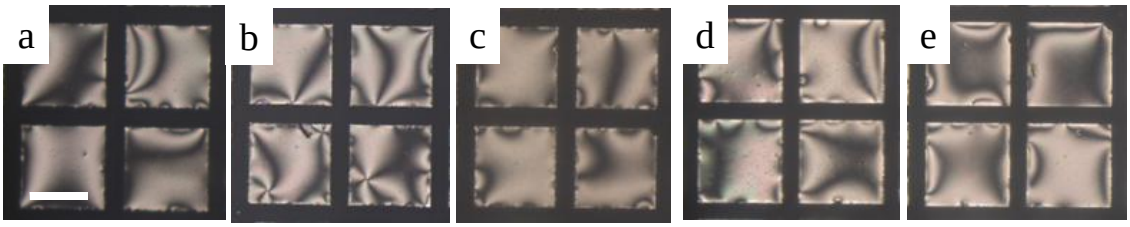

Figure 4.6. Polarized light microscopy images of the response of HBA doped LCs when 40µM creatinine was hydrolyzed by a) 80, b) 40, c) 10, d) 8, and e) 5 µg ml^{-1} creatinine deiminase. Scale bar = 200 µm.

Further decreasing the concentration to 100 µM and 50 µM increases the response time to approximately 13 minutes and 25 minutes, respectively. The concentration of less than 50 µM does not show any significant changes in the values of grayscale intensity of the

micrographs obtained at certain time intervals. Since the response time of LCs is proportional to the amount of ammonia released from the enzymatic reaction, the results can be correlated with the creatinine concentration present in the system. Therefore, the concentration of creatinine can be calculated as a function of time taken by the LC to change their orientation from planar to homeotropic. Figure 4.7b describes the correlation between the concentration of creatinine and the time taken by the LC to show an optical response from bright to dark. We mark two observations from this figure. First, when the concentration is high as 1 mM (a sign of renal failure), the LC optical change is as fast as 2.5 minutes with a standard deviation of 0.8 minutes. Second, when the concentration lies between 50 to 100 µM, (which is considered as healthy), the transition becomes comparatively slower and response time ranges from 13.9 to 24 minutes. So our system is quite capable of measuring the creatinine concentration in real-time quantitatively and able to differentiate between healthy human and human seeking medical attention for renal dysfunction.

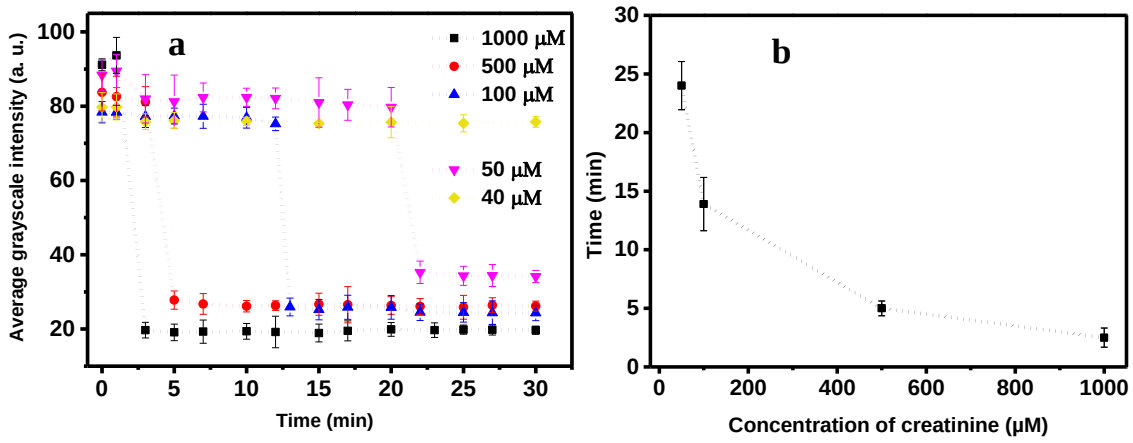

Figure 4.7. (a) Average grayscale intensity of micrographs plotted as a function of the response time of LC during hydrolysis of different concentration of creatinine by creatinine deiminase (0.04 mg mL^{-1}). (b) Response time *vs.* concentration graph describing the time required for complete homeotropic orientation of LCs coupled to enzymatic hydrolysis of different concentration of creatinine.

After establishing that hydrolysis of creatinine by creatinine deiminase can be monitored by the optical appearances of the LCs at the aqueous interface, we determined the detection limit of the enzymatic activity of the creatinine deiminase. A 2.5 ml optical cell was filled with an aqueous solution of 1mM creatinine, after few minutes calculated volume from the 1 mg mL^{-1} stock solution of creatinine deiminase was added to make its

required final concentration. Figure 4.8 shows the effect of varying concentration of the creatinine deiminase on the optical appearances of HBA doped LCs when introduced in the optical cell containing an aqueous solution of 1mM creatinine. When 80 μg mL^{-1} creatinine deiminase was introduced, the transition of LCs from planar to homeotropic was as fast as 1.5 min (Figure 4.8a). As the concentration of the creatinine deiminase gets decreased in the system, the response of LCs for the optical transition becomes slow and changes to dark in 3, 15 and 25 min when 40, 10, 7 μg mL^{-1} creatinine deiminase were used, respectively. (Figure 4.8b,c,d). On further decreasing the concentration of creatinine deiminase to 5 μg mL^{-1} did not induce changes in the optical appearance of the LCs and the LCs remains bright, owing to their planar orientation (Figure 4.8e).

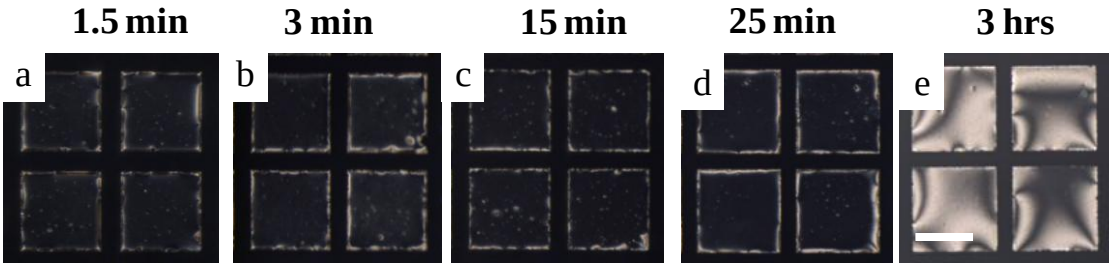

Figure 4.8. Polarized light microscopy images of the kinetic response of HBA doped LCs when 1000 μM creatinine was hydrolyzed by a) 80, b) 40, c) 10, d) 7, and e) 5 μg mL^{-1} creatinine deiminase. (Time taken by LCs during hydrolysis to change the orientation from planar to homeotropic is mentioned above the particular image). Scale bar = 200 μm.

Next, we examined the possibility of determining the creatinine in the presence of other biomolecules such as human hemoglobin, L-ascorbic acid, and glucose. In an optical cell, first, the mixture of 0.1 μM hemoglobin, 5mM glucose, 0.08 mM L-ascorbic acid and 1mM creatinine was filled in the optical cell containing HBA doped 5CB grid. The initial bright appearance of the LCs changed to dark in 11 minutes upon the addition of the enzyme (Figure 4.9a,b). However, the same mixture without creatinine did not change the orientation of LC from planar to homeotropic when monitored up to 3 hours (Figure 4.9c,d). This observation suggests a potential application of LC-based design to detect creatinine in a more complex environment such as real samples.

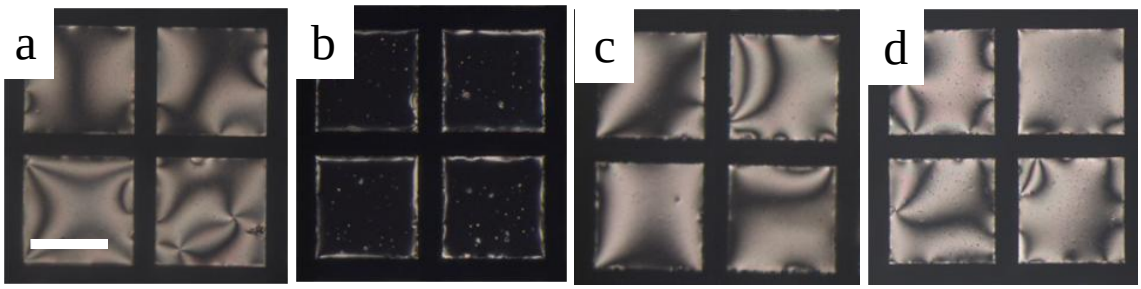

Figure 4.9. Polarized microscopy images of the HBA doped LCs in contact with mixture of 0.1 µM human hemoglobin, 5 mM glucose, 0.08 mM L-ascorbic acid and 0.04 mg ml^{-1} creatinine deiminase in the presence of 1 mM creatinine at (a) 0 min (b) 11 min. Polarized microscopy images of the HBA doped LCs in contact with a mixture of 0.1 µM human hemoglobin, 5 mM glucose, 0.08 mM L-ascorbic acid and 0.04 mg ml^{-1} creatinine deiminase in the presence of 0 mM creatinine at (c) 0 min and (d) 3 hrs. Scale bar = 200 µm.

4.3.3 Reversible ordering transition of LC biosensor by HCl

To establish that deprotonation of HBA molecules is responsible for the orientational transitions of LC molecules, we sought to observe the effect of the addition of exogenous acid on LC anchoring after enzymatic hydrolysis of creatinine at the aqueous-LC interface. We introduced different concentrations of HCl in the LC filled grid (doped with HBA) after enzymatic hydrolysis with 1 mM creatinine. Figure 4.10 shows the effect of the addition of different concentration of exogenous HCl on the orientational ordering transition of the LC. We observed that the addition of 1 mM HCl leads to the rapid change in the optical appearance of the LC from dark to bright which remained stable over several hours (Figure 4.10a, b). This concludes that 1 mM HCl is able to neutralize the entire ammonium ions produced from the hydrolysis of 1 mM creatinine. When we introduced 0.5 mM HCl, it was found that an immediate ordering transition of the LC to the bright optical appearance within 30 s followed by dark image as it was in original (Figure 4.10c, d). This suggests that 0.5 mM HCl is able to neutralize the effect of only 0.5 mM of the ammonium ions which could protonate the dissociated HBA molecules leading to the transient planar orientation of the LC molecules followed by original dark appearance within 25 minutes. When 0.1 mM HCl is added to the system, the sudden bright appearance turned to dark in 4 minutes suggesting that the effect of HCl was compensated by the bulk water (Figure 4.10e, f). Further decrease in the concentration of HCl leads to similar interfacial events as expected (Figure 4.10). Considering the amount

of HBA molecules at the LC-aqueous interface, the concentration of HCl was reduced to 0.01 nM which does not have any effect to the dissociated HBA molecules at the interface (Figure 4.10k, l).

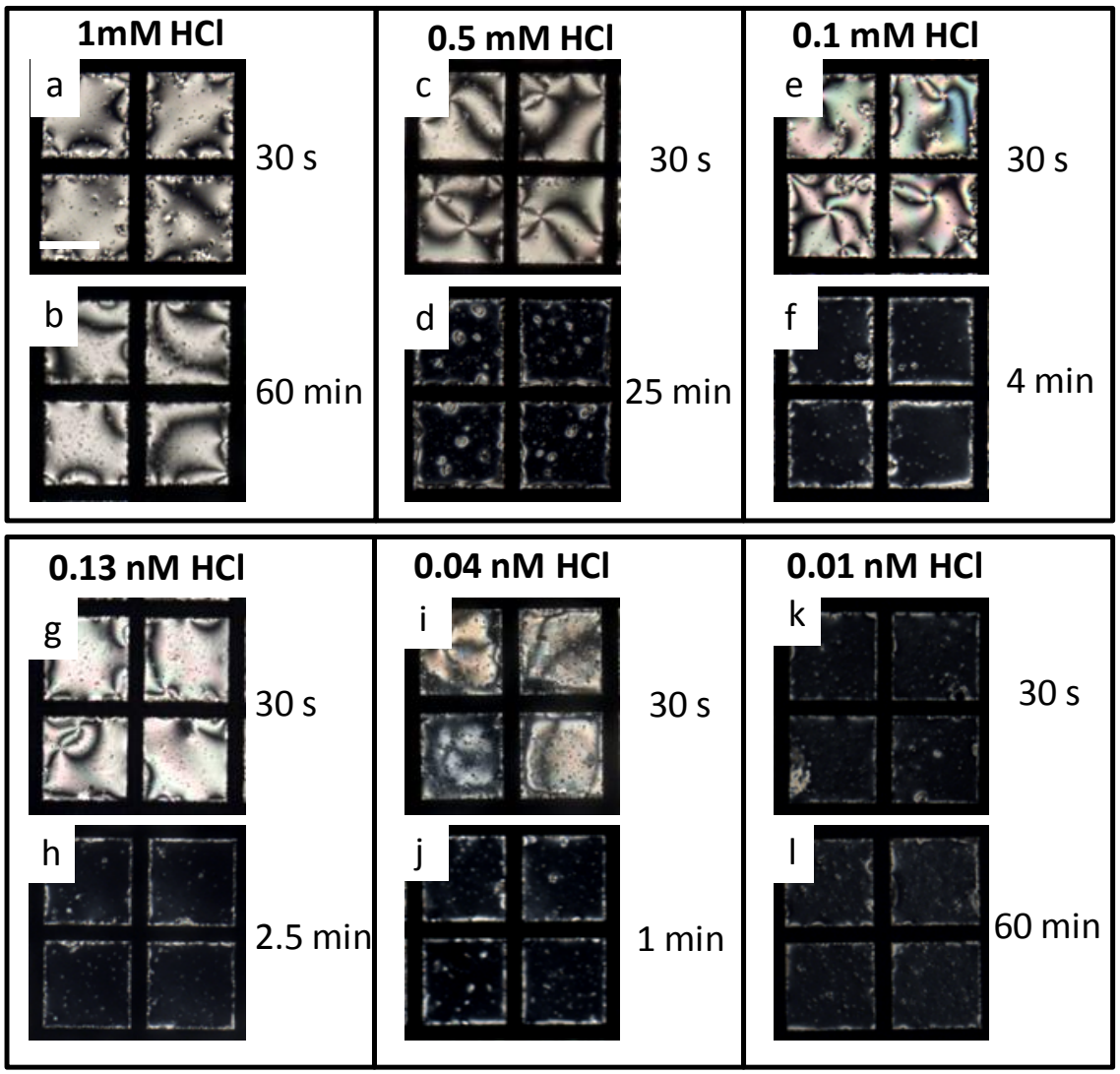

Figure 4.10. Reversible ordering transition on introduction of different concentration of HCl after enzymatic hydrolysis of 1 mM creatinine: (a,b) 1 mM HCl; (c,d) 0.5 mM HCl; (e,f) 0.1 mM HCl; (g,h) 0.13 nM HCl; (i,j) 0.04 nM HCl; (k,l) 0.01 nM HCl. Scale bar = 200 µm.

4.4 Conclusions

We have been successful in developing a liquid crystal based label-free biosensor for creatinine which exploits the optical properties of the LC and shows the change in visual appearances from bright to dark during enzymatic hydrolysis. As the ammonia is released

during the hydrolysis, the LC molecules change their orientation from planar to homeotropic. This transition can be attributed to the deprotonation of HBA molecules at the LC-aqueous interface. The LC-based creatinine biosensor being able to detect the creatinine levels as low as that of a healthy adult can be a promising system for differentiating between the creatinine level of a healthy adult and a person with renal dysfunction. Along with this, the sensor is simple, specific, fast and can be made easily available to the patient.

4.5 Experimental Section

4.5.1 Materials

Creatinine deiminase microbial, creatinine, human hemoglobin, α-D-glucose, 4-Cyano-4-pentylbiphenyl (5CB), N,N-dimethyl-N-octadecyl-3-aminopropyltrimethoxysilyl chloride (DMOAP), hydrochloric acid, sodium hydroxide were purchased from Sigma-Aldrich (St. Louis, MO). 4′-n-Hexylbiphenyl-4-carboxylic acid, 99% was purchased from Alfa Aesar (Heysham, England). L-Ascorbic acid was obtained from HiMedia (Mumbai, India). Sulfuric acid, chloroform and hydrogen peroxide (30% w/v) were purchased from Merck (Mumbai, India). Ethanol was obtained from Jebsen & Jenssen GmbH and Co., Germany (S D Fine-Chem, Ltd.). Deionization of a distilled water (DI water) source was performed using a Milli-Q-system (Millipore, Bedford, MA). Fisher's Finest Premium grade glass microscopic slides and cover glass were obtained from Fischer Scientific (Pittsburgh, PA). Gold specimen grids (20 μm thickness, 50 μm wide bars, 283 μm grid spacing) were obtained from Electron Microscopy Sciences (Fort Washington, PA).

4.5.2 Treatment of glass microscope slides with DMOAP

Glass microscope slides were cleaned with piranha solution (70:30 (% v/v) H_2SO_4:H_2O_2) for 1 h at 100 °C according to the published procedure.[16] They were then rinsed with water, ethanol and methanol and dried under a stream of gaseous N_2, followed by heating to 120 °C overnight. The "piranha-cleaned" glass slides were immersed into 0.1% (v/v) DMOAP solution in DI water for 30 minutes at room temperature. The slides were then rinsed with DI water to remove the unreacted DMOAP from the surface. The DMOAP coated slides were dried under a stream of N_2 and kept at 100 °C.

4.5.3 Preparation of optical cells

Cleaned gold TEM specimen grids were placed on DMOAP-coated glass slides. The grids were filled with approximately 0.2 μL of 0.3% HBA doped 5CB, and the excess LC was removed with the help of a syringe to produce a planar interface. Subsequently, the grid was immersed in 2.5 mL optical cell containing creatinine solution of a known concentration in DI water at room temperature. After a few minutes, the required aqueous solution of creatinine deiminase from the stock solution of 1 mg ml^{-1} was introduced into the optical well to make the final concentration of 0.04 mg ml^{-1} enzyme as and when needed.

4.5.4 Optical characterization of LC films

The orientational ordering of the LC was determined using a Zeiss polarizing microscope Scope. A1 with cross polars (X50). For the investigation of the grayscale intensity of the images, images were processed using Image J free access software (developed by U. S. National Institutes of Health, Bethesda, Maryland, USA).

References

1. Levey, A. S; Perrone, R. D; Madias, N. E. *Annu. Rev. Med*. **1988**, *39*, 465–490.
2. Narayanan, S.; Appleton, H. D. *Clin. Chem.* **1980**, *26*, 1119–1126.
3. Stark, J. L. *Nursing* **1994**, *24*, 58–61.
4. Sena, F. S.; Syed, D.; McComb, R. B. *Clin. Chem*. **1988**, *34*, 594-595.
5. Jaffe, M. Z. *Z. Physiol. Chem.* **1886**, *10*, 391–400.
6. Fossati, P.; Prencipe, L.; Berti, G. *Clin. Chem.* **1983**, *29*, 1494-1496.
7. Lo, S. C.; Tsai, K. S. *Clin. Chem.* **1994**, *40*, 2326–2327.
8. Weber, J. A.; van Zanten, A. P. *Clin. Chem.* **1991**, *37*, 695–700.
9. Skurup, A.; Kristensen, T.; Wennecke, G. *Clin. Chem. Lab. Med*. **2008**, *46*, 3–8.
10. Meyerhoff, M.; Rechnitz, G. A. *Anal. Chim. Acta*. **1976**, *85*, 277–285.
11. Killard, A. J.; Malcolm, S. R. *Trends in Biotechnol.* **2000**, *28*, 433–437.
12. Lad, U.; Khokhar, S.; Kale, G. M. *Anal. Chem.* **2008**, *80*, 7910–7917.
13. Tsuchida, T.; Yoda, K. *Clin. Chem.* **1983**, *29*, 51–55.
14. Shepherd, M. D. S. *Clin. Biochem. Rev*. **2011**, *32*, 109–114.
15. Zinellu, A.; Caria, M. A.; Tavera, C.; Sotgia, S.; Chessa, R.; Deiana, L.; Carru, C. *Anal. Biochem.* **2005**, *342*, 186-193.
16. Brake, J. M.; Daschner, M. K.; Luk, Y-Y.; Abbott, N. L. *Science* **2003**, *302*, 2094−2097.
17. Lin, I. H.; Miller, D. S.; Bertics, P. J.; Murphy, C. J.; de Pablo, J. J.; Abbott, N. L. *Science* **2011**, *332*, 1297-1300.
18. Brake, J. M.; Abbott, N. L. *Langmuir* **2002**, *18*, 6101−6109.
19. Brake, J. M.; Mezera, A. D.; Abbott, N. L. *Langmuir* **2003**, *19*, 6436−6442.
20. Lockwood, N. A.; de Pablo, J. J.; Abbott, N. L. *Langmuir* **2005**, *21*, 6805−6814.
21. Price, A. D.; Schwartz, D. K. *J. Am. Chem. Soc.* **2008**, *130*, 8188−8194.
22. Brake, J. M.; Daschner, M. K.; Abbott, N. L. *Langmuir* **2005**, *21*, 2218−2228.
23. Lockwood, N. A.; Mohr, J. C.; Ji, L.; Murphy, C. J.; Palecek, S. P.; de Pablo, J. J.; Abbott, N. L. *Adv. Funct. Mater.* **2006**, *16*, 618-824.
24. Agarwal, A.; Sidiq, S.; Setia, S.; Bukusoglu, E.; de Pablo, J. J.; Pal, S. K.; Abbott N. L. *Small* **2013**, *9*, 2785−2792.
25. Sivakumar, S.; Wark, K. L.; Gupta, J. K.; Abbott, N. L.; Caruso, F. *Adv. Funct. Mater.* **2009**, *19*, 2260−2265.
26. Sidiq, S.; Das, D.; Pal, S. K. *RSC Adv*. **2014**, *4*, 18889−18893.

27. Gupta, J. K.; Zimmerman, J. S.; de Pablo, J. J.; Caruso, F.; Abbott, N. L. *Langmuir* **2009**, *25*, 9016−9024.
28. Kinsinger, M. I.; Sun, B.; Abbott, N. L.; Lynn, D. M. *Adv. Mater.* **2007**, *19*, 4208-4212.
29. Lee, D. Y.; Seo, J. M.; Khan, W. *Soft Matter* **2010**, *6*, 1964-1970.
30. Seo, J. M.; Khan, W.; Park, S. Y. *Soft Matter* **2012**, *8*, 198-203.
31. Khan, M.; Park, S. Y. *Anal. Chem.* **2014**, *86*, 1493-1501.
32. Bi, X.; Hartono, D.; Yang, K. L. *Adv. Funct. Mater*. **2009**, *19*, 3760–3765.
33. Wei, Y.; Jang, C. H. *J. Mater. Sci*. **2015**, *50*, 4741-4748.
34. Hu, Q. Z.; Jang, C. H. *J. Mater. Sci.* **2012**, *47*, 969-975.

Chapter 5

Application of Poly-L-lysine Coated Liquid Crystal Droplets in Detection of Proteins

Part A

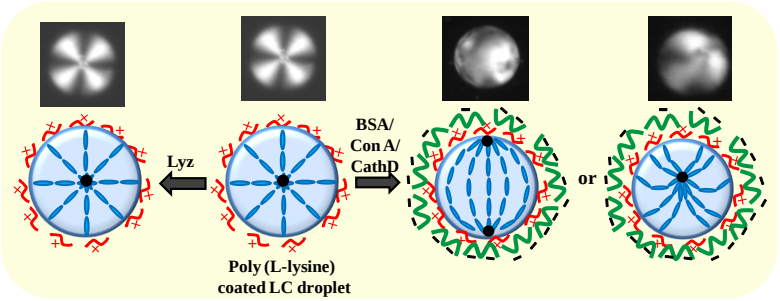

Liquid crystal (LC) droplets offer an interesting and sensitive platform for label-free imaging of adsorbates. However, the high mobility of LC droplets makes their characterization difficult. In this part, we demonstrate the utility of poly-L-lysine (PLL) coated LC-droplets for real-time monitoring of protein adsorption. The study established the role of electrostatic interactions in tuning the director transition in PLL-LC droplets. The study will strengthen the principles to tailor LC droplets for recognizing biomolecular interactions.

Part B

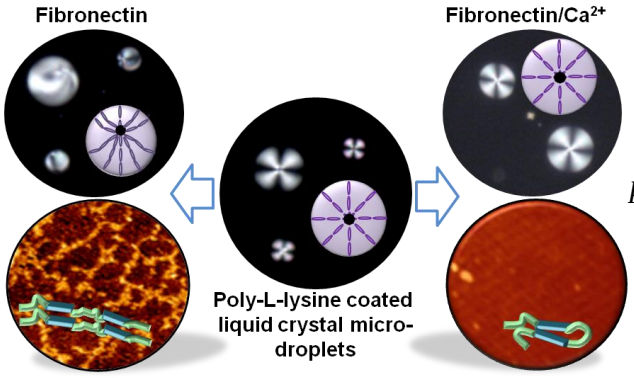

The work reports the first example of LC droplet-based system to study the conformational changes in fibronectin (FibN), an extracellular matrix (ECM) protein, at interfaces and provides considerable insights about mode of interaction between PLL and FibN. The work not only strengthens the understanding of protein-polymer interactions but will also help to develop principles to comprehend the fibrillation process within complex ECM assembly.

Part A: Reproduced with permission from Taylor and Francis (Verma, I.; Sidiq, S.; Pal, S. K. *Liq. Cryst*. **2019**, *46*, 1318-1326)
Part B: Reprinted (Adapted)/Reproduced with permission from (Verma, I.; Pani, I.; Sharma, D.; Maity, S.; Pal, S. K. *J. Phys. Chem. C* **2019**, *123*, 13642-13650). Copyright (2019) American Chemical Society.

5.1. Part A: Protein Triggered Ordering Transitions in Poly-L-lysine Coated Liquid Crystal Emulsion Droplets

5.1.1 Introduction

The understanding of protein interactions with surfaces (majorly driven by non-covalent forces) forms a basis to develop the fundamental principles of biological processes inside the cells and for various biomedical applications.[1-5] Considering the basic importance of cooperative electrostatic interactions between proteins and other biomolecules/membranes in the biological system, it becomes crucial to design stimuli-responsive interfaces for protein adsorption and principles to identify such interactions between proteins and the modified surfaces. Currently, there are numerous physicochemical methods available to detect and study protein interactions such as affinity chromatography, protein arrays, surface plasmon resonance, quartz crystal micro balance, FTIR spectroscopy, NMR spectroscopy, and X-ray diffraction but the costly instrumentation and complexity involved limit their widespread use in daily life.[6]

Nematic liquid crystal (LC) confined within micrometer-sized droplets in aqueous media has been considered as the new class of functional materials for the broad range of sensing and interfacial applications.[7-24] Due to their tunable optical properties, large surface areas and rich phases, LC droplets have shown tremendous potential as the optical biosensors. The detection principle lies within the change in director configurations of the LCs inside the droplets that can be optically observed with the naked eye, eliminating the need for expensive and complex detection systems for signal transduction. For instance, LC microdroplets have been applied as a sensing tool for developing immunoassays[13], to detect glucose[18], bacteria, and viruses[10], bacterial endotoxin at $pgmL^{-1}$ concentration[15,] and many more[17,19-24]. Recently, we reported that adsorption of poly-L-lysine (PLL) (cationic peptide) could induce homeotropic orientational ordering of LCs at LC-aqueous interface.[23] The homeotropic ordering is mainly due to the intermolecular hydrogen bonding between PLL and the 5CB LC. Also, the LC droplets prepared by alternate multilayer assembly of PLL and polystyrene sulphonate (PSS) (an anionic polyelectrolyte) with outermost being PLL showed radial director configuration of the LC. We had also observed that adsorption of Annexin V (an anionic protein) on (PLL-PSS) coated LC droplets could trigger the radial to bipolar configuration transition of LC. The change in the configuration was proposed to be caused due to the perturbation of

intermolecular interactions between PLL and the LC in the presence of Annexin V. In this context, PLL functionalized LC-aqueous interfaces can be of great utility as the director configuration of the LCs can allow the optical investigation of non specific protein adsorption at those interfaces. Literature survey reveals few reports wherein LC confined within planar interfaces has been employed for detection of bovine serum albumin (BSA) at aqueous interfaces.[32-35] Recently, adsorption of BSA on polyelectrolyte modified radial LC droplets was demonstrated to trigger the director configuration transitions to bipolar with a detection limit of 10 μg/mL of BSA.[21] However, the study lacks to offer the real-time monitoring of protein detection along with the higher observation time (30 min) limiting their application in biosensing. On the other hand, there is only one report concerning the detection of concanavalin A (ConA) utilizing LC-aqueous planar interface where specific binding of ConA with saccharide leads to the reorientation of LCs at the interface.[35] Although their LC system is capable of detecting ConA up to 0.01 μg/mL, the longer response time (~ 2 hours) and the ambiguous optical appearance of LCs at a lower concentration of ConA imply the difficulty in its quantification and detection at those interfaces. As far as cathepsin D (CathD) is concerned, no effort has been made yet to understand the adsorption of CathD on the orientational behaviour of decorated LC interfaces.

5.1.2 Objective

In this work, first, we aimed to study how PLL coated LC droplets can optically respond to the various anionic proteins (with varying electronegativities). Second, we sought to determine how their respective binding with PLL would affect the detection limits for those proteins at the interfaces. Therefore, we extend this tool to probe, in detail, the adsorption of different anionic proteins at PLL functionalized LC-aqueous interfaces by monitoring director configuration transitions in LC droplets. To elucidate the protein-induced director configuration transition in PLL modified LC droplets, three proteins: BSA, ConA, and CathD were studied which not only differ significantly in their respective electronegativities at physiological pH but also, span a broad range of functions in biological systems.[25-31] We have chosen these three proteins because of their inherent anionic nature and hypothesized that possible formation of electrostatic complexes between PLL and those proteins might lead to an ordering transition of the LC at aqueous-LC interfaces. In this regard, the physiochemical properties such as isoelectric point (pI) of these proteins are relevant to predict the net charge on them at a particular

pH (Table 5.1). For example, at physiological pH (7.4) all proteins are negatively charged with BSA being most anionic followed by ConA and CathD, respectively, as confirmed by zeta potential measurements (Table 5.1). Thus, the zeta potential values at pH 7.4 are in good agreement with their respective pIs.[25,30,31] As PLL being positively charged, we, therefore, sought to understand the fundamental insight into the formation of charged complexes in the presence of these anionic proteins and how they couple to the ordering of the LC at those interfaces. In addition, keeping in mind the wide ranges of functions these proteins serve, it becomes essential to understand the mechanism of protein adsorption at polymeric surfaces for various biomedical applications.

Table 5.1. Isoelectric points and zeta potential values of BSA, ConA, and CathD.

Protein	Isoelectric Point	Zeta Potential at pH 7.4 (mV)
BSA	4.5	-11.7 ± 1.5
ConA	5.0-5.5	-7.7 ± 0.7
CathD	6.8	-6.8 ± 0.9

Herein we observed that radial director configuration of PLL-LC could be triggered to bipolar/pre-radial due to the presence of these anionic proteins for up to 100 ng/mL of concentration and showed varying detection limits for the three studied proteins. The difference in detection limits and response times of these proteins can be attributed to the varying response of director configuration transition of LC due to the different electrostatic binding affinity of a particular protein with PLL which is largely determined by anionic charges present on that particular protein. Overall, the results would aid in understanding the interfacial electrostatic binding conduct of proteins at decorated LC-aqueous interfaces, which would lead to the development of principles for various interfacial and biosensing applications.

5.1.3. Results and Discussion

5.1.3.1 Addition of protein on PLL-LC emulsion

It should be noted that images in work were captured after several attempts to show the transition in the same droplets by using the following method. The protein solution was added very carefully from the side at an angle avoiding the contact of pipette tip with emulsion so as to not disturb the focused frame hastily (shown in Schematic 5.1 below).

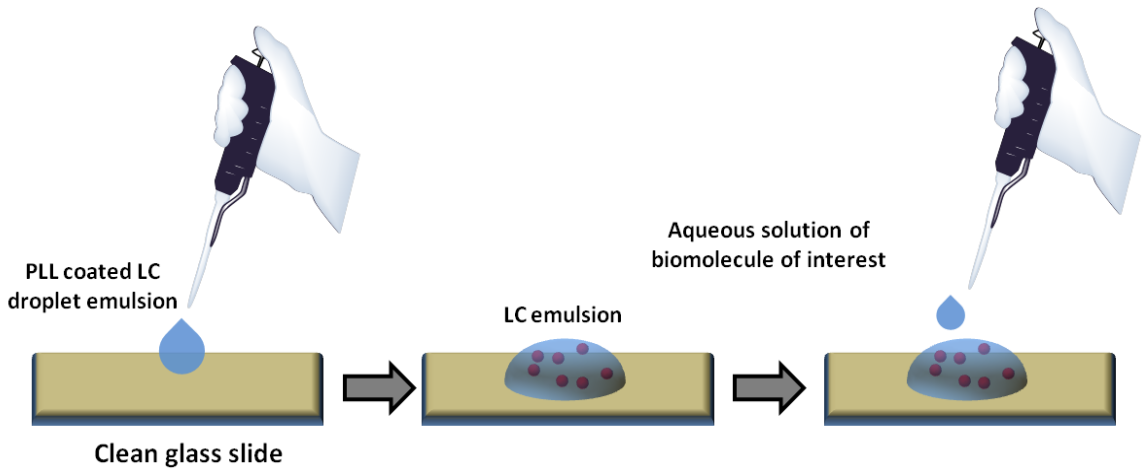

Schematic 5.1. Sequential addition of PLL-LC emulsion on a glass slide followed by addition of protein solution.

5.1.3.2 Optical imaging of PLL- LC droplets in the presence of BSA, ConA, and CathD

The adsorption of PLL on 5CB droplets stabilized the droplets in aqueous media and all the poly-dispersed PLL-5CB droplets exhibit radial director configuration under polarized microscope (POM) (Figure 5.1a) and show a point defect in centre when observed under bright field (BF), which is a result of homeotropic surface anchoring of 5CB at LC-aqueous interface.[23] It is important to note here that PLL-5CB droplets tend to settle down on the glass substrate and can have weaker non-covalent interactions with glass. However, this interaction does not affect the radial director configuration at least within the observation period (15 min). Next, we sought to observe the orientational response of PLL-5CB droplets towards the BSA at physiological pH 7.4. Interestingly, when PLL-5CB droplets were exposed to 1 mg/mL BSA solution (as shown in Figure 5.1b,c), the initial radial configuration of the droplets starts turning into bipolar/pre-radial in < 2s. However, it took approximately 5s for all the droplets to change their director configuration from radial to bipolar/pre-radial. The radial to bipolar/pre-radial configuration transition can mainly be attributed to the adsorption of BSA at LC droplets surface due to ionic interactions between PLL and BSA. Figure 5.1d illustrates the schematic corresponding to the change in the director profile of PLL-coated LC droplets due to the interaction of BSA with PLL. To elucidate the BSA triggered director configuration transition in PLL-5CB droplets, fluorescence microscopy was carried out using FITC labeled BSA. Epifluorescence microscopy image in Figure 5.2a shows the

presence of strong fluorescence on the surface of the 5CB droplets which confirms the preferential adsorption of FITC-BSA on PLL-5CB droplet while the corresponding BF image (Figure 5.2b) confirms the bipolar director configuration in the particular 5CB droplet.

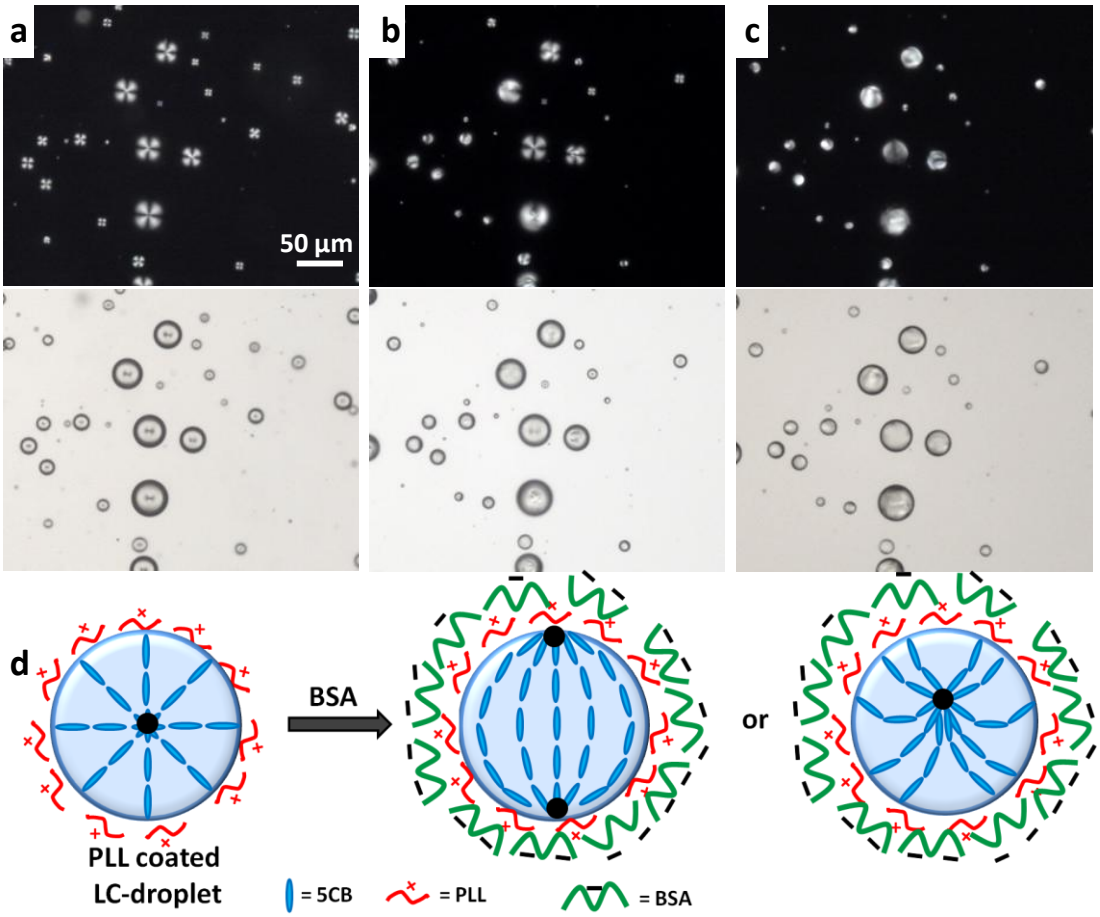

Figure 5.1. (a-c) Polarized optical (top) and corresponding bright-field (bottom) micrographs of PLL coated LC droplets: (a) suspended in TBS and after (b) 2s and (c) 5s of subsequent exposure to 1 mg/mL BSA. The LC droplets were in radial states (a) before but started radial to pre-radial transition in 2 s (b) while becoming bipolar in 5 s after addition of 1 mg/mL BSA (c). (d) Cartoon representation of director profile in 5CB droplets upon adsorption of BSA on PLL-5CB droplets.

In our previous report, we showed by PMIRRAS measurements that PLL could induce the homeotropic ordering in LC due to intermolecular hydrogen bonding between NH_3^+ of PLL's side chains and CN of 5CB LC.[23] In the present case, we decorated LC droplets with a single layer of PLL which imparts radial director configuration of LC and can be attributed to the intermolecular interactions between PLL and LC as suggested earlier.[23]

Here, we propose that the adsorption of anionic protein likely perturbs the intermolecular interactions between PLL and LC due to strong ionic interactions between protein and PLL and thus reorients the LCs in a bipolar/pre-radial configuration (as earlier shown in Figure 5.1d).

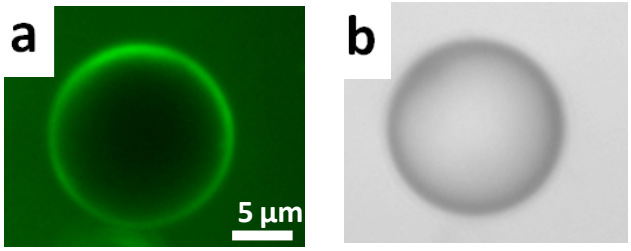

Figure 5.2. Epi-fluorescence (a) and corresponding bright-field (b) images of PLL-coated LC droplet suspended in 5mM TBS at pH 7.4 after incubation with 1 mg/mL FITC-labelled BSA. Green fluorescence at the droplet surface confirms the adsorption of BSA on PLL modified 5CB droplet and bright-field microscopy confirms the bipolar configuration of PLL-LC droplet in the presence of BSA.

Another plausible and least feasible mechanism could be that protein-PLL interaction can displace the PLL away from the droplets surface giving rise to the configurational transition. In that case, the LC droplets will be not stable and will coalesce within a few hours.[9] However, BSA adsorbed PLL-LC droplets have been visually found to be stable against coalescence in aqueous solutions for a minimum of 3 days (Figure 5.3), therefore minimizing the possibility of this mechanism.

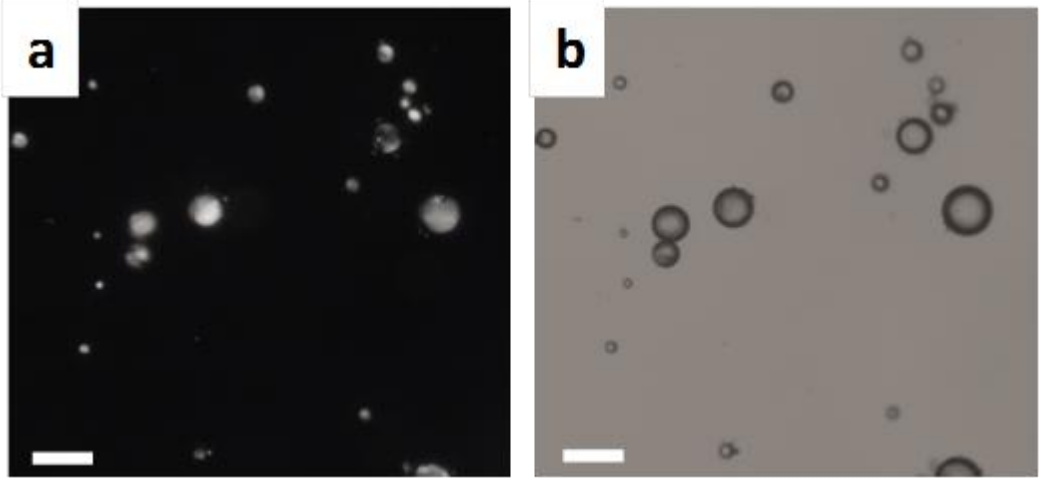

Figure 5.3. Polarized optical (a) and corresponding bright-field (b) micrographs of BSA modified PLL coated LC droplets after 3 days of the addition of 1 mg/mL BSA. Scale bar = 50 µm.

Next, we sought to observe the real-time examination of the PLL-5CB droplets while varying the concentration of BSA (C_{BSA}), keeping the volume of PLL-5CB droplets and observation time constant (~ 5µL and 15 min respectively). We find that upon decreasing the concentration of BSA, the number of PLL-5CB droplets showing director configuration transition from radial to bipolar/pre-radial also decreases. For eg., upon subsequent exposure to C_{BSA} of 40 µg/mL, all the PLL-5CB droplets changed their director configuration to bipolar/predial (Figure 5.4a,b) whereas when C_{BSA} was reduced to 20 and 10 µg/mL simultaneously, approximately 65 % and 40% of the PLL-LC droplets changed to bipolar/pre-radial (Figure 5.4c-f). In the presence of C_{BSA} ranging from 10 µg/mL to 1 µg/mL, a mixture of radial/pre-radial/bipolar exists with a decreasing number of pre-radial/bipolar droplets as the concentration decreases. Moreover, when PLL-5CB droplets were exposed to 0.5 µg/mL of BSA, PLL-5CB droplets did not show the director configuration transition from radial to bipolar or pre-radial within 15 min (Figure 5.4g,h).

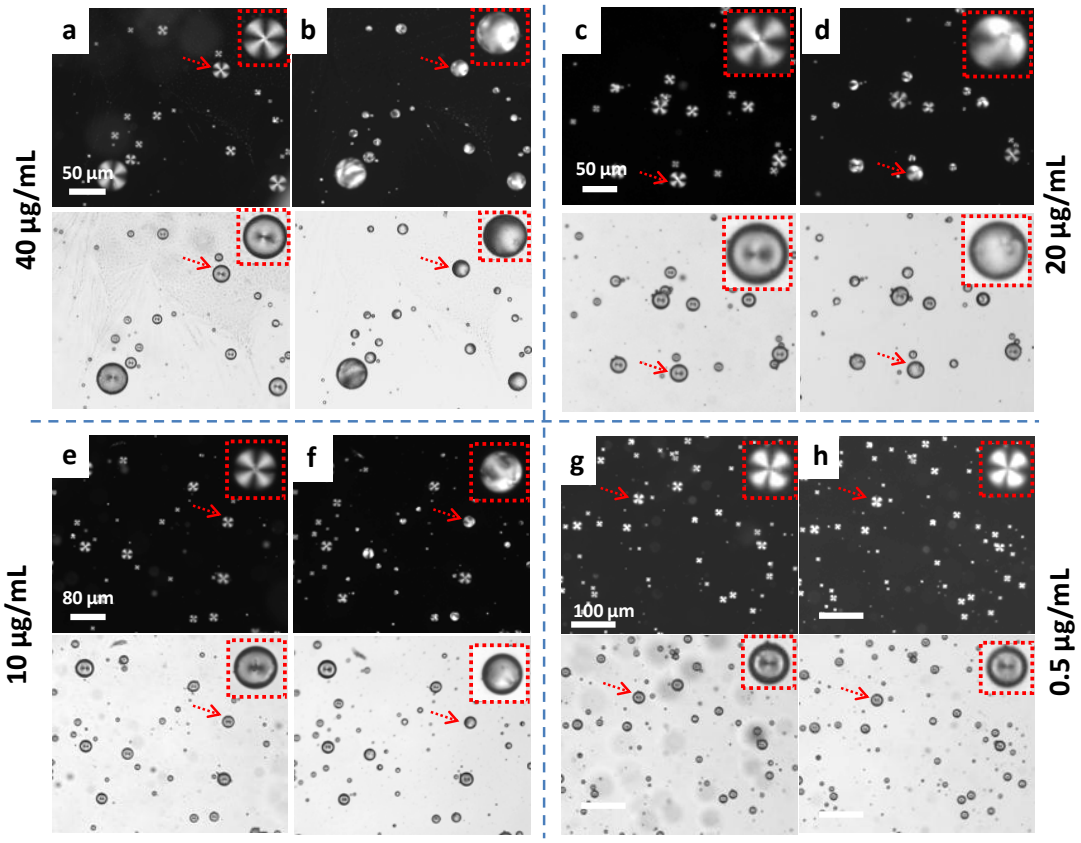

Figure 5.4. (a-h) Polarized optical (top) and corresponding bright-field micrographs (bottom) of PLL coated LC droplets before (a,c,e,g) and after 15 min of simultaneous addition of (b) 40 (d) 20 (f) 10 and (h) 0.5 µg/mL BSA on 5 µL PLL-coated LC droplets

at pH 7.4. The insets within (a-h) illustrate the higher magnification version of the arrow marked LC droplet, which represents the changed configuration in the particular droplet.

Next, we modulated the sensitivity of PLL-5CB droplets towards BSA by decreasing the volume of PLL-5CB emulsion from 5 µL to 1 µL (Figure 5.5). It was observed that only 20 µg/mL of BSA is required now to induce the configuration transition in all the PLL-5CB droplets. Similarly, 10, 1, and 0.1 µg/mL of BSA are able to change approximately 70 %, 55 %, and 35 % of the total LC droplets to pre-radial/bipolar, respectively. For a concentration of BSA ranging from 0.1 to 0.01 µg/mL of BSA, LC droplets could still change the director configuration to bipolar/pre-radial but in a very small fraction of the droplets which are difficult to report. Below 0.01 µg/mL BSA, all the PLL-LC droplets remain radial.

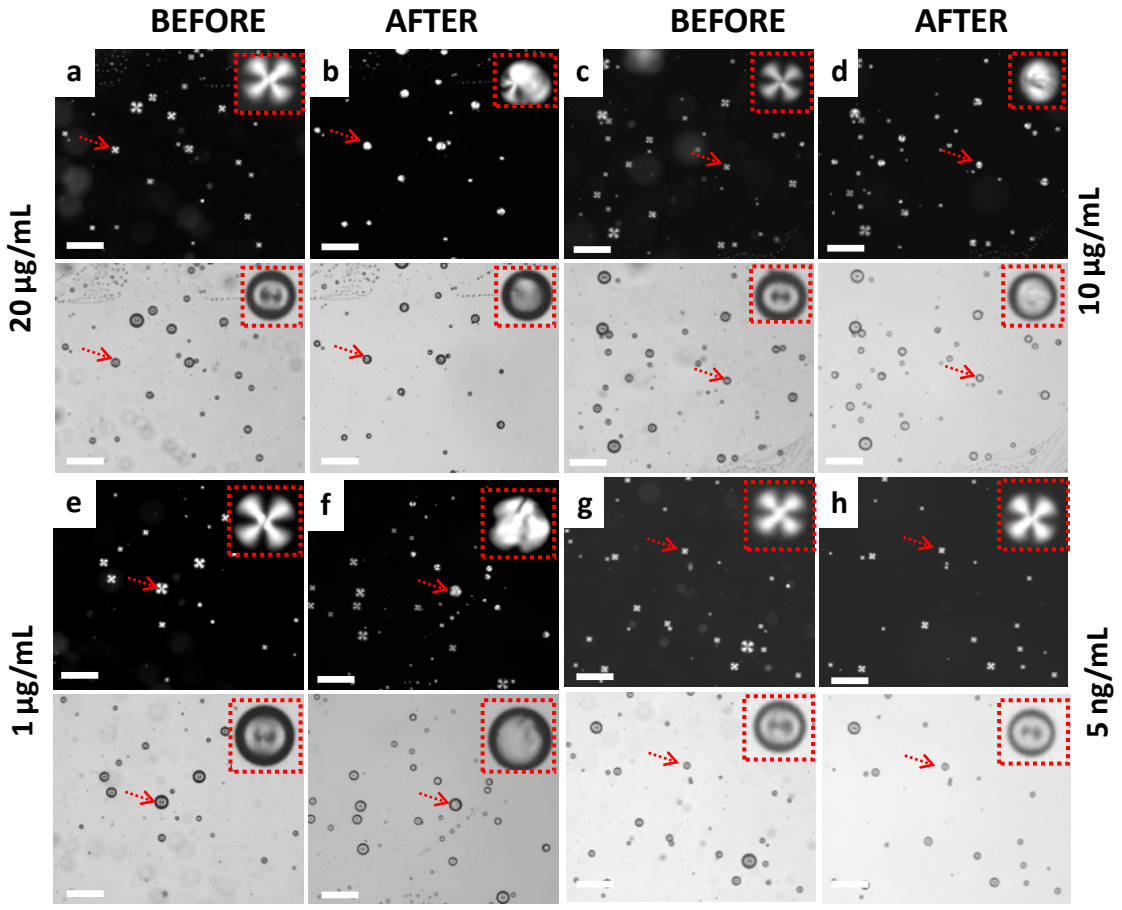

Figure 5.5. (a-h) Polarized optical (top) and corresponding bright-field (bottom) micrographs of PLL coated LC droplets before (a,c,e,g) and after 15 min in contact with (b) 20 (d) 10 (f)1 (h) 5 ng/mL BSA on 1 µL PLL-coated LC droplets at pH 7.4. The insets within (a-p) illustrate the higher magnified version of the arrow marked LC droplet. Scale bar = 100 µm.

Therefore, the sensitivity of PLL-5CB droplets for the detection of BSA was found extremely modulated by reducing the volume of the emulsion. The difference in the detection limit of BSA upon varying emulsion volume can be contributed to the two factors here. First is the reduced volume of PLL-LC emulsion which results in the lesser number of droplets, therefore the amount of BSA required to trigger the configurational transitions of PLL-5CB droplets is consequently decreased; second is that the reduced volume of emulsion itself decreases the dilution of BSA thus ultimately raises the available amount of BSA to adsorb at the PLL-LC droplets.

Motivated by the high sensitivity of director configuration in PLL-5CB droplets towards adsorption of BSA, next we sought to exploit the PLL-5CB droplets for detection of ConA. Since ConA possesses overall a negative charge at physiological pH, it can be predicted that ConA can also interact electrostatically with interfacial cationic PLL to trigger a configuration transition in LC droplets. As observed from POM and BF images in Figure 5.6a,b, the introduction of 1 mg/mL ConA on PLL-5CB droplets could also cause the LC director to move to the bipolar/pre-radial configuration in PLL-5CB droplets in ~ 5s. However, it takes~20 s after addition of 1mg/mL of Con A to induce the bipolar/pre-radial configuration in all the droplets which is slightly higher than the response time required by 1 mg/mL C_{BSA} (~5 s).

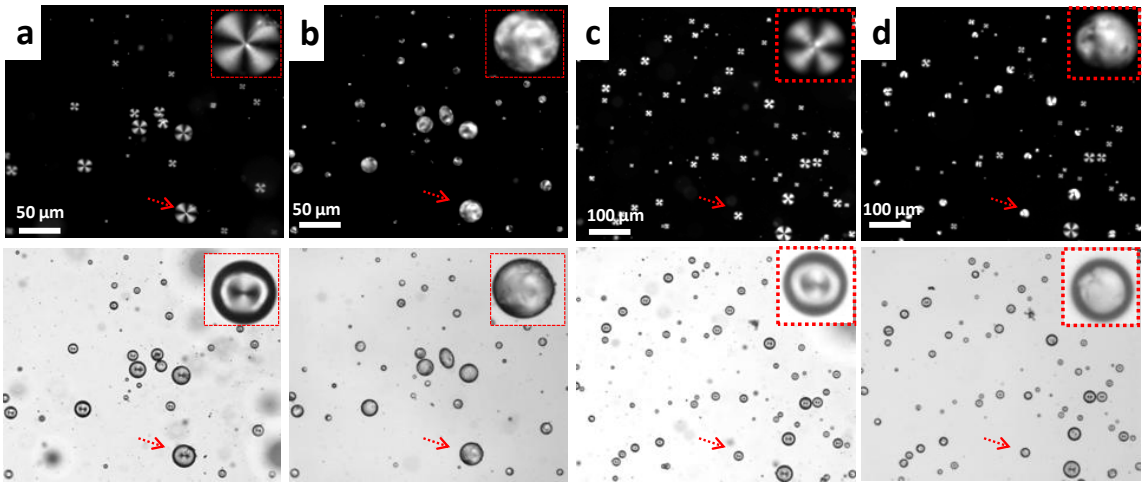

Figure 5.6. Polarized optical (top) and corresponding bright-field (bottom) micrographs images of PLL coated LC droplets in contact with: (a,c) 0, (b)1 mg/ml (d) 0.75 mg/ml Con A. The LC droplets were in radial states (a,c) before but transitioned to bipolar/pre-radial state (b,d) after exposure to Con A. The insets within (a-d) illustrate the higher

magnification version of the arrow marked LC droplet which represents the changed configuration in the particular droplet.

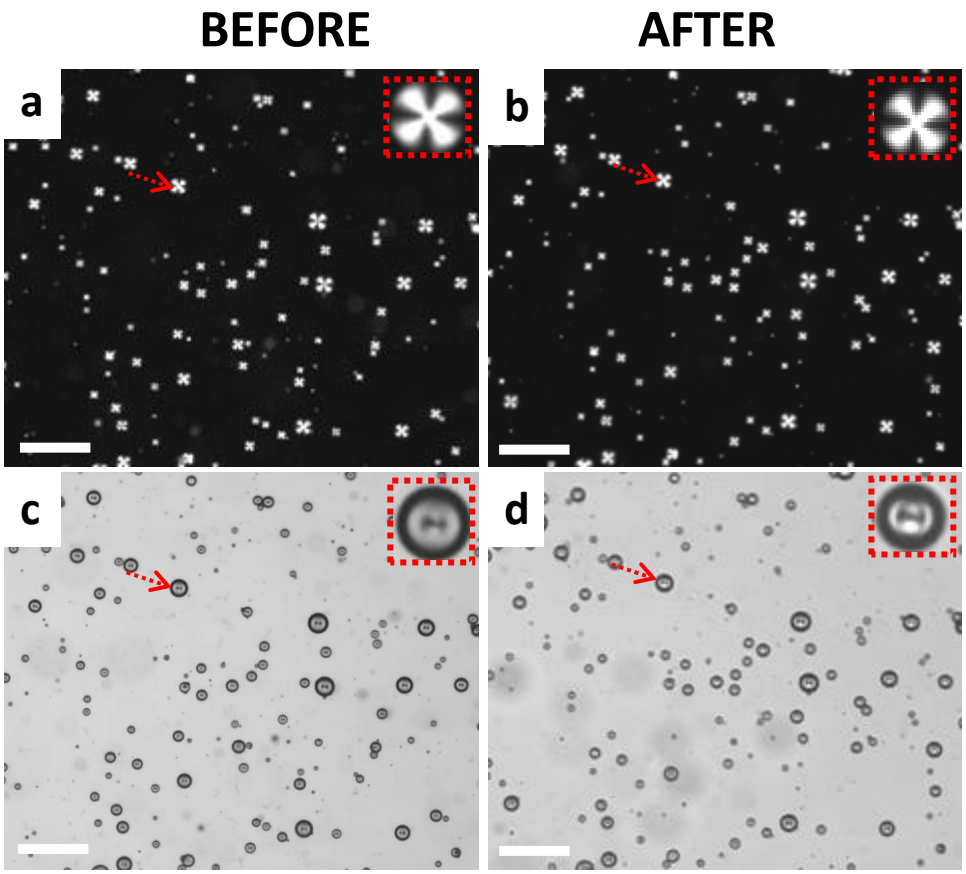

Figure 5.7. Polarized optical (a,b) and corresponding bright-field (c,d) micrographs of PLL coated LC droplets before (a,c) and 15 min after addition of (b,d) 0.05 mg/mL Con A on 5 µL of PLL-coated LC droplets at pH 7.4. The LC droplets were in radial states before and remained radial. The insets within (a-d) illustrate the higher magnification version of the arrow marked LC droplet. Scale bar = 100 µm.

Next, we monitored the director configuration of PLL-5CB droplets upon decreasing the concentration of ConA while keeping the emulsion volume 5 µL. The number of LC droplets exhibiting director configuration transition to bipolar/pre-radial droplets also decreases with a decrease in C_{ConA} and radial, bipolar/pre-radial droplets coexist. For example, in the presence of 0.75 mg/mL ConA, approximately 70% of the LC droplets showed the director configuration transition to pre-radial or bipolar while remaining droplets retained radial (Figure 5.6c,d). Similarly, 0.5 mg/mL ConA could change the director configuration in only 45-50 % of the droplets. For the concentration of ConA ranging from 0.5 mg/mL to 0.1 mg/mL, only a small fraction of droplets (40 to 20 %)

showed bipolar/pre-radial configuration. Below 0.1 mg/mL of ConA, the PLL-LC droplets remained radial (Figure 5.7). This configuration transition in the presence of ConA can also be attributed to the non-specific adsorption of ConA on PLL-LC droplets via ionic interactions, which is also evident through the fluorescence microscopy study (Figure 5.8).

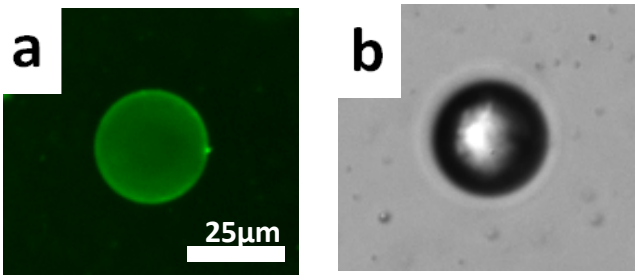

Figure 5.8. Epifluorescence (a) and corresponding bright-field (b) images of PLL-coated 5CB droplet suspended in 5mM Tris buffer at pH 7.4 after incubation with 1 mg/mL FITC-labelled ConA. Green fluorescence at the droplet surface confirms the adsorption of ConA on PLL modified 5CB droplet.

The detection limit of PLL-LC droplets towards ConA was manipulated by decreasing volume of PLL-LC emulsion from 5 to 1 µL. It was realized that PLL-5CB droplets now can respond to lesser C_{ConA} via director configurational transitions (Figure 5. 9). Now, 0.5 mg/mL of ConA could induce the transition in more than 95 % of the total LC droplets. Upon varying the concentration of ConA to 0.1 mg/mL and 0.05 mg/mL could trigger the director configuration transitions to bipolar/pre-radial in approximately 70 and 55 % of the droplets, respectively. Up to 0.01 mg/mL, there was some small fraction of bipolar/pre-radial droplets observed; however, it becomes difficult to analyze the droplets with less transition percentage. Moreover, the PLL-5CB droplets could not respond to 0.5 µg/mL of ConA and remained radial even after 15 minutes of addition. Overall, it is evident that when emulsion volume is 5 µL, at least 0.500 mg/mL of ConA was necessary to trigger the radial to the bipolar/pre-radial configuration in approximately 50 % of PLL-5CB droplets while this value reduces to 0.05 mg/mL when emulsion volume is reduced to 1 µL. These results show that similar to BSA, the detection limit of ConA can also be amended by varying the volume of LC emulsion.

Inspired the exceptional ability of PLL modified LC droplets to report the non-specific binding to anionic proteins BSA and ConA, we sought to explore the possible interfacial interactions between PLL and CathD via orientational transitions of PLL-5CB droplets.

Zeta potential measurements reveal that CathD carries overall a negative charge at pH 7.4, yet small as compared to the other two studied proteins.

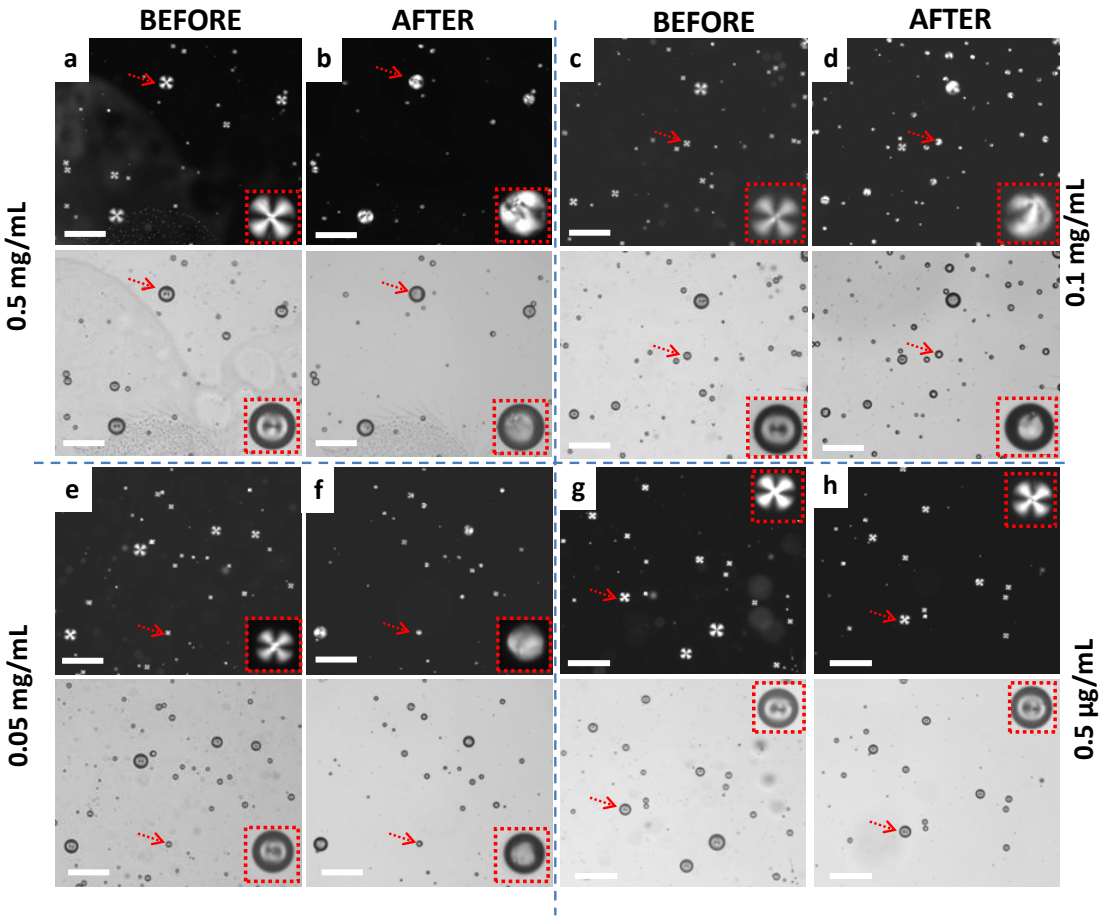

Figure 5.9. (a-h) Polarized optical (top) and corresponding bright-field (bottom) micrographs of PLL coated LC droplets before (a,c,e,g) and after 15 min of subsequent addition of b) 0.5 mg/mL d) 0.1 mg/mL f) 0.05 mg/mL h) 0.5 µg/mL Con A on 1 µL PLL-coated LC droplets at pH 7.4 . The LC droplets were in radial states before but transitioned to the bipolar state after addition of ConA. The insets within (a-h) illustrate the higher magnification version of the arrow marked LC droplets. Scale bar = 100 µm.

Figure 5.10 shows the POM and corresponding BF images of PLL-5CB emulsion (5µL) after exposure to different concentration of CathD. Interestingly, CathD also induces radial to bipolar/pre-radial configuration transition of PLL-5CB droplets; however it takes 10s to initiate the configuration transition and requires a higher concentration of CathD (of 1.5 mg/mL) as compared to BSA and ConA to induce the configuration transition in all droplets. Careful observations reveal that it required at least 1.2 mg/mL of CathD to induce radial to bipolar/pre-radial transition in 100 % of the droplets. Further decreasing

the C_{CathD} to 1 mg/mL and 0.5 mg/mL leads to the change in LC droplets from radial to bipolar in approximately only 90 % and 50 % of the total LC droplets, respectively. Upon reducing the volume of LC emulsion to 1 μL, the detection limit of CathD was found to be reduced to 0.25 mg/mL with a transition in approximately 50 % of the LC droplets.

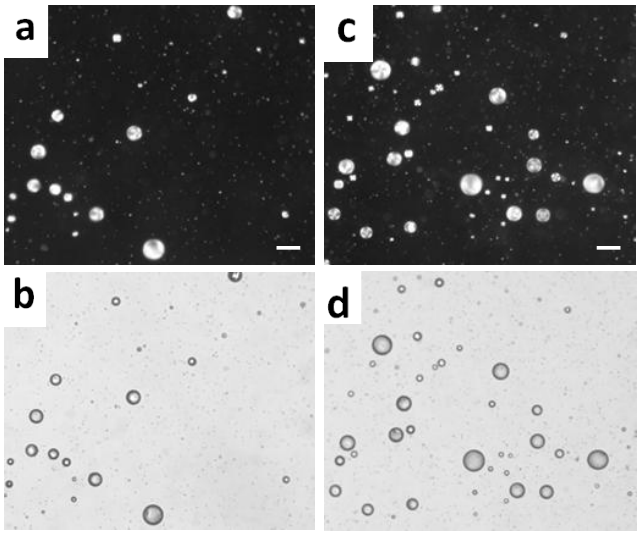

Figure 5.10. Polarized optical images (a,c) and corresponding bright-field images (b,d) of PLL-5CB droplets in contact with different concentration of CathD: (a,b) 1.5 and (c,d) 1 mg/mL (LC emulsion = 5 μL). Adsorption of CathD on PLL-LC droplets can also result in configuration transition of PLL-5CB droplets from radial to bipolar/pre-radial. Scale bar = 50 μm.

5.1.3.3 Zeta potential of PLL-LC droplets

Since orientational transitions in PLL-5CB droplets are prominently taking place through non-specific binding of anionic proteins and interfacial PLL residues, we carried out a series of experiments to realize the zeta potential measurements of PLL-5CB droplets and protein adsorbed PLL-5CB droplets (Figure 5.11). It is not surprising that zeta potential of PLL-5CB droplets is positive (+42 mV), mainly due to the adsorbed cationic lysine units of PLL at LC-aqueous interface. However, upon adsorption of BSA, ConA or CathD at PLL-5CB droplets, the zeta potential values become negative and drop to -17.5, -9.4 and -3.2 mV respectively confirming the adsorption of anionic proteins over cationic PLL-5CB droplets. We propose that more the anionic charge density offered by protein elevated the possibility of ionic interactions between protein and cationic PLL residues and faster and significant the response of LC director configuration in LC droplets. We corroborated the trend between electronegativities of proteins and response of PLL-LC

droplets by using other protein: human hemoglobin (pI is 6.87) possess overall negative charge at pH 7.4. It was found that 250 μg/mL of hemoglobin could trigger ordering transition in approximately 40-50 % of the total PLL-LC droplets (volume of emulsion = 1μL) while droplets remain radial when 100 μg/mL hemoglobin was added (Figure 5.12). The zeta potential of hemoglobin coated PLL-LC droplets was -2.6 mV. The zeta potential value and the percentage transitions for hemoglobin are in good accordance with that of CathD.

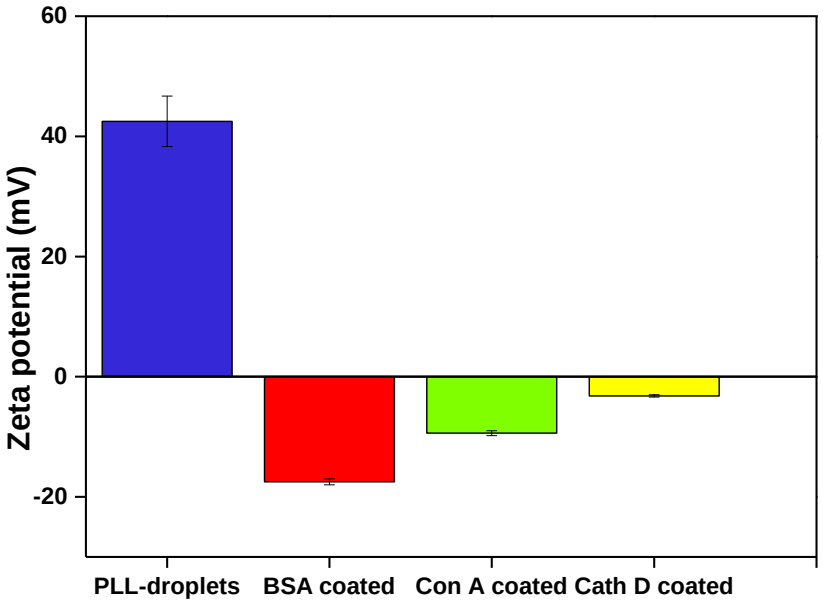

Figure 5.11. Zeta potential values of 5CB-droplets: PLL coated 5CB droplets, 1 mg/mL BSA, ConA and CathD adsorbed PLL-5CB droplets.

5.1.3.4. Selectivity of PLL-LC droplets for anionic proteins

Having established that PLL modified LC droplets offers a stimuli-responsive interface that allows the adsorption of anionic proteins via non-specific binding to PLL, we sought to realize the relevance of ionic interactions between the two binding moieties and thus proposed that a cationic protein at pH 7.4 would not trigger the director configuration transition in PLL-5CB. As a proof of concept, we chose lysozyme, a single chain polypeptide of 129 amino acids, as its isoelectric point is quite high (~11.3) and therefore lysozyme possesses a net positive charge at physiological pH.[37] Figure 5.13 shows the POM images of PLL-5CB droplets before and after exposure to 1 mg/mL lysozyme. The presence of lysozyme did not affect the director configuration of LC droplets suggesting that cationic PLL restricts the adsorption of cationic lysozyme at PLL-5CB droplets

surface and thus retains the radial configuration in PLL-5CB droplets. Although additional non-covalent interactions between proteins and PLL residues cannot be ruled out, it is evident that ordering of LC droplets is largely influenced by attractive ionic interactions between anionic protein and cationic PLL. Therefore, we note that director configuration of PLL-5CB droplets is triggered selectively by the adsorption of anionic proteins and hence can be exploited to as an optical, label-free, fast and sensitive platform for the selective detection of anionic proteins over cationic proteins at physiological pH.

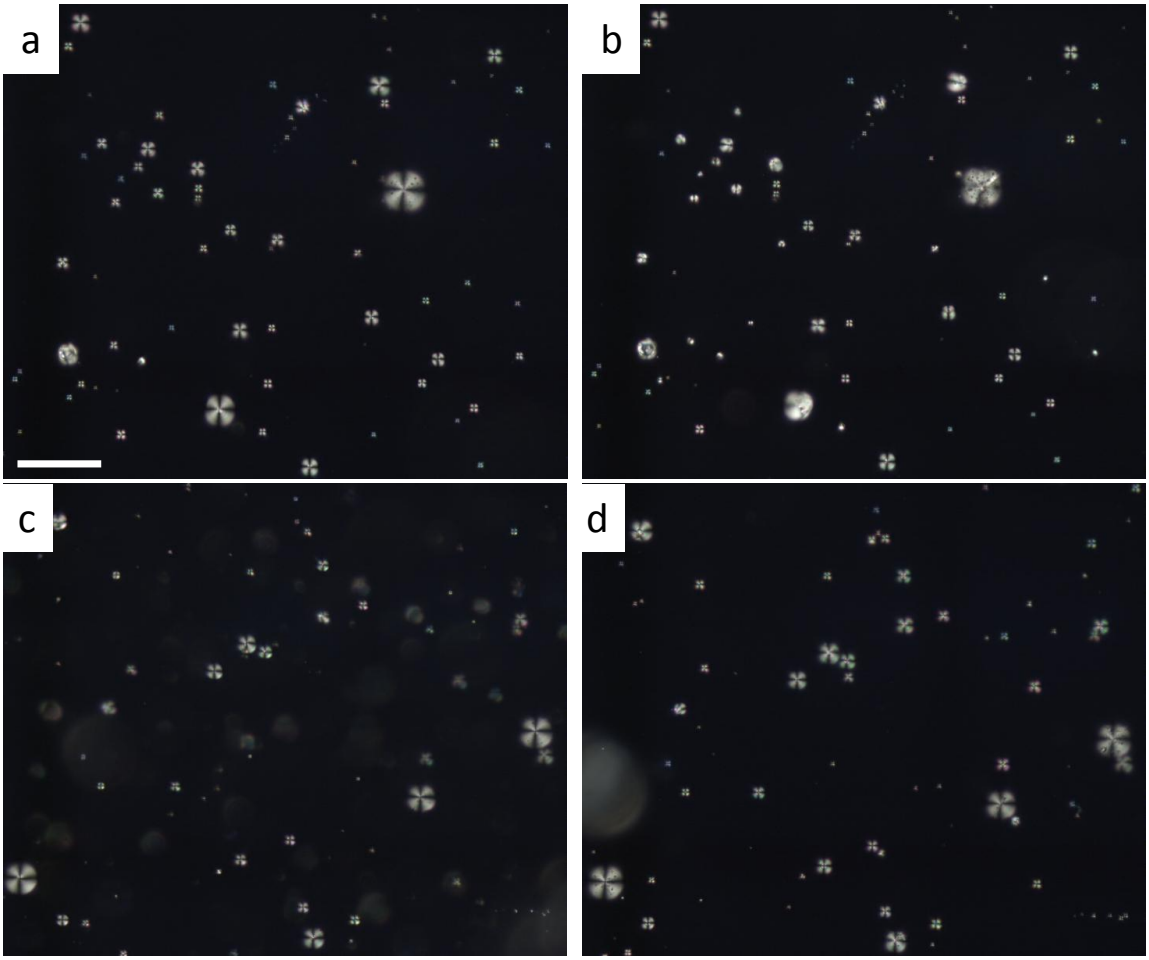

Figure 5.12. Polarized optical microscopy images of PLL droplets at 0 min (a,c) and 10 min (b,d) after addition of 250 μg/mL (b) and 100 μg/mL (d) of aqueous solution of hemoglobin. Scale bar = 100 μm.

From the above results, it is clear that the ordering transition in PLL-LC droplets is not only predominantly triggered by negatively charged proteins only but also differ significantly for the three studied proteins in terms of their low detection limits and response time. Such a difference in sensitivity of LC droplets towards various proteins

could be attributed to the anionic density possessed by a protein molecule in aqueous solution as suggested from zeta potential measurements. Table 5.2 summarizes various sensitivity aspects associated with the PLL-5CB droplets for the detection of BSA, ConA and CathD.

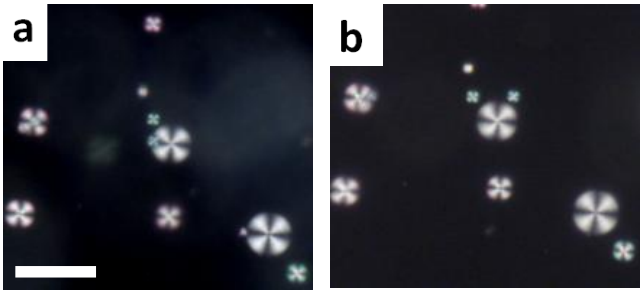

Figure 5.13. Polarized optical images of PLL coated LC droplets: (a) suspended in tris buffer and (b) in contact with 1 mg/mL lysozyme. PLL-LC droplets retained the radial configuration after addition of lysozyme suggesting the absence of adsorption of the cationic protein at the cationic PLL-LC droplet's surface. Scale bar = 50 μm.

Table 5.2. Sensitivity of PLL-5CB droplets towards BSA, ConA and CathD

Protein	Zeta Potential[a]	Detection Limit[b]		Response time[c] (s)	Response time[d] (s)
		5 μL emulsion	1 μL emulsion		
BSA	-17.5 ± 0.5	10	0.1	2	5
ConA	-9.4 ± 0.4	500	50	5	20
CathD	-3.2 ± 0.2	500	250	10	30

[a] of protein adsorbed PLL-LC droplets (mV); [b] of protein for > 35 % transition (μg/mL); [c] of LC to initiate the transition (radial to bipolar/pre-radial) ; [d] of LC for 100% transition (radial to pre-radial/bipolar) (1 mg/mL protein)

5.1.4 Conclusions

We have demonstrated the implication of director configurations of LC droplets to report the real-time adsorption of anionic proteins such as BSA in few seconds, primarily driven by electrostatic interactions between protein and cationic PLL, as confirmed by POM, bright field and fluorescence microscopy. Additionally, it is demonstrated that director configuration in PLL-LC droplets can respond to ConA, a lectin protein, and CathD, a tumor marker, within 1 min of response time and these proteins can be quantified with detection limits of 0.1, 50 and 250 μg/mL for BSA, ConA, and CathD respectively.

Overall, we found that sensitivity and response time of PLL-5CB droplets differ for the three proteins and follow the similar order as the anionic charge density possessed by these proteins after adsorption on PLL-LC droplets as confirmed by zeta potential measurements. Director configuration transitions in PLL-5CB droplets are found more fast and responsive to BSA, the most anionic protein among three, followed by ConA and CathD (slightly lesser anionic than BSA). Overall, PLL-5CB droplets provide a responsive LC interface that enables a fast, label-free, quantitative platform to optically and selectively detect real-time adsorption of negatively charged proteins and hence can find promising application in biosensing and interfacial applications.

5.1.5 Experimental section

5.1.5.1 Materials

Bovine serum albumin (BSA), concanavalin A from Canavalia ensiformis (Jack bean) (Con A), cathepsin D from bovine spleen (CathD), lysozyme from chicken egg white (Lyz), human haemoglobin, fluorescein conjugated BSA (FITC-BSA), FITC labelled ConA (FITC-ConA), poly-L-lysine (PLL) solution 0.1 % (w/v) in H_2O, 4-Cyano-4-pentylbiphenyl (5CB LC) and 5mM tris buffered saline (TBS) (pH 7.4) was obtained from Sigma-Aldrich (St. Louis,MO). Deionization of a distilled water (DI water) source was performed using a Milli-Q-system (Millipore, bedford, MA). Fisher's Finest Premium grade glass microscopic slides were obtained from Fischer Scientific (Pittsburgh, PA).

5.1.5.2 Preparation of PLL modified LC droplets

Sumyra et al. reported the preparation of PLL modified LC droplets using polyelectrolyte multilayer technique.[23] Here, we have prepared the LC droplets with single coating layer of PLL using the below described method. 10 μL of 5CB in 1mL DI water was vortexed for 10 s and sonicated for 10 min. The resultant white emulsion was centrifuged at 5000 rpm for 5 min and the supernatant was replaced by 1 mg/mL PLL aqueous solution. The PLL-5CB droplets were kept for 15 min at room temperature for the adsorption of PLL on the 5CB droplets. The PLL-5CB droplets were then washed with DI water through centrifugation in order to remove the excess PLL and then the PLL-5CB droplets were re-suspended in TBS for further experiments. Size of the polydispersed PLL coated 5CB droplets ranges from 5 μm to 40 μm as observed by polarized optical microscopy (POM).

To estimate the number of droplets in the emulsion, 1 µL of the PLL-5CB droplet solution was placed on a clean glass slide and multiple POM images were captured to illustrate the large sample area. From the POM images, the total number of droplets was counted to be ~ 2 x 10^3 droplets per µL. Aqueous solutions of BSA, ConA, CathD and Lyz were prepared in TBS. In a typical experiment, a certain volume of emulsion was placed on the glass slide and 5 µl of the protein solution of required concentration was added on that. The droplets were imaged after certain time under polarized optical and bright field microscope.

5.1.5.3 Optical characterization of PLL-LC droplets

The orientational ordering of the LC was determined using a Zeiss polarizing microscope Scope. A1 with cross polars (X200 and X1000). All the images were captured using a AxioCam Camera. It should be noted that images in this work were captured after several attempts to show the transition in same droplets by using the following method. The protein solution was added very carefully from the side at an angle avoiding the contact of pipette tip with emulsion so as to not disturb the focused frame hastily. Also the subsequent protein/water addition on focused PLL-LC droplets causes more disturbances on the upper droplets as compared to the bottom droplets. The small droplets (1-5 µm) (even if at the bottom) were found more dislocated; however the larger droplets were found very stable and more or less at the same location after addition of proteins.

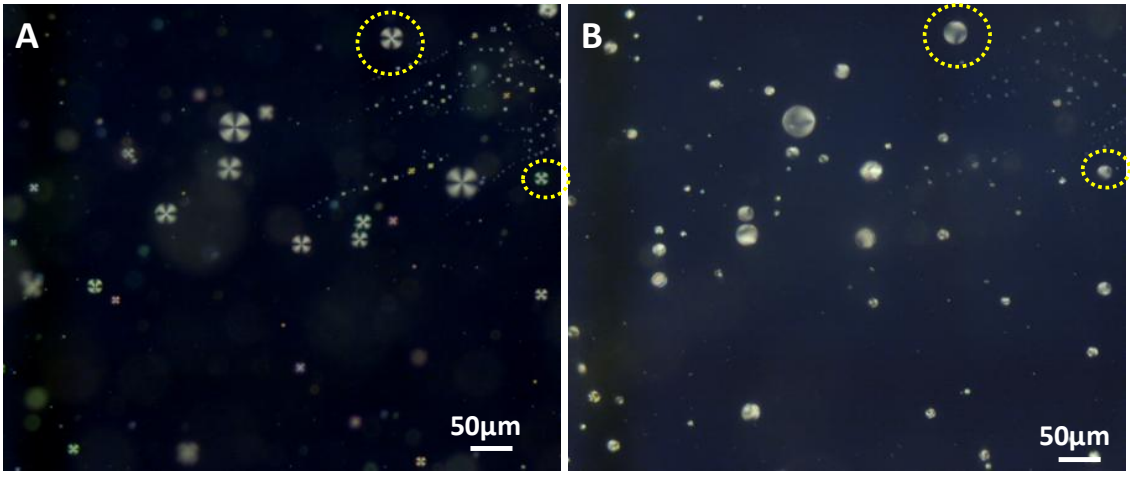

Figure 5.14. POM images of PLL-LC droplets before (A) and just after (B) abrupt addition of 2 mg/mL BSA. Few droplets are on the same position (indicated by circles), however, majority of the droplets are moved to a different location and also out of the focused frame. The droplets cannot be considered adsorbed on surfaces.

If the protein solution is added abruptly (Figure 5.14), the majority of LC droplets abruptly moves out of the frame and settles at a different place. Therefore, adsorption of LC droplets on the glass surface can be ruled out.

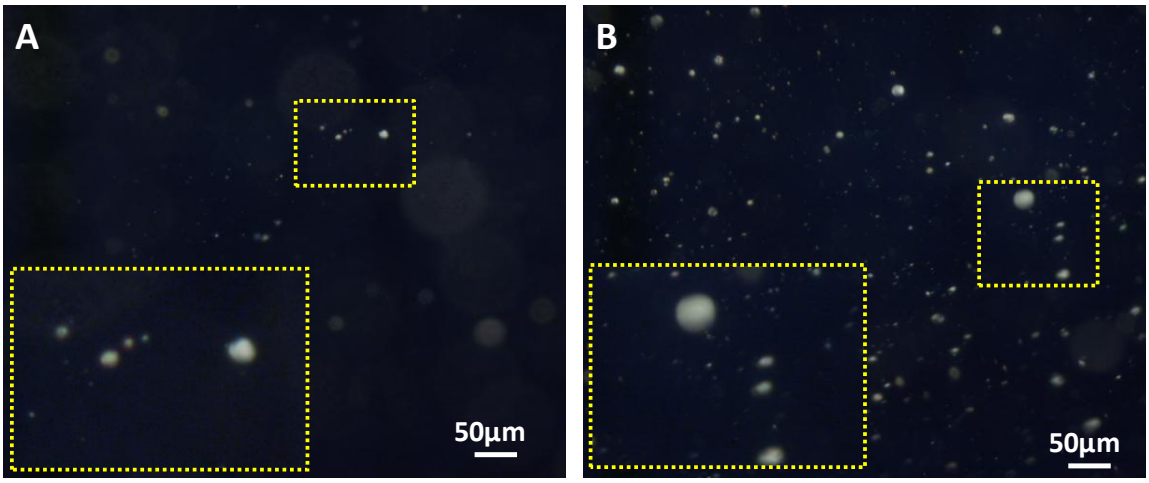

Figure 5.15. POM images of PLL-LC droplets after incubating with 2 mg/mL BSA: (A) mobile droplets in the upper plane and (B) less mobile droplets in bottom plane showing bipolar configuration. Insets show the magnified yellow marked area.

Next, we demonstrate that protein adsorbed PLL-LC droplets show bipolar configuration regardless of their location (diffusing or on the surface) on the glass slide. PLL-LC droplets (50 µL) were incubated with 2 mg/mL BSA (50 µL) for 15 min in a small tube. Upon transferring on a glass slide, again, the droplets were found in different planes (Figure 5.15). However, the configuration was bipolar in the diffusing droplets as well as in droplets on the bottom plane also confirming that the radial to bipolar transition is due to the adsorption of protein on PLL-LC droplets and not due to glass surface.

5.1.5.4 Epifluorescence imaging of PLL-LC droplets

Fluorescence imaging was performed with a Zeiss (Scope. A1) fluorescence microscope. The samples were viewed using a fluorescence filter cube with a 460 nm excitation filter and a 534 nm emission filter. Images were obtained with an AxioCam camera.

5.1.5.5 Zeta potential measurements

Zeta potential measurements of the PLL coated 5CB droplets were carried out using Zetasizer Nano ZS90 (Malvern Instruments Inc.) at room temperature under a cell-driven voltage of 30 V, in which 40 µL of PLL-5CB droplets were diluted with TBS to make

total 800 μL solution before adding into the zeta potential cuvets and the average of 5 scans was taken for each measurement. For experiments with proteins, 10 μL of 1 mg/mL BSA or Con A or CathD was added to the 40 μL droplets solution and incubated for 15 minutes before diluting to 800 μL with TBS.

5.2 Part B: Label-free Imaging of Fibronectin Adsorption at Poly-L-lysine Decorated Liquid Crystal Droplets

5.2.1 Introduction

Liquid crystal (LC) droplets suspended in aqueous media belong to a new class of facile functional systems that can perform a broad array of biosensing and interfacial applications.[7-24,38] The detection principle behind LC-based sensors is based on the change in the director configurations of the LC molecules inside the droplets that can be easily perturbed by biomolecular events occurring at the interface. The anisotropic optical property of nematic LC allows the label-free characterization of distinct director configurations of the LC by the naked eye under polarized light. Thus, LC-based sensing technology eradicates the requirement of costly and complicated detection systems for signal transduction. Previously, LC micro-droplets have been applied as an optical sensing tool for developing immunoassays[22], detecting bacterial endotoxin at pg/mL concentration[15], bacteria and viruses[10], cells[20,23], DNA[24], proteins[19,38] and many more. Recently, we found that the adsorption of poly-L-lysine (PLL, cationic peptide) can trigger a homeotropic ordering of LCs imparting the dark optical appearances of the LC under the crossed polars at LC-aqueous interface.[23] Moreover, the PLL decorated LC droplets demonstrated potential applications in the detection of cells[23], DNA[24] and anionic proteins[38] due to a transition in LC director triggered by interfacial intermolecular interactions between PLL and the anionic biomolecules. In this study, we extend this tool to understand the adsorption and conformational behavior of a protein, fibronectin (FibN), at PLL coated LC droplets to provide detailed insights about the intermolecular interactions that influence the ordering of the LC occurring at the interface of the LC droplets.

FibN is a multifunctional glycoprotein that exists ubiquitously as two isoforms in body fluids as well as in the extracellular matrix (ECM) and connective tissues.[39] In blood plasma, it circulates as a soluble and compact form in significant quantities (250-400 μg/ml). However, FibN plasma concentration deviates greatly from the normal range in various diseased states such as disseminated intravascular coagulation (DIC), primary biliary cirrhosis, pancreatic carcinoma and cryofibrinogenaemia.[40] On the other hand, it is assembled in an insoluble bioactive fibrillar state in the ECM where it is known to mediate an assortment of biological functions including tissue repair, cellular migration during wound healing, inflammation, embryogenesis, and tumorigenesis.[41,42] Since

several pathological conditions involve altered conformational states of FibN, it becomes very important to understand its adsorption properties at chemically modified surfaces and interfaces in light of structural changes and aggregation of the protein.[43,44] Fibrillar assembly formation of FibN can be induced via several cell-free routes using force mediated assembly by imparting mechanical tension or shear forces, chemical agents (denaturants, oxidizing agents, reducing agents, cationic or anionic compounds), peptidic FibN fragments, and surface-initiated assembly.[45,46]

5.2.2 Objective

Owing to the enormous biological importance of FibN, understanding of conformations of FibN molecules upon adsorption on polymeric surfaces is of great interest. Therefore, the aim of the study reported in this work is mainly two-fold. First, we visually sought to investigate the ability of PLL-LC droplets for label-free imaging of FibN in aqueous phase by exploiting the change in the director configurations of the LC. Second, we sought to provide additional insight into the structural changes and morphology of FibN molecules in contact with PLL coated aqueous-LC interfaces using circular dichroism, fluorescence studies and atomic force microscopy.

5.2.3 Results and Discussion

5.2.3.1 Adsorption of FibN at multilayer modified PLL-LC droplets

Our initial experiments were carried out to determine the orientational behaviour of PLL coated LC droplets in the vicinity of FibN. As shown in polarized optical micrographs (POM) and bright-field (BF) images (Figure 5.16a,b), PLL-LC droplets when dispersed in water (pH 7.0-7.2), exhibited radial director configuration of LC. Radial configuration of LC droplets is defined by the homeotropic orientation of LC molecules at the LC-aqueous interface giving rise to a topological defect at the center (Figure 5.16b). PLL chains can adsorb at LC-aqueous interface mainly through H-bonding between lysine residues and the C≡N group of 5CB (4-Cyano-4'-pentylbiphenyl) LC leading to homeotropic/radial orientation of LC inside droplets as reported earlier.[23,24,38] Interestingly, within 1 min of exposure to the aqueous solution of FibN (1 mg/mL), the central topological defect in 5CB droplets moved towards the poles of the droplets to adopt a so-called bipolar or pre-radial LC director configuration (Figure 5.16c,d). All the LC droplets changed to

bipolar/pre-radial in 10 min as can be seen under POM and BF with the disappearance of defect from the center (Figure 5.16).

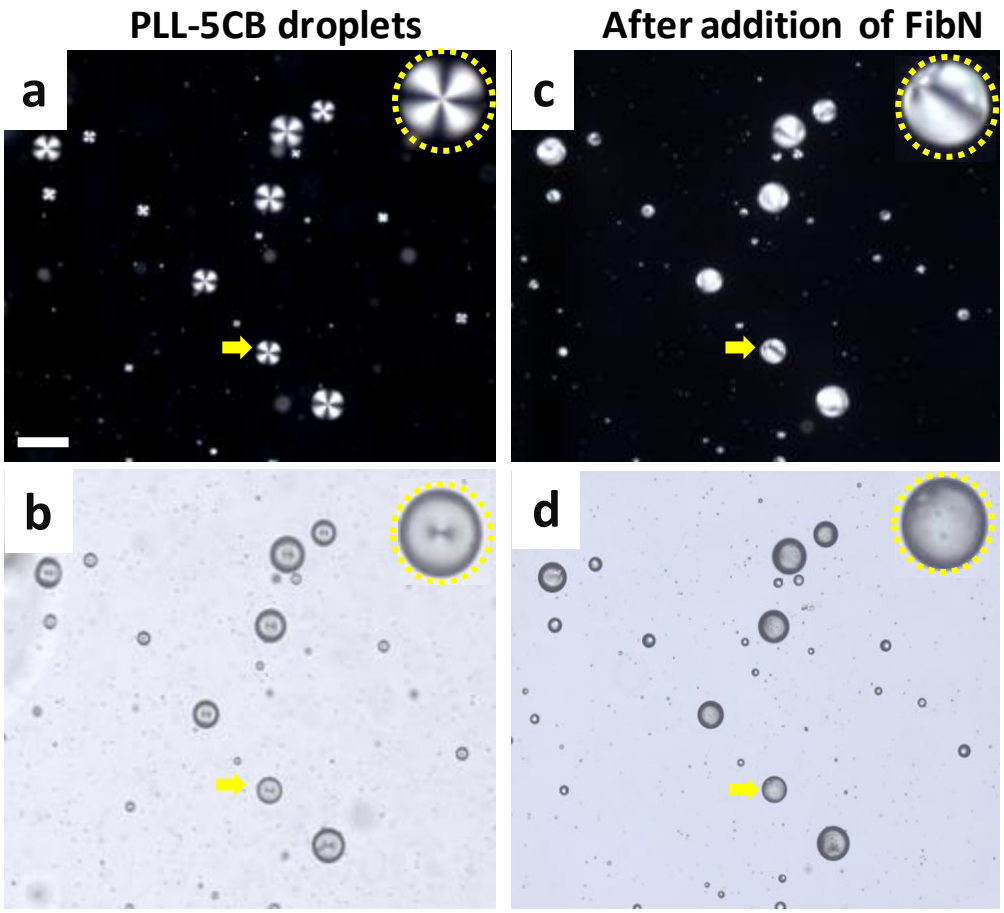

Figure 5.16. Polarized optical micrographs (a,c) and corresponding bright-field images (b,d) of PLL-LC droplets before (a,b) and after (c,d) 10 min of subsequent addition of 1 mg/mL FibN solution, respectively. Inset at the right of the image represents the magnified version of LC droplet indicated by yellow arrows. PLL-LC droplets adopt radial configuration (evident with a central topological defect in the bright-field) which changes to bipolar/pre-radial configuration (disappearance of the central defect) in the presence of FibN. Scale bar = 50 μm.

This observation is consistent with our recent report in which we showed that adsorption of anionic proteins (selectively over cationic proteins) could trigger an ordering transition in PLL-LC droplets.[38] At pH 7.0-7.2 (pH of aqueous media used), FibN acquires an overall anionic charge and hence, the radial-to-bipolar configuration transition of the LC droplets may be due to the non-specific adsorption of FibN molecules at PLL-LC-aqueous interface. This is driven by attractive ionic interactions between interfacial

cationic PLL residues and FibN. In order to confirm adsorption of FibN molecules, zeta potential measurements were carried out on PLL-LC droplets (Figure 5.17). The positive zeta potential value of PLL-LC droplets, which is approximately + 40 mV, signifies the coating of cationic PLL residues on the surface of LC droplets.[23,24,38] On the other hand, it drops to negative (– 12 mV) in case of FibN coated PLL-LC droplets which significantly confirms the adsorption of anionic FibN molecules at PLL-LC droplets.

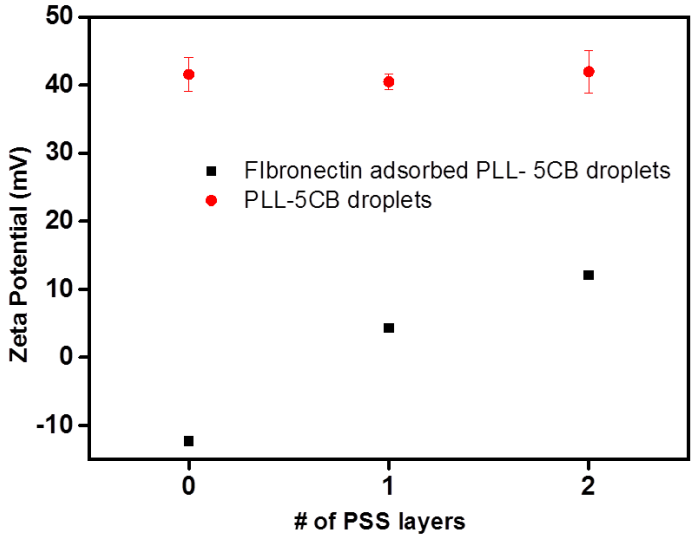

Figure 5.17. Zeta potential measurements of multilayered PLL-LC droplets before and after incubation with 1 mg/mL FibN. A drop in magnitude of zeta potential of LC droplets suggests the adsorption of anionic FibN at LC-aqueous interface.

As a deviation from the normal concentration of FibN in blood serum is associated with several diseases[40], our next goal was to investigate the sensitivity of the LC droplets towards various concentrations of FibN. Figure 5.18 illustrates POM images of PLL 5CB droplets after subsequent exposure to different concentrations of FibN solutions keeping the exposure time (10 min) and LC emulsion volume (1 µL) constant. It was found that up to 300 µg/mL of FibN led to configuration transition in all the LC droplets. However, a subsequent decrease in concentration led to the co-existence of bipolar, pre-radial and radial droplets as observed at concentrations of 50 and 10 µg/mL FibN. In addition, LC droplets did not show significant changes at a concentration of FibN below 10 µg/mL. Although a concentration of FibN can be qualitatively depicted using PLL-LC droplets, it is still not sufficient to differentiate between several disorders associated with higher or lower ranges of FibN in blood plasma. In this context, we sought to modulate the optical

response of LC droplets and the detection range of FibN by optimizing LC interfacial features through tailoring the LC core.

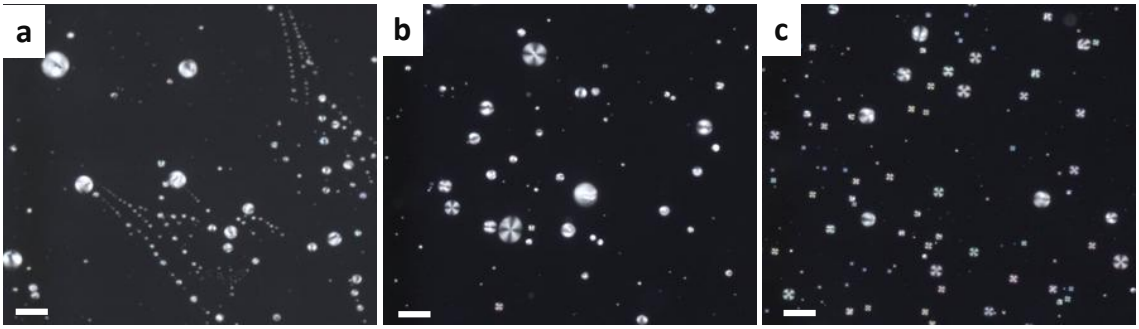

Figure 5.18. Polarized optical micrographs of PLL-LC droplets after 10 min of exposure to a) 300, b) 50 and c) 10 μg/mL FibN solution. Scale bar = 50 μm.

Previously, Abbott et al. demonstrated that polyelectrolyte multilayer films formed at interfaces of LC droplets can modulate the interaction of analytes with LC and significantly tune the sensing behaviour of LCs.[7] Inspired by their finding, the surface of LC droplets was modified with polyelectrolyte multilayer films (PEM) composed of alternate layers of polystyrene sulphonate (PSS), a negatively charged polymer, and PLL on LC droplets with the outermost layer being PLL as previously described.[23] By this method, two different LC cores were prepared with one and two PSS/PLL bilayers with PLL layer as the outermost layer. Here onwards, PLL-LC (single PLL layer), (PLL-PSS) LC (one bilayer of PLL and PSS) and $(PLL\text{-}PSS)_2$ LC (two bilayers of PLL and PSS) droplets will be indicated by 0-PSS, 1-PSS and 2-PSS LC droplets respectively, where the prefix number denotes the total number of alternate PSS layers on the droplets. Figure 5.19a and 5.19c illustrate 1-PSS and 2-PSS LC droplets, respectively, clearly adopting radial configuration inside the droplets consistent with our previous report.[23] Interestingly, upon addition of 1 mg/mL FibN, the director configuration of LC inside 1-PSS and 2-PSS LC droplets consequently changed to bipolar/pre-radial from radial which suggested the applicability of the designed LC cores to detect FibN (Figure 5.19b and 5.19d). The change in configuration transition of LC in these cores can be attributed to the adsorption of FibN molecules on PEM modified LC droplets. The observations are consistent with the results from zeta potential measurements (Figure 5.17). However, upon lowering the concentration of FibN, the number of LC droplets showing the transition from radial to bipolar/pre-radial differs significantly for a particular concentration of FibN (Figure 5.20).

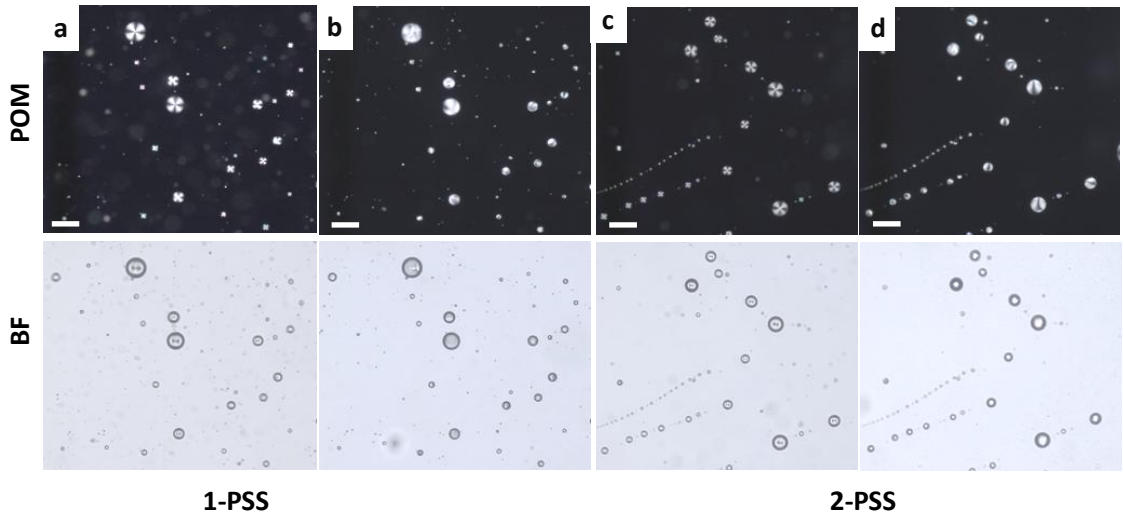

Figure 5.19. Polarized optical micrographs (top) and corresponding bright-field (bottom) micrographs of (a,b) 1-PSS LC droplets and (c,d) 2-PSS LC droplets: (a,c) before and (b,d) after subsequent addition of 1 mg/mL FibN solution. Scale bar = 50 μm.

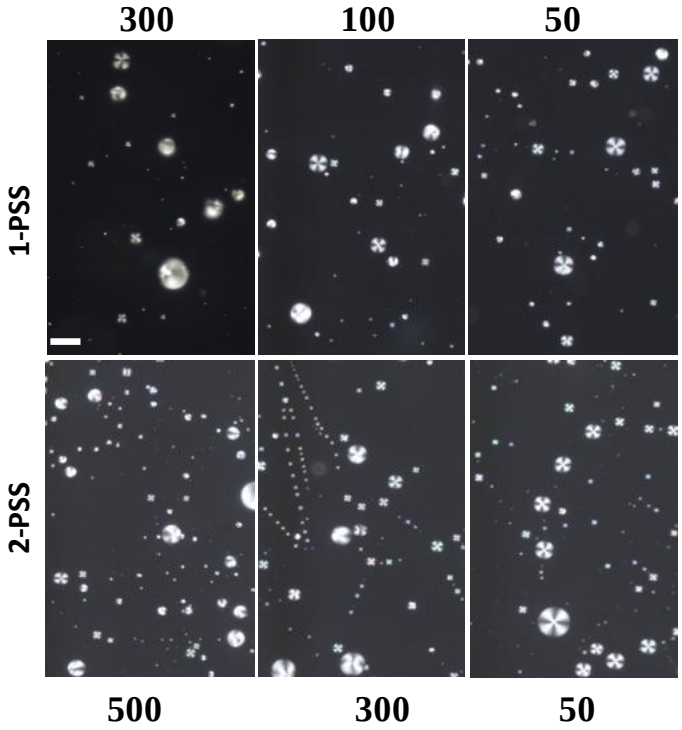

Figure 5.20. Polarized optical micrographs of (1-PSS) and (2-PSS) PLL coated LC droplets after addition of different concentration of FibN solution. Numbers indicated top and below the particular image indicate the concentration of FibN (μg/mL) on (1-PSS) and (2-PSS) PLL coated LC droplets, respectively. Scale bar = 50 μm.

To elaborate clearly, we plotted the percentage of the LC droplets that changed from radial to bipolar/pre-radial as a function of FibN concentrations in case of the three types of PEM decorated LC cores studied (Figure 5.21a). We note two key observations from here: (a) the number of PLL-coated 5CB droplets (irrespective of the LC core used) exhibiting director configuration change from radial to bipolar/pre-radial decreases as the concentration of FibN decreases, and (b) concentration of FibN required to trigger the configuration transition in PLL-coated LC droplets depends considerably on the number of PEM of PSS/PLL on LC droplets. When the number of PSS/PLL layer on LC droplets is increased sequentially from 0 to 2, the percent transition curve shifts towards right suggesting the reduced sensitivity of PLL-coated 5CB droplets towards FibN prominently due to the intrusion of PSS layers in-between 5CB and FibN. For simplicity, we have compared the concentrations of FibN considering the particular fraction of LC droplets (30-40% and 90-100%) showing a transition in director configuration (Figure 5.21b). For example, the concentration of FibN required to achieve 90-100 percent transition in LC droplets is increased from 300 μg/mL (0-PSS) to 500 μg/mL (1-PSS) and then to 1000 μg/mL (2-PSS) depending upon the number of PSS/PLL layers on the LC core. Similarly, the concentration of FibN required to trigger the configuration transition in droplets in approximately 30-40% of the droplets is also increased as PSS layers go from 0 to 2 (from 10 μg/mL (0-PSS) to 100 μg/mL (1-PSS) and then to 300 μg/mL (2-PSS). Therefore, by controlling the number of PSS layers embedded in PEM on PLL-5CB droplets, it is possible to modulate the lower concentration limit of FibN and generate distinct sensing behaviour of LC towards an aqueous solution of FibN. Table 5.3 illustrates the likely association between percent transitions of PLL-5CB droplets in the presence of physiologically important concentration levels of FibN associated with various physical disorders. Although the polymer-coated LC droplet-based design operates on non-specific adsorption of proteins, the strategy provides new insightful approaches for the development of LC-based biosensors with improved interfacial features for desired sensitivity towards analyte.

Recently, we found that ordering transitions in PLL-LC droplets caused by anionic proteins are principally influenced by anionic charge density possessed by protein molecules.[38] Here, we went beyond that and seek to experimentally demonstrate the plausible interacting sites in biomolecules responsible for this director configuration transition in LC droplets. Structurally, a FibN molecule encloses several divalent-cation

binding sites (carboxylate ions) and hence shows strong affinity towards Ca^{2+} as compared to monovalent ions such as Na^{+}.[47,48] To explore the possible binding sites in FibN to PLL, we performed a series of experiments where PLL-5CB droplets were exposed to the same concentration of FibN solution (0.5 mg/mL) pre-incubated with different concentration of Ca^{2+} ions (Figure 5.22).

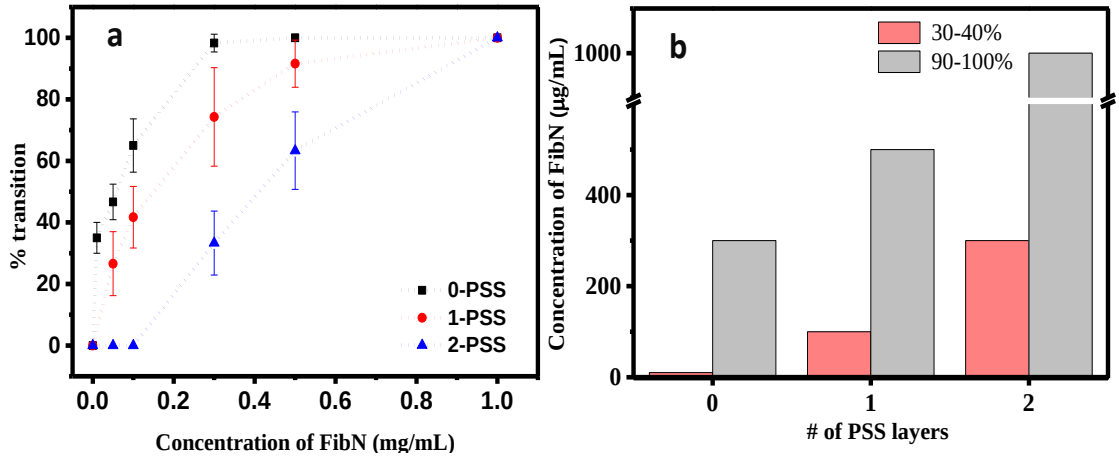

Figure 5.21. (a) Percentage transition of PLL-modified radial LC droplets to pre-radial/bipolar as a function of FibN concentration and PEM modified LC droplets. (b) Plot showing FibN concentration versus layers of PSS with approximately 30-40% and 90-100% transition in LC droplets from radial to bipolar/pre-radial.

Table 5.3. Estimated response of PLL-LC droplets to physiologically important concentration of FibN[40]

Physical Disorder	Concentration of Fibronectin (µg/mL)	Estimated percent transition in PLL-LC droplets (%)		
		Number of PSS layers		
		0	1	2
Breast and colon cancer	500-800	100	90-100	60-100
Primary biliary cirrhosis	500-700	100	90-100	>60
Healthy	250-400	>90	>75	≤ 40
ODIC	100	65	42	0

We chose 0.5 mg/mL FibN because it is sufficient to trigger the configuration transition in all PLL-5CB droplets within the observation time of 10 min. It was observed that at 100 μM of Ca^{2+} or above, PLL-5CB droplets do not change their director configuration after exposure to FibN solutions and hence exhibit radial configuration; however, below that concentration, a mixture of radial or bipolar droplets (10 μM) or only bipolar (1 μM) droplets were observed. Interestingly, when the experiments were repeated with a similar concentration range of monovalent cation such as Na^{+}, we observed that PLL-LC droplets demonstrate only bipolar configuration. These results indicate that in the presence of sufficient amount of Ca^{2+}, FibN may not be able to trigger the configuration transition within PLL-5CB droplets primarily due to the unavailability of the anionic sites in FibN molecules to bind with PLL. Therefore, it can be inferred that the configuration transition in PLL-LC droplets is mainly associated with the electrostatic interactions between PLL and FibN, which can be effectively curtailed by Ca^{2+}.

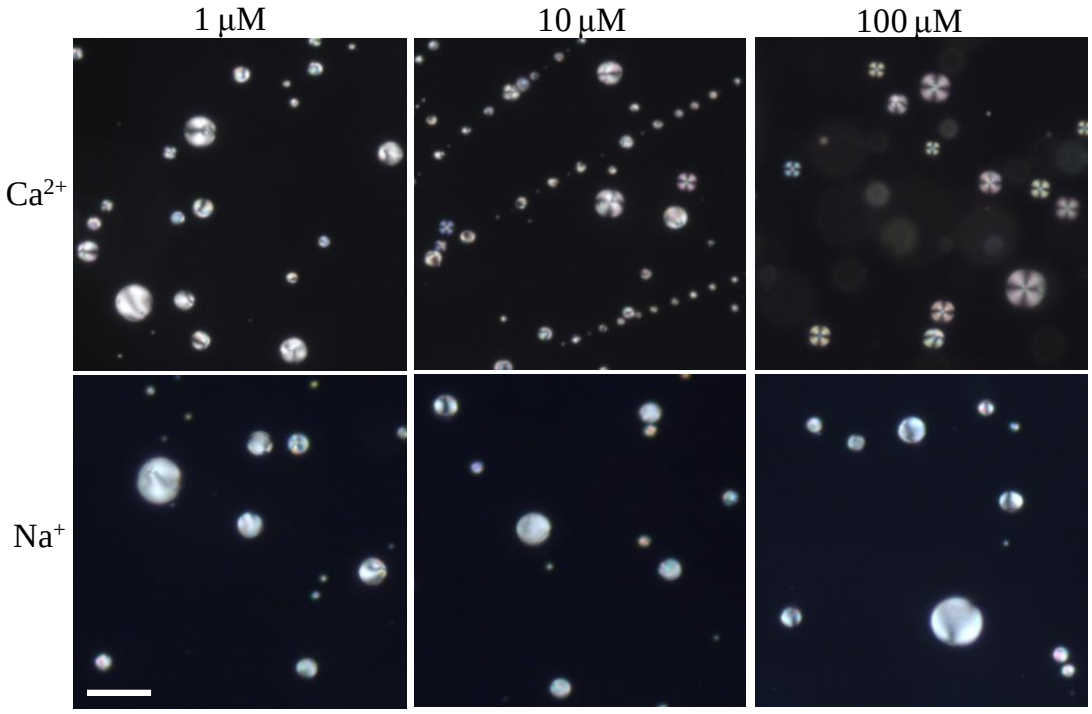

Figure 5.22. Polarized optical microscopy images of PLL-LC droplets followed by an introduction of a pre-incubated mixture of 0.5 mg/mL FibN and Ca^{2+}/Na^{+}. Values above images indicate the concentration of ions (depicted on the left). Scale bar = 50 μm.

To visualize the adsorption of FibN on PLL-LC droplets, we performed ThT binding assay as it provides a convenient means to substantiate the aggregation of proteins, due to its selectivity for amyloid fibrils and β-sheet rich structures. ThT exhibits a low

fluorescence emission in the vicinity of native proteins encompassing different secondary structure; however, upon binding with β-sheet rich motifs, it displays an intense fluorescence emission at 482 nm.[49] Figure 5.23a shows the epifluorescence and corresponding bright-field images of ThT loaded PLL-5CB droplets when coated with different proteins. Bright-field images confirmed the radial and bipolar director configuration of PLL-5CB droplets (control) and proteins coated PLL-5CB droplets, respectively. Interestingly, it was found that ThT fluorescence was low on PLL-5CB droplets; whereas, strong fluorescence was seen at the surface of FibN coated PLL-LC droplets. These results suggest the presence of β-sheet rich FibN molecules on the PLL-LC droplets. As a control; we repeated the experiment with an α-helix rich protein, i.e., BSA, and all β-sheet rich protein, i.e., ConA. As reported by us recently, BSA and ConA can effectively adsorb on PLL-LC droplets and trigger an ordering transition in those droplets.[38] On BSA-coated LC droplets, ThT fluorescence is not strongly observed at the LC droplets suggesting the absence of aggregating structures at the droplets. In the case of ConA, a strong ThT fluorescence was seen on the droplets, which could be due to the presence of β-sheet rich structures of ConA.

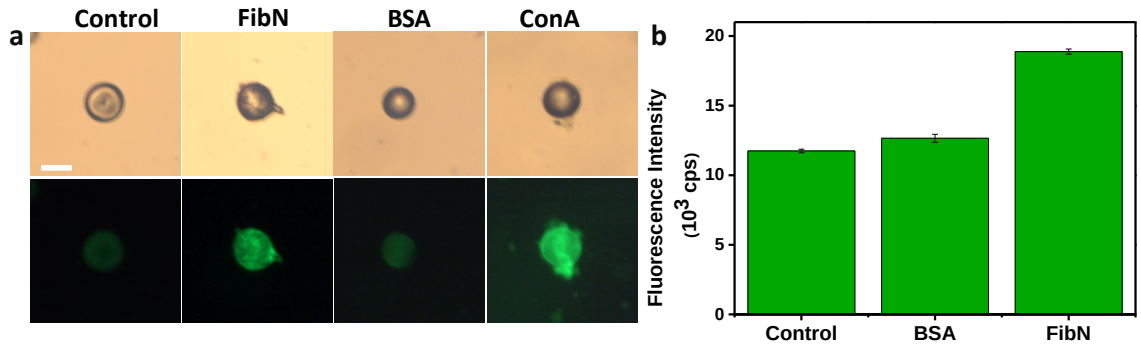

Figure 5.23. (a) Bright-field (top) and corresponding epifluorescence images (bottom) of ThT fluorescence after incubation of PLL-5CB droplets with no protein, FibN and BSA. Plot (b) represents the fluorescence intensity of ThT on PLL-5CB droplets emulsion incubated with BSA and FibN. Scale bar is 10 μm.

We further quantitatively analyzed the fluorescence of ThT when PLL-LC droplets were incubated with FibN and BSA. Enhancement of fluorescence intensity of ThT was observed in the presence of FibN coated PLL-LC droplets as compared to that of BSA coated PLL-LC droplets. The difference in ThT intensity of the two proteins (BSA and FibN) in contact with PLL-LC droplets can be explained by the difference in the β-sheet content of native BSA and FibN proteins as latter is rich in β-sheet motifs (Figure 5.23b).

As a control, we compared the ThT fluorescence of native FibN as well as in the presence of PLL. As expected, we observed comparable fluorescence intensities for ThT and FibN-ThT in solution.

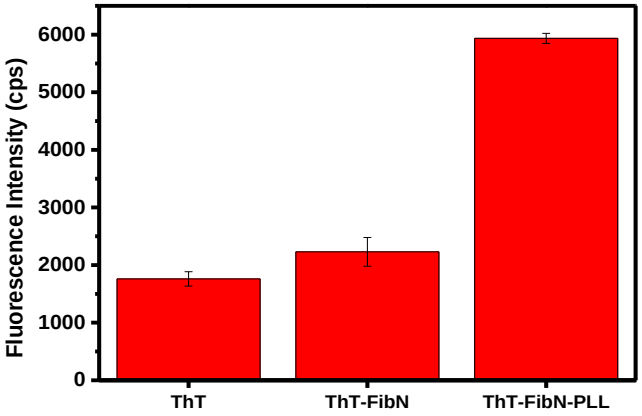

Figure 5.24. Fluorescence intensity of ThT, ThT-FibN and ThT-FibN-PLL in solution.

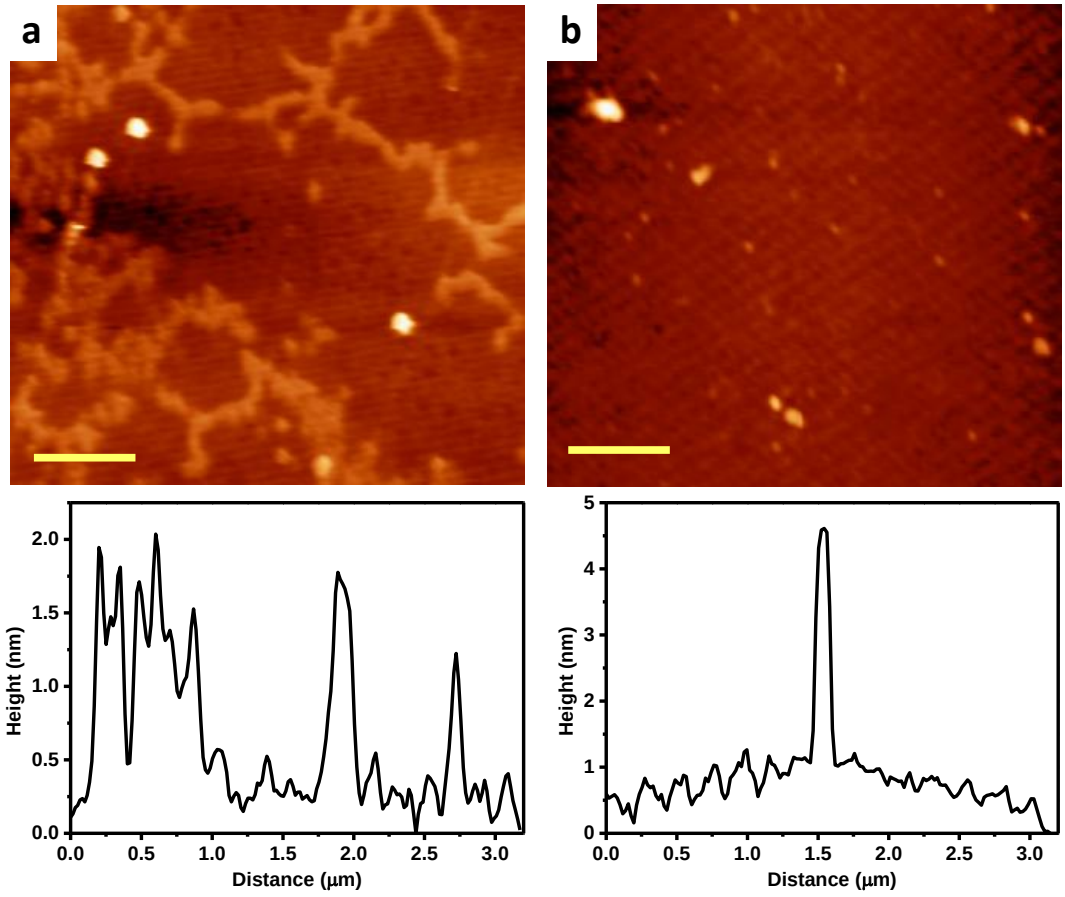

Figure 5.25. Atomic force microscopy images (top) and their respective height profiles (bottom) showing the topography of FibN in the presence of (a) PLL coated LC droplets and (b) LC droplets. Scale bar in (a) and (b) = 640 nm.

In addition, it was found that the fluorescence intensity of FibN-PLL-ThT was ~ 2.5 times higher than that of only FibN-ThT (Figure 5.24). This subtle increment in ThT intensity of FibN-PLL could be due to easily accessible binding sites in the presence of PLL which were earlier buried inside the hydrophobic core of native FibN. Since, ThT intensity enhancement during amyloid formation is thousands of times,[50] we can rule out the formation of amyloid fibrils of FibN in the presence of PLL. To further elucidate that PLL-FibN interactions do not lead to the formation of amyloid fibrils, we performed AFM imaging of FibN-PLL-LC droplets. The compact morphology of FibN observed in the presence of LC droplets transformed into filamentous structures in the presence of PLL-LC droplets (Figure 5.25). These thin filaments were often crossing each other. As reported earlier,[51-53] the heights observed here (in absence and presence of PLL) are typical for FibN molecules in closed (4-5 nm) and open/extended conformations (less than 3 nm), respectively.

5.2.3.2 Structural changes in FibN induced by PLL

Cell response to FibN not only depends on the surface density of protein but on its conformational state as well. In order to validate further that FibN adopts an extended conformation in contact with PLL-LC droplets, we monitored the conformational changes of FibN in the presence of PLL (in solution) and PLL coated LC droplets. It is well known that the secondary structure of FibN is mainly constituted of compact β-sheets which are effectively stabilized in the presence of Ca^{2+} or Na^{+} ions.[47,48] Figure 5.26 shows the CD spectra of FibN in the absence and in the presence of monovalent and divalent cations. The CD spectra of pure FibN shows a negative band at 212 nm, an indicative of compact β conformation in aqueous solution, and a positive band at 228 nm which is in excellent agreement with the earlier report.[54] The strong positive band in the 228 nm region of the CD spectrum of FibN is an unusual and distinct feature that it shares with only a small number of other proteins and is generally assigned to the contribution from most commonly occurring peptide side-chain conformations of L-tyrosine, L-phenylalanine, L-tryptophan and disulfide-bonded domains of the protein. CD spectra of FibN in the presence of Ca^{2+} and Na^{+} ions show the intact peaks at 212 and 228 nm suggesting that the ions do not alter the secondary structure of the protein significantly.

Interestingly, we found that in either case (i.e., presence of bulk PLL or with PLL coated LC droplets), CD spectra of FibN shows a plummet in the magnitude of ellipticity of the

negative band at 212 nm and complete elimination of positive band at 228 nm (Figure 5.27a). This positive peak at 228 nm is considered to be associated with the disulphide bonds at the C terminus of each subunit of the dimeric protein which stabilize the secondary structure of the protein.[54] In addition, FibN consists of a number of intrachain disulphide bonds that may also contribute to this positive peak in CD.[55] The change in positive band implies that in presence of PLL, FibN suffers conformational changes around its disulphide bonds which may induce a transformation of the native and compact state of FibN into a more extended/elongated structure as proposed by Hormann et al.[56] The origin of the positive band at 228 nm can also be attributed to the aromatic residues of FibN such as L-tyrosine, L-phenylalanine and L-tryptophan.[54] Thus, these residues might also be participating during interaction of FibN with PLL.

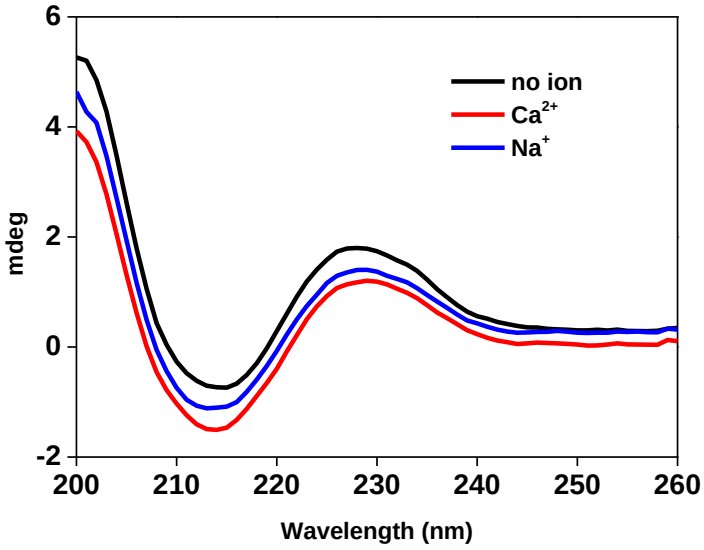

Figure 5.26. Ellipticity graph of 1 mg/mL FibN in aqueous solution without and with ions.

In order to confirm that the conformational changes in FibN are indeed induced by PLL, we sought to restrict interactions between PLL and FibN by Ca^{2+} and compare CD spectra of ion bound and unbound FibN in the presence of PLL. As expected, FibN pre-loaded with Ca^{2+} retains its compact β-conformation in the presence of PLL and does not show attenuation in both the peaks (Figure 5.27b). However, FibN pre-incubated with Na^{+}, demonstrate the significant conformational changes in the presence of PLL. These findings strongly complement our initial results that FibN suffers secondary structural changes in the presence of PLL that can effectively be inhibited by Ca^{2+}. It is reported earlier that Ca^{2+} binds significantly to gelatin binding fragments of FibN (that consists of

$I_6II_{1,2}I_{7\text{-}9}$ modules).[57,58] Vlierberghe et al. suggested that the nature of interactions between gelatin (cationic) and FibN (anionic) is both electrostatic and hydrophobic.[59] Addition of polyamines to FibN inhibits the binding of this complex with gelatin affinity columns.[60] Thus, these results strongly indicate that PLL may mainly interact with FibN through its gelatin binding domains which may disturb the intramolecular interactions in the compact form of FibN to generate an extended filamentous form (as confirmed by AFM).

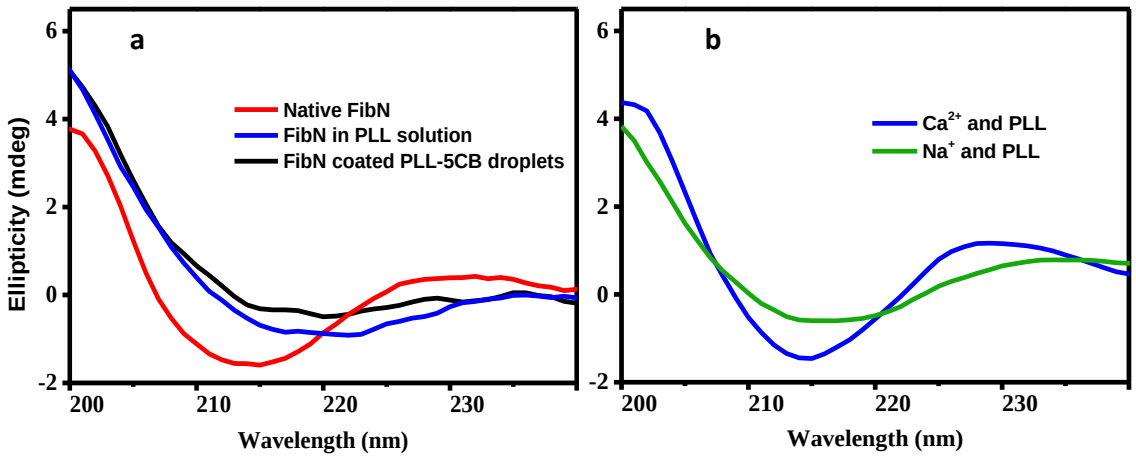

Figure 5.27. Ellipticity graphs of 1 mg/mL FibN (a) in aqueous media, in PLL solution and presence of PLL coated LC droplets and (b) incubated with Ca^{2+} and Na^{+} ions in the presence of PLL.

Further, we monitored the intrinsic fluorescence of tryptophan (Trp) residues of FibN in order to investigate the nature of changes surrounding their environment in the presence of PLL. FibN encloses a large number of Trp residues (approx. 80) which are effectively localized and arranged inside the different modules of the molecule in a homogeneous way along the chains. Thus, it is suggested that Trp residues in a homologous sequence may have similar local environments.[61] Figure 5.28 represents intrinsic fluorescence spectra of native FibN in solution which shows emission maxima at 357 nm confirming that Trp residues are buried inside a hydrophobic core consistent with prior reports.[62,63] It is evident that fluorescence of Trp is significantly quenched in the presence of PLL. It is also observed that quenching of fluorescence of Trp is directly dependent on the concentration of PLL. Such decrease in Trp fluorescence clearly indicates that Trp residues, which were earlier buried inside the hydrophobic core, are exposed to the aqueous environment in the presence of PLL; thus, quenching the initial fluorescence.

The exposure of Trp residues to the aqueous phase indicates the unfolded/open state of FibN molecules.

It is well known that FibN opening and unfolding is promoted by chemical factors and FibN conformations are modulated by electrostatic changes.[51,52,64-66] We believe that similar mechanism may be responsible here where compact FibN transforms into monomeric filamentous form after interactions with PLL in PLL-LC emulsion or bulk solution. Further literature survey reveals that the compact conformation of FibN is preserved by intramolecular ionic interactions between III_{2-3} and III_{12-14} modules.[67] Modules of FibN III_{2-3} are negatively charged whereas that of FibN III_{12-14} are positively charged.[65] It was proposed earlier that negatively charged surfaces open the FibN molecules via interacting with III_{12-14} module. The negatively charged silica surface (hydrophilic) may interfere with the electrostatic intramolecular interactions of FibN thus destabilizing the forces (hydrophobic in nature) that maintain the compact form of FibN.[32] Conversely, on methylated silica surface (hydrophobic and no charge), there is no destabilization of intramolecular FibN interactions that keep it in compact conformation upon surface adsorption. Herein, it is likely that PLL interacts with negatively charged domains/modules of FibN at the PLL coated LC droplets, for instance, III_{2-3}, which may disturb the intramolecular interactions of FibN and promotes the unfolding of molecules or leading to an open-state of FibN.

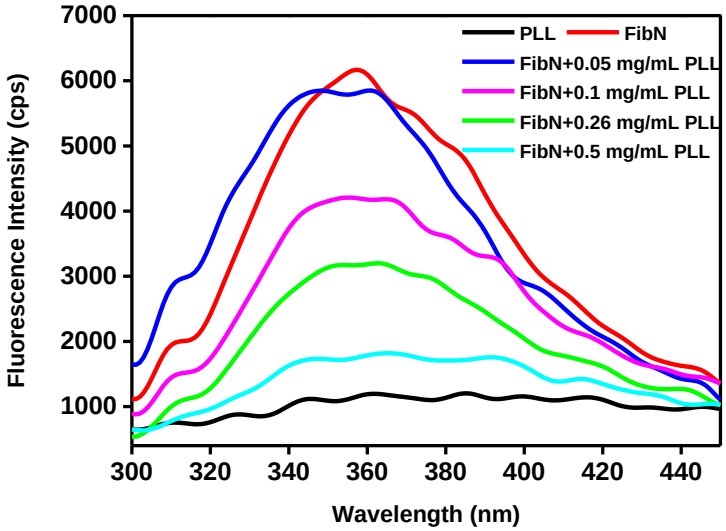

Figure 5.28. Intrinsic fluorescence of tryptophan residues: Fluorescence emission spectra of FibN (0.01 mg/mL), PLL (0.5 mg/mL) and mixtures of PLL-FibN at varying concentration of PLL.

Earlier, Nelea et al. reported FibN filament formation on the negatively charged PSS surfaces whereas large spherical FibN particles (with heights ranging from 10 to 50 nm) were observed on positively charged surfaces such as PLL, PAA (Poly(allylamine hydrochloride)), APTES (3-aminopropyl-triethoxysilane) and so on.[52] They observed that negatively charged surfaces promote extension and assembly of FibN into filaments while positively charged surfaces result compact form of FibN. In our case, we observed network of thin filaments of FibN (of height lesser than 3 nm) in the presence of cationic PLL. The observation of filamentous structures of FibN in the presence of cationic PLL is new but not peculiar. To account for the differences between our findings and those reported earlier,[52] we have analyzed the two systems employed in both studies. First, we would like to state that the PLL systems used in studies by us and Nelea *et al*. differ significantly in the degree of polymerization. Nelea et al.[52] have employed PLL of low molecular weight (~30 kDa) in their study, whereas we used high molecular weight of PLL (~225 kDa). Needless to say, only high molecular weight of PLL (~225 kDa) can induce an ordering transition of the LC from bipolar to radial. Therefore, both the PLL systems (as indicated above) strongly vary with respect to their degree of charge, hydrophilicity/hydrophobicity, and number of functional groups and so on. We believe that the above differences in properties (of PLL systems) could play a significant role which might affect the magnitude of interactions between PLL and FibN in both studies. This hypothesis is supported by studies carried out by Rico et al.[49] and Gugutkov et al.[69] where they have shown that minute variations in the polymer chemistry can influence the FibN conformations on polymeric surfaces. For instance, adsorption of FibN on poly(methyl acrylate) and poly(ethyl acrylate) solid surfaces [despite the same nature of charged surfaces (anionic)] resulted in the formation of globular and fibrillar networks, respectively. Their study also demonstrated that with an increase in the number of methyl groups in the side chain, the molecular mobility of the interacting polymer at the surface is enhanced which, in turn, increases the self-association of FibN. Second, we would like to comment on the geometry of surfaces used for FibN adsorption on PLL surfaces in both studies. Nelea et al. have used PLL functionalized solid surfaces (covalently bound) to image the conformations of adsorbed FibN.[52] This is in striking contrast to the LC-aqueous interfaces (fluid-fluid) used in our study which is primarily driven by supramolecular interactions and the competitive binding among LC, PLL and FibN at the LC-aqueous interface. We hypothesized that the geometry of LC-aqueous interface might allow the FibN to access the binding groups in PLL with greater ease. The observed

change in the director configuration within PLL-coated LC droplets (from radial to bipolar configuration) is also indicative of stronger interactions between FibN-PLL and subsequent weakening of PLL-LC interactions at those interfaces. In addition, all the complementary biophysical techniques, *i.e.* CD and fluorescence provide conclusive evidence of FibN unfolding upon interaction with PLL in our study. Hence, the extended filamentous form observed in AFM in contradiction to Nelea et al.[52] might be due to enhanced interactions between PLL-FibN rendered by greater conformational flexibility of PLL on LC droplets (and in bulk solution) in comparison with solid surfaces. All these factors as indicated above might be responsible for the observed differences between our findings and those reported by Nelea et al.[52] However, a conclusive remark regarding the exact biomolecular phenomena at the interface requires further investigation which is beyond the scope of this work.

5.2.4 Conclusions

This work mainly explores the insights about the adsorption phenomenon of FibN protein at PLL coated LC droplets by monitoring director configuration of LC droplets. Adsorption of anionic FibN molecules at PLL-coated LC droplets switches director configuration of LC from radial to bipolar/pre-radial within a few seconds. The response of LC towards FibN was considerably modulated by the introduction of multiple polyelectrolyte layers within the PLL coated LC droplets. Droplets with the different number of PSS layers (varied from 0 to 2) showed different responses to the same concentration of FibN, i.e., the droplets with more PSS layers being less responsive to FibN. Overall, differently modified PLL-LC droplets can chart and differentiate between ranges of physiologically important concentrations of FibN through the percent transition in the LC droplets. It was further seen that Ca^{2+} when bound with FibN (which consists anionic Ca^{2+} -binding sites) inhibits structural changes in FibN in the presence of PLL and does not affect the ordering of PLL-LC droplets. This suggests the dominance of electrostatic interactions between PLL and FibN molecules directing the ordering transition in LC droplets. From the CD studies, complete elimination of positive peak at 228 nm of FibN was observed. This led us to the conclusion that the otherwise compact structure of the FibN suffered significant conformational changes, mainly around disulfide bonds of molecules, in bulk solution of PLL as well as on the PLL coated LC droplets. The unfolding of FibN molecules induced by PLL on LC droplets was confirmed using AFM. Formation of monomeric filaments was observed in the presence

of PLL that was not observed otherwise in the compact form of FibN. Recently, another group and we reported the amphiphile decorated LC-aqueous interfaces (planar geometry) that monitor protein aggregation at nanomolar concentrations.[70-72] However, our study demonstrates the first example of LC droplet-based system to study the conformational changes in proteins at interfaces and provides considerable insights about the mode of interaction between PLL and FibN. The work will not only strengthen the understanding of various interfacial phenomena but will also help to develop principles to comprehend the fibrillation process within complex ECM assembly.

5.2.5 Experimental Section

5.2.5.1 Materials

Fibronectin from bovine plasma (FibN), bovine serum albumin (BSA), concanavalin A (ConA), poly-L-lysine (PLL) solution 0.1 % (w/v) in H_2O (Molecular weight~225kDa), 4-Cyano-4'-pentylbiphenyl (5CB) LC, poly(4-styrenesulfonic acid) sodium salt (PSS), thioflavin T (ThT), calcium chloride ($CaCl_2$) and sodium chloride (NaCl) were obtained from Sigma-Aldrich (St. Louis, MO). Deionization of a distilled water (DI water) source was done using a Milli-Q-system (Millipore, bedford, MA). Fisher's Finest Premium grade glass microscopic slides were obtained from Fischer Scientific (Pittsburgh, PA) as also mentioned in our earlier reports.

5.2.5.2 Fabrication of PLL-LC droplets

PLL-5CB droplets were prepared as described in the first part of this chapter and elsewhere.[23,24] Briefly, 10 μL of 5CB in 1mL DI water was vortexed for 10 s followed by sonication for 10 min. The resultant LC emulsion was subsequently centrifuged and the supernatant was replaced by 1 mg/mL PLL aqueous solution. After 15 min of incubation, the PLL-5CB droplets were then re-suspended in DI water after centrifugation for further experiments. Size of the polydispersed PLL coated 5CB droplets was found in the range between 5 μm to 40 μm as observed by polarized optical microscopy (POM).[23,24,38] In the radial to bipolar transition curves, percentage transition was approximated from 300-400 droplets in each experiment and the average percentage transition from three set of experiments was plotted in the transition curves. Polyelectrolyte multilayers (PEM) of PLL and PSS on LC droplets were prepared by adsorption of PSS and PLL on LC droplets via layer by layer technique as described previously.[23] Briefly, 10 μL of 5CB in

1mL of PSS solution (1mg/mL) was vortexed for 10 s followed by sonication for 10 min. The resultant PSS-LC emulsion was subsequently centrifuged and washed with water once. Finally, the supernatant was replaced by 1 mg/mL PLL aqueous solution. After 15 min of incubation, the PLL-PSS 5CB droplets were then centrifuged and supernatant was replaced by 1 mL of water. Similarly, PEM films composed of two and three PSS/PLL bilayers on LC droplets were fabricated with outermost layer being PLL. Stock solution of FibN (2-3 mg/mL) was freshly prepared by dissolving solid FibN in DI water at 37 ^{o}C for 30 min.

5.2.5.3 Optical characterization of PLL-LC droplets

The characterization of PLL-LC droplets has been done as per previous reports.[23,24,38] In a typical experiment, 1 μL of PLL-5CB emulsion was placed on the glass slide and 8 μl of the protein solution of required concentration was added carefully on that. Note that the LC droplets may stay at their parent location if the protein solution is introduced carefully.[38] After 10 min, the LC droplets were imaged under polarized optical and bright field microscope. The director configuration of LCs in emulsion was determined using a Zeiss polarizing microscope Scope. A1 with crossed polars (X200). All the images were captured using an AxioCam Camera.

5.2.5.4 Epifluorescence imaging of PLL-LC droplets via ThT assay

A certain volume of PLL-5CB droplets emulsion (100 μL) was incubated with 50 μL of water (control), 1 mg/mL of FibN or BSA for 20 min followed by addition of stock solution of ThT to give a final concentration of 120 μM. Fluorescence imaging was performed with a Zeiss (Scope. A1) fluorescence microscope. The samples were viewed after 4 hours of incubation time using a fluorescence filter cube with a 460 nm excitation filter and a 534 nm emission filter. Images were obtained with an AxioCam camera at constant exposure time (800 ms). For each protein, triplicates were performed and 4 to 10 droplets were analysed each time.

5.2.5.5 Steady-state fluorescence of ThT on PLL-LC droplets

The steady state fluorescence measurements were performed on a FluoroMax-4 spectrofluorometer from Horiba Jobin Yvon at ~25 °C. Samples were prepared by the incubation of 1 mg/mL protein (50 μL) (FibN or BSA) with PLL-5CB emulsion for 20 min followed by addition of stock ThT. Final concentration of ThT used for all of the

fluorescence studies was kept 100 μM. After 1 hour incubation time, the fluorescence intensity of ThT (three measurements) was collected at the following parameters: λ_{ex} = 440 nm, λ_{em} = 485 nm, excitation slit width = 2 nm, emission slit width = 2 nm, integration time = 2 seconds. All the fluorescence data were acquired using the FluorEssence software (provided with the instrument) which were later re-plotted using Origin Pro version 9 software. For recording intrinsic fluorescence of tryptophan residues of FibN, the samples were excited at 280 nm with excitation slit width = 2.5 nm and emission slit width = 5 nm. Samples of FibN, PLL and their mixtures were freshly prepared before recording spectra.

5.2.5.6 Circular dichroism measurements

The far-UV CD spectra were obtained on a Chirascan spectrophotometer (Applied Photophysics, U.K.). The samples were filled in a 1 mm path length quartz cell and recorded spectra with a scan range of 200−260 nm and step size of 1 nm. Bulk samples were prepared by mixing aqueous solution of FibN with PLL. For experiments with ions, FibN was pre-incubated with aqueous solution of $CaCl_2$ or NaCl (5 mM) for 1 hour before mixing with PLL solution. Final concentrations of FibN and PLL were kept 1 mg/mL and 0.05 mg/mL for all of the experiments. CD spectra of mixture of Fib and PLL were recorded after 10 min of preparation. Sample preparation of LC droplets is as follows: 250 μL of PLL-LC droplets were incubated with 100 μL of 3 mg/mL FibN for 2 hours of enough adsorption time. The FibN coated PLL-LC droplets were then centrifuged at 5000 rpm for 5 min to remove the excess FibN from bulk and were subsequently re-suspended in 300 μL of DI water. For each sample, the spectra were averaged over 10 scans and were corrected against the buffer using the ProData software provided with the CD instrument. The spectra were re-plotted using OriginPro 9.0 software.

5.2.5.7 Atomic force microscopy

AFM images of FibN were acquired on an Innova atomic force microscope (Bruker). The AFM was operated in the tapping mode. For imaging, the silicon nitride cantilever probe with radius ~8 nm was used. PLL-LC droplets or LC droplets were incubated with 1 mg/mL FibN for 4 hours before AFM imaging. The droplets were centrifuged and re-suspended in DI water before imaging. The samples (3 μL) was loaded on a freshly cleaved, water-washed muscovite mica (Grade V-4 mica from SPI, PA) and allowed to

air dry for 15–20 min. The images were collected in NanoDrive (v8.03) software. The collected AFM images were further processed and analyzed using WSxM version 4 beta 8.1 software.[73] The AFM images (and height profile of compact and filamentous FibN) reported in the work are typical.

5.2.5.8 Zeta potential measurements

Zeta potential measurements of the PLL-5CB droplets and PEM coated 5CB droplets has been done as reported earlier[24,38] using Zetasizer Nano ZS90 (Malvern Instruments Inc.) at room temperature under a cell-driven voltage of 30 V. Samples were prepared as follows: 50 μL of stock PLL-5CB droplets were diluted with DI water to make total 800 μL solution before adding into the zeta potential cuvette. For experiments with proteins, 50 μL of 1 mg/mL FibN was added to the 50 μL droplets emulsion and incubated for 15 minutes before diluting to 800 μL with DI water. The average of at least 3 scans was taken for each measurement.

References

1. Cross, M. C.; Toomey, R. G.; Gallant, N. D. *Biomed. Mater.* **2016**, *11*, 022002.
2. Wei, Q.; Becherer, T.; Angioletti-Uberti, S.; Dzubiella, J.; Wischke, C.; Neffe, A. T.; Lendlein, A.; Ballauff, M.; Haag, R. *Angew. Chem. Int. Ed*. **2014**, *53*, 8004-8031.
3. Ofran, Y.; Rost, B. *J. Mol. Biol.* **2003**, *325*, 377–387.
4. Yan, C.; Wu, F.; Jernigan, R. L.; Dobbs, D.; Honavar, V. *Protein J.* **2008**, *27*, 59–70.
5. Braun, P.; Gingras, A. C. *Proteomics* **2012**, *12*, 1478–1498.
6. Berggård, T.; Linse, S.; James, P. *Proteomics* **2007**, *7*, 2833–2842.
7. Tjipto, E.; Cadwell, K. D.; Quinn, J. F.; Johnston, A. P.; Abbott, N. L.; Caruso, F. *Nano Lett*. **2006**, *6*, 2243–2248.
8. Sivakumar, S.; Gupta, J. K.; Abbott, N. L.; Caruso, F. *Chem. Mater*. **2008**, *20*, 2063–2065.
9. Gupta, J. K.; Sivakumar, S.; Caruso, F.; Abbott, N. L. *Angew. Chem. Int. Ed*. **2009**, *121*, 1680–1683.
10. Sivakumar, S.; Wark, K. L.; Gupta, J. K.; Abbott, N. L.; Caruso, F. *Adv. Funct. Mater.* **2009**, *19*, 2260–2265.
11. Gupta, J. K.; Zimmerman, J. S.; de Pablo, J. J.; Caruso, F.; Abbott, N. L. *Langmuir* **2009**, *25*, 9016-9024.
12. Kinsinger, M. I.; Buck, M. E.; Abbott, N. L.; Lynn, D. M. *Langmuir* **2010**, *26*, 10234-10242.
13. Aliño, V. J.; Pang, J.; Yang, K. L. *Langmuir* **2011**, *27*, 11784−11789.
14. Khan, W.; Choi, J. H.; Kim, G. M.; Park, S. Y. *Lab Chip* **2011**, *11*, 3493-3498.
15. Lin, I. H.; Miller, D. S.; Bertics, P. J.; Murphy, C. J.; de Pablo, J. J.; Abbott, N. L. *Science* **2011**, *332*, 1297-1300.
16. Aliño, V. J.; Tay, K. X.; Khan, S. A.; Yang, K. L. *Langmuir* **2012**, *28*, 14540-14546.
17. Bera, T.; Fang, J. *J. Mater. Chem*. **2012**, *22*, 6807-6812.
18. Kim, J.; Khan, M.; Park, S. Y. *ACS Appl. Mater. Interfaces* **2013**, *5*, 13135–13139.
19. Bera, T.; Fang, J. *Langmuir* **2013**, *29*, 387-392.

20. Yoon, S. H.; Gupta, K. C.; Borah, J. S.; Park, S.-Y.; Kim, Y. K.; Lee, J.-H.; Kang, I. K. *Langmuir* **2014**, *30*, 10668-10677.
21. Bera, T.; Deng, J.; Fang, J. *J. Phys. Chem. B* **2014**, *118*, 4970−4975.
22. Khan, M.; Park, S.-Y. *Colloids Surf. B: Biointerfaces* **2015**, *127*, 241-246.
23. Sidiq, S.; Krishna Prasad, G. V. R.; Mukhopadhaya, A.; Pal, S. K. *J. Phys. Chem. B* **2017**, *121*, 4247-4256.
24. Verma, I.; Sumyra, S.; Pal, S. K. *ACS Omega* **2017**, *2*, 7936–7945.
25. Peters, T. J. All about albumin: biochemistry, genetics, and medical applications. San Diego, Calif.: Academic Press, **1995**.
26. Senear, D. F.; Teller, D. C. *Biochemistry* **1981**, *20*, 3076–3083.
27. Emsley, J.; White, H. E.; O'Hara, B. P.; Oliva, G.; Srinivasan, N.; Tickle, I. J.; Blundell, T. L.; Pepys, M. B.; Wood, S. P. *Nature* **1994**, *367*, 338–345.
28. Maric, P.; Ozretic, P.; Levanat, S.; Oreskovic, S.; Antunac, K. Beketic-Oreskovic, L. *Coll. Antropol*. **2011**, *35*, 241-247.
29. Masson, O.; Prebois, C.; Derocq, D.; Meulle, A.; Dray, C.; Daviaud, D.; Quilliot, D.; Valet, P.; Muller, C.; Liaudet-Coopman, E. *Plos One* **2011**, *6*, e16452.
30. Entlicher, G.; Koštíř, J. A.; Kocourek, J. *Biochim. Biophys. Acta.* **1971**, *236*, 795-797.
31. Canduri, F.; Ward, R. J.; Azevedo Jr., W. F. D.; Gomes, R. A. S.; Arni, R. K. *Biochem. Mol. Bio. Int.* **1998**, *45*, 797-803.
32. Brake, J. M.; Abbott, N. L. *Langmuir* **2007**, *23*, 8497-8507.
33. Das, D.; Sidiq, S.; Pal, S. K. *Chemphyschem.* **2015**, *16*, 753-760.
34. Alino, V. J.; Sim, P. H.; Choy, W. T.; Fraser, A.; Yang, K. L. *Langmuir* **2012**, *28*, 17571−17577.
35. Wang, Y.; Hu, Q.; Tian, T.; Gao, Y.; Yu, L. *Analytica Chimica Acta* **2016**, *937*, 119-126.
36. Lehninger, Albert L et al, Principles of Biochemistry, 2nd Edition. New York: Worth Publishers, 1993, 142.
37. Wetter, L. R.; Deutsch, H. F. *J. Biol. Chem.* **1951**, *192*, 237-242.
38. Verma, I.; Sidiq, S.; Pal, S. K. *Liq. Cryst.* **2019**, *46*, 1318-1326.
39. Hynes, R. O. (1990) *Fibronectins* (Springer, New York).
40. Stathakis, N. E.; Fountas, A.; Tsianos, E. *J. Clin. Pathol*. **1981**, *34*, 504–508.
41. Chifflet, S.; Bolatto, C.; Tolosa, S. *J. Biochem. Biophys. Meth.* **2004**, *59*, 139–143.
42. Asem, E. K.; Conkright, M. D. *Comp. Biochem. Physiol*. **1995**, *112*, 247–255.

43. Jin, H.; Varner, J. *Br. J. Cancer*, **2004**, *90*, 561–565.
44. Guo, W.; Giancotti, F. G. *Nat. Rev. Mol. Cell Biol*., **2004**, *5*, 816–826.
45. Llopis-Hernandez, V.; Cantini, M.; Gonzalez-Garcia, C.; Manuel Salmeron-Sanchez, M. *International Materials Reviews* **2015**, *60*, 245-264.
46. Cantini, M.; Rico, P.; Salmerón-Sánchez, M. Fibronectin Fibrillogenesis at the cell–material interface. In *Biomimetic Approaches for Biomaterials Development*; Wiley-VCH Verlag GmbH & Co. KGaA: Weinheim, Germany, **2012**; 189– 212.
47. Khan, M. Y.; Jaikaria, N. S.; Frenz, D. A.; Villanueva, G.; Newman, S. A. *J. Biol. Chem.* **1988**, *263*, 11314–11318.
48. Godfrey, W. A.; E. R. Michael. *Biochem. Biophys. Res. Commun.* **1983**, *111*, 1045–1053.
49. Nilsson M. R. *Methods*. **2004**, *34*, 151–60.
50. Bascetin, R.; Admanea, K.; Agniela, R.; Boudoub, T.; Doussineauc, T.; Antoinec, R.; Galleta, O.; Leroy-Dudala, J.; Vendrely, C. *Int. J. Biol. Macromol*. **2017**, *97*, 733–743.
51. Bergkvist, M.; Carlsson, J.; Oscarsson, S. *J. Biomed. Mater. Res. A* **2003**, *64*, 349-356.
52. Nelea, V.; Kaartinen, M. *J. Str. Biol.* **2010**, *170*, 50-59.
53. Erickson, H. P.; Carrell, N. A. *J. Biol. Chem*. **1983**, *258*, 14539–14544.
54. Khan M. Y.; Villanuevag, G.; Newman, S. A. *J. Biol. Chem.* **1989**, *264*, 2139–2142.
55. Marko Vic-Housley, Z.; Schulthess, T.; Engel, J. *J. Biol. Chem.* **1985**, *366*, 985–991.
56. Hörmann, H.; Richter, H. *Biopolymers* **1986**, *25*, 947-958.
57. Turner, P. M.; Lorand, L. *Biochemistry* **1989**, *28*, 628-635.
58. Radek, J. T.; Jeong, J. M.; Murthy, S. N.; Ingham, K. C.; Lorand, L. *Proc. Natl. Acad. Sci. USA* **1993**, *90*, 3152-3156.
59. Vlierberghe, S. V.; Vanderleyden, E.; Dubruel, P.; Vos, F. D.; Schacht, E. *Macromolecular Bioscience* **2009**, *9*, 1105-1115.
60. Vuento, M.; Vaheri, A. *Biochem J.* **1978**, *175*, 333-336.
61. Lai, C. S.; Homandberg, G.; Miziorko, H.; Wolff, C. *Biopolymers* **1987**, *26*, 1381-1389.

62. Patel, S.; Chaffotte, A. F.; Goubard, F.; Pauthe, E. *Biochemistry* **2004,** *43*, 1724-1735.
63. Brumfeld, V.; Werber, M. M. *Archives of biochemistry and biophysics* **1993**, *302*, 134-143.
64. Williams, E. C.; Janmey, P. A.; Ferry, J. D.; Mosher, D. F. *J. Biol. Chem.* **1982**, *257*, 14973-14978.
65. Pernodet, N.; Rafailovich, M.; Sokolov. J.; Xu D.; Yang, N.-L.; McLeod, K. *J. Biomed. Mater. Res.* A **2003**, *64*, 684-692.
66. Dargahi, M.; Nelea, V.; Mousa, A.; Omanovica, S.; Kaartinen, M. T. *RSC Adv.* **2014**, *4*, 47769-47780.
67. Johnson, K. J.; Sage, H.; Briscoe, G.; Erickson, H. P. *J. Biol. Chem.* **1999**, *274*, 15473-15479.
68. Rico, P.; Hernandez, J. C. R.; Moratal, D.; Altankov, G.; Pradas, M. M.; Salmeron-Sanchez, M. *Tissue Eng. Part A* **2009**, *15*, 3271– 3281.
69. Gugutkov, D.; Gonzalez-Garcia, C.; Hernandez, J. C. R.; Altankov, G.; Salmeron-Sanchez, M. *Langmuir* **2009**, *25*, 10893–10900.
70. Pani, I.; Swasthi, H. M.; Mukhopadhyay, S.; Pal, S. K. *J. Phys. Chem. C* **2019**, *123*, 1305-1312.
71. Verma, I.; Rajeev, N. P.; Mohiuddin, G.; Pal, S. K. *J. Phys. Chem. C* **2019**, *123*, 6526-6536.
72. Sadati, M.; Apik, A. I.; Armas Perez, J. C.; Martinez Gonzalez, J.; Hernandez Ortiz, J. P. Abbott, N. L.; de Pablo, J. J. *Adv. Mater.* **2015**, *25*, 6050–6060.
73. Horcas, I.; Fernandez, R.; Gomez-Rodriguez, J. M.; Colchero, J.; Gomez-Herrero, J.; Baro, A. M.. *Rev. Sci. Instrum.* **2007**, *78*, 013705.

CHAPTER 6

Poly-L-lysine Coated Liquid Crystal Droplets for Sensitive Detection of DNA and its Applications in Controlled Release of Drug Molecules

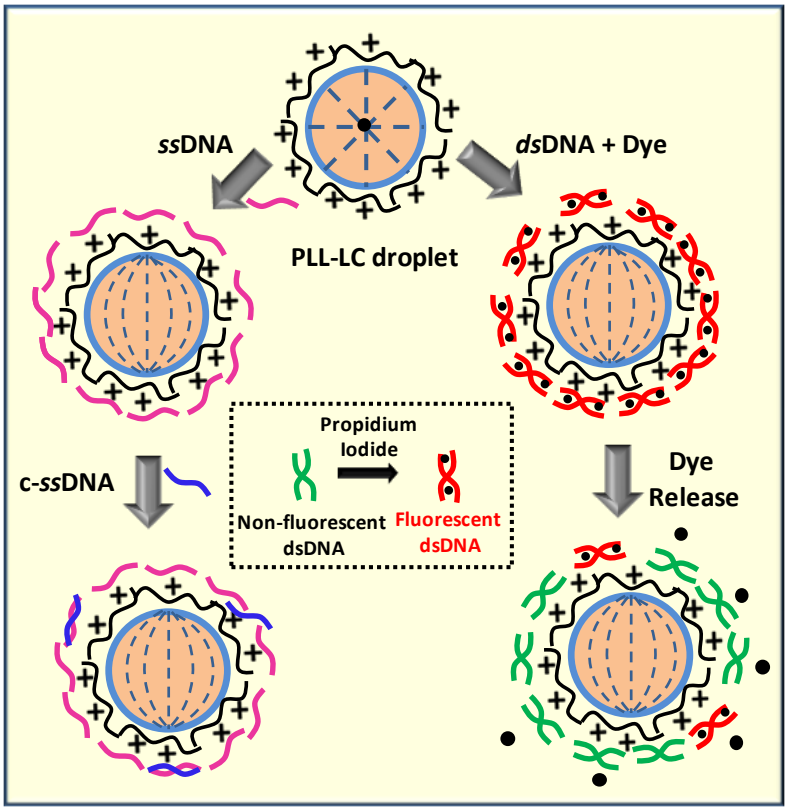

Interactions between DNA and adsorbed poly-L-lysine (PLL) on liquid crystal (LC) droplets were investigated using polarizing optical microscopy and epifluorescence microscopy. Adsorption of DNA (single-stranded DNA/double-stranded DNA) at PLL coated LC droplets was found to trigger an LC reorientation within the droplets leading to pre-radial/bipolar configuration of those droplets. In addition, dsDNA adsorbed PLL droplets have been found to be effectively used to displace (controlled release) propidium iodide (a model drug) encapsulated within dsDNA over time. These observations suggest the potential for a label-free droplet-based LC detection system that can respond to DNA and may provide a simple method to develop DNA-based drug nano-carriers.

Source: Verma, I.; Sidiq, S.; Pal, S. K. *ACS Omega* **2017**, *2*, 7936-7945 (<https://pubs.acs.org/doi/full/10.1021/acsomega.7b01175>).

6.1 Introduction

Recently, micrometer-sized liquid crystal (LC) droplets dispersed in aqueous media have been exploited to the development of functional materials for the realization of a new class of sensitive communicators of targeted species.[1-17] Due to having a large surface area with high spatial resolution and very high sensitivity, they offer routes towards the advancement of new passive biosensors. The detection principle is based on the change in configurational transition of the LC within the droplets that can be easily visualized with the naked eye under an optical microscope. For example, droplet-based LCs have been reported as a sensing platform for developing immunoassays[4], to detect glucose[5], bacterial endotoxin at $pgmL^{-1}$ concentration[6], bacteria and viruses[7], KB cancer cells[9], cholic acid[10], and many more.[11-14] Recently, we have shown that layer-by-layer coating of poly-L-lysine (PLL) on LC droplets can provide a simple design for cell-based sensors.[17-19] In addition, these PLL-coated droplets were shown to be useful for the detection of healthy and apoptosis cells that are difficult to achieve *via* other analytical techniques. In this work, we have exploited the behavior of PLL coated LC droplets which could be particularly useful for sensitive detection of DNA and can find applications in controlled release of drug molecules from DNA functionalized LC droplets.

DNA has been widely offering numerous applications in sensing, diagnostics and gene therapy[20-22] and more recently, self-assembled DNA nanostructures have emerged as the promising candidates to serve as nanocarriers for drug delivery, primarily due to their biocompatibility and the natural ability of DNA to associate with several anti-cancer agents, for e.g., Doxorubicin[23]. Efforts are being made on developing relevant designs to predict and study drug release behavior as well as release mechanisms applicable to a wide range of nano-sized dosage forms.[24,25] As DNA-based drug delivery systems start to advance toward clinical use; we wanted to further explore LC-aqueous interface of PLL-LC droplets to develop the new principles for understanding and to study the real time-controlled release profile of anti-cancer drugs encapsulated in DNA molecules. Literature survey reveals a wide range of approaches to detect DNA using LCs.[26-32] For example, Schwartz and co-workers showed that interactions between ssDNA and a cationic surfactant led to changes of surfactant coverage at LC/aqueous interface and triggered an orientational ordering transition of the LC from homeotropic to a planar state.[26,27] Subsequent hybridization with complementary ssDNA governed a reorientation of the LC

at those interfaces. The same group also demonstrated that conformational change of the adenosine aptamer upon binding with adenosine led to LC reorientation at LC/aqueous interface.[28] Yang and co-workers developed a new strategy of detecting DNA targets using self-assembled cholesterol-labeled DNA probes at LC/aqueous interface in a planar geometry.[29] Tan et al. demonstrated that the conformational changes of the DNA probe mediated by various metal ions cause the reorientation of the LCs.[30] Wu and coworkers described the detection of a target gene in high sensitivity through changes in the optical response of the LC caused by the formation of self-assembly of DNA dendrimers from hairpin DNA probes by hybridization chain reaction at surfactant doped LC–aqueous interface.[31] Park et al. demonstrated use of LC-based DNA biosensor for the detection of traces of myricetin that propitiate the cleavage of DNA and thus results in an ordering transition of the LC.[32] Recently, Yang and coworkers reported that assembly of DNA-lipid amphiphiles could not trigger the orientational ordering of LCs at LC/aqueous interface. However, in the presence of lipids, the DNA-lipids preferred to form net-like structures which disappeared after hybridization with the complementary DNA.[33.] However, no efforts have been made previously that can exploit the speed and sensitivity of LC droplets to detect DNA. In this work, we first demonstrated that PLL coated LC droplets can be used to detect DNA which is mediated by topological defects leading to configurational transitions of those droplets. In addition, responsive DNA functionalized PLL droplets have been found useful to displace propidium iodide (PI), a model drug, encapsulated in DNA over time, thereby providing a template for controlled drug release.

6.2 Objective

The study was motivated by two goals. First, we sought to develop a simple design for the detection of DNA using a droplet-based LC sensor that can be observed as changes in the optical appearance of the LC using optical microscopy. The design builds from our prior reports[17-19] that demonstrated a simple layer-by-layer (LbL) method to prepare PLL-coated droplets in which PLL strongly interacts with the LC and triggers a configurational transition of the LC from bipolar to radial. We hypothesized that negatively charged DNA could strongly adsorb on positively charged PLL coated LC droplets leading to LC reorientation of those droplets. Second, we sought to demonstrate a simple template that can displace a model drug encapsulated in DNA over time from these LbL nano-films and can be a promising approach to develop a new and alternative way for drug delivery. We

have been successful to show that under physiological conditions, the DNA adsorbed PLL droplets exhibit release of PI encapsulated in DNA molecules over time.

6.3 Results and Discussion

6.3.1 Director configuration of LC droplets in the presence of ssDNA

First, we aimed to fabricate single PLL layer coated LC (5CB/E7) droplets and sought to determine the ordering of the LC within those droplets. In the presence of PLL, LC emulsion droplets undergo an ordering transition from bipolar to radial confirming adsorption of PLL at LC-aqueous interfaces. The stabilization of radial droplets is primarily due to the intermolecular hydrogen bonding between 5CB LC and PLL, as reported earlier.[17] Under cross polarizers, they exhibited radial configuration having a crosslike appearance (Figure 6.1a). This was further supported by bright-field micrograph that shows a single point defect at the center of the droplets (indicated by the blue arrow in Figure 6.1c). Our next experiment was to determine whether these PLL-coated LC micro-droplets would respond to the presence of anionic DNA. Interestingly, the addition of 30 μM ssDNA on 5 μL (~10^4 droplets) of PLL-5CB droplet emulsion resulted in a rapid change (< 10s) in the director configuration of the LC molecules from radial to bipolar/pre-radial when observed under crossed polars (as shown in Figure 6.1b). Bright-field microscopy confirms the bipolar/pre-radial configuration exhibiting two point defects at the poles of the droplets (indicated by blue arrows in Figure 6.1d). This experiment suggests that DNA is likely adsorbed on PLL coated LC droplets and the rapid ordering transition is likely due to strong electrostatic interaction between negatively charged DNA and positively charged PLL (*vide infra*). Adsorption of ssDNA on the PLL modified 5CB droplets was investigated by the fluorescence and bright field microscopy of PLL-5CB droplets. The strong fluorescence on the surface of the 5CB droplet (Figure 6.2a) confirmed the presence and adsorption of FAM-ssDNA at PLL-5CB droplets and the bright field microscopy image of the same droplet (Figure 6.2b) reveals bipolar configuration of the PLL modified 5CB droplets which further supports the adsorption of negatively charged ssDNA on positively charged PLL-5CB droplets. These observations established that the configuration transition mediated by topological defects of the PLL-5CB droplets could be monitored to provide a fast and real-time optical detection of ssDNA. This is primarily driven due to strong electrostatic interactions

between negatively charged oligonucleotides and positively charged PLL moieties at the interface.

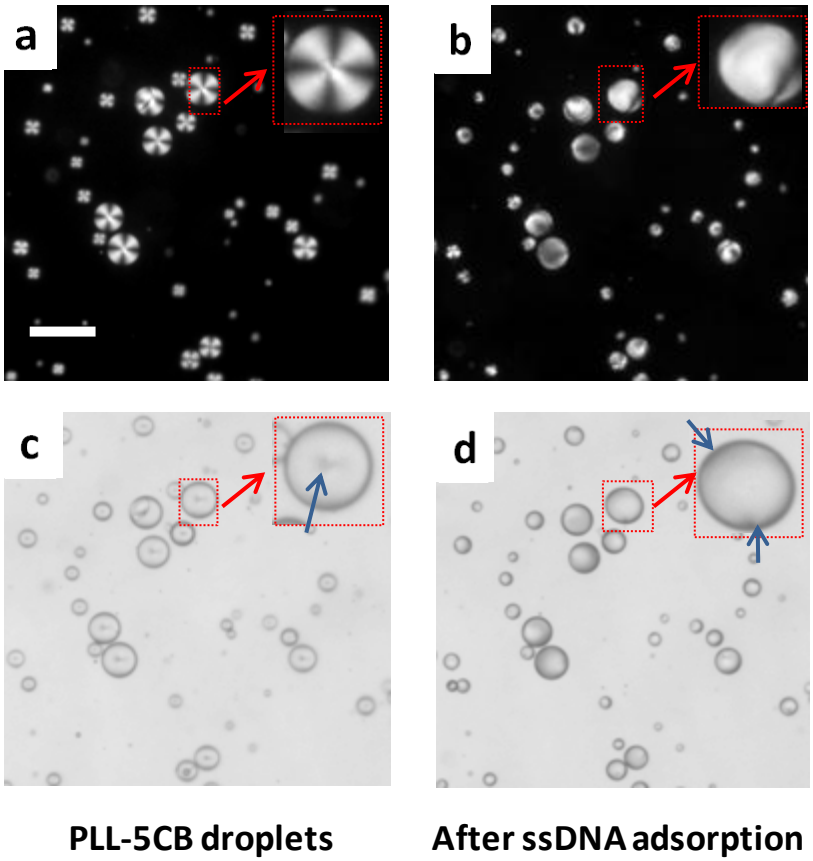

Figure 6.1. Polarized optical and corresponding bright-field micrographs images of PLL coated LC droplets in contact with: (a,c) 0 µM ssDNA and (b, d) 30 µM ssDNA. The LC droplets were in radial states (a,c) before but transitioned to bipolar/pre-radial state (b,d) 10 s after addition of ssDNA. The insets within (a-d) indicate the higher magnification version of the red arrow marked LC droplet. Blue arrows in (c,d) indicate the point defect in the center of a radial droplet and two defects at the poles of a bipolar droplet, respectively. Scale bar = 50 µm.

In the next experiment, we determined the effect of varying concentration of ssDNA on the orientational ordering of the LC with PLL-5CB droplets. Figure 6.3a,e and 6.3b,f correspond to the POM images of the PLL-LC droplets before and after 10s of the addition of 10 µM and 5 µM ssDNA, respectively. The corresponding bright field micrographs are shown in Figure 6.3c,g and 6.3d,h, respectively. A change in the configuration of the droplets from radial to bipolar/pre-radial was observed in both cases. After careful investigation of these images it was found that when the concentration of

ssDNA is 10 μM (C_{ssDNA} = 10 μM), most of the PLL-5CB droplets are able to induce the configurational transition of the LC within those droplets. In contrast, introduction of 5 μM ssDNA (C_{ssDNA} = 5 μM) revealed co-existence of both bipolar and radial LC droplets. Therefore, in the next set of experiments, we sought to draw an analogy between the number of droplets demonstrating radial-to-bipolar/pre-radial transition upon adsorption of varying concentration of ssDNA. From the transition plot (Figure 6.4a), we observed that the number of PLL-5CB droplets demonstrating radial-to-bipolar/pre-radial transition decreases with the decrease in the concentration of ssDNA added. More precisely, we note three key findings. First, for $C_{ssDNA} \geq 10\mu M$, all the droplets (100 %) change their configuration from radial to pre-radial/bipolar. Second, for 0.2 μM < C_{ssDNA} < 10 μM, only fraction of the droplets (10-90 %) shows the radial to pre-radial/bipolar transition which decreases with the decrease in the concentration of ssDNA (upto 0.2 μM). Third, there is no configuration transition of the PLL-5CB droplets observed when the concentration of C_{ssDNA} < 0.2 μM.

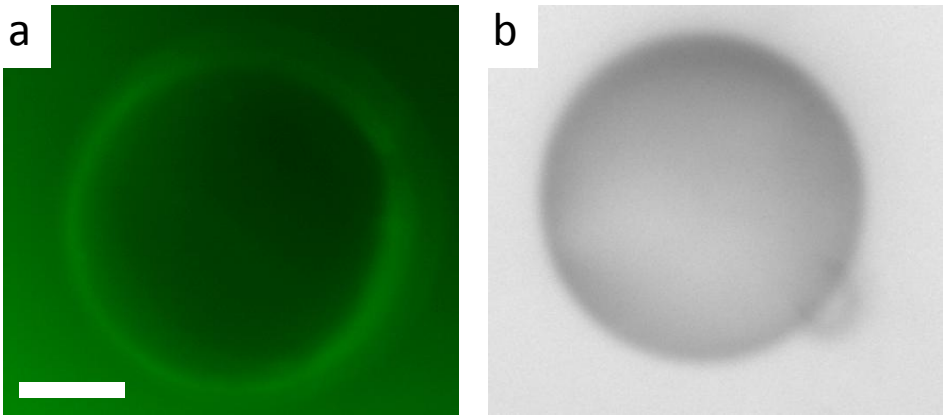

Figure 6.2. Epi-fluorescence microscopic image (a) and corresponding bright-field image (b) of a PLL-coated 5CB droplet following 60 min incubation with 30 μM FAM tagged fluorescent ssDNA. Green fluorescence present on the surface of the droplet supports the adsorption of ssDNA while bright-field image confirms the bipolar configuration of the droplet. Scale bar = 10 μm.

In Figure 6.4b, Zeta potential (ζ-) measurements reveal that PLL-5CB droplets have cationic charge density with ζ- value of +49.6 mV particularly due to the cationic amino groups of the PLL chains adsorbed at the LC/aqueous interface. This value decreases in magnitude with increasing concentration of ssDNA attaining a saturation value of approx -15.6 mV at C_{ssDNA}=10 μM. The negative ζ- values can be attributed to the anionic

phosphate groups of ssDNA backbone adsorbed at the surface of PLL-5CB droplets. From the percent transition plot and the ζ- measurements, we found that 10 µM ssDNA is the minimum concentration of ssDNA required to show the configurational transition of all the radial 5CB droplets to bipolar/pre-radial. Below this concentration, some PLL-5CB droplets show the bipolar/pre-radial configuration while others remain in radial configuration likely due to not enough adsorption of ssDNA on PLL-5CB droplets.

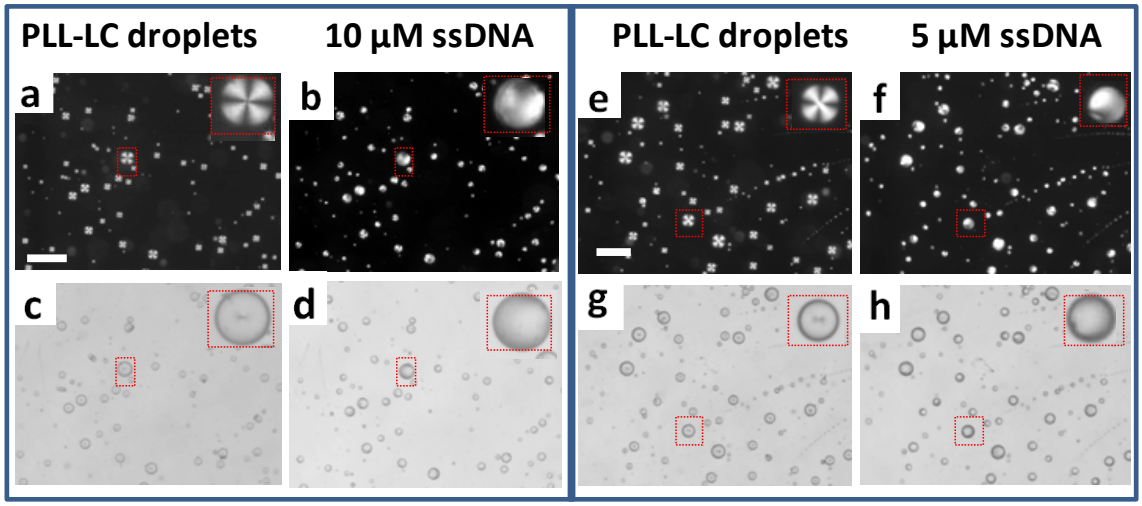

Figure 6.3. Polarized optical (a,b,e,f) and bright-field (c,d,g,h) images of the PLL-LC droplets before (a,c,e,g) and after 10s of addition of 10 µM (b,d) and 5 µM (f,h) ssDNA respectively. The insets within (a-h) illustrate the higher magnification version of the arrow marked LC droplet. Scale bar = 70 µm.

It may be hypothesized that the sensitivity of the PLL-5CB droplets towards ssDNA can be increased by modulating the volume of PLL-5CB emulsion. To verify this, the volume of PLL-5CB droplets emulsion is reduced from 5 µL to 1 µL following by addition of the constant volume (5 µL) of different concentrations of ssDNA. Interestingly, as shown in Figure 6.4c, the concentration of ssDNA required to trigger the configurational transition (radial to bipolar/pre-radial for all the droplets) of the LC within the droplets is reduced to 1µM. We found that when the concentration of ssDNA is in between 1 and 0.05 µM (1µM < C_{ssDNA} > 0.05 µM), co-existence of the radial, pre-radial and bipolar droplets were observed. The number of bipolar droplets decreases with decreasing concentration of ssDNA. However, below 0.05 µM of ssDNA (C_{ssDNA} < 0.05 µM), no change in the director configuration was observed in the PLL-5CB droplets. Therefore, we infer that the sensitivity of the PLL-5CB droplets towards ssDNA can be increased to 50 nM by

decreasing the volume of the emulsion of PLL-5CB droplets to 1 µL. The huge decrease in the detection limit of ssDNA from 200 nM to 50 nM by decreasing the volume of emulsion from 5 µL to 1 µL can be attributed to the following two factors. First, the reduced number of droplets in the sample, which reduces the requirement of the amount of the anionic ssDNA needed to trigger a transition in PLL-5CB droplets. Second, the reduced volume of the emulsion results in the less dilution of the ssDNA sample, thus ultimately raising the amount of ssDNA available for adsorption at PLL-5CB droplets.

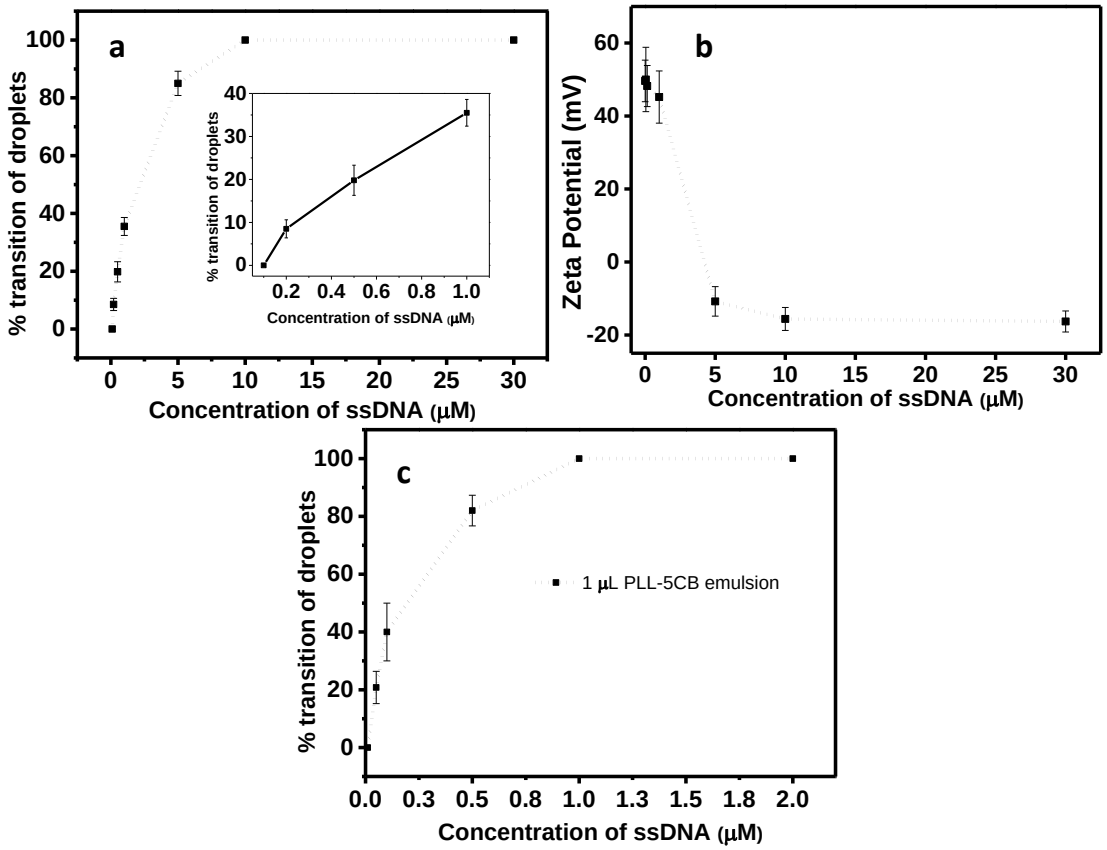

Figure 6.4. Graph (a) shows % conversion of PLL-LC droplets configuration from radial to bipolar/pre-radial on the addition of varying concentration of ssDNA with a fixed amount of PLL-5CB droplets (5 µL). Inset in (a) shows the enlarged view of the plot representing the concentration of ssDNA less than 1 µM. (b) Zeta Potential of PLL coated LC droplets with varying concentrations of ssDNA. (c) Graph showing % transition of PLL-LC droplets configuration from radial to bipolar/pre-radial on the addition of varying concentration of ssDNA with a fixed volume of PLL-5CB droplets (1 µL) (with limit of detection = 50 nM ssDNA with a change in approximately 20% of the droplets).

6.3.2 Characterization of polyplex formation

Next, we sought to monitor the hybridization of ssDNA at PLL-5CB droplets with its complementary ssDNA sequence (c-ssDNA) on those droplets. To our surprise, the addition of c-ssDNA onto ssDNA coated PLL-5CB droplets does not trigger the reordering in the orientational transition of LC molecules; these droplets remain bipolar or pre-radial as before (Figure 6.5).

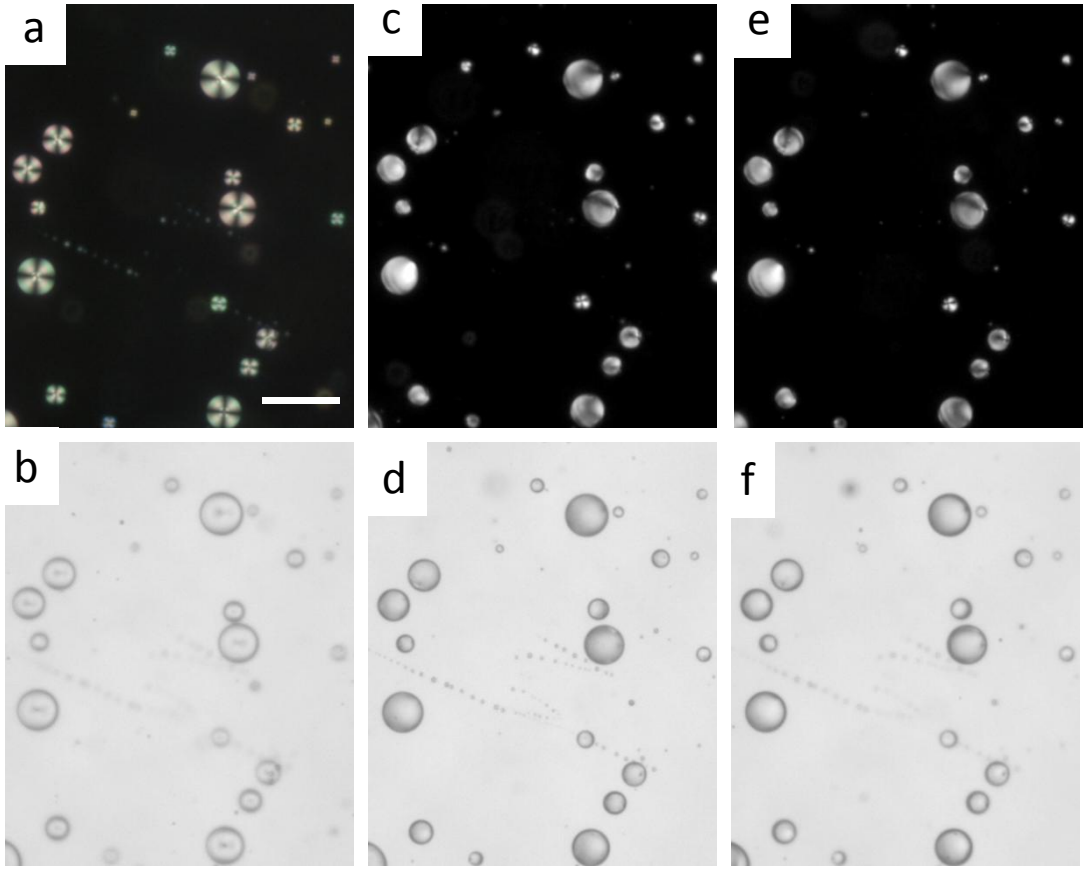

Figure 6.5. LC's response to ssDNA adsorption and hybridization with c-ssDNA: Polarized microscopy images (a,c,e) and bright-field images (b,d,f) of the PLL coated 5CB droplets before (a,b), after subsequent adsorption of 10 μM ssDNA (c,d) and after addition of 10 μM complementary ssDNA target (e,f). Scale bar = 50 μm.

This observation is in contrary to the earlier findings by Schwartz and co-workers which demonstrated that ssDNA and dsDNA impose different orientational ordering of LC molecular axis at surfactant laden LC-aqueous interface.[26,27] They proposed that the ionic interaction between anionic phosphate backbone of ssDNA and cationic surfactant along with the hydrophobic interaction between nucleobases and LC are likely responsible for homeotropic to planar orientational ordering of the LCs, while upon hybridization, the

nucleobases no longer remain exposed to interact with the LC thereby, allowing more surfactant molecules to self-assemble at LC-aqueous interface leading to the reorientation of the LCs to homeotropic alignment. In our case, the reordering of the LC does not take place in the presence of c-ssDNA. We propose a plausible event taking place in the ssDNA-PLL-5CB system. First, ssDNA forms a very strong ionic complex with PLL (i.e., *polyplex*) at LC/aqueous interface, thereby causing an orientational transition of PLL-LC droplets from radial to bipolar/pre-radial. Being a high molecular weight cationic polymer, PLL can be expected to effectively neutralize the repulsion between ssDNA and c-ssDNA and allow the hybridization to occur between nucleobases of the two strands without disturbing the PLL-ssDNA interaction at the droplet interface. Second, the hybridized dsDNA remains adsorbed at the surface of PLL-LC droplets and maintains the anionic charge density on PLL-LC droplets required to retain the bipolar/pre-radial configuration of those droplets. Therefore, we add that perhaps hydrophobic interactions between nucleobases and LCs do not play any significant role in determining the internal configuration of the director of LCs inside the PLL-LC droplets. In addition, hybridization could also be restricted due to the formation of polyplexes between ssDNA and PLL at LC/aqueous interface.

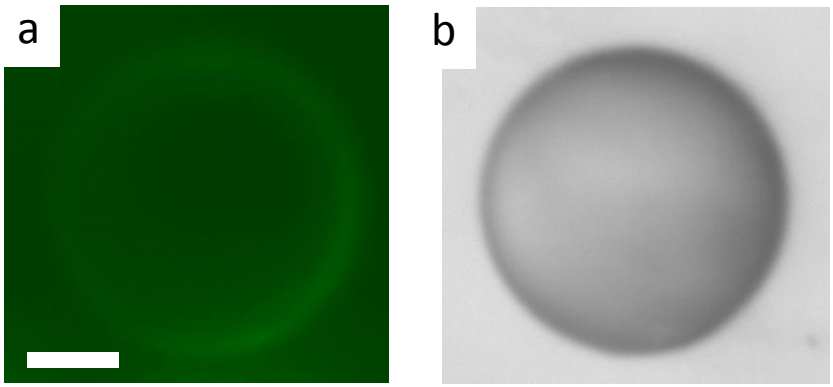

Figure 6.6. Epi-fluorescence microscopic image (a) and corresponding bright-field image (b) of an ssDNA adsorbed PLL-5CB droplet after incubation with 30 μM FAM tagged fluorescent c-ssDNA. Little fluorescence at the surface of droplets shows the presence of c-ssDNA while the bright field image confirms the bipolar configuration of PLL-LC droplet. Scale bar = 10 μm.

In order to prove the above hypothesis, we carried out a series of experiments. First, we intend to visually locate the c-ssDNA upon addition to ssDNA-PLL-5CB droplets. When

FAM-c-ssDNA-(ssDNA-PLL-5CB) droplets were imaged under fluorescence and bright field microscopy, green fluorescence was spotted around the surface of the bipolar 5CB droplets confirming the presence of c-ssDNA on the ssDNA-PLL-5CB droplets (Figure 6.6). Here, we would like to state that the fluorescence observed on FAM-c-ssDNA-(ssDNA-PLL-5CB droplets) was less intense than that of the FAM-ssDNA-PLL-5CB droplets (keeping the exposure time constant). This can be explained by the restricted adsorption of FAM-c-ssDNA molecules on the ssDNA-PLL-5CB droplets, primarily due to the less exposed nucleobases of the ssDNA for H-bonding with c-ssDNA (after ssDNA forms polyplex with PLL), (*vide infra*) at LC-aqueous interface. Next, we aimed to determine the formation of polyplex between ssDNA and PLL at LC/aqueous interface. For that, 30 µM FAM-ssDNA was incubated with PLL-5CB droplets in the presence of excess PLL. Fluorescence microscopic and bright-field investigations in Figure 6.7 reveal the intense fluorescent structures present at the bipolar droplets' surface and in the surrounding solution. The observed fluorescent structures are proposed as a result of complex formation between ssDNA and PLL, i.e., polyplexes resulting probably due to the attractive electrostatic interaction between negatively charged phosphate backbone of ssDNA and positively charged PLL.

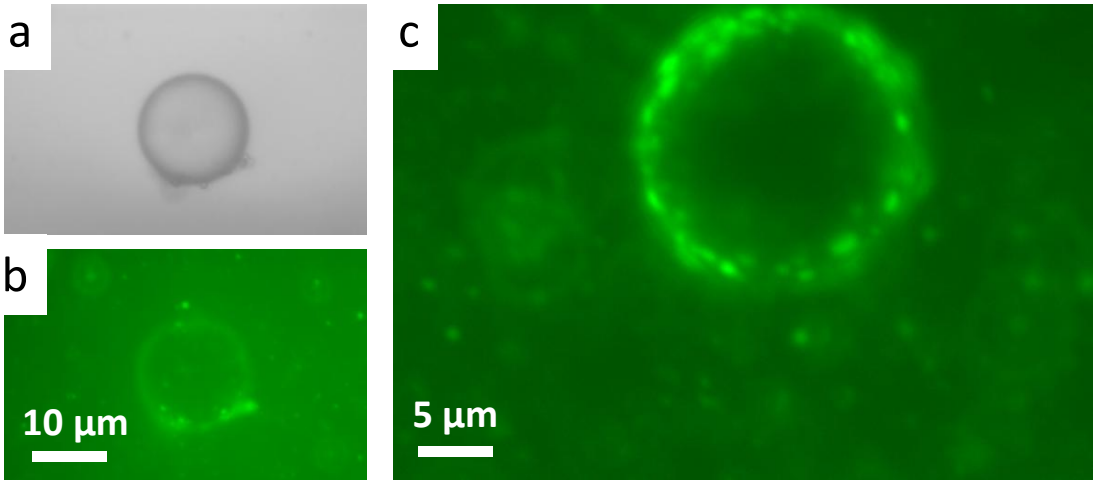

Figure 6.7. Bright-field (a) and corresponding epi-fluorescence microscopic image (b) of a PLL-5CB droplet after adsorption of 30 µM FAM tagged fluorescent ssDNA in the presence of excess PLL. Epi-fluorescence microscopic image (c) corresponds to another PLL-5CB droplet after adsorption of 30 µM FAM fluorescent ssDNA clearly showing the presence of fluorescent polyplexes at the surface of the droplet.

We further employed atomic force microscopy (AFM) to characterize the morphology of polyplex formed. In Figure 6.8a, AFM image of polyplexes shows the spherical-shaped structures with their sizes ranging from ~60 nm to ~400 nm in diameter, consistent with the previous reports.[34,35] When ssDNA or PLL alone were observed by AFM (Figure 6.8b or c), no such structures were observed which confirms the formation of compact nano complexes between PLL and ssDNA as shown in Figure 6.8a.

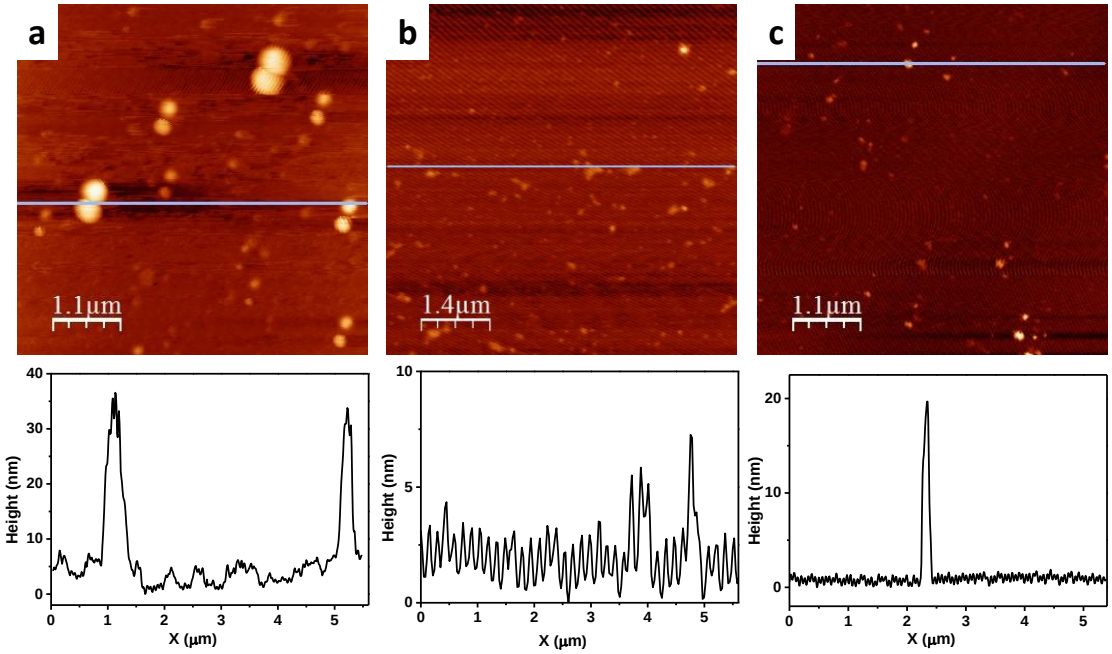

Figure 6.8. AFM topography of the (a) polyplex (complexes of PLL and ssDNA), (b) ssDNA and (c) PLL onto hydrophilic mica substrate. The respective height profiles corresponding to the lines drawn on the images are shown below each image.

Further, to understand the strength of the polyplex along with its ability to release ssDNA from polyplex, the effect of polyplex on the orientational configuration of PLL-5CB droplets was monitored. 5 µL of the pre-incubated mixture of 0.5 mg/mL PLL and 50 µM ssDNA was added to 5 µL PLL-5CB droplets already placed on a glass slide. It was observed that the radial configuration of the PLL-5CB droplets remains unchanged upon introduction of polyplex, suggesting the unavailability of ssDNA to cause the configurational transition of the PLL-5CB droplets (Figure 6.9a,b). Moreover, when 30 µM of free ssDNA was added on the same PLL-5CB droplets, the LC droplets changed their configuration from radial to bipolar/pre-radial in less than 10s (Figure 6.9c). These observations strengthen our proposition that ssDNA forms a very stable and strong polyplex with PLL. As a result, ssDNA is not freely released from the polyplex. Thus, it

is unable to interact with PLL at the surface of PLL-5CB droplets, ultimately failing to trigger the configurational transition of the LC droplets.

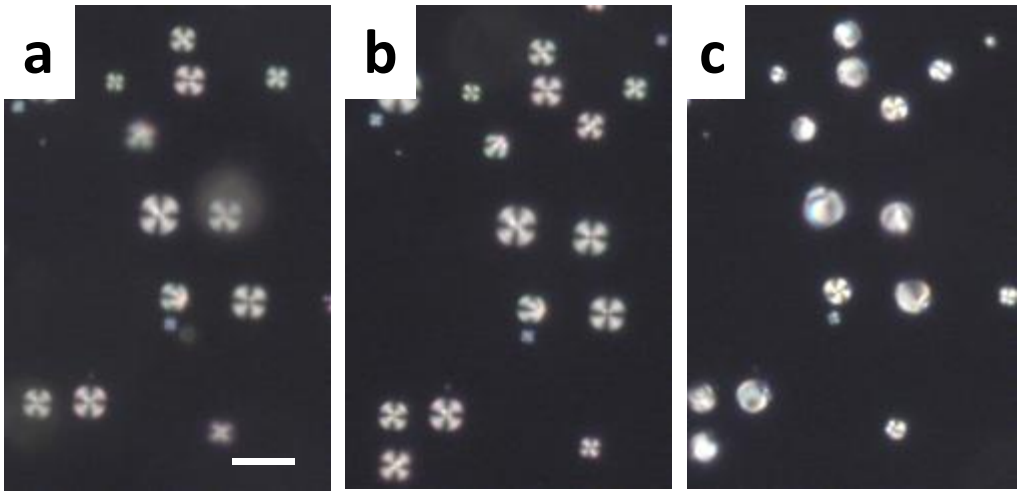

Figure 6.9. Polarized microscopy images of PLL-5CB droplets (a) before (b) after addition of pre-incubated mixture of 0.5 mg/mL PLL and 50 μM ssDNA and (c) after 30s of subsequent addition of free ssDNA. Scale bar = 50 μm.

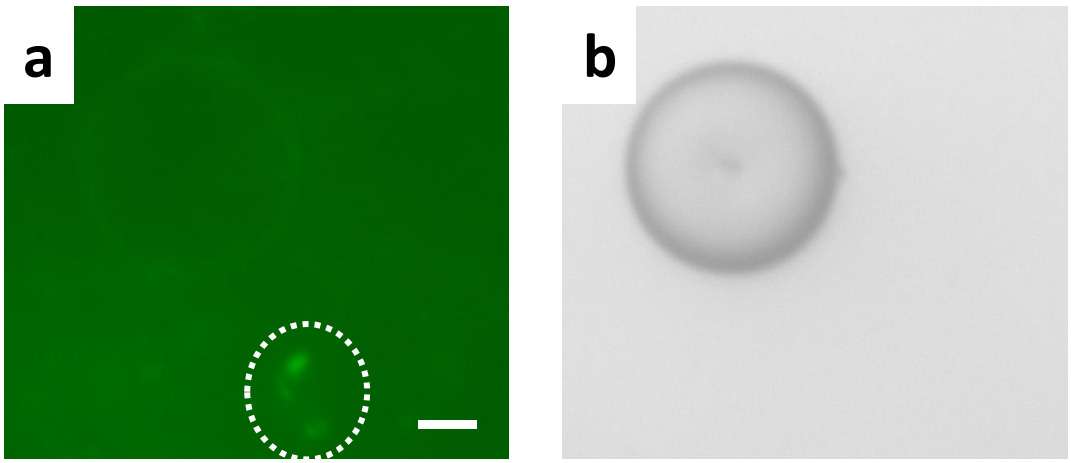

Figure 6.10. Epi-fluorescence microscopic image (a) and corresponding bright-field image (b) of PLL-coated 5CB droplets suspended in tris buffer after the pre-incubated mixture of PLL and 50 μM FAM tagged fluorescent ssDNA. Scale bar = 10 μm.

To further visually locate the ssDNA in the polyplex on PLL coated 5CB droplets, fluorescent polyplex was prepared by adding 50 μM FAM-ssDNA with 0.5 mg/mL PLL and then subsequently incubated with PLL-5CB droplets for 30 minutes in the dark. As expected, PLL-LC droplets were seen to retain radial configuration with a single defect at the center of the droplets as observed under bright-field microscopy. In fluorescence

microscopy, little fluorescence around the droplet was observed and intensely fluorescent polyplex structures (highlighted in Figure 6.10a) were observed near the 5CB droplet suggesting that very small amount of ssDNA from polyplex is adsorbed at the surface of PLL-5CB droplet. Besides, this amount of anionic charge density of ssDNA cannot induce bipolar/pre-radial configuration in PLL-coated 5CB droplets (Figure 6.10b). In addition, the literature survey reveals how the PLL's high affinity for DNA has been the limiting factor in successful transfection during gene delivery. High molecular weight PLL-based polyplexes have shown a reduced capacity for dissociation than their low molecular weight counterparts which dissociate readily and are more efficient in transfection.[36] Our experiments add further insight in understanding how the orientational ordering of LC inside the PLL-coated 5CB droplets is triggered by anionic charge density of DNA at the LC/aqueous interface provided by either polyplex formation after adsorption of ssDNA or c-ssDNA after hybridization at LC/aqueous interface.

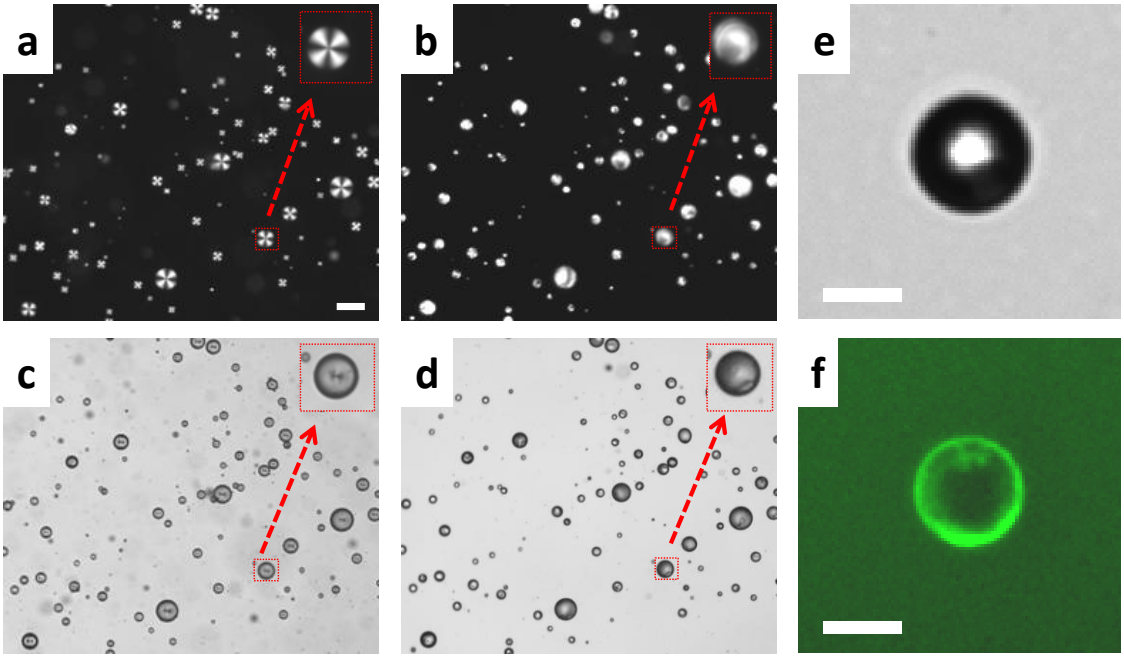

Figure 6.11. Polarized optical and corresponding bright-field micrographs images of PLL-5CB droplets (a,c) before and (b,d) in contact with 30 µM dsDNA. The LC droplets were in radial states (a,c) before but transitioned to bipolar/pre-radial state (b,d) after addition of dsDNA. The insets within (a-d) indicate the higher magnification version of the red arrow marked LC droplet. Scale bar = 50 µm. Bright-field microscopic (e) and corresponding epi-fluorescence image (f) of a PLL-coated 5CB droplet following 60 min incubation with 30 µM FAM tagged fluorescent dsDNA. Green fluorescence present on

the surface of the droplets supports the adsorption of FAM tagged dsDNA. Scale bar = 10 μm.

Next, we sought to verify the role of interactions of nucleobases with 5CB LC or PLL in decoding the orientational transitions of PLL-5CB droplets. As a proof of concept, we chose dsDNA which offers anionic phosphate backbone and unexposed nucleobases and further hypothesized that dsDNA would provide a similar orientational response of PLL-5CB droplets as was seen with ssDNA. When 5 μL of 30 μM dsDNA was introduced on 5 μL PLL-5CB emulsion droplets, initial radial droplets started changing their configuration to bipolar/pre-radial within seconds of addition and 100 % droplets changed to bipolar/pre-radial within 10 min as observed under POM and bright field microscopy (Figure 6.11a-d). When fluorescently labeled dsDNA was used, dsDNA was preferentially located at the surface of the droplets confirming the adsorption of dsDNA at the surface of PLL-5CB droplets (Figure 6.11e,f). The configuration transition of PLL-LC droplets upon adsorption of dsDNA reveals the importance of electrostatic forces between DNA (ssDNA/dsDNA) and PLL over hydrophobic interactions between nucleobases and 5CB molecules. This proves that hydrophobic interactions between ssDNA and LC are unlikely responsible for configuration transition from radial to bipolar/pre-radial in PLL-LC droplets.

6.3.3 Application of DNA modified PLL-LC droplets in controlled drug delivery

After establishing the principles that trigger DNA-induced configurational transition in PLL coated LC droplets, we plan to exploit stronger affinity of those PLL-LC droplets for DNA and sought to demonstrate if our novel PLL coated LC droplets could provide a platform to understand and study the controlled drug release profile from dsDNA based drug delivery systems. For this, we propose that anti-cancer drug molecules intercalated in dsDNA can be released over time when dsDNA-drug complex comes in contact with PLL-LC droplets as a result of competitive interaction between dsDNA and PLL-5CB droplets. As a proof of concept, propidium iodide (PI) displacement assay was used as this along with ethidium bromide displacement fluorescence assay is the most common method to investigate the binding of polyammonium cations to DNA.[37-40] This assay was employed due to the two important functions that PI fulfills. First, PI binds to dsDNA only (not ssDNA) enhancing fluorescence emission of PI (20-30 times more than that of the isolated PI) providing a straightforward quantification of the PI encapsulated in

dsDNA (as confirmed in Figure 6.12). This fluorescence assay rules out the contribution of fluorescence intensity from the released PI present in the solution. Second, it (PI) intercalates in between the dsDNA strands *via* non-covalent interactions such as H-bonding and pi-pi stacking interactions with its nucleobases, similar to the mechanism by which various anti-tumor drugs such as doxorubicin bind to the DNA bases.[41] Therefore, PI presents itself as the best drug substitute.

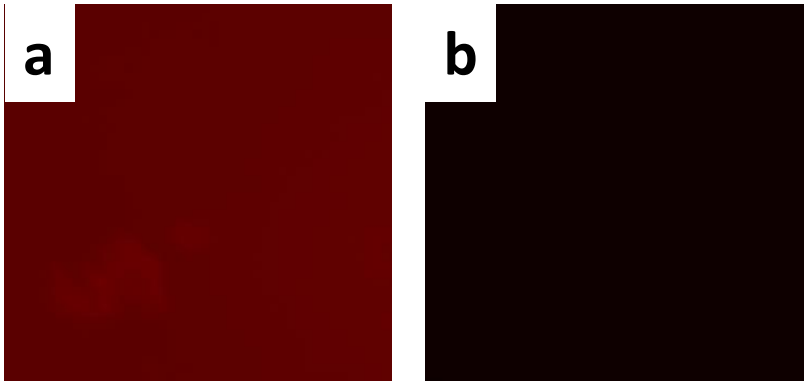

Figure 6.12. Epifluorescence image of the pre-incubated solution of propidium iodine bound FAM tagged (a) dsDNA showing red fluorescence (b) ssDNA showing no fluorescence at same exposure time.

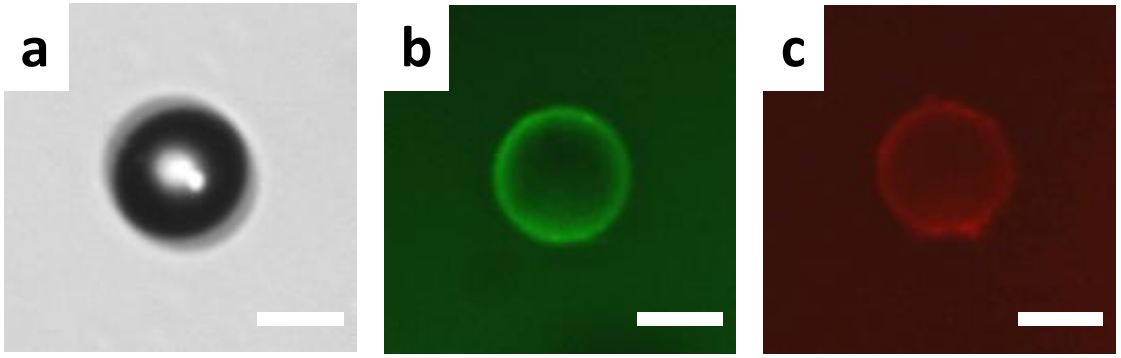

Figure 6.13. Bright-field image (a) showing the bipolar configuration and epi-fluorescence microscopic images (b) under 460 nm excitation filter and a 534 nm emission filter showing green fluorescence of FAM-dsDNA and (c) red fluorescence of PI on a PLL-5CB droplet following 30 min incubation with PI intercalated FAM tagged dsDNA. Scale bar = 10 μm.

Motivated by this, next, we designed experiments to observe the effect of the dsDNA-PI complex on the configuration of the PLL-LC droplets. Herein, PI encapsulated FAM labeled dsDNA was incubated with PLL-LC droplets for 30 min before the observation.

In Figure 6.13, bright field microscopy reveals the bipolar droplets confirming the configurational transition of the PLL-LC droplets. Fluorescence microscopy reveals the direct correspondence between the location of PI (red) and dsDNA (green) fluorescence at the surface of the droplets confirming the adsorption of dsDNA-PI complex at PLL-LC droplets. In particular, the fluorescent PI was favorably confined at the LC/aqueous interface of the droplet where the green fluorescent dsDNA was present.

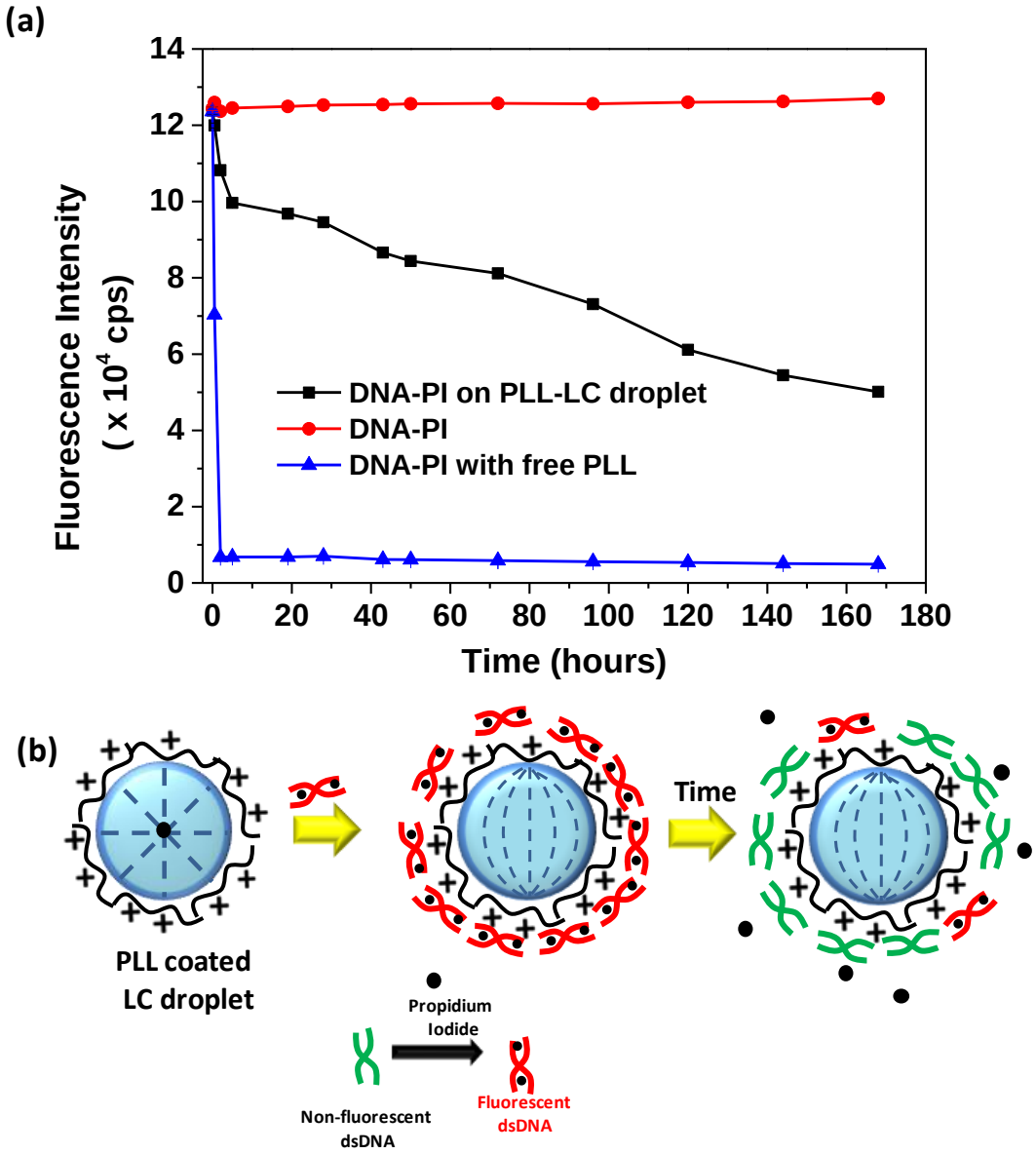

Figure 6.14. (a) Fluorescence intensity vs. time plot showing fluorescence intensity of propidium iodide in the presence of TBS buffer (red curve), an aqueous solution of PLL (blue curve) and PLL-LC droplets (black curve) at pH 7.4. Decay in fluorescence of PI in the presence of PLL-LC droplets and PLL indicates the controlled and fast release of PI from DNA-PI complex, respectively. (b) Schematic illustration demonstrating the

preservation of the orientational configuration of the LC droplets during PI release from its complex with DNA induced by PLL-5CB droplets over time.

Next, we studied the behaviour of PI release profile from DNA at room temperature upon the interaction of the dsDNA-PI complex with PLL-5CB droplets with time using steady-state fluorescence. Herein, we used non-fluorescent dsDNA and incubated it with PI as to avoid the complexity in the system. The detected fluorescence intensity of the PI was plotted against the droplets incubation time (Figure 6.14a). In presence of PLL solution, it can be seen that fluorescence intensity of PI upon addition of PLL decreased to almost half within 30 min and to minimum in 2 hours reflecting that PLL effectively and swiftly displaces the PI from dsDNA-PI complex whereas, in absence of PLL, the fluorescence intensity of PI remains approximately same over a period of 6 days suggesting the stable intercalation of PI in dsDNA strands over this period of time. This observation is in agreement with the previous studies where binding of the various PLLs to plasmid DNA has been studied using a fluorescence quenching assay involving ethidium bromide.[42,43] However, when the dsDNA-PI complex was incubated with PLL-5CB droplets, the red fluorescence intensity of PI started decreasing gradually, dipping to approx. its one-third value in 144 hours (demonstrated by black plot in Figure 6.14a). These data show that PI binding sites in DNA become gradually unavailable with increasing PLL-DNA binding at LC-aqueous interface. The gradual decrease in the fluorescence intensity can be explained by the limited effectiveness of the PLL bound on 5CB droplets than the free PLL which rapidly displaces the PI from DNA. Figure 6.14b shows the cartoon representation of the orientational configurations of the PLL-LC droplets upon adsorption of DNA-PI complex and after the release of PI from the complex induced by PLL-5CB droplets over time.

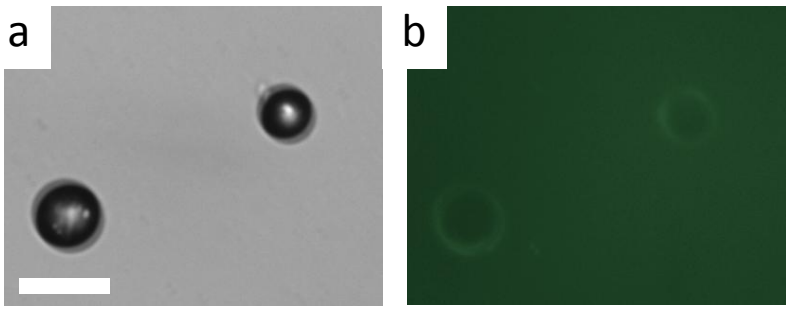

Figure 6.15. Bright-field (a) and corresponding epi-fluorescence microscopic image (b) 460 nm excitation filter and a 534 nm emission filter of PLL-LC droplets after incubation with PI-(FAM-DNA) complex after six days confirming the bipolar configuration of LC

droplets along with the presence of FAM-DNA at the surface of LC droplets. Scale bar = 20 µm.

Even after six days, (DNA-PI)-PLL-5CB droplets were found to retain their bipolar configuration confirming the sustained and stable adsorption of FAM tagged dsDNA at PLL-LC droplets (Figure 6.15). Hence, the PLL-5CB droplets have been shown as a novel prototype where LC (5CB) droplet interface slowly induces drug release from DNA while maintaining the adsorption of DNA at the interface which can be monitored by the internal configuration of the LC droplets.

6.4 Conclusions

In summary, our study describes that PLL-coated LC droplets provide a simple method to detect ssDNA/dsDNA at LC-aqueous interfaces. Our approach is able to detect oligonucleotides through changes in the configurational transition of the droplets from radial to bipolar or pre-radial. The method is highly sensitive, and we believe electrostatic interactions between PLL and DNA (and not hydrophobic interaction of nucleobases) plays a major role in the ordering transition. We also show that DNA functionalized PLL-coated droplets can be used as a simple measure to study the controlled drug (model) release from DNA-drug complex utilizing the stronger competitive interaction of DNA with PLL that weaken the interaction between DNA and drug. These findings demonstrated the use of PLL coated LC droplets to study other biological interactions and also open a new venture in further development to study controlled drug release from DNA based drug delivery systems.

6.5 Experimental Section

6.5.1 Materials

Oligonucleotides sequences TGG TGA AGT AGA TGT GTA (ssDNA), TAC ACA TCT ACT TCA CCA (C-ssDNA), TTT CGC AAT GAC TGT ACT (NC-ssDNA), 5'6-Fluorescein tagged -TGG TGA AGT AGA TGT GTA (FAM-ssDNA) were purchased from IDT Technologies. 4-Cyano-4-pentylbiphenyl (5CB), propidium iodide (PI), tris buffered saline (TBS) and poly-L-lysine (PLL) solution 0.1 % (w/v) in H_2O (Mol. Wt. 250 kDa) were obtained from Sigma-Aldrich (St. Louis, MO). The E7 LC was obtained from Merck (Mumbai, India). Deionization of a distilled water (DI water) source was

performed using a Milli-Q-system (Millipore, bedford, MA). Fisher's Finest Premium grade glass microscopic slides were obtained from Fischer Scientific (Pittsburgh, PA).

6.5.2 Preparation of PLL modified LC droplets

Recently, Sumyra and coworkers reported the fabrication of polyelectrolyte modified PLL-LC droplets.[17] In this work, we have coated the LC droplets with single layer by modifying their method. PLL-LC (5CB or E7) droplets were formed as follows. First, 5CB droplets were prepared by vortexing 10 μL of LC in 1mL DI water, followed by sonication for 5 minutes. The resultant emulsion was centrifuged at 5000 rpm for 5 min and the supernatant was replaced by 1 mg/mL PLL solution. The PLL-LC droplets were kept for 30 min at room temperature for the adsorption of PLL on the LC droplets. Adsorption of PLL on the surface of the LC droplets leads to the radial configuration of the director of LC molecules inside the droplet. The PLL-modified LC droplets were then washed with DI water through centrifugation in order to remove the excess PLL and were re-suspended in DI water or TBS at different pH for further experiments.

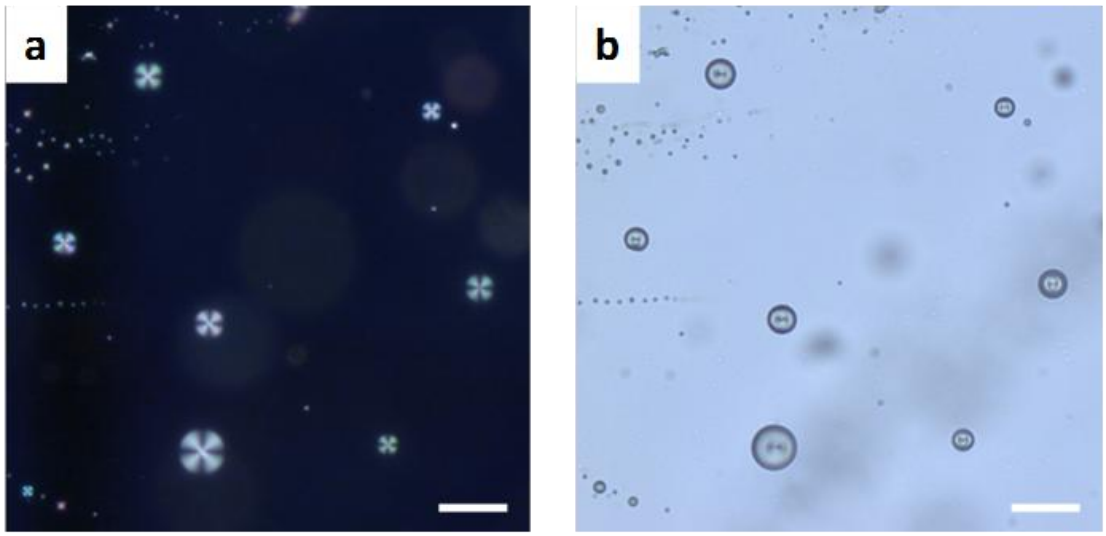

Figure 6.16. Polarized (a) and corresponding bright field (b) microscopy images of PLL modified 5CB droplets suspended in DI water after 82 days. Scale bar = 50 μm.

To estimate the number of droplets in the emulsion, 1 μL of the PLL-5CB droplet solution was placed on a clean glass slide and multiple POM images were captured to illustrate the whole sample area. From the POM images, the total number of droplets was counted to be ~2 x 10^3 droplets per μL. Size of the polydispersed PLL coated LC droplets

ranges from 5 μm to 40 μm as conceived from the POM images. These PLL coated LC droplets were observed to be stable in radial configuration for atleast a month or so (as shown in Figure 6.16) and the zeta potential measurement has been measured as + 25.0 mV suggesting the coating of cationic PLL residues.

6.5.3 Optical characterization of PLL-LC droplets

The orientational ordering of the LC was determined using a Zeiss polarizing microscope (Scope. A1 with cross polars with magnifications X200 and X1000). All the images were captured using a AxioCam Camera.

6.5.4 Adsorption of ssDNA

In experiments associated with the adsorption of ssDNA on PLL coated 5CB droplets, 5 μL of the aqueous solution of ssDNA of different concentrations was added on 5 μL of 5CB emulsion (if not stated otherwise) already placed on a clean glass slide. The droplets were real time imaged under polarized optical and bright field microscope. For the transition curve of adsorption of ssDNA, fixed volume of PLL-LC emulsion droplets (5 μL or 1 μL) was exposed to different concentrations of ssDNA with a constant adsorption time (20 min) and the percent transition of the droplets from radial to pre-radial/bipolar upon addition of ssDNA (calculated from three sets of experiments) was plotted against the concentration of ssDNA. Excess PLL containing PLL-5CB droplets were prepared by sonicating 10 μL 5CB in 1 mL aqueous solution of PLL and used as such, without removing the unbound PLL by centrifugation. These experiments were also reproduced using PLL modified E7 droplets.

6.5.5 Zeta potential measurements

Zeta potential measurements of the PLL coated 5CB droplets were carried out using Zetasizer Nano ZS90 (Malvern Instruments Inc.) at room temperature under a cell-driven voltage of 30 V. In a typical experiment, 40 μL of PLL-5CB droplets was diluted with water to make total 800 μL solution before transferring into the zeta potential cuvette and the average of 5 scans was taken for each measurement. For experiments with ssDNA, 10 μL of stock solution of ssDNA was added to the 40 μL PLL-5CB droplet emulsion to make the final required concentration of ssDNA and incubated for 15 minutes before diluting to 800 μL aqueous solutions.

6.5.6 Epifluorescence imaging of PLL-LC droplets

50 µL of PLL coated 5CB droplets were incubated with 30 µL of 30 µM FAM-ssDNA (final concentration of ssDNA becomes 11.25 µM) for 60 minutes and washed thrice with buffer prior to fluorescence imaging performed with a Zeiss (Scope. A1) fluorescence microscope. For experiments with complementary ssDNA on ssDNA-PLL modified 5CB droplets, 30 µL of 30 µM FAM tagged c-ssDNA was introduced in 11.25 µM ssDNA coated PLL-5CB emulsion (80 µL) and incubated for 30 minutes prior to fluorescence investigation. The samples were viewed using a fluorescence filter cube with a 460 nm excitation filter and a 534 nm emission filter. Images were obtained with an AxioCam camera attached to the microscope.

6.5.7 Steady-state fluorescence of PLL-LC droplets

All the steady state fluorescence measurements were carried out on a FluoroMax-4 spectrofluorometer from Horiba Jobin Yvon at ~25°C. dsDNA was prepared by mixing equal volumes of ssDNA and c-ssDNA of same molar concentration for 12 hours at RT. Hybridization of the ssDNA and c-ssDNA has been confirmed by the gel electrophoresis (Figure 6.17). Encapsulation of PI with dsDNA was carried out by mixing together 150 µM dsDNA and 375 µM PI and incubated for 48 hours in dark with occasional mild stirring. 6 µL of the stock mixture containing 150 µM dsDNA and 375 µM PI was added in 200 µL TBS (pH 7.4) or 200 µL 0.5 mg/mL PLL or 200 µL PLL coated 5CB droplets emulsion suspended in TBS (pH 7.4) and kept for incubation for 10 minutes in dark at room temperature. Aliquots from the samples were withdrawn at different time intervals and the fluorescence intensity of PI (three measurements) was collected at the following parameters: λ_{ex} = 540 nm, λ_{em} = 617 nm, excitation slit width = 1 nm, emission slit width = 4 nm, integration time = 2 seconds. All the fluorescence data were acquired using the FluorEssence software (provided with the instrument) which were later re-plotted using Origin Pro version 9 software.

6.5.8 Atomic force microscopy

Samples of PLL or ssDNA were prepared by diluting 10 times the aqueous solution of 0.5 mg/mL PLL or 50 µM ssDNA. 5 µL of the diluted sample was loaded on a freshly cleaved, water-washed muscovite mica (Grade V-4 mica from SPI, PA), allowed to air dry for 15-20 minutes. Polyplexes were prepared by mixing together the aqueous

solutions of ssDNA and PLL yielding final concentrations of 50 µM ssDNA and 0.5 mg/mL PLL, respectively, which was further diluted 10 times before proceeding for AFM as described above.

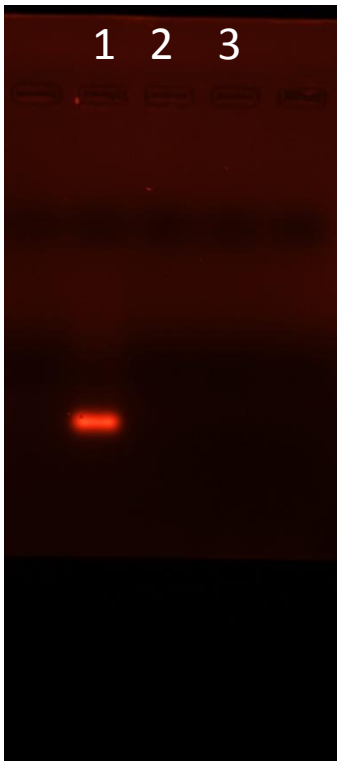

Figure 6.17. Gel electrophoresis (DNA and ethidium bromide assay): Well 1 contains single strand DNA sequence and its complementary ssDNA. Well 2 contains only ssDNA and well 3 contains ssDNA with its non complementary ssDNA sequence.

References

1. Gupta, J. K.; Sivakumar, S.; Caruso, F.; Abbott, N. L. *Angew. Chem. Int. Ed.* **2009**, *121*, 1680–1683.
2. Sivakumar, S.; Gupta, J. K.; Abbott, N. L.; Caruso, F. *Chem. Mater*. **2008**, *20*, 2063–2065.
3. Tjipto, E.; Cadwell, K. D.; Quinn, J. F.; Johnston, A. P.; Abbott, N. L.; Caruso, F. *Nano Lett*. **2006**, *6*, 2243–2248.
4. Aliño, V. J.; Pang, J.; Yang, K. L. *Langmuir* **2011**, *27*, 11784−11789.
5. Kim, J.; Khan, M.; Park, S.-Y. *ACS Appl. Mater. Interfaces* **2013**, *5*, 13135–13139.
6. Lin, I. H.; Miller, D. S.; Bertics, P. J.; Murphy, C. J.; de Pablo, J. J.; Abbott, N. L. *Science* **2011**, *332*, 1297-1300.
7. Sivakumar, S.; Wark, K. L.; Gupta, J. K.; Abbott, N. L.; Caruso, F. *Adv. Funct. Mater*. **2009**, *19*, 2260–2265.
8. Aliño, V. J.; Tay, K. X.; Khan, S. A.; Yang, K.-L. *Langmuir* **2012**, *28*, 14540-14546.
9. Yoon, S. H.; Gupta, K. C.; Borah, J. S.; Park, S.-Y.; Kim, Y. K.; Lee, J.-H.; Kang, I.-K. *Langmuir* **2014**, *30*, 10668-10677.
10. Bera, T.; Fang, J. *Langmuir* **2013**, *29*, 387-392.
11. Khan, M.; Park, S.-Y. *Colloids Surf. B: Biointerfaces* **2015**, *127*, 241-246.
12. Bera, T.; Deng, J.; Fang. J. *J. Phys. Chem. B* **2014**, *118*, 4970−4975.
13. Bera, T.; Fang, J. *J. Mater. Chem.* **2012**, *22*, 6807-6812.
14. Gupta, J. K.; Zimmerman, J. S.; de Pablo, J. J.; Caruso, F.; Abbott, N. L. *Langmuir* **2009**, *25*, 9016-9024.
15. Khan, W.; Choi, J. H.; Kim, G. M.; Park, S.-Y. *Lab Chip* **2011**, *11*, 3493-3498.
16. Kinsinger, M. I.; Buck, M. E.; Abbott, N. L.; Lynn, D. M. *Langmuir* **2010**, *26*, 10234-10242.
17. Sidiq, S.; Krishna Prasad, G. V. R.; Mukhopadhaya, A.; Pal, S. K. *J. Phys. Chem. B* **2017**, *121*, 4247-4256.
18. Sidiq, S.; Pal, S. K. *Proc. Indian Natn. Sci. Acad.* **2016**, *82*, 75-98.
19. Setia, S.; Sidiq, S.; *De, J.; Pani, I.;* Pal, S. K. *Liq. Cryst.* **2016**, *43*, 2009-2050.
20. Niemz, A.; Ferguson, T. M.; Boyle, D. S. *Trends Biotechnol*. **2011**, *29*, 240–250.

21. Kirby, J.; Heath, P. R.; Shaw, P. J.; Hamdy F. C. *Adv. Clin. Chem*. **2007**, *44*, 247–292.
22. Stone, D. *Viruses* **2010**, *2*, 1002–1007.
23. Mohan, P.; Rapoport, N. *Mol. Pharmaceutics* **2010**, *7*, 1959-1973.
24. D'Souza, S. A. *Advances in Pharma.* **2014**, *2014*, 1-12.
25. Schwarzl, R.; Du, F.; Haag, R.; Netz, R. R. *Eur. J. Pharm. Biopharm.* **2017**, *116*, 131-137.
26. Price, A. D.; Schwartz, D. K. *J. Am. Chem. Soc.* **2008**, *130*, 8188-8194.
27. McUmber, A. C.; Noonan, P. S.; Schwartz, D. K. *Soft Matter* **2012**, *8*, 4335–4342.
28. Noonan, P. S.; Roberts, R. H.; Schwartz, D. K. *J. Am. Chem. Soc*. **2013**, *135*, 5183−5189.
29. Lai, S. K.; Hartono, D.; Yang, K-L. *Appl. Phys. Lett*. **2009**, *95*, 153702-153704.
30. Xiao, F.; Tan, H.; Wu, Y; Liao, S.; Wu, Z.; Shen, G.; Yu, R. *Analyst* **2016,** *141***,** 2870-2873.
31. Tan, H.; Li, X.; Liao, S.; Yu, R.; Wu, Z. *Biosens. Bioelectron.* **2014**, *62*, 84–89.
32. Munir, S; Park, S-Y. *Sens. Actuators B Chem.* **2016**, *233*, 559–565.
33. Zhou, J.; Dong, Y.; Zhang, Y.; Liu, D.; Yang, Z. *Nanomaterials* **2016**, *6*, 229-238.
34. Wolfert, M. A.; Schacht, E. H.; Toncheva, V.; Ulbrich, K.; Nazarova, O.; Seymour, L. W. *Gene Ther*. **1996**, *3*, 269-273.
35. Mann, A.; Richa, R.; Ganguli, M. *J. Control. Release* **2008**, *125*, 252-262.
36. Ilarduya, C. T.; Sun, Y.; Düzgüneş, N. *Eur. J. of Pharma. Sci*. **2010**, *40*, 159–170.
37. Cain, B. F.; Baguley, B. C.; Denny, W. A. *J. Med. Chem*. **1978**, *21*, 658-668.
38. Gershon, H.; Ghirlando, R.; Guttman, S. B.; Minsky, A. *Biochemistry* **1993**, *32*, 7143-7151.
39. Zadmard, R.; Schrader, T. *Angew. Chem*. **2006**, *118*, 2769-2772; *Angew. Chem.Int. Ed*. **2006**, *45*, 2703-2706.
40. Izumrudov, V. A.; Zhiryakova, M. V.; Goulko, A. A. *Langmuir* **2002**, *18*, 10348-10356.
41. K. Vogel, K.; Wang, S.; Lee, R. J.; Chmielewski, J.; Low, P.S. *J. Am. Chem. Soc.* **1996**, *118*, 1581-1586.
42. Xu, Y.; Szoka, F. C. *Biochemistry* **1996**, *35*, 5616–5623.
43. Wolfert, M. A.; Dash, P. R.; Nazarova, O.; Oupicky, D.; Seymour, L. W.; Smart, S.; Strohalm, J.; Ulbrich, K. *Bioconjug. Chem*. **1999**, *10*, 993–1004.

Conclusions and Future Outlook

The work in this thesis mainly addresses the fundamental challenges towards the development of stimuli-responsive interfaces formed between liquid crystals (LCs) and aqueous phase for potential applications in bio-sensing and diagnostics. In particular, interfacial events occurring at those interfaces involving biomolecules can lead to surface-driven ordering transitions of the LCs (providing an optical output), which can be performed under ambient light without the need of electrical power. The 1st chaper of this thesis briefly introduces the potential of aqueous-LC interface as a sensing platform for the detection of biomolecules and small molecules. In the 2nd chapter of the thesis, we have shown ordering transition of the LC in contact with cyclic lipopeptides at LC-water interfaces for application in label-free detection of toxic amyloids at nanomolar concentrations. The results certainly motivate the community to explore more sustainable lipopeptide-based LC materials for the expansion of multifunctional detection assays. The scope of this approach can also be extended for monitoring other biomolecular interactions (such as an enzymatic activity) as well. Not only this, we believe that self-assembly of these lipopeptides at LC-aqueous interface in curved geometry (such as LC droplets) will reveal a set of rich information about their molecular organization at those interfaces. In the 3rd chapter of this thesis, we report a new strategy for label-free detection of lead (II) ions in aqueous media based on aptamer-metal ion binding events. Herein, we overcome the challenge of detection of small ions at LC-aqueous interfaces with remarkable sensitivity and selectivity. This approach opens a wide array of opportunities for sensing of other toxic metal ions and small molecules/biomolecules (such as ochratoxin and thrombin) based on their specific binding with the aptamers. In the 4th chapter of this thesis, we demonstrate a simple design for label-free and selective detection of an important biomarker, creatinine. In the near future, we believe that the model can be customized and commercialized with industrial support, thus may enable the clinical diagnosis of creatinine handy and more simpler. It can also be predicted that a similar approach using LC emulsions may lead to enhanced sensitivity of the target biomarker. In the 5th and 6th chapters of this thesis, we show the utility of poly-L-lysine (PLL) coated LC emulsion droplets in real-time imaging of proteins and DNA. We further believe that these PLL-LC droplets can also be useful and employed to detect (in real-time) specific biomolecular interactions such as thrombin-heparin and DNA-protein binding events, to name a few. The PLL coated droplets show stability in terms of

mobility/motion and orientational ordering of LCs even in contact with glass substrate. Since the recognition of LC droplets as potential and sensitive optical sensor material, it had been challenging for researchers to characterize the mobile LC droplets without interfering with the ordering of the droplets. Thus, the work reported in the last two chapters itself is path-breaking as it eliminates one of the significant technological limitations associated with LC droplets (i.e. mobility) and will encourage researchers to develop novel LC droplet-based sensors.

APPENDICES

Appendix A

A.1 Zeta potential of proteins

Zeta potential of proteins were measured using Zetasizer Nano ZS90 (Malvern Instruments Inc.) with a cell-driven voltage of 30 V. Protein solution (final concentration = 5 μM) were freshly prepared in 20 mM TBS (pH 7.4). The aqueous solution (800 μL) of a certain protein was added into the zeta potential cuvette and the average of three scans was taken for each measurement.

Table A.1 Isoelectric points[1-5] and experimentally determined zeta potential values of proteins (5 μM)

Protein	Isoelectric Point	Zeta Potential (mV)
BSA	4.5	-17.8 ± 2.6
Hb	6.87	-1.7 ± 0.1
Cyto	10-10.5	+5.4 ± 0.2
ConA	4.8-5.5	-9.7 ± 0.8
FibN	5.0-5.5	-3.1 ± 0.7

A.2 Circular dichroism spectra of ConA and FibN

The far-UV CD experiments were performed on a Chirascan spectrophotometer (Applied Photophysics, U.K.) with a scan range of 200−260 nm and step size of 1 nm. A quartz cell (1 mm path length) was used to hold the solution of interest. Aqueous solutions of 5 μM Fib and 1 μM ConA were freshly prepared in 20 mM TBS (pH 7.4). For each sample, the spectra were averaged over 5 scans and were corrected against the buffer signal using the ProData software provided with the CD instrument.

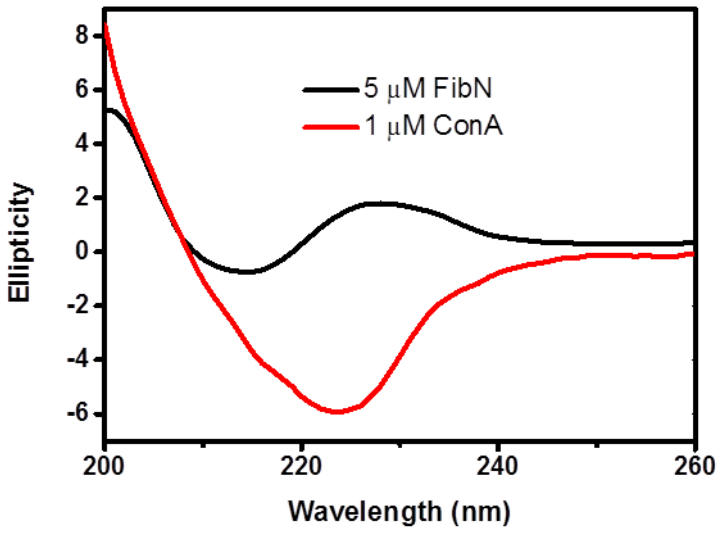

Figure A.2. Circular dichroism spectra of FibN and ConA in 20 mM TBS (pH 7.4).

Appendix B

B.1 Deposition of monolayers of Surfactin (SFN) onto LC film by Langmuir-Schaefer method

Monolayers of SFN were made using KSV NIMA Langmuir Blodgett instrument. A Langmuir film balance with a paper Wilhelmy plate is used to measure surface pressure (π). The trough area was cleaned several times using DI water and acetone prior to use. Water was used as the subphase to fill the trough. 60 μL of stock SFN solution (0.2 mg/mL) in chloroform was carefully spread onto the subphase using a microsyringe and left for 15 minutes at room temperature for the solvent to evaporate. The π-mean molecular area (A_m) isotherm was obtained using KSV NIMA software by compressing the barriers at a constant rate of 2 mm/min. To deposit SFN monolayers at the aqueous-LC interface, the Langmuir-Schaefer method was used as reported earlier.[6,7] Briefly, at required surface pressure, glass slide holding LC within TEM grid was horizontally lowered in contact with the monolayers at the air-aqueous interface and immediately immersed into optical wells containing buffer of interest for analysis under polarized optical microscope. All the observations were done at room temperature.

Figure B.1-A shows that surface pressure-area isotherm of SFN (π–A isotherm) monolayer consists of three different parts (denoted as I, II and III on the figure) at the air/water interface consistent with the previous report[8]. At the beginning of the compression, SFN molecule occupied large molecular area (part I) suggesting the

existence of monolayer in liquid-expanded (LE) state. On further compression, surface pressure increased progressively (part II) which indicates the formation of monolayer in a liquid-condensed (LC) state. Further compression of monolayer leads to a "pseudo plateau" region (part III) which appears at a collapse pressure (π_t) of about 35 mN/m and can be regarded as a transition from monolayer to multilayer. We found that liquid-expanded monolayers of SFN (at 10 mN/m), after transfer onto the LC film, resulted in planar alignment of the LC (Figure B1-B), indicating the low areal density is insufficient to orient LC at this phase. However, when liquid condensed (22 mN/m) monolayer and multilayer state (37 mN/m) monolayer was transferred to the LC-film, a homeotropic orientation of LC was observed at pH 7.2 (Figure B.1-C,D). These observations indicate that presence of a monolayer of SFN with sufficient areal density is able to orient the LC homeotropically. This observation is in agreement with previous studies[6,7] reporting Langmuir-Schaefer transfer of various lipids which concluded that molecular density of amphiphiles at the interface strongly regulates the orientation of LC they are in contact with.

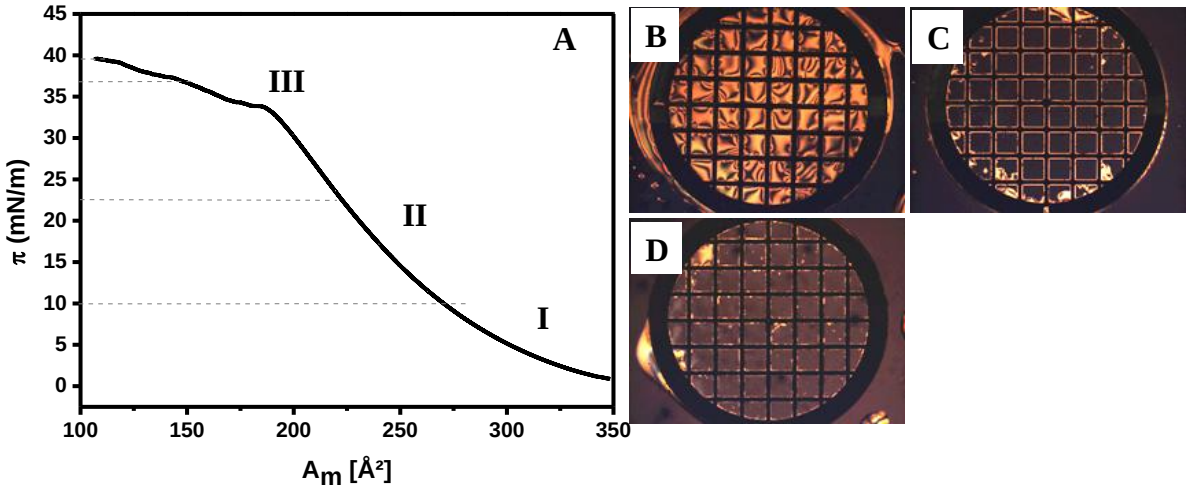

Figure B.1. (A) Surface pressure (π)-area per molecule (A_m) isotherm of SFN on water subphase at room temperature. Polarized optical images of E7 films confined in a grid placed on DMOAP functionalized glass when layer of SFN is transferred at surface pressure of (B) 10 mN/m, (C) 22 mN/m and (D) 37 mN/m and immersed in TBS buffer (pH 7.2).

B.2 Interactions between proteins and SFN in bulk solution: A fluorescence study

The fluorescence emission spectra have been recorded on a Perkin Elmer LS 55 fluorescence spectrometer using a 10 mm path length quartz cuvette. Fluorescence spectra

have been measured from 315 to 500 nm with excitation wavelength fixed at 295 nm. Excitation and emission slit widths were fixed at 5 and 10 nm respectively for recording Hb and BSA solution. For Cyto, the excitation and emission slit widths were kept 10 and 20 nm respectively. Aqueous solutions of proteins and mixture of protein-SFN were freshly prepared (10 min prior to spectra collection) in 1 mM TBS (pH 7.2). The final concentrations of Hb, BSA, Cyto and SFN in recorded samples were 5, 5, 15 and 100 μM, respectively. Proteins exhibit intrinsic fluorescence due to hydrophobic amino acids (for eg. tryptophan (Trp) residue) which are preferentially located in the hydrophobic domain of protein. Therefore, variations in fluorescence intensity/wavelength shifts of Trp emission can be monitored to extract information regarding protein conformation in presence of ligands.

Hb and SFN: The fluorescence emission of Trp in Hb, centred at 336 nm, is quenched significantly in water due to the efficient energy transfer from Trp to heme group of Hb.[9] However, in the presence of SFN, fluorescence intensity of Hb is increased suggesting that the penetration of hydrophobic chains of SFN molecule inside hydrophobic cavity and subsequent inhibition of fluorescence quenching of Trp with heme (Figure B.2-a). Thus, hydrophobic interaction between SFN monomer and Hb complex becomes evident, besides electrostatic interaction between negative residues of SFN and positive residues of Hb.

SFN and Cyto: The fluorescence spectrum of Cyto in TBS shows peaks at 392 nm and 430 nm (Figure B.2-b). The emission maximum at 392 nm arises due to the tryptophan residue which is present in the protein while the peak at 430 nm is attributed to the self-absorption of the fluorescence light by the porphyrin system of the protein.[10] Addition of SFN caused a huge blue shift in the peak from 392 to 352 nm with a slight increase in the fluorescence intensity. These changes when combined together signify the SFN binding with the protein molecules and causing the changes around hydrophobic environment of proteins.[11]

SFN and BSA: The fluorescence spectrum of native BSA was centred at 345 nm in TBS buffer which is primarily due to two tryptophan residues in protein. In the presence of SFN, we observed a blue shift of the emission maxima from 345 to 330 nm which is consistent with the changes in the environment of the tryptophan residues and an increase of hydrophobicity in the vicinity of this residue (Figure B.2-c).[12] Thus, overall the results

support the binding of SFN and BSA in bulk aqueous phase prominently due to hydrophobic interactions besides the prospective electrostatic or hydrogen bonding.

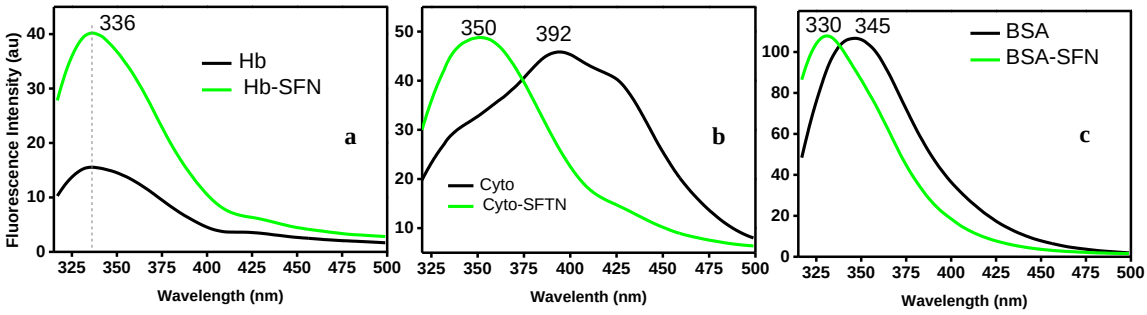

Figure B.2. Fluorescence spectra of a) Hb, b) Cyto and c) BSA in absence and in the presence of SFN at pH 7.2.

B.3 Circular dichroism measurements

A Chirascan spectrophotometer (Applied Photophysics, U.K.) was employed to record the CD spectra. Samples were taken in a 1 mm path length quartz cell and scanned from 200 to 260 nm with 1 nm step size. The mixtures of proteins and SFN were prepared in 1 mM TBS (pH 7.4) and 10 min prior to the spectra collection. The final concentration of Hb, Cyto, BSA and ConA in mixture was 1 μM each, of FibN was 2 mg/mL and of SFN was 5 μM. For each sample, the spectra were averaged over 5 scans and the buffer signal was corrected using the ProData software available with the CD instrument.

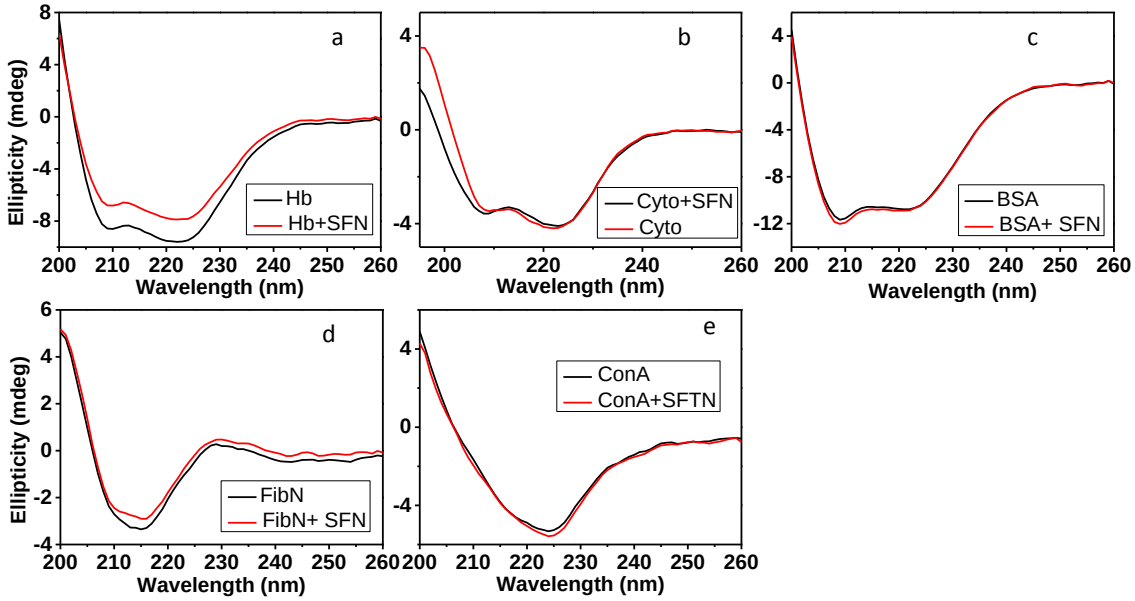

Figure B.3. CD spectra of proteins in the absence and presence of SFN in aqueous solution (pH 7.4). (a-c) CD peaks in spectra of Hb, Cyto and BSA confirms the α-helical

nature of these proteins. (d,e) CD spectra of FibN and ConA confirm the β-sheet rich secondary structure of these two proteins. In presence of SFN, the peak bands of each protein remain significantly unchanged. Thus, it is substantiated that the presence of SFN did not influence the protein's secondary structure.

References

1. Peters, T. J. San Diego (CA): Academic Press; **1995**.
2. Koepke, J. A.; Miller, L. *Ann. Clin. Lab Sci.* **1972**, *2*, 335-342.
3. Malmgren, L.; Olsson, Y.; Olsson, T.; Kristensson, K. *Brain Research* **1978**, *153*, 477-493.
4. Entlicher, G.; Koštíř, J. A.; Kocourek, J. *Biochim. Biophys. Acta* **1971**, *236*, 795–797.
5. Tooney, N. M.; Mosesson M. W.; Amrani, D. L.; Hainfeld, J. F.; Wall, J. S. *J Cell Biol.* **1983**, *97*, 1686-1692.
6. Lin, I. H.; Miller, D. S.; Bertics, P. J.; Murphy, C. J.; de Pablo, J. J.; Abbott, N. L. *Science* **2011**, *332*, 1297−1300.
7. Meli, M.-V.; Lin, I. H.; Abbott, N. L. *J. Am. Chem. Soc.* **2008**, *130*, 4326−4333.
8. Maget-Dana, R.; Ptak, M. *J. Colloid Interface Sci.* **1992**, *153*, 285−291.
9. Liu, W.; Guo, X.; Guo, R. *Int. J. Biol. Macromol*. **2007**, *41*, 548–557.
10. Löwenich, D.; Kleinermanns, K. *Photochem. Photobiol*. **2007**, *83*, 1308−1312.
11. Mondal, S.; Das, B. *Spectrochim. Acta A Mol. Biomol. Spectrosc*. **2018**, *198*, 278−282.
12. Zou, A.; Liu, J.; Jin, Y.; Liu, F.; Mu, B. *J. Disper. Sci. Technol*. **2014**, *35*, 48–55.

List of Publications

1. **Verma**, **I.**; Valsala Selvakumar, S. L.; Pal, S. K. Surfactin Laden Aqueous-Liquid Crystal Interface Enabled Identification of Secondary Structure of Proteins. *J. Phys. Chem. C* **2019**. DOI: 10.1021/acs.jpcc.9b10275.

2. **Verma**, **I.**; Devi, M.; Sharma, D.; Nandi, R.; Pal, S. K. Liquid Crystal based Detection of Pb (II) ions using Spinach RNA as Recognition Probe. *Langmuir* **2019**, *35*, 7816-7823.

3. **Verma**, **I.**; Pani, I.; Sharma, D.; Maity, S.; Pal, S. K. Label-free Imaging of Fibronectin Adsorption at Poly-L-lysine Decorated Liquid Crystal Droplets. *J. Phys. Chem. C* **2019**, *123*, 13642-13650.

4. **Verma**, **I.**; Rajeev, N.; Mohiuddin, G.; Pal, S. K. Ordering Transitions in Liquid Crystals Triggered by Bioactive Cyclic Amphiphile: Potential Application in Label-Free Detection of Amyloidogenic Peptides. *J. Phys. Chem. C* **2019**, *123*, 6526-6536.

5. **Verma**, **I.**; Sidiq, S.; Pal, S. K. Protein Triggered Ordering Transitions in Poly-L-lysine Coated Liquid Crystal Emulsion Droplets. *Liq. Cryst*. **2019**, *46*, 1318-1326.

6. **Verma**, **I.**; Sidiq, S.; Pal, S. K. Poly-L-lysine Coated Liquid Crystal Droplets for Sensitive Detection of DNA and Their Applications in Controlled Release of Drug Molecules. *ACS Omega* **2017**, *2*, 7936-7945.

7. **Verma**, **I.**; Sidiq, S.; Pal, S. K. Detection of Creatinine using Surface-Driven Ordering Transitions of Liquid Crystals. *Liq. Cryst*. **2016**, *43*, 1126-1134.

8. Sidiq, S.; **Verma**, **I.**; Pal, S. K. pH-Driven Ordering Transitions in Liquid Crystal Induced by Conformational Changes of Cardiolipin. *Langmuir* **2015**, *31*, 4741−4751.

Conferences/Workshops

1. Poster presentation titled " Liquid Crystal Based Simple System to Detect Secondary Structure of Proteins" at 25th National Conference on Liquid Crystals (NCLC) held in October, 2019 at Chitkara University, Punjab.
2. Poster presentation titled "Poly-L-lysine coated liquid crystal droplets for sensitive detection of DNA and their applications in controlled release of drug molecules" at International Liquid Crystal Conference held in July, 2018 at Kyoto, Japan.
3. Poster Presentation entitled "Design of a novel strategy based on liquid crystal to detect biologically important events" at International Conference on Frontiers in Chemical Sciences held at IIT-Guwahati in December, 2018.
4. Poster presentation titled "Poly-L-lysine coated liquid crystal droplets for sensitive detection of DNA and their applications in controlled release of drug molecules" at ACS on Campus India Roadshow held in February, 2018 at IISER Mohali, Mohali.
5. Poster presentation titled "Poly-L-lysine coated liquid crystal droplets for detection and quantification of bovine serum albumin, concanavalin A and cathepsin D" in 24th NCLC held in October, 2017 at IISER Mohali, Mohali.
6. Oral presentation on "Biocompatible liquid crystal droplets inducing slow drug release from DNA" in 23rd NCLC held in December, 2016 at ISM-IIT Dhanbad.
7. Poster presentation titled "Detection of creatinine using surface-driven ordering transitions of liquid crystals" in 3rd International Conference of Young Researchers on Advanced Materials (IUMRS-ICYRAM) held at Indian Institute of Science, Bangalore in December, 2016.
8. Poster presentation titled "pH responsive liquid crystal-based sensor for monitoring of enzymatic catalysis of creatinine" in 21st NCLC held at VSSD College, Kanpur in November 2014.
9. Attended "Science of Synthesis" workshop (Thieme) held at IISER Mohali on September 7, 2019.
10. Attended a workshop on "Academic Publishing for Quality Research: How to Get Published & Avoid Pitfalls" organized by Wiley at IISER Mohali on December 7, 2019.

Honors, awards and recognitions

1. The Dewan Jawahar Lal Nayar Memorial prize for best poster at 21st National Conference on Liquid Crystals (NCLC-21) in Nov, 2014 held at VSSD College, Kanpur.

2. Liquid crystal picture selected as the featured artwork of June 2018 at International Liquid Crystal Society's website.

Featured Artwork

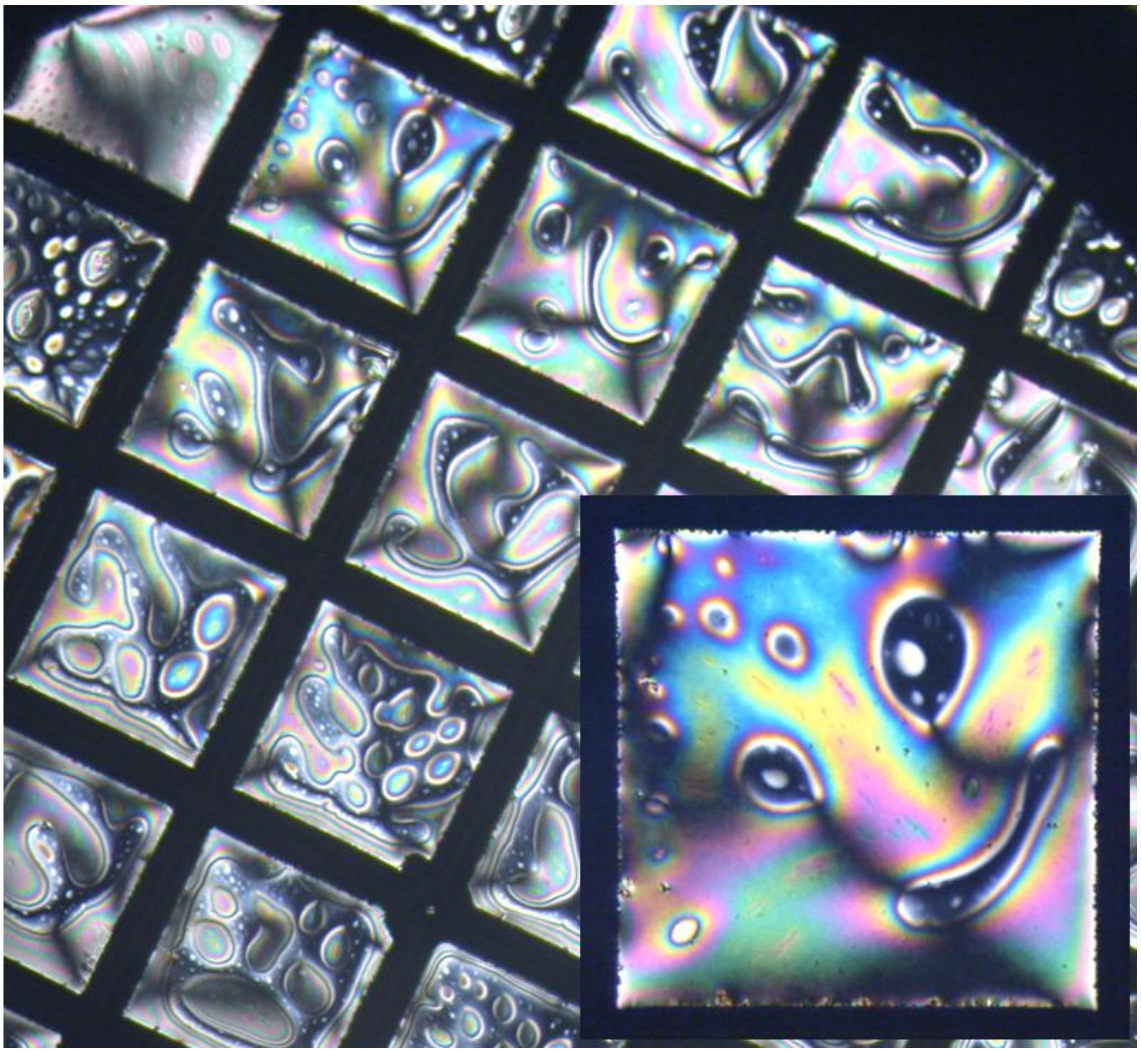

Link: https://www.ilcsoc.org/art-contest/gallery/page-24/#june.

Description: Organization of a well ordered protein at nematic liquid crystal (LC)-aqueous interface led to the perturbation of pre-adsorbed monolayer of amphiphilic molecules at the interface in a patterned and systematic fashion. The colorful regions (tilted alignment of LC at interface) correspond to protein rich areas while the dark domains (homeotropic alignment of LC) correspond to amphiphile rich areas. The LC was confined within a transmission electron microscopy grid of 20 μm thickness. The images were captured using a Zeiss polarising microscope Scope.A1 with cross polars (×50 and x100)

Jury comment: A collage of liquid crystal "smilies" is nicely composed and surprises with a rich variety of forms.

VITA

Indu Verma

Indu Verma was born and raised in Hapur, a small town of Uttar Pradesh, where she did her schooling. In 2009, she joined IISER Mohali as BS-MS student based on her IIT-JEE rank. She was awarded INSPIRE Scholarship by Department of Science and Technology, Govt. of India from 2009 to 2014. In her MS thesis, she worked under the mentorship of Dr. Angshuman Roy Choudhury studying co-crystallization of active pharmaceutical drugs ingredients with organic acids. She graduated in 2014, receiving Integrated BS-MS degree with majors in Chemistry. She had successfully qualified GATE (Chemistry) in 2014. In the same year, Indu joined IISER Mohali for Ph.D. program through direct admission and began working under the guidance of Dr. Santanu Kumar Pal in August 2014. Her research interest includes the design of stimuli-responsive interfaces formed between liquid crystals and aqueous phases for applications in label-free biosensing. During her Ph.D. program, Indu attended several national conferences and an international conference where she presented her work as poster/oral presentations. She has authored and co-authored eight publications in reputed peer-reviewed international journals.